# Engineering biomass combustion fly-ash derived zeolites for post-combustion CO<sub>2</sub> capture

A Thesis Submitted for the Degree of Doctor of Philosophy

By

Ben A. Petrovic

Department of Chemical Engineering, Brunel University London

2024

#### **Abstract**

Mitigation of CO<sub>2</sub> emissions through the use of carbon removal technologies is widely recognised as a pivotal tool on the path to net-zero GHG emissions. Beyond these targets, net-negative emissions will be essential to stabilise global temperatures. Technologies such as bioenergy with carbon capture and storage, considered a net-negative emission technology is therefore poised for a significant share in the power generation mix. However, this is associated with the production of a significant quantity of waste ash residues such as fly ash. Valorisation of this waste stream provides an opportunity to simultaneously mitigate the requirement for waste disposal (i.e. landfilling) and provide a pathway to value-added products, zeolites. In this thesis, industrially produced biomass combustion fly ashes have been comprehensively characterised and subsequently investigated for their potential as zeolite precursors. Suitable design of experiment techniques have been employed to systematically assess the influence of various factors on the alkaline fusion assisted hydrothermal synthesis to maximise the CO<sub>2</sub> equilibrium adsorption capacity. The bulk biomass combustion fly ash has been shown to present a CO<sub>2</sub> adsorption capacity of over 1.8 mmol·g<sup>-1</sup> at 50 °C and 1 bar, with a stable capacity of 87% of that after 40 cycles. This adsorbent was then produced at a larger scale to facilitate breakthrough performance assessments in a fixed-bed temperature swing adsorption system designed and built during this research. The process was optimised via Taguchi design of experiment to reveal the influential factors on the bed utilisation efficiency. The results indicate a usable bed capacity of approximately 0.6 mmol·g<sup>-1</sup> corresponding to a bed utilisation efficiency of 62% under the optimal factor and level configuration. These findings underscore the feasibility of industrial biomass combustion fly ashes as feedstocks in the preparation of zeolitic adsorbents/catalyst for post-combustion CO<sub>2</sub> capture.

#### **Peer-reviewed Journal Publications**

- Ben Petrovic, Mikhail Gorbounov, Salman Masoudi Soltani. Influence of surface modification on selective CO<sub>2</sub> adsorption: A technical review on mechanisms and methods. *Microporous and Mesoporous Materials*. 2021; Vol. 312, January 2021:110751. DOI: 10.1016/j.micromeso.2020.110751
  - BP (1<sup>st</sup>/lead Author): Writing (Original Draft & Editing); MG (2<sup>nd</sup>/contributing author): Writing (Original Draft & Editing); SMS (corresponding author): Supervision, Funding Acquisition, Writing (Review & Editing), Resources, Conceptualisation, Project Administration.
- Ben Petrovic, Mikhail Gorbounov, Salman Masoudi Soltani. Impact of Surface Functional Groups and Their Introduction Methods on the Mechanisms of CO<sub>2</sub> Adsorption on Porous Carbonaceous Adsorbents. Carbon Capture Science and Technology. 2022; Vol. 3, June 2022:100045. DOI: 10.1016/j.ccst.2022.100045
  - BP (1<sup>st</sup>/lead Author): Writing (Original Draft & Editing); MG (2<sup>nd</sup>/contributing author): Writing (Original Draft & Editing); SMS (corresponding author): Supervision, Funding Acquisition, Writing (Review & Editing), Resources, Conceptualisation, Project Administration.
- Mikhail Gorbounov, Jessica Taylor, Ben Petrovic, Salman Masoudi Soltani. To DoE or not to DoE? A Technical Review on & Roadmap for Optimisation of Carbonaceous Adsorbents and Adsorption Processes. South African Journal of Chemical Engineering. 2022; Vol. 41, July 2022, pp. 111–28. DOI: 10.1016/j.sajce.2022.06.001
  - MG (1<sup>st</sup>/lead Author): Writing (Original Draft & Editing); JT (2<sup>nd</sup>/contributing author): Writing (Original Draft & Editing); BP (3<sup>rd</sup>/contributing author): Writing (Original Draft & Editing); SMS (corresponding author): Supervision, Funding Acquisition, Writing (Review & Editing), Resources, Conceptualisation, Project Administration.
- Mikhail Gorbounov, Ben Petrovic, Serap Ozmen, Peter Clough, Salman Masoudi Soltani. Activated carbon derived from Biomass combustion bottom ash as solid sorbent for CO<sub>2</sub> adsorption. Chemical Engineering Research and Design. 2023; Vol. 194, June 2023, pp. 325–343. DOI: 10.1016/j.cherd.2023.04.057.
  - MG (1<sup>st</sup>/lead Author): Writing (Original Draft & Editing), Methodology, Investigation, Data Analysis, Material Characterisation; BP (2<sup>nd</sup>/contributing author): Methodology, Investigation, Data Analysis, Material Characterisation; SO (3<sup>rd</sup>/contributing author) Material Characterisation; PC (4<sup>th</sup>/contributing author) Resources, Material Characterisation; SMS (corresponding author): Supervision, Funding Acquisition, Writing (Review & Editing), Resources, Conceptualisation, Project Administration.
- 5. **Ben Petrovic,** Mikhail Gorbounov, Salman Masoudi Soltani. Synthesis of biomass combustion fly ash derived zeolites for CO<sub>2</sub> adsorption: Optimisation of hydrothermal synthetic pathway. *Carbon Capture Science & Technology*. 2024 Sep 1. DOI: 10.1016/j.ccst.2024.100245.

**BP** (1<sup>st</sup>/lead author): Writing (Original Draft & Editing), Conceptualisation, Methodology, Investigation, Formal Analysis, Validation, Visualisation; **MG** (2<sup>nd</sup>/contributing author): Methodology; Validation; Visualisation; **SMS** (corresponding author): Supervision, Funding Acquisition, Writing (Review & Editing), Resources, Conceptualisation, Project Administration.

#### **Peer-reviewed Conference Proceedings**

- Ben Petrovic, Mikhail Gorbounov, Abhishek Lahiri, Salman Masoudi Soltani. Biomass Combustion Fly Ash-Derived Nanoporous Zeolites for Post-Combustion Carbon Capture. 2021. In: 2021 IEEE 21st International Conference on Nanotechnology (NANO). IEEE; 2021. p. 233–236. DOI: 10.1109/NANO51122.2021.9514342
  - BP (1<sup>st</sup>/lead Author): Writing (Original Draft & Editing), Methodology, Investigation, Data Analysis, Material Characterisation; MG (2<sup>nd</sup>/contributing author): Methodology, Investigation, Data Analysis, Material Characterisation; AL (3<sup>rd</sup>/contributing author) Material Characterisation; SMS (corresponding author): Supervision, Funding Acquisition, Writing (Review & Editing), Resources, Conceptualisation, Project Administration.
- Mikhail Gorbounov, Ben Petrovic, Abhishek Lahiri, Salman Masoudi Soltani. Application of Nanoporous Carbon, Extracted from Biomass Combustion Ash, in CO<sub>2</sub> Adsorption. 2021. In: 2021 IEEE 21st International Conference on Nanotechnology (NANO). IEEE; 2021. p. 229-232. DOI: 10.1109/NANO51122.2021.9514288
  - MG (1<sup>st</sup>/lead Author): Writing (Original Draft & Editing), Methodology, Investigation, Data Analysis, Material Characterisation; BP (2<sup>nd</sup>/contributing author): Methodology, Investigation, Data Analysis, Material Characterisation; AL (3<sup>rd</sup>/contributing author) Material Characterisation; SMS (corresponding author): Supervision, Funding Acquisition, Writing (Review & Editing), Resources, Conceptualisation, Project Administration.
- 3. Ben Petrovic, Mikhail Gorbounov, Serap Ozmen, Peter Clough, Salman Masoudi Soltani. Synthesis of Nanoporous Type A and X Zeolite Mixtures from Biomass Combustion Fly Ash for Post-Combustion Carbon Capture. In: 2022 IEEE 22nd International Conference on Nanotechnology (NANO). IEEE; 2022; p. 221–224. DOI: 10.1109/NANO54668.2022.9928679
  BP (1st/lead Author): Writing (Original Draft & Editing), Methodology, Investigation, Data Analysis, Material Characterisation; MG (2nd/contributing author): Methodology, Investigation, Data Analysis, Material Characterisation; SO (3rd/contributing author) Material Characterisation; PC (4th/contributing author) Resources, Material Characterisation; SMS (corresponding author): Supervision, Funding Acquisition, Writing (Review & Editing), Resources, Conceptualisation, Project Administration.
- Mikhail Gorbounov, Ben Petrovic, Serap Ozmen, Peter Clough, Dilyara Bekmuratova, Salman Masoudi Soltani. Development of Nanoporosity on a Biomass Combustion Ash-derived Carbon for CO<sub>2</sub> Adsorption. In: 2022 IEEE 22nd International Conference on Nanotechnology (NANO). IEEE; 2022. p. 245–248. DOI: 10.1109/NANO54668.2022.9928660
  - MG (1<sup>st</sup>/lead Author): Writing (Original Draft & Editing), Methodology, Investigation, Data Analysis, Material Characterisation; BP (2<sup>nd</sup>/contributing author): Methodology, Investigation, Data Analysis, Material Characterisation; SO (3<sup>rd</sup>/contributing author) Material Characterisation;

PC (4<sup>th</sup>/contributing author) Resources, Material Characterisation; **DB** (5<sup>th</sup>/contributing author) Investigation; **SMS** (corresponding author): Supervision, Funding Acquisition, Writing (Review & Editing), Resources, Conceptualisation, Project Administration.

#### **Oral Presentations at Conferences**

- 1. **Ben Petrovic,** Mikhail Gorbounov, Salman Masoudi Soltani. Biomass Combustion Ash in CO<sub>2</sub> Capture. UKCCSRC Spring 2021 Conference, 20-21 April 2021, Sheffield, UK.
- 2. **Ben Petrovic**, Mikhail Gorbounov, Abhishek Lahiri, Salman Masoudi Soltani. Biomass Combustion Fly Ash-Derived Nanoporous Zeolites for Post-Combustion Carbon Capture. 21st IEEE International Conference on Nanotechnology, 28-30 July 2021, online
- 3. **Ben Petrovic**, Mikhail Gorbounov, Serap Ozmen, Peter Clough, Salman Masoudi Soltani. Synthesis of Nanoporous Type A and X Zeolite Mixtures from Biomass Combustion Fly Ash for Post-Combustion Carbon Capture. 22nd IEEE International Conference on Nanotechnology, 4-8 July 2022, Mallorca, Spain.

#### **Declaration**

I do solemnly declare that all the material presented and contained in this thesis is my original work.

I do solemnly declare that the materials from this thesis have not been used in any other submission for fulfilment of any academic award.

I do solemnly declare that whilst being registered as a candidate for the research degree at Brunel University of London, I have not been a registered nor an enrolled student for another award at Brunel University of London or any other professional/academic institution.

I do solemnly declare that I have undertaken the programme of studies related to and in connection with the programme of research following the requirements associated with my research degree registration.

#### Acknowledgement

I am grateful to my supervisory team for their guidance and support during my PhD. To my first supervisor, Dr Salman Masoudi Soltani, thank you for your advice, guidance, and encouragement; the journey has been arduous but I'm incredibly grateful all the same. I also thank Dr George Fern, my second supervisor and Dr Peter Hewitson, my Research Development Adviser, for ensuring my continued academic career at Brunel was a supported and prosperous one.

Secondly, I want to thank the entirety of the staff within the Chemical Engineering Department and the Experimental Techniques Centre.

I want to acknowledge the UK Carbon Capture and Storage Research Centre (UKCCSRC) for their unwavering support of this research and for connecting me with a wider research community. I also thank the representatives from Drax, Dr James Hammerton, Dr Jeni Reeve and Dr Ben Dooley for their insights, collaboration, and of course, ash.

To my research group, thank you for the collaboration and support that made this journey more productive but mostly, more enjoyable.

Finally, I am deeply grateful to my family for their unwavering support. Thank you for your patience and encouragement throughout this process.

## **Table of Contents**

Abstract	2
Peer-reviewed Journal Publications	3
Peer-reviewed Conference Proceedings	5
Oral Presentations at Conferences	
Declaration	
Acknowledgement	
Table of Contents	
Table of Figures	
Table of Tables	
List of Acronyms	
·	
1. Introduction	
1.1. Global Warming and the Climate Crisis	
1.2. The Abatement of Greenhouse Gas Emissions	
1.2.1. Post-Combustion Carbon Capture Processes	
1.3.1. Materials for CO <sub>2</sub> Capture <i>via</i> Adsorption	
1.3.2. Biomass Combustion Ash as an Adsorbent Precursor: Research Motivation	
1.4. Research Aim and Objectives	30
1.5. Thesis Outline	30
2. Literature Review	31
2.1. Carbon Capture and Storage Technologies	31
2.1.1. Pre-combustion Carbon Capture	
2.1.2. Oxy-fuel Combustion	
2.1.3. Post-combustion Carbon Capture	
2.2.1. Physical Adsorption	
2.2.2. Adsorbent Materials	
2.2.3. Equilibrium	
2.2.3.1. Isotherm Models	
2.2.4. Rate Phenomena	
2.2.4.1. Adsorption Kinetics	
2.2.5. Fixed Bed Adsorption	
2.2.5.2. Heat Transfer	
2.2.5.3. Pressure Drop	
2.2.5.4. Dispersion	
2.3. Biomass Combustion Products	
2.4. Zeolite Synthesis and Development	
2.4.1. Fly Ash Zeolites	45

	2.4.2. Biomass Combustion Fly Ash Utilisation Challenges	
	2.4.3. Biomass Fly Combustion Fly Ash Zeolites in CO <sub>2</sub> Capture	
	.5. Synthesis of Zeolitic Materials from Biomass Combustion Fly Ash	48
	2.5.1. Hydrothermal Synthesis	
	2.5.2. Alkaline Fusion	
	.6. Key variables in Alkaline Fusion Assisted Hydrothermal Synthesis	
	2.6.1. NaOH to Fly Ash Ratio	
	<ul><li>2.6.2. Hydrothermal Temperature</li><li>2.6.3. Hydrothermal Time</li></ul>	
	2.6.4. Liquid to Solid Ratio	
	2.6.5. Other Factors	
	.7. Statistical Design of Experiments	52
	2.7.1. Designs	53
	2.7.2. Statistical Analysis	54
	2.7.3. Design Of Experiments in the Synthesis of Biomass Combustion Fly Ash Derived	
	Zeolites 55  8. Research Gap	56
3.	Characterisation Methods	
Э.		
	.1. Material Characterisation	
	.2. Scanning Electron Microscopy and Energy Dispersive X-ray Spectroscopy	
	.3. Fourier Transform Infrared Spectroscopy	
	.4. X-ray Diffraction	59
	.5. Particle Size Analysis	60
	.6. Surface Area and Porosity	60
	.7. Thermogravimetric Analysis	61
	3.7.1. Proximate Analysis and Decomposition	62
	3.7.2. Adsorption and Desorption Analysis	
	.8. Adsorption Kinetics	63
	.9. Volumetric Equilibrium Gas Adsorption	63
	.10. Adsorbent Selectivity	64
	.11. Enthalpy of Adsorption	65
	.12. Compressive Strength	65
	.13. Design of a Fixed-bed Reactor	65
	3.13.1. Design Intent	
	3.13.2. Final Design	
	3.13.3. Piping & Instrumentation Diagram	
	3.13.3.1. Node 1 – Synthesising Simulated Flue Gas	
	3.13.3.2. Node 2 – Fixed-bed Reactor	69
	3.13.3.3. Node 3 – Gas Analysis	70
	3.13.1. Reactor Control	
4.	Characterisation of Biomass Combustion Fly Ash	72
	1 Introduction	72

4	4.2.	Surface Morphology Analyses	73
	4.1.	Elemental Analysis	75
	4.2.	Proximate Analysis	77
	4.3.	Phase Identification	78
	4.4.	Thermogravimetric Analysis	81
	4.5.	Fourier Transform Infrared Spectroscopy	84
	4.6.	Particle Size Analysis	85
	4.7.	Pore Structure and Surface Area	85
	4.8.	Carbon Dioxide Adsorption	87
	4.9.	Conclusions and Potential Routes for Application in CO <sub>2</sub> Separation	88
5. De	•	ynthesis, Characterisation and Performance Evaluation of Biomass Combustion Fly A	
	5.1.	Introduction	90
	5.2.	Influence of NaOH/FA Ratio	91
	5.2	2.1. Phase Identification of Initial Products	92
		2.2. Product Morphology – Initial NaOH/FA Ratio Investigation	
		2.3. Elemental Composition Estimated <i>via</i> EDS – Initial NaOH/FA Ratio Investigation  Taguchi Optimisation	
•		3.1. Phase Identification from the Taguchi Optimisation	
		3.2. Product Morphology – Taguchi Optimisation	
	5.3	3.3. Elemental Composition Estimated <i>via</i> EDS – Taguchi Optimisation	
	5.4.	Impact of Fly Ash on Zeolite Product	103
		Porosity and Surface Area Analysis	
	5.6.	Adsorption Equilibria	105
	5.7.	Adsorption Kinetics	107
	5.8.	Enthalpy of Adsorption	109
;	5.9.	Working Capacity	109
;	5.10.	. Conclusion	110
6.	Sc	cale-up and Structuring of Fly Ash Derived Zeolites	112
(	6.1.	Introduction	112
(	6.2.	Impact of Stirring Conditions	112
	6.2	2.1. Analysis of Surface Morphology	
	_	2.2. Phase Identification	
•		Impact of Degree of Washing	
		3.1. Analysis of Surface Morphology	
(		Scale-up Quality	
	6.5.	Thermal Stability of Fly Ash Zeolites	
		Powder Extrusion with Kaolin Binder	
		6.1. Compressive Strength Testing	
		6.2. Pellet Adsorption Capacity	

6.6.3. Pellet Adsorption Kinetics	123
6.6.4. Surface Morphology	125
6.6.5. Elemental Composition – EDS	
6.6.6. Phase Identification	
6.7. Conclusion	128
7. Lab-scale Fixed-bed Adsorption of CO <sub>2</sub> by Biomass Combustion Fly Ash Derived Z 130	eolites
7.1. Introduction	130
7.2. Binderless Wet Granulation	130
7.3. Surface Morphology – Comparison	131
7.4. Elemental Composition via Energy Dispersive X-ray Spectroscopy - Comparison	132
7.5. Apparent BET Surface Area – Comparison	133
7.6. Equilibrium CO <sub>2</sub> Adsorption	134
7.7. Adsorption Kinetics - Comparison	136
7.8. Enthalpy of Adsorption	138
7.9. Working Capacity	139
7.10. Adsorbent Selectivity – CO <sub>2</sub> /N <sub>2</sub>	139
7.11. Assessment of Operating Variables on Adsorption Breakthrough	140
7.11.1. Taguchi L9 OA	141
7.11.2. Breakthrough Optimisation and Statistical Analysis	
7.11.3. Analysis of Variance	
7.11.4. Validation Experiments	
7.12. Conclusion	149
8. Conclusions & Future Work	151
8.1. Conclusions	151
8.2. Future Work	152
9. References	154
Appendix A – CO <sub>2</sub> Adsorption Isotherms	188
Appendix B – 2 Adsorption Isotherms	192
Appendix C - N <sub>2</sub> Adsorption/Desorption Isotherms at 77K	194

# **Table of Figures**

Figure 1.1: Contribution of each gas to the UK GHG inventory, 2023.
Figure 1.2: UK emission inventory (MtCO <sub>2</sub> equivalent) by sector between 1990 and 2023 [4]24
Figure 1.3: Position of biomass varieties and solid fossil fuels in the chemical classification system [36]
29
Figure 2.1: Basic schematic of pre-combustion carbon capture
Figure 2.2: Basic schematic of an oxy-fuel combustion process
Figure 2.3: Basic schematic of post-combustion CO2 capture
Figure 2.4: IUPAC classification of isotherms [59,60]
Figure 3.1: A typical programme sequence employed to analyse the adsorption of CO <sub>2</sub> via TGA62
Figure 3.2: Final process design schematic of the fixed-bed reactor designed, built, commissioned and
tested in this work6
Figure 3.3: Revised piping & instrumentation diagram for the fixed-bed reactor after completion of th
risk assessment process66
Figure 3.4: State machine schematic for the developed fixed-bed reactor control system
Figure 4.1:BFA SEM: a) 10kV, 500pA and 0.5kX magnification; b) 10kV, 500pA and 0.5kX
magnification; c) 20kV, 500pA and 2kX magnification; d) 10kV, 500pA and 2kX magnification; e
10kV 500pA and 1kX magnification; f) 10kV, 500pA and 3kX magnification7.
Figure 4.2: BFA SEM: a) 20kV, 300pA and 1kX magnification; b) 20kV, 300pA and 2kX
magnification; c) 10kV, 50pA and 3kX magnification; d) 10kV, 100pA and 3kX magnification74
Figure 4.3: BFA SEM: a) 20kV, 300pA and 3kX magnification; b) 20kV, 300pA and 5kX
magnification; c) 10kV, 50pA and 10kX magnification; d) 20kV, 50pA and 15kX magnification7
Figure 4.4: Powder X-ray Diffractograms of the four fly ash batches
Figure 4.5: Thermogravimetric analysis and derivative thermogravimetric curves of the four fly as
batches. Tests conducted with a ramp rate of 10 °C/min from 25 to 1100 °C. Gas atmospheres air (top)
nitrogen (middle) and carbon dioxide (bottom).
Figure 4.6: FTIR spectrum of biomass combustion fly ash (FA1).
Figure 4.7: Particle size analysis of the as-received fly ash measuring using a Beckman Coulter LS230
Red line representing the differential volume (left y-axis); black line representing the cumulative
volume (right y-axis)
Figure 4.8: Nitrogen adsorption/desorption isotherms measured at 77K; linear BET plot provided as a
inset, datapoints coloured red are not included in the model fitting.
Figure 4.9: Pore size distribution plot of FA1.
Figure 4.10: Equilibrium CO <sub>2</sub> adsorption isotherms measured at 273K for the four FA batches, with th
Sips isotherm model fit
Figure 5.1: Diffractograms of the products produced during the initial NaOH/FA ratio study9

Figure 5.2: SEM images of ZF1-2.0/4/90 produced with an accelerating voltage of 15 kV94
Figure 5.3: Main effects plots for SNRs and data means from the Taguchi L9 DoE99
Figure 5.4: Contour plots of CO <sub>2</sub> uptake for a) L/S vs T <sub>cry</sub> ; b) t <sub>cry</sub> vs T <sub>cry</sub> ; c) t <sub>cry</sub> vs L/S9
Figure 5.5: Powder x-ray diffractogram for crystalline zeolites produced in the L9 OA and the predicte
optimum, ZOPT. Diffractograms provided for type X and type A zeolites adjacent to the x-axis 100
Figure 5.6: SEM images of ZOPT-2.2/10/90/5 at 2500x (left) and 3300x (right) magnification10
Figure 5.7: SEM images of ZOPT-2.2/10/90/5 at higher magnification
Figure 5.8: N <sub>2</sub> adsorption/desorption isotherm measured at 77 K (BET) with the linear BET plot (inset)
Figure 5.9: Equilibrium CO <sub>2</sub> adsorption isotherms (discrete) and the fitted Toth isotherm mode (continuous line)
Figure 5.10: ZOPT CO <sub>2</sub> adsorption kinetic model fitting; PFO, PSO, Elovich and W&M Intraparticl Diffusion model shown
Figure 5.11:CO <sub>2</sub> adsorption kinetics (ZOPT) at 50 °C and 1 bar fitted with three Intraparticle Diffusion model functions
Figure 5.12: Adsorption enthalpy ZOPT-CO <sub>2</sub> estimated using Toth isotherm model fit
Figure 5.13: Working CO <sub>2</sub> adsorption capacity of the optimised BFA-derived zeolite. Adsorption at 5
°C, 100 mol%CO <sub>2</sub> at 1 atm for 2 h; desorption at 150 °C, 100 mol%N <sub>2</sub> at 1 atm for 1 h
Figure 6.1: SEM images of ZOPT-ST8 (top) and ZOPT-ST10 (bottom); accelerating voltage 15kV
Figure 6.2: Powder x-ray diffractograms of samples produced during assessment of stirring conditions ZOPT-2.2/90/10/5 provided for comparison.
Figure 6.3: Scanning electron images of ZOPT-PH7 (left) and ZOPT-PH11 (right). Accelerating voltag of 10 kV.
Figure 6.4: Powder x-ray diffractograms of samples produced during assessment of washing degree
Figure 6.5: Yield and CO <sub>2</sub> adsorption capacity of the replicate ZOPT batches. Capacity estimated vi
TGA at 50 °C, 1 bar CO <sub>2</sub> after degassing for 1 under N <sub>2</sub> .
Figure 6.6: Weight change of the bulk ZOPT adsorbent during high temperature desorption and 50 °C adsorption
Figure 6.7: CO <sub>2</sub> adsorption kinetics at 50 °C and 1 bar for the dried extrudates (left) and calcined (right)
The dashed line represents the experimental data and the solid line the fitted Elovich kinetic mode
Figure 6.8: Scanning electron microscope images of ZOPT-0K-D (left) and ZOPT-0K-C (right) 12:
Figure 6.9: Scanning electron microscope images of ZOPT-45K-D (left) and ZOPT-45K-C (right).12

Figure 6.10: Powder x-ray diffractograms of the extruded biomass ash derived fly ash zeolite
adsorbents; diffractograms of the bulk ZOPT sample and 100 wt% kaolin provided for comparison.
128
Figure 7.1: Scanning electron microscope images of the bulk ZOPT powder (left) and the bulk ZOPT
granule (right)
Figure 7.2: N <sub>2</sub> adsorption/desorption isotherm measured at 77 K; linear BET plot (inset). Produced for
bulk ZOPT adsorbent
Figure 7.3: Equilibrium CO <sub>2</sub> adsorption isotherms for measured volumetrically for ZOPT-BULK 135
Figure 7.4: CO <sub>2</sub> adsorption vs time measured via TGA at 50 °C for the granulated and powder form of
ZOPT-BULK. The dashed line represents the experimental data and the solid line the fitted Elovich
model
Figure 7.5: The enthalpy of adsorption determined between CO2 and ZOPT-BULK via analysis of the
equilibrium adsorption isotherms (Toth) between 0 and 50 °C up to 1 bar(a)
Figure 7.6: Working capacity of ZOPT-BULK estimated via TGA simulating a TSA cycle in the
temperature range of 50(CO2) and 150 °C (N2) at 1 bar(a)
Figure 7.7: Equilibrium N <sub>2</sub> adsorption isotherms for ZOPT-BULK
Figure 7.8: Experimentally determined CO2 fixed-bed adsorption breakthrough curves as per the
Taguchi L9 DoE. The inset graph is of the same datasets
Figure 7.9: Main effects plots for the SNR ratios with the objective of maximising usable bed adsorption
capacity
Figure 7.10: Main effects plots for the SNR ratios with the objective of maximising bed utilisation.
Figure 7.11: Normal probability plot of residuals for the 2 factor ANOVA
Figure 7.12: Breakthrough curves for the confirmation experiments conducted at factor and level
configurations of $v_s$ = 2 cm·s <sup>-1</sup> ; $C_0$ = 16 mol%; $T_A$ = 40 °C Error! Bookmark not defined.

## **Table of Tables**

Table 1: Physical properties of flue gas components
Table 2: Ash-derived zeolites in the published literature and their CO <sub>2</sub> adsorption capacities. *Capacity
estimated from isotherm plot; reproduced from [71]
Table 3-1 Kinetic models investigated for quality of fit in this thesis.:
Table 3-2 Equilibrium adsorption models investigated for quality of fit in this thesis
Table 3-3: Existing fixed-bed reactors used for the evaluation of ash-based sorbents
Table 4-1: Surface elemental composition of the four fly ash batches evaluated via EDS76
Table 4-2: Proximate analysis as per ASTM D3172
Table 4-3: Powder Diffraction Files (PDF) of the phases identified
Table 4-4: Equilibrium isotherm model fitting via non-linear regression results
Table 5-1: Experimental conditions employed in the initial alkaline fusion assisted hydrothermal study.
Uptake measured at 50 °C, 1 bar(a) measured via TGA
Table 5-2: Surface elemental composition of ZF1-2.0/4/90 evaluated via EDS (averaged over 10
different surface areas)95
Table 5-3: Factor and level configuration of the Taguchi L9 DoE
Table 5-4: Experimental conditions employed in the Taguchi L9 DoE. Uptake measured at 50 °C, 1
bar(a) measured via TGA95
Table 5-5: Response table for the signal to noise ratios
Table 5-6: ANOVA results for the Taguchi L9 design
Table 5-7: Surface elemental composition of ZOPT-2.2/10/90/5 evaluated via EDS averaged over 10
distinct sample areas
Table 5-8: Yield and uptake of samples produced at conditions 2.2/10/90/5 using FA1, FA2, FA3 and
FA4
Table 5-9: Textural properties of ZOPT estimated via the N <sub>2</sub> adsorption/desorption at 77K105
Table 5-10: Equilibrium isotherm model fitting via non-linear regression results
Table 5-11: Toth fitted isotherm model constants
Table 5-12: Adsorption kinetic model fitting via non-linear regression results
Table 6-1: Stirring conditions, yield and uptake of samples produced during synthesis method
adjustments. ZOPT provided in row 1 for comparison
Table 6-2: Washing conditions and uptake of samples produced during synthesis method adjustments.
ZOPT provided in row 1 for comparison
Table 6-3: Synthesis yields and CO <sub>2</sub> adsorption capacities from the 35 individual batches
Table 6-4: Adsorption capacities estimated via TGA after high temperature desorption. Adsorption at
50 °C, 100 mol%CO <sub>2</sub> at 1 atm for 2 h

Table 6-5: Samples produced during the pelletisation campaign investigating kaolin as binder for pell	et
extrusion and their associated radial crush strengths, N·mm <sup>-1</sup>	22
Table 6-6: Samples produced during the pelletisation campaign investigating kaolin as binder for pelletisation	et
extrusion and their associated equilibrium CO2 adsorption capacities estimated via TGA at 50 °C,	1
bar(a)	23
Table 6-7: Results of the biomass combustion fly ash zeolite pellets kinetic modelling. Experiment	al
data produced via TGA under at 50 °C, 1 bar CO <sub>2</sub>	24
Table 6-8: Elovich kinetic model constants estimated via non-linear regression	25
Table 6-9: Elemental composition of pelletised fly ash zeolites, estimated via EDS	27
Table 7-1: Elemental analysis estimated via EDS for the original ZOPT sample and the bulk-ZOF	Υ
adsorbent. 13	33
Table 7-2: Textural properties of ZOPT estimated via the $N_2$ adsorption/desorption at 77K	3
Table 7-3: Equilibrium isotherm model fitting via non-linear regression results	35
Table 7-4: Toth fitted isotherm model constants estimated via non-linear regression for ZOPT-BUL.	Κ.
13	36
Table 7-5: Results of the adsorption kinetic modelling for the bulk ZOPT adsorbent (powder) and the	he
derived bulk ZOPT granules; the model constants from the original ZOPT sample is provided f	or
comparison	36
Table 7-6: Elovich kinetic model constants estimated via non-linear regression for powdered an	ıd
granulated ZOPT-BULK	37
Table 7-7: Adsorption selectivity for ZOPT-OG and ZOPT-BULK at three temperatures. Pu	re
selectivity has been estimated at 1 bar(a) and the separation factor at 1 bar(a) adsorption pressures	15
mol% CO <sub>2</sub>	39
Table 7-8: Factors and levels employed in the Taguchi L9 OA investigating the adsorption proce	SS
configurations impact on bed adsorption capacity14	12
Table 7-9:Experimental design (Taguchi L9) with factor configurations for each run and associate	ed
results from analysis of the breakthrough curves14	12
Table 7-10: Response table for the SNR ratios with the objective of maximising usable bed adsorption	on
capacity14	14
Table 7-11: Response table for the SNR ratios with the objective of maximising bed utilisation 14	15
Table 7-12: Results of the ANOVA for the bed utilisation efficiency data means with three factor	ŝ.
	16
Table 7-13: Linear model analysis of the bed utilisation efficiency and the main effects of all thr	
factors	
Table 7-14: Results of the ANOVA for the bed utilisation efficiency data means with two factors14	

Table 7-15:Linear model analysis of the bed utilisation efficiency and the main effects with two factors			
147			
Table 7-16: Confirmation experiments conducted at the optimum design point which maximises the			
adsorption bed's usable capacity. The mean response and the associated standard deviation are also			
given			
Table 7-17: Linear Driving Force model fitting data for the breakthrough experiments defined as part			
of the L9 Taguchi OA and confirmation experiments Error! Bookmark not defined.			

#### **List of Acronyms**

ANOVA Analysis of variance

AFHT Alkaline-fusion hydrothermal

ASTM American society for testing and materials

ASU Air separation unit
BBD Box-Behnken design

BCP Biomass combustion product

BE Bioenergy

BECCS Bioenergy with carbon capture and storage

BET Brunauer–Emmett–Teller
BFA Biomass combustion fly ash

BFA Biomass fly ash

BJH Barrett-Joyner-Halenda

CAPEX Capital expenses
CAPEX Capital expenditure

CBU Composite building units
CCD Central composite design
CCS Carbon capture and storage

CCUS Carbon capture, utilisation and storage

CDR Carbon dioxide removal

CFA Coal fly ash

CI Confidence interval

DFT Density Functional Theory

DI Deionised

DTG Derrivative thermogravimetry

EDS Energy dispersive x-ray spectroscopy

FA Fly ash
FAU Faujasite

FBR Fixed-bed reactor

FGD Flue gas desulphurisation

FTIR Fourier transform infrared spectroscopy

GHG Greenhouse gas
HT Hydrothermal

IGCC Integrated gasification combined cycle

IPCC Intergovernmental panel on climate change

IPD Intraparticle diffusion

IUPAC International union of pure and applied chemistry

KPI Key performance indicator

LDF Linear driving force

LTA Linde type A

LUB Length of unused bed MEA Monoethanolamine

MOF Metal-organic framework

MTZ Mass transfer zone
OA Orthogonal array
OFAT One-factor-at-a-time
OPEX Operational expenses
OPEX Operating expenditure

PCCC Post-combustion carbon capture

PDF Powder diffraction file

PFO Pseudo-first order

PSA Pressure swing adsorption

PSO Pseudo-second order
PTFE polytetrafluoroethylene

PVSA (or VPSA) Vacuum-pressure swing adsorption

RMSE Root mean square error

RPM Revolutions per minute

RSD Relative standard deviation

RSM Response surface methodology

SEM Scanning electron microscopy

SNR Signal to noise ratio

TFM Modified PTFE

TGA Thermogravimetric analysis
TSA Temperature swing adsorption

TVSA Temperature-vacuum swing adsorption

UNFCC United Nations Framework Convention of Climate Change

VOC Volatile organic compounds VSA Vacuum swing adsorption

XRD X-ray diffraction
XRF X-ray fluorescence

#### 1. Introduction

#### 1.1. Global Warming and the Climate Crisis

Anthropogenic climate change has been attributed to the emission of greenhouse gases (GHG). Considering the extent of emission, CO<sub>2</sub> is considered the most significant of these gases [1], despite a Global Warming Potential of 1. The UK ratified the United Nations Framework Convention of Climate Change (UNFCC) in December 1993 establishing annual publication of national GHG emission inventories<sup>1</sup>. Annual emissions of CO<sub>2</sub> represent the bulk of the GHG inventory with the largest contributions coming from the generation of power and road transport. After ratification of the UNFCC in 1990, significant reductions in GHG emissions have been achieved as a result of fuel switching, structural change and a drive for efficiency improvements [2]. The Climate Change Act <sup>2</sup> that became Law in the UK on the 26<sup>th</sup> November 2008 however, set legally binding targets of an 80% reduction in GHG emission by 2050 compared to base levels (1990). Eleven years later, owing to the sustained public pressure in the UK, the UK government declared a climate emergency in June 2019 increasing this target to a 100% reduction of GHG emissions<sup>3</sup> compared to 1990 levels by the year 2050 [3]. In doing so, the UK became the first major global economy which had legislated for net-zero GHG emissions.

Figure 1.1 presents the emissions estimates in the UK's National Inventory Report submitted to the UNFCC in 2025 for the years between 1990 and 2023 [4] in terms of CO<sub>2</sub> equivalence based on global warming potentials. The largest share of these emissions by some distance is CO<sub>2</sub> itself at 78.7 %. If a rise in global temperature of over 2 °C is to be avoided as was set out in the Paris Agreement targets [5], technologies such as Carbon Capture and Storage (CCS) will be pivotal. Scenarios which are compatible with these ambitions rely on both emission reduction and net carbon dioxide removal (CDR) from the atmosphere [6]. Most integrated assessment models are unable to find a solution to meet these targets without the use of CCS [7]. Out of the some 114 scenarios assessed by the IPCC in their Fifth Assessment Report which lead to forcing values of around 2.6 Wm<sup>-2</sup> (likely probability for 2 °C), most (104) show net-CDR after 2050, mostly achieved by bioenergy with CCS (BECCS) [6]. The total CDR would be somewhere between 200 and 400 GtCO<sub>2</sub> through the 21<sup>st</sup> century or 10 GtCO<sub>2</sub> per year in 2100 [6]. Transition pathways, limiting temperature rise to 1.5 °C are consistently characterised by

<sup>-</sup>

<sup>&</sup>lt;sup>1</sup> Under the Kyoto Protocol

<sup>&</sup>lt;sup>2</sup> Climate Change Act 2008. Available at: https://www.legislation.gov.uk/ukpga/2008/27/contents

<sup>&</sup>lt;sup>3</sup> The Climate Change Act 2008 (2050 Target Amendment) Order 2019. Available at: https://www.legislation.gov.uk/ukdsi/2019/9780111187654

sharp and immediate reductions in CO<sub>2</sub> emissions (3 - 7% per year on average between 2030 and 2050) with sustained net-negative emissions (*i.e.* CDR) ranging between 1.3 - 29 Gt<sub>CO2</sub>yr<sup>-1</sup> post-2050 [8].

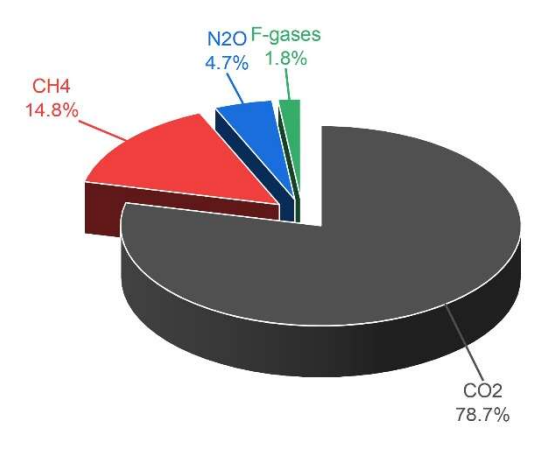


Figure 1.1: Contribution of each gas to the UK GHG inventory, 2023.

CCS as defined by the IPCC is a three-stage strategy for reducing CO<sub>2</sub> emissions encompassing the: separation; transportation; and storage of CO<sub>2</sub>. The first accounts for approximately two thirds of the total cost [9]. As a result, large-scale deployment of CCS has been rendered insurmountable even with governmental incentives and regulatory drivers such as the UK's Ten Point Plan<sup>4</sup> which features CCS as a breakthrough technology [10,11]. Considering the current situation, CCS is the only technology capable of delivering the reductions in GHG emissions from power generation but also from sectors which are considered notoriously difficult to decarbonise such as cement, iron and steel, refineries and the wider petrochemical industry.

#### 1.2. The Abatement of Greenhouse Gas Emissions

Sustainable energy policy aiming to mitigate the worst climate change scenarios features three pillars. The first seeks to maximise process efficiency; the 'low-hanging fruit' for emissions reductions as it requires the smallest investment/change and is often associated with a reduction in OPEX. The second describes adoption of alternative energy sources such as renewable and nuclear due to the lower level of associated CO<sub>2</sub> and other pollutant emissions [12]. Energy security, however, is a major challenge in this regard and the flexible dispatchability of fossil-fuelled thermal power cannot be replicated by either renewables or nuclear. The third approach is the capture of carbon dioxide and its' subsequent permanent storage. This acknowledges that in some areas, there will be a period where fossil fuel use is largely unavoidable. The thermal generation sector has already taken considerable strides towards

<sup>&</sup>lt;sup>4</sup> The UK's Ten Point Plan details mobilisation of £12B of government support with up to £1B allocated to point 8: *Investing in Carbon Capture, Usage and Storage.* 

increasing energy conversion efficiency; up to 2030 this sector is expected to have a considerable share in the European generation mix [13]. The EU energy strategy foresees a 40% carbon emission reduction and a 27 % share for renewables in primary energy consumption by 2030 [13]. Although there have been significant improvements with regards to emission reductions in the UK since 1990 (Figure 1.2), UK's GHG emissions totalled around 395 MtCO<sub>2</sub>e.

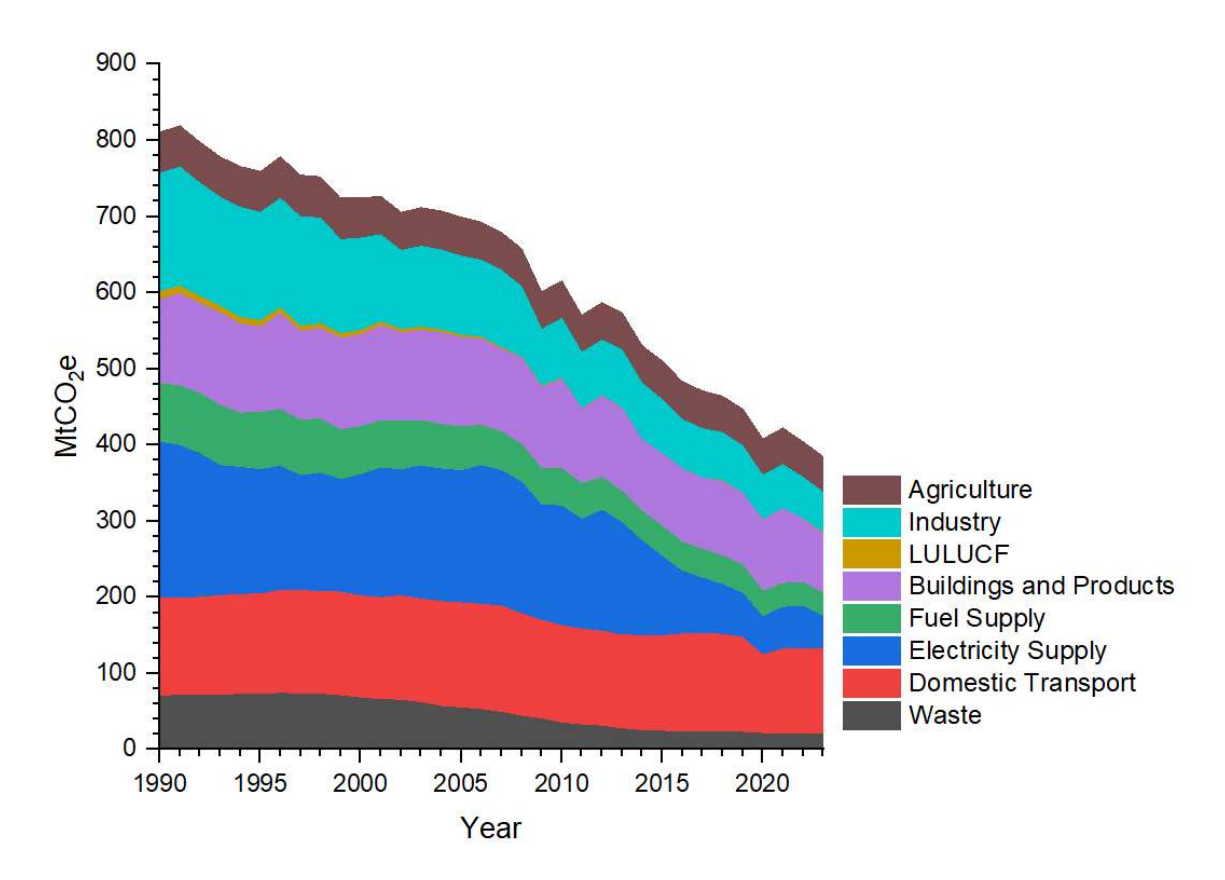


Figure 1.2: UK emission inventory (MtCO<sub>2</sub>equivalent) by sector between 1990 and 2023 [4].

Whilst it is possible to remove CO<sub>2</sub> directly from the air, the primary focus is the decarbonisation of large, single-point sources, *e.g.* fossil-fuel fired thermal power plants. Within this, three classes of 'capture' technologies exist: pre-combustion, oxyfuel combustion and post-combustion. Pre-combustion entails the removal of CO<sub>2</sub> from the fuel source prior to combustion or its conversion to syngas and is mainly employed in integrated gasification combined cycle (IGCC) plants, fertiliser or hydrogen production plants [14]; the greatest contribution to cost arises from the complex fuel conversion processes. The term oxyfuel combustion refers to the combustion of fuel in a mixture of oxygen and recycled flue gas. The oxygen is produced in an air separation unit *via* cryogenic distillation or other less energy-intense alternatives [15]. Post-combustion capture as the name suggests, comprises the removal of CO<sub>2</sub> from flue gases after combustion/conversion. Often considered the most viable among current technologies as it can be added to existing plants (*i.e.* retrofitted) without necessitating significant changes to the plant or process [16]. In thermal power generation plants, including fossil

fuel, biomass, municipal waste and other waste to energy plants, post-combustion capture is the typical route [13]. That said, a subset of emerging technologies including chemical looping combustion (CLC) offer alternative strategies for CO<sub>2</sub> separation at large point-sources. These technologies employ solid oxygen carriers for the indirect combustion of fuels which inherently produces a CO<sub>2</sub> stream of high purity thus negating the requirement for any downstream processing (as in the case for PCCC) [17]. Although promising, such technologies are considered lower TRL and necessitate further development before large-scale deployment [18].

Whilst CCS can deliver substantial reductions to the emissions of large, fossil-fuel reliant point sources, such interventions do not contribute to the reduction of atmospheric GHGs. Net removal of GHGs offers benefits extending the short-term. Over the medium to long-term, GGR can counter the residual emissions required to reach net-zero and ultimately facilitate the net-removal of CO<sub>2</sub> likely required for climate remediation. BECCS along with direct air capture (DAC) are currently considered the most scalable GGR technologies and Drax Power Station in the UK along with C-Capture are piloting the first BECCS facility in Europe. The Royal Society and Royal Academy of Engineering<sup>5</sup> have identified that even with significant emission reductions, around 130 MtCO<sub>2</sub> per year must be removed by GGR to achieve the 2050 net-zero ambitions; BECCS and DAC would need to account for over 50% of this. BECCS is a broad term for a group of multidisciplinary technologies involving capturing and storing CO<sub>2</sub> from processes in which biomass is either converted into various types of fuels (e.g. liquid biofuels) or directly burned to produce heat and power (direct biomass combustion). The Energy Technologies Institute<sup>6</sup> have estimated that by 2050, approximately 55 Mt of CO<sub>2</sub> per year could be removed by BECCS, equating to roughly half of the UK's 2050 emission targets.

#### 1.2.1. Post-Combustion Carbon Capture Processes

To date, several separation technologies are applicable to the capture CO<sub>2</sub> post-combustion including absorption, cryogenics, membranes, mineralisation and adsorption. Among these, absorption is the most conventional economically feasible large-scale applications [19]. These processes, however, possess some far reaching limitations including substantial energy costs, regeneration difficulties, concerns around toxicity, secondary pollution and corrosion, especially with the benchmark solvent monoethanolamine (MEA) [7].

<sup>&</sup>lt;sup>5</sup> Greenhouse Gas Removal. Available from: https://royalsociety. org/topics-policy/projects/ greenhouse-gas-removal/

<sup>&</sup>lt;sup>6</sup> The evidence for deploying bioenergy with CCS (BECCS) in the UK. Available from: https://www.eti.co.uk/library/the-evidence-for-deploying-bioenergy-with-ccs-beccs-in-the-uk

#### 1.3. Adsorption

As a unit operation, adsorption is either physical or chemical. Physical adsorption, often termed physisorption is governed by van der Waals interactions and electrostatic forces; chemical or chemisorption involves the adsorbate reacting chemically, with the surface of the adsorbent. Most adsorbents are highly porous materials, and the adsorption of adsorbate species takes place primarily on the walls of the pores or at specific sites inside the adsorbent. Different materials exhibit different adsorption mechanisms, for example [20]: in MOFs, CO2 interacts with uncoordinated metal sites and/or surface functionalities; in carbonaceous materials the CO2 reacts with surface functional groups present in the pristine material or those that are introduced through modification. Adsorption processes are cyclic, involving both adsorption and desorption operations. These processes are accomplished via temperature (TSA), pressure (PSA); vacuum swing adsorption (VSA), or any combination of these. In both PSA and VSA, the gas is released from the sorbent (desorbed) by reducing the pressure in the column relative to the adsorption pressure. The difference lies in the fact that the adsorption takes place at atmospheric pressure with VSA thus requiring the application of a vacuum to the column. In PSA, the desorption takes place under atmospheric pressure. In TSA, the column containing a saturated bed is heated, the rise in temperature forces the removal of adsorbed species. In addition to these conventional strategies for sorbent regeneration, innovative techniques such as moisture swing, and electric swing have emerged [21] as well as pH, magnetic induction, microwave and ultrasound swing, among others [22]. These processes rely on alternative stimuli to regenerate the adsorbent to reduce the energy penalty of the adsorption process and improve the economics of CO<sub>2</sub> capture. The success the adsorption-CCS approach however, depends on the selection or development of a suitable adsorbent.

#### 1.3.1. Materials for CO<sub>2</sub> Capture via Adsorption

Throughout the literature, there is a vast number of materials which can be used for the selective capture of CO<sub>2</sub>. These materials are broadly categorised into either organic (generally carbon-based), and inorganic adsorbents. Metal-organic frameworks (MOFs) consist of metal oxide corners connected by organic linkers and are synthesised in a self-assembly process from these building blocks [23]. They are a relatively novel class of crystalline porous materials which have attracted considerable attention due to their somewhat unique structural properties. Generally, the interactions between the framework and CO<sub>2</sub> molecules is critical and increasing the strength of these interactions augments the material's CO<sub>2</sub> capacity, especially at low partial pressure [24]. To this end, strategies for improving MOFs for CO<sub>2</sub> capture include precise pore-size control to enhance the molecular sieving effect; introducing open metal sites [25]; including polar functional groups either through post-synthesis modification or direct assembly; and the incorporation of extra framework cations. Zeolites (aluminosilicate-based porous materials) are often considered some of the most suitable adsorbents for CO<sub>2</sub> capture although the capacity is heavily dependent on the partial pressure of the CO<sub>2</sub> within the gaseous mixture [14]. Zeolite

13X is generally indicated as a benchmark material for low temperature CO<sub>2</sub> capture applications. Zeolites are naturally occurring microporous crystalline aluminosilicate framework materials that can also be synthesised from various precursors such as coal fly ash and other waste materials. They are widely investigated for the capture of CO<sub>2</sub> owing to the molecular sieving effect and the strong dipolequadrupole interactions between CO<sub>2</sub> and alkali-metal cations in the framework [26]. The type and occupancy of cations in the crystalline framework induces both modifications to the electrical field within the pores but also the structure morphology which can significantly influence the kinetics of CO<sub>2</sub> adsorption [27]. A synthetic zeolite 13X has been shown to have a capacity of around 3 mmol<sub>CO2</sub>g<sup>-1</sup> at 0.15 bar of CO<sub>2</sub> at 313 K [28]. The interactions between CO<sub>2</sub> and silica-based materials tend to be weak and as such these materials are generally characterised by a relatively low CO<sub>2</sub> uptake. The attraction of these materials arises from the potential for surface modification with various functional groups that act to increase the adsorbents affinity towards CO<sub>2</sub>. The morphological flexibility and porosity is often considered the sole reason that these materials can be functionalised with suitable organic and inorganic groups [29], which also unfortunately increases the energy required for regeneration. Carbonaceous adsorbents describe a number of distinct materials which can include activated carbons, carbon nanomaterials and various pyrogenic carbon materials such as biochar and charcoals. These materials possess several advantages such as high thermal/chemical stability, conductivity (both electrical and thermal) and mechanical strength. In the context of CO<sub>2</sub> capture their assets lie in their hydrophobicity and low cost [30]. The key limitation with carbonaceous adsorbents is the proper control of pore size particularly in the ultra-micropore region which is ideal for CO<sub>2</sub> adsorption.

A large selection of the solid adsorbents available for CO<sub>2</sub> capture preferentially adsorb CO<sub>2</sub> over competing gases such as N<sub>2</sub> or CH<sub>4</sub> as a result of the polarizability and quadrupole moment possessed by CO<sub>2</sub> [31], encouraging a range of electrostatic van der Waals forces (i.e. London, Debye and Keesom). Most studies in the field of adsorption-based CCS seek to reduce the cost of CO<sub>2</sub> capture by improving efficiency and hence reducing the energy requirements, this entails developing new and cheaper adsorbents and their associated processes [32]. Developing new adsorbents involves careful tailoring of the physicochemical properties with a view to satisfy the following requirements [33]:

- 1. Low-cost of manufacture and operation;
- 2. High selectivity towards CO<sub>2</sub> over other molecules competing for adsorption sites;
- 3. Adequate chemical, thermal and mechanical stabilities;
- 4. Fast adsorption rate;
- 5. High working capacity;
- 6. Facile regeneration and/or reuse; and
- 7. Abundant availability.

#### 1.3.2. Biomass Combustion Ash as an Adsorbent Precursor: Research Motivation

It's widely accepted that the combustion of sustainable biomass does not contribute to net GHG emissions since the CO<sub>2</sub> released upon combustion is that which is captured during the growth of the biomass. The use of biomass as an alternative to fossil fuels has gained traction in recent years even with concerns of long-term sustainability. The global production of biomass with potential for energy applications is estimated to be around 3 billion tonnes for forest residues [34]; between 1.1 and 3.1 billion tonnes for agricultural residues [34]; about 1.1 billion tonnes for municipal solid wastes [35] plus sewage sludge and other biomass resources [34,36,37]. Total bioenergy potential estimates for 2050 range between 60 and 1548 EJyr<sup>-1</sup> [8] with the lower estimates limited by marginal or degraded land deployment, land allocation for natural parks or due to consideration of predominantly residues [8]. The upper range is usually defined based on economic analysis, involving technological developments that improve yield/availability, whereas the lower range considers ecological and biophysical concerns and the natural limit to sustainable bioenergy deployment [38]. Around 95 - 97% of the energy produced from biomass is produced via combustion resulting in the production of a near 500 million tonnes of biomass ashes at a mean ash yield of 6.8% [39]. Comparatively, around 800 million tonnes of coal ashes are produced globally [40]. Although there has been very little research in the area, recent investigations have shown that Biomass Combustion Products (BCPs) have good potential to serve as much cheaper adsorbents than commercially available activated carbons [41]. With specific surface areas for wood ashes between  $8 - 150 \text{ m}^2\text{g}^{-1}$  compared to  $1.3 - 12.5 \text{ m}^2\text{g}^{-1}$  for coal ashes [42], BCPs also possess a number of attractive properties such as the presence of oxygen containing surface functional groups namely, hydroxyl, silanol, phenolic and carboxylic. Additionally, an increased prevalence of alkali and alkaline earth metals/oxides, hydroxides and carbonates elevate the alkalinity of the BCPs facilitating improved performance in the capture of CO<sub>2</sub> [43]. This elevated alkaline content tends to make these waste materials unsuitable for the conventional applications that coal ash finds itself. Additionally, posing significant environmental challenges in terms of waste disposal, compared to its coal counterpart.

The biomass fuel used at Drax power plant, located in Selby, UK – one of the world's largest biomass combustion thermal power plants in the world – is typically wood and woody biomass (WWB) pellets; the ash formed from its combustion tends to have some of the lowest ash yields when compared to other variants such as animal biomass and agricultural biomass [39] with ash yield increasing as you move vertically away from the stems/stumps toward the foliage. Wood grown in hotter climates typically produces more ash although this is also dependent on the age and type (hardwood has higher ash content than soft) [36]. Figure 1.3 illustrates the typical composition of various biomass sources but even for specific classes, the composition is heavily dependent on the species, growing conditions, harvest

time/technique, transport and storage, method of processing and the combustion itself [44] thereby, rendering a generic study on the valorisation of BCPs impossible.

Globally, the utilization of combustion ash is not more than 30% [45] and in the UK nearly 30% of fly ash is directly landfilled [46]. BCPs tend to have a greater occurrence of hazardous and mobile compounds when compared to coal ash, including heavy metals, especially Cd and Zn. As a result, there are serious concerns around contamination both in the global and local sense for air, water, soil and plants [47]. This high likelihood of leaching various toxic compounds renders its disposal either costly or environmentally reprehensible. In 2019, Drax burnt over 7 Mt of biomass primarily from the USA which is more than the UK's entire production of wood enabling them to provide 12 % of the UK's renewable energy [48]. The 13.4 TWh of energy produced by Drax using biomass constitutes approximately 40% of the total UK's bioenergy production [49]. Given the lack of suitable applications, high chance of environmental contamination, likelihood of alkalinity and leaching and etc., valorisation of this waste is not only beneficial in the environmental context but also of high social and economic significance [50]. Thereon, the in-situ carbon capture from the increasingly growing biomass combustion facilities using a continually co-generated waste stream (i.e. BCP) could be a simple yet efficient and viable route towards an accelerated deployment of BECCS in the UK and the rest of the world.

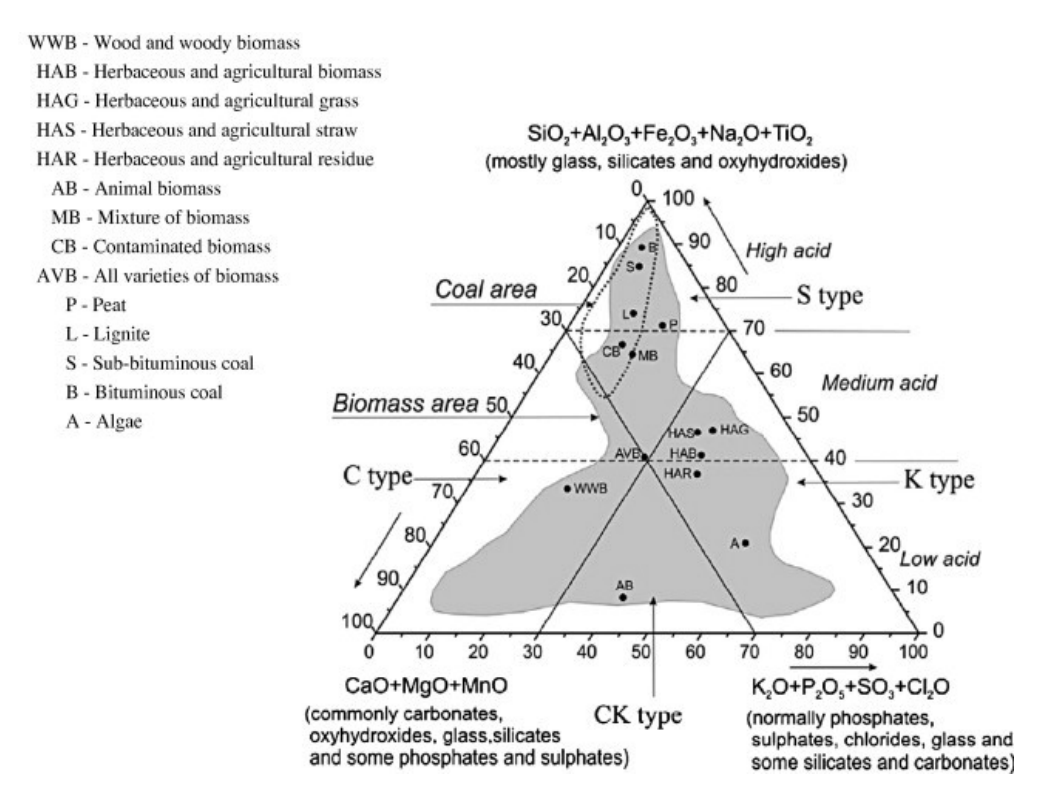


Figure 1.3: Position of biomass varieties and solid fossil fuels in the chemical classification system [36].

#### 1.4. Research Aim and Objectives

This research aims to valorise an abundantly available industrial-grade waste to synthesise, characterise and test a cost-effective yet efficient adsorbent for use in carbon capture and storage. In this context, the research objectives comprise:

- 1. To characterise industrial-grade biomass combustion fly ash generated at Drax Power Station, Selby, UK to understand the associated physicochemical properties;
- 2. To synthesise and characterise an effective CO<sub>2</sub> adsorbent using biomass combustion ash as the precursor;
- 3. To study the adsorbent's CO<sub>2</sub> adsorption performance *via* thermogravimetric and volumetric analyses;
- 4. To prepare granules/pellets, study and improve the associated mechanical stability; and
- 5. To evaluate and optimise the performance of the prepared adsorbents in a fixed-bed reactor.

#### 1.5. Thesis Outline

The subsequent chapter of this thesis presents a review of technologies available for carbon capture and storage with focus primarily in the post-combustion capture context before discussing the application of adsorption-based processes and the mechanisms and phenomena which underpin them. Chapter 3 details the experimental methods and materials employed throughout the work. Chapters 4 through 7 will present and discuss the work conducted and results obtained in completion of this research's objectives: characterisation of biomass combustion fly ash; synthesis, characterisation and optimisation of biomass-combustion fly-ash derived zeolites; and the assessment of breakthrough performance of structured, fly-ash derived-adsorbents *via* lab-scale fixed-bed adsorption. The final chapter will present the work's conclusions and proposals for future work which would support these findings.

#### 2. Literature Review

#### 2.1. Carbon Capture and Storage Technologies

#### 2.1.1. Pre-combustion Carbon Capture

Pre-combustion carbon capture encompasses technologies which remove carbon from the fuel prior to completion of combustion [51]. Typically, this entails pre-treating the fuel before the combustion stage such as in Integrated Gasification Combined Cycle (IGCC) plants or steam methane reforming. In both cases the pre-treatment produces syngas, a mixture of CO, CO<sub>2</sub>, H<sub>2</sub> and H<sub>2</sub>O which then undergoes a water gas shift reaction converting CO to CO<sub>2</sub>. Water is then condensed from the product stream, with CO<sub>2</sub> removed the remaining H<sub>2</sub> is then employed as a fuel downstream.

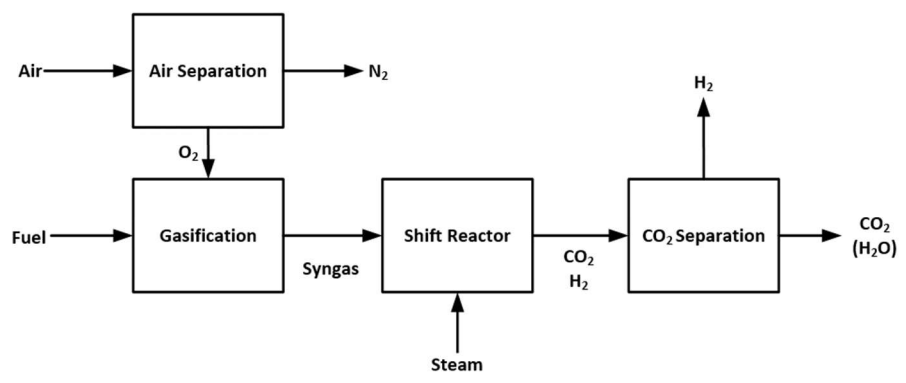


Figure 2.1: Basic schematic of pre-combustion carbon capture.

#### 2.1.2. Oxy-fuel Combustion

Oxy-fuel combustion is not by nature a carbon capture process, it's an advanced combustion technology utilising a mixture of pure  $O_2$  and recycled flue gases. The flue gas a result of this is predominantly  $H_2O$  and  $CO_2$  and their separation relatively straight forward. Oxygen is produced for the process by separation from  $N_2$  in an air separation unit (ASU) utilising membranes or cryogenics. Most fuels are suitable for oxy-fuel combustion and the high concentration of  $CO_2$  makes its separation relatively inexpensive. Contrastingly however, the separation of  $O_2$  from air is intensive both in terms of energy and cost reducing the overall process efficiency substantially [52].

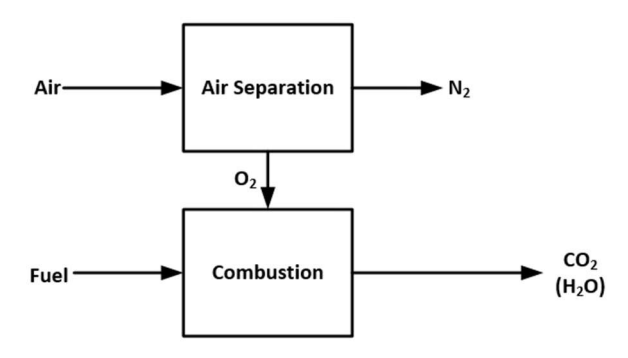


Figure 2.2: Basic schematic of an oxy-fuel combustion process.

#### 2.1.3. Post-combustion Carbon Capture

Post-combustion carbon capture (PCCC) technologies remove CO<sub>2</sub> from flue gases after combustion. The flue gas typically consists of CO<sub>2</sub>, N<sub>2</sub>, H<sub>2</sub>O and O<sub>2</sub> making the separation of CO<sub>2</sub> more complex. This option however is considered the most suitable for commercial deployment with the primary advantage in the possibility to retrofit PCC plants to existing emitters with relative simplicity.

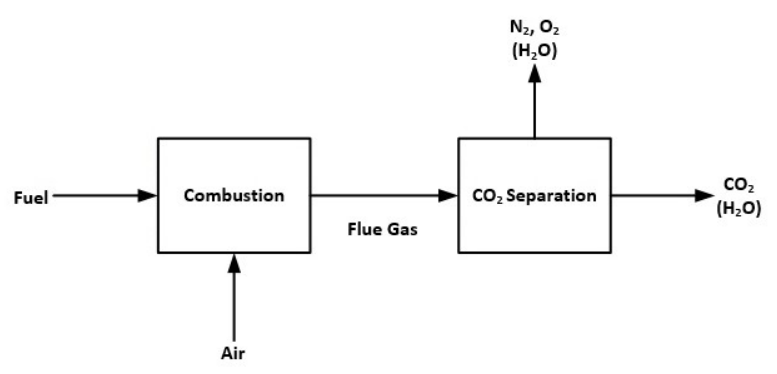


Figure 2.3: Basic schematic of post-combustion CO2 capture.

#### 2.2. Adsorption

As a unit operation, adsorption is either physical or chemical. Physical adsorption or physisorption is governed by van der Waals interactions and electrostatic forces, the same as those which give rise to the non-ideality of real gases as well as the condensation of vapours. Chemical or chemisorption involves the adsorbate reacting chemically, with the surface of the adsorbent; the same forces which would give rise to new chemical compounds. The difference between these two schemes is often distinguished by the following features [53]:

- Physisorption is non-specific interaction between an adsorbate and adsorbent typically characterised by a low enthalpy of adsorption (< 40 kJ·mol<sup>-1</sup>) whereas chemisorption is often characterised by higher enthalpy of adsorption (40 800 kJ·mol<sup>-1</sup>) [54,55];
- Chemisorption requires a link between the adsorptive and a reactive part of the adsorbent, often
  limiting adsorption to a monolayer. At high relative pressures, physical adsorption will often
  occur as a multilayer;
- Physisorbed molecules return to the bulk fluid phase without change during desorption, chemisorbed molecules which have undergone reaction or dissociation will not be recovered by desorption;
- The energy of chemisorption will be of the same magnitude as that in a comparable chemical reaction. Physisorption will always be exothermic and involves energies akin to the adsorptive's energy of condensation, although this will be significantly greater in the case of very narrow pores;
- Chemisorption may involve an activation energy, as such, low temperature systems may not be sufficient to achieve thermodynamic equilibrium. In systems without rate-determining transport processes, physically adsorbing systems will reach equilibrium relatively quickly.

Given that most adsorbents are highly porous materials and adsorption takes place primarily on the walls of the pores it is poignant to state that pore sizes exist within three classifications: micro- (< 2nm), meso- (2 - 50 nm) and macro-pores (> 50 nm) [56]. Pores are rarely uniform and will often be interconnected with varying diameter. With this in mind, an increase to an adsorbent's specific surface area will tend the material to an enhance adsorption capacity by providing a larger area which can facilitate adsorption. The extent of adsorption though, is also influence by both the temperature and pressure of the operation with adsorption favouring lower temperatures and higher pressures. This and the effect of molecular and adsorbent-adsorbate interactions are discussed in the subsequent sections.

#### 2.2.1. Physical Adsorption

The physical adsorption of any adsorptive as elucidated to in the previous sub-section is heavily dependent on weak Van der Waals and electrostatic forces. This section will discuss these in the context of the CO<sub>2</sub> molecule. Carbon dioxide is a linear molecule comprised of an individual carbon atom covalently bonded to two oxygen atoms, this symmetry leaves the molecule without a permanent dipole as each oxygen atom pulls the electron density towards itself equally. The distribution of charge in the CO<sub>2</sub> molecule however is not spherically symmetric and hence, produces a quadrupole moment. This arises due to the stronger electronegativity of oxygen compared to carbon resulting in polarisation of the electron density towards the oxygen atoms away from the carbon creating partial charges at the oxygen ( $\delta$ ) and carbon ( $\delta$ ) atoms. In the context of CO<sub>2</sub> separation from flue gas, the other gaseous constituents include nitrogen, water, oxygen among nitrogen and sulphur oxides and other trace impurities. In this regard, the properties for flue gas constituents are provided in Table 1 [57]. The dipole moment is a measure of separation between positive and negative charges within a molecule and quantifies the degree of polarity. The quadrupole moment accounts for charge distribution beyond a simple dipole and is a measure of the asymmetry in molecules charge distribution. Polarisability is often given in units of volume and can be considered as the volume surrounding a molecule which can be influenced by an electric field. The dipole moment is the principal interaction, followed by the quadrupole; an increase in polarisability will result in enhance interactions with an adsorbent's surface.

Table 1: Physical properties of flue gas components.

Component	Dipole Moment	Quadrupole Moment x10	Polarisability	Kinetic Diameter
	(×10 <sup>-18</sup> esu·cm)	(×10 <sup>-26</sup> esu·cm <sup>2</sup> )	$(\times 10^{-25}  \text{cm}^3)$	(Å)
$N_2$	0	1.52	17.403	3.640
$CO_2$	0	4.30	29.110	3.300
H <sub>2</sub> O	1.8546	0	14.500	2.641
$O_2$	0	0.39	15.812	3.467

Van der Waals or dispersion forces relate to the ability of an atom/molecule's electron density to be distorted, *i.e.* polarizability [58]. These are the greatest contributor to physisorption and are comprised of Keesom, Debye and London Dispersion Forces. Keesom forces are those which occur between

permanent dipoles, Debye between a permanent dipole and an induced dipole, and London Dispersion Forces which are the dominant and most universal of the three, present for both polar and nonpolar molecules. Conversely, electrostatic forces require a surface to be polar. They arise due to polarisation forces, field-dipole, and field gradient-quadrupole interactions. The magnitude of the force that arises during physical adsorption is influenced by the adsorbate molecule's size, polarity, quadrupolarity and polarizability, that said the strength of the adsorbent's electric field and the local field gradient of the surface also contribute [53].

#### 2.2.2. Adsorbent Materials

Within the literature there are a vast number of materials used for the selective capture of CO<sub>2</sub>. The variations between these materials give rise to equally diverse characteristic isotherms; the IUPAC defines typical isotherm classifications (I through VI) as exhibited in Figure 2.4 [59,60]. Type I isotherms present a concave shape relative to the relative pressure  $(P/P_0)$  axis, with a steep rise at low relative pressures reaching a limiting value as the relative pressure tends towards 1. This type is generally present in microporous materials with the limiting capacity a result of the adsorbent's finite micropore volume [53]. Type I(a) and I(b) isotherms differ in the rate at which the adsorbed amount approaches the limit with I(a) being indicative of narrow micropores generally less than 1 nm in diameter whereas I(b) would suggest a wider distribution of micropores and potentially even narrow mesopores. Type II isotherms are concave to the P/P<sub>0</sub> axis before progressing towards linearity and finally becoming convex. This type is usually observed in non-porous or macroporous materials as it is indicative of unrestricted adsorption (i.e. multimolecular adsorption or multilayer). The completion of the monolayer is generally taken at the start of the linear region in the isotherm, from here the multilayer begins forming. The ordinate at which the multilayer begins forming can be used to provide an estimate of the amount of adsorbate required to cover the adsorbent's surface. Type III isotherms are those which are continuously convex to the P/P<sub>0</sub> axis and are indicative of weak adsorbate-adsorbent interactions typical for non-porous or macroporous adsorbents. Type IV isotherms are somewhat similar to type II in the low relative pressure region however, they exhibit a saturation plateau at higher relative pressures which can be reduced to a mere inflection point [53,59]. These isotherms are typical for mesoporous materials with IV(a) possessing hysteresis not observed in IV(b); hysteresis indicates a deviation from complete reversibility and in the case of type IV isotherms this is associated with the filling (adsorption) and emptying (desorption) of the adsorbate via capillary condensation. A lack of hysteresis in type IV isotherms is characteristic of materials with a pore size below 4 nm [59]. Type V isotherms which possess some similarity to type III and would be displayed by porous (micro- or meso-) adsorbents with weak adsorbate interactions. The explanation for the plateau and hysteresis is consistent with type IV isotherms. Type VI isotherms are uncommon and describe stepwise adsorption for highly uniform structures. The aforementioned isotherms are defined in the context of physical adsorption. Chemical

adsorption generally gives rise to a simpler isotherm which is comparable to type I(a). In this case, a plateau in the adsorbed amount exists due to the completion of a chemically attached monolayer.

#### 2.2.3. Equilibrium

Adsorption as a unit operation is predominantly reliant on the physical adsorption of molecules and is likened to the process of condensation. The attachment of molecules to an adsorbent surface involves both Van der Waals and electrostatic forces with the former influenced by the ease of which an atom or molecules electric potential can be distorted, *i.e.* polarisability and the former influenced by polarisation forces. As the basis for all processes, the thermodynamics which underpin adsorption can provide both the definition and theory behind adsorption phenomena but also facilitate characterisation and comparison of adsorbent materials. When an adsorptive with three degrees of translational freedom is constrained to the surface of an adsorbent it loses at least one of these degrees of freedom as a consequence of the adsorbate-adsorbent interactions. Physical adsorption is always exothermic and hence associated with the release of heat ( $\Delta H_{ads} < 0$ ). For any spontaneous process there is a decrease in the Gibbs free energy ( $\Delta G < 0$ ) and in the case of adsorption, due to the loss of translational freedom and hence the more ordered adsorbed state, there must also be a decrease in entropy ( $\Delta S < 0$ ). The classical equilibrium approach to describing adsorption thermodynamics is the most well established and frequently used. This approach requires the assumption that the solid adsorbent is considered inert so that only two phases exist in equilibrium: the bulk gas phase and the adsorbed phase.

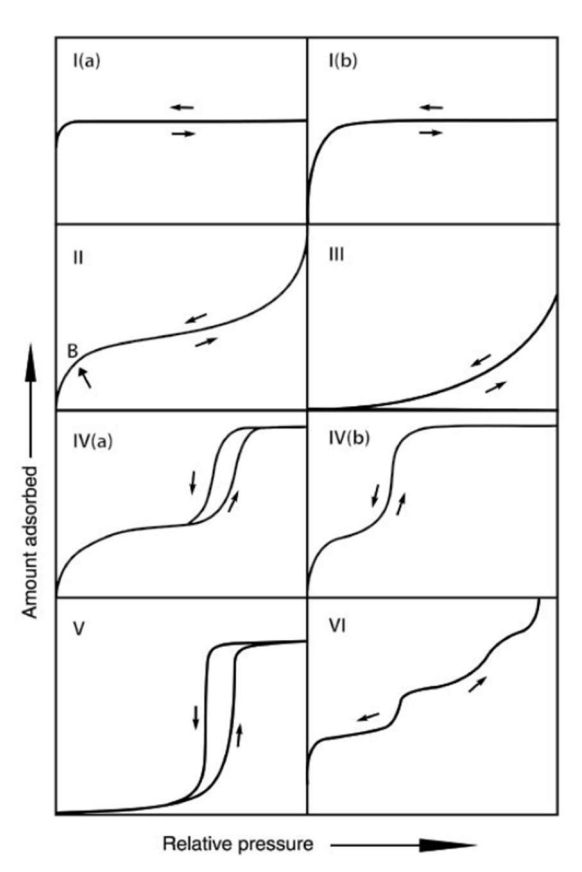


Figure 2.4: IUPAC classification of isotherms [59,60].

#### 2.2.3.1. Isotherm Models

An adsorption isotherm details a set of equilibrium loading data as a function of bulk gas phase concentration or pressure, in the case of gaseous adsorption. A wide range of theoretical, empirical and semi-empirical models exist to describe experimental isotherm datasets; whilst those with more parameters may be able to account for nuances in the adsorption phenomena, in most cases simpler is better [58]. Adsorption on a surface can be described in the simplest terms by considering an energetically uniform surface lacking of any interaction between the adsorbed molecules [61], i.e. the enthalpy of adsorption is constant. The Langmuir isotherm which also considers a monolayer limit to the adsorbate coverage is based upon the dynamic equilibrium between adsorbed and bulk gas phases. The fundamental basis was that the rate of adsorption  $(k_a)$  from the bulk phase to the surface was directly proportional to the product of the adsorptive's partial pressure (p) and the remaining surface not yet covered by adsorbate  $(1 - \theta)$ . Langmuir also considered the rate of desorption  $(k_d)$  from the surface to the bulk phase to be directly proportional to the surface coverage  $(\theta)$ . At equilibrium the adsorption and desorption rates are equal, the resulting relation is given in EQ. 1 with the typical presentation of this provided in EQ. 2. The Langmuir constant  $k_L$ , is exponentially related to the positive value of the adsorption energy (E) through EQ. 3, or alternatively regarded as a function of the enthalpy and entropy of adsorption [53,62,63]. In EQ. 3 the pre-exponential factor K, is equal to the ratio of the adsorption and desorption coefficients,  $k_a/k_d$  [53]. Theoretical models are based on parameters which have a direct physical interpretation and a number of assumptions with regard to the adsorbed state. These conditions are rarely present and therefore empirical and semi-empirical isotherm models can be more useful.

$$k_{a}p(1-\theta) = k_{d}\theta$$

$$\theta = \frac{q}{q_m} = \frac{k_L P}{1 + k_L P}$$

$$k_L = Ke^{\left(\frac{E}{RT}\right)}$$

The hyperbolic function in Langmuir's model suggests that at low pressures, EQ. 2 reduces to EQ. 4 or Henry's Law. Henry's law is the simplest equilibrium concept in that the extent of adsorption is proportional to the phase concentration [58]. All isotherm equations should reduce to Henry's Law at the limit of zero loading to ensure thermodynamic consistency; in the absence of this the equation or data is likely fundamentally flawed [58]. Yet despite this consistency requirement, the isotherm proposed by Freundlich which is one of the most employed models, does not reduce to Henry's Law at zero coverage nor to a saturated condition at elevated partial pressures.

$$\theta = \frac{q}{q_m} = k_L P$$

The Freundlich isotherm recognises that the heat of adsorption is not constant as assumed by the Langmuir model but instead, decreases logarithmically as the extent of adsorption increases. This implies that there is an exponential distribution of adsorption sites with respect to an adsorption energy

that can differ depending on the adsorption site. This relation is provided in EQ. 5 where  $k_F$  is the Freundlich constant, and  $n_F$  is the dimensionless heterogeneity factor ( $n_F > 1$ ).

$$q = k_F P^{\frac{1}{n_F}}$$

The Sips equation which is often remarked as the Langmuir-Freundlich isotherm is a modification of the Freundlich model which addresses the problem of limitless adsorption as pressure increases [64] hence improving the model fit. This combined model is provided in EQ. 6 and the resemblance to the Langmuir model is clear. In this equation  $k_S$  is considered the adsorption affinity parameter and n, an empirical parameter. It can be seen that with a value of  $n_S$  equal to 1, the equation would reduce to the Langmuir model. The Sips model however is not thermodynamically consistent at low pressures.

$$\theta = \frac{q}{q_m} = \frac{(k_S P)^{n_S}}{1 + (k_S P)^{n_S}}$$
 EQ. 6

As an alternate extension to the Langmuir model, the isotherm model proposed by Toth (EQ. 7) considers the observation that an increase in adsorbent heterogeneity tends to improve adsorption [65,66]. The model is also thermodynamically consistent as it reduces to Henry's law at low pressures and reaches saturation at high pressures [67–70]. The model constants b and  $n_T$  represent the predicted saturation capacity, the affinity parameter and the Toth constant, respectively [71]. The constant  $n_T$  is regarded as an indication of the adsorbent's heterogeneity and will often be less than 1. At a value of 1, the equation reduces to the Langmuir model demonstrating an adsorbent's homogeneity [72]. The Toth constant is also temperature dependent and typically tends towards unity as the temperature increases [73]. With the model there is also an assumption of an asymmetric distribution of adsorption site energy suggesting most have an energy below the mean [74].

$$\theta = \frac{q}{q_m} = \frac{k_T P}{[1 + (k_T P)^{n_T}]^{\frac{1}{n_T}}}$$
EQ. 7

Adsorption with adsorbents which possess surface heterogeneity can also be characterised by the adoption of multi-site forms of the aforementioned isotherm models. One such model which still finds use today is the dual-site Langmuir model, first described in an effort to model more than one adsorption site [75]. The equation is provided in EQ. 8 and is essentially a summation of the individual Langmuir model for n adsorption sites; the dual-site equation is provided in EQ. 9. Although the addition of independent fitting parameters as the number of adsorption sites increases improving the fit of the isotherm model [76] the advantage when more than two sites are employed is considered negligible [77].

$$q = \sum_{i=1}^{n} \frac{q_{m(i)} k_{L(i)} P}{1 + k_{L(i)} P}$$
EQ. 8

$$q = \frac{q_{m(1)}k_{L(1)}P}{1 + k_{L(1)}P} + \frac{q_{m(2)}k_{L(2)}P}{1 + k_{L(2)}P}$$
EQ. 9

## 2.2.4. Rate Phenomena

The mechanisms of adsorption involve both the transport of CO<sub>2</sub> from the bulk fluid to the active adsorption sites and the physical or chemical interaction between the CO<sub>2</sub> molecule and the active site.

# 2.2.4.1. Adsorption Kinetics

The kinetics of an adsorption process describes the rate at which a specific adsorptive rescinds a degree of translational freedom and affixes itself to the surface of a separate, solid phase. These models often find applications in the wider engineering, and scientific communities. The simplest kinetic model which has found use in describing adsorption processes employs a first order rate equation. First presented by Lagergren in 1898 [78] in his study on the adsorption of sugar by charcoal, the model assumes that the rate of adsorption is dependent upon and hence proportional to the number of adsorption sites which remain unoccupied. The differential equation is given in EQ. 10; the integrated form is provided in EQ. 11 (to provide an expression for  $q_t$  as a function of time) where  $q_t$  is the adsorbed amount at time t,  $q_e$  is the adsorbed amount at equilibrium and  $k_I$  is the adsorption rate constant. The integrated form is often referred to as the Pseudo-First-Order (PFO) rate equation as it is a function of loading rather than concentration as would be expected for typical reaction rate kinetics. This is somewhat intuitive as with any unit operation, there must be a driving force.

$$\frac{dq_t}{dt} = k_1(q_e - q_t)$$

$$\theta = \frac{q_t}{q_e} = 1 - e^{-k_1 t}$$
 EQ. 11

In contrast, the kinetic equation proposed by Ho and McKay in 1999 [79], in their study of dye adsorption onto various adsorbents, assumes the rate of adsorption is dependent upon the interaction itself between the adsorptive and the adsorbent's surface. This implies that there is a greater dependence on more complex mechanisms such as chemisorption. The differential form of the Pseudo-Second-Order (PSO) rate equation is provided in EQ. 12 and the integrated form in EQ. 13 where  $k_2$  is the adsorption rate constant.

$$\frac{dq_t}{dt} = k_2(q_e - q_t)^2$$

$$\theta = \frac{q_t}{q_e} = \frac{q_e k_2 t}{1 + q_e k_2 t}$$
 EQ. 13

An alternative to the PSO model which also describes the mechanism of adsorption involving chemisorption is the Elovich kinetic model. Originally proposed by Zeldovich and Elovich in the 1930s and to describe gas adsorption on solids and later modified by Elovich in 1962 to its current form which is widely employed in fields such as catalysis [80]. The equation is provided in EQ. 14 where  $\alpha$  is the

initial adsorption rate and  $\beta$ , the desorption constant; the integrated form is provided in EQ. 15. The model accounts for factors such as the availability of active adsorption sites and the strength of the interactions between adsorbate and adsorbent. The model assumes that the adsorption rate decreases exponentially with an increase in surface coverage. The initial adsorption rate is dependent on the number of available sites whereas the exponential term represents the diminishing rate as the adsorbent surface tends toward saturation.

$$\frac{dq_t}{dt} = \alpha e^{-\beta q_t}$$

$$q_t = \frac{1}{\beta} \ln(1 + \alpha \beta t)$$
 EQ. 15

Zeolites possess pores predominantly in the microporous region and hence their adsorption kinetics are often limited by intraparticle or more accurately, intracrystalline diffusion. In 1947 *Boyd et al.* reported an intraparticle diffusion model [81] but the form more often cited in the literature is of the simplified relationship described by Weber and Morris, given in EQ. 16 [82] where  $k_{IPD}$  is the Intraparticle Diffusion (IPD) rate constant and C often taken as an indication of the thickness of the boundary layer [83]. Recently, in the work of Wang and Guo, piecewise IPD functions have been fit to experimental datasets with a view to ensure consistency with the IPD theory [84].

$$q_t = k_{IPD} + C EQ. 16$$

## 2.2.5. Fixed Bed Adsorption

Adsorption classically takes place in large vessels, the complete process being cyclic, involving adsorption and desorption operations. Of the vessels used for adsorption processes, the fixed bed is the most common. These feature a fixed bed of adsorbent usually randomly packed although novel contactor design is part of active research including development of monolithic structures [85-87]. Fixed beds are flexible in terms of their operation with compatibility for TSA, PSA and VSA [88,89] and both operational and design simplicity [90–92]. Due to the large adsorbent mass within the fixed bed system, TSA cycles are lengthy which increases the required number of beds to facilitate continuous operation ultimately making deployment impractical from a footprint perspective [93]. Heat transfer in fixed beds is also relatively poor meaning an adsorbate-adsorbent interaction characterised by high adsorption enthalpy would reduce the processes performance; PSA systems are considered most suitable for physisorbents [94]. Feed gas flow rate is often limited by the tolerable pressure drop across the bed which is often driven by the operating costs of the system but also constraints in maximum downwards load permissible that avoids crushing the bed [95]. Common solutions to this are to increase the bed diameter effectively reducing the superficial gas velocity. Increases to the adsorbent particle size effectively increases the void fraction in the bed which will reduce the associated pressure drop but can have negative implications on mass transfer [96].

Alternative vessel designs such as fluidised beds and moving beds with both featuring improved heat and mass transfer by transporting the solid adsorbent material within the cycle improving both the equipment and plant size and heat and mass transfer characteristics [93,97]. Productivity in TSA cycles is higher in fluidised beds due to the improved heat transfer in the bed [95]. The adsorbent in fluidised is circulated by the incoming feed stream at the bottom of the vessel which acts to fluidise the bed permitting the fluid velocity is above the minimum fluidisation value. Transport of the adsorbent between adsorber and desorber allows for continuous cyclic operation exploiting the improved heat and mass transfer when compared to fixed beds [88,98]. This also provides opportunity for heat recovery from the solids lending fluidised to TSA operations [99–102]. Their adoption at scale has been limited due to operational complexity but there is huge incentive given the associated improvements to pressure drop, heat and mass transfer kinetics and feed flow rate constraints [98,103,104]. Moving bed reactors are less complex operationally but introduce significant design complexity when considering the need to move the bed between individual operations; rotary beds can alleviate some of this complexity but gas containment becomes challenging and limits suitability for PSA systems [105]. Pressure drop is decreased relative to fixed beds as the beds themselves can be shorter for the same feed conditions [106]. Moving the bed between heating/cooling also improves the cycle time and heat transfer but not to the same extent as fluidised beds [106,107].

# 2.2.5.1. Mass Transfer

The effectiveness of adsorption-based PCC systems is reliant upon the mass transfer within the adsorption vessel. Although fixed-beds are considered relatively simple, the mass transfer of CO<sub>2</sub> from the fluid phase to the solid is often multi-step involving both external and internal mechanisms. The external mass transfer defines the transport of CO<sub>2</sub> from the bulk gas phase to the adsorbent's external surface while internal mass transfer defines the transport (*i.e.* diffusion) of CO<sub>2</sub> within the adsorbent particle. This intraparticle or more applicably, intracrystalline transport is often rate-determining for uniformly microporous solids such as zeolites. That said, the two mass transfer mechanisms both contribute to the overall kinetics of the adsorption process from bulk phase to active adsorption site.

In the context of fixed-bed gas-solid contactors, when the feed fluid passes through the bed, a boundary layer/film forms around each adsorbent particle. This layer facilitates transport of the target adsorptive, CO<sub>2</sub> from the bulk gas phase to the adsorbent's external surface *via* molecular diffusion. This film diffusion is governed by gas velocity, system pressure and particle size. As previously mentioned, this is not the rate-limiting step for zeolite-CO<sub>2</sub> systems so long as the adsorption process is sufficiently well-designed. That said, where the adsorbent particle size is large and/or the feed flow rate is low, the boundary layer thickness increases and the overall rate of mass transfer across the film is reduced.

Upon reaching the adsorbent's external surface, the adsorptive must diffuse into the zeolite's internal pore structure before reaching the final adsorption site. This is typically the rate-determining system for

zeolites where the nature of the pore structure including pore size distribution, micropore contribution and tortuosity can have significant impact on intraparticle diffusion. Although zeolites often present highly ordered microporous pore systems, lower quality frameworks such as those synthesised from fly ashes often present increased non-uniformity which can influence overall intraparticle diffusion. This can be to the benefit of the separation process if the zeolite presents a degree of mesoporosity as hierarchical pore structures can promote intraparticle diffusion by decreasing the diffusional resistance [108]. The effective intracrystalline diffusivity of CO<sub>2</sub> is typically much lower than in the bulk gas phase [109]. Intracrystalline diffusion in zeolites can be influenced by a number of factors including [110]:

- Intracrystalline channel geometry and dimensions;
- Shape, size and polarity of the diffusing adsorptive;
- Cation distributions, size, charge and number;
- Adsorptive concentration within the frameworks;
- Temperature;
- Lattice defects such as stacking faults;
- The presence of impurity molecules in the diffusion pathways;
- Structural changes due to penetrants; and
- Structural changes associated with physical and chemical treatments.

In general, mass transfer in fixed-bed adsorption columns is described by a set of differential equations which encapsulate both the bulk-gas-film diffusion and intraparticle/intracrystalline diffusion mechanisms. Under isothermal conditions, the overall resistance to mass transfer is expressed as a combination of external and internal diffusional resistances. The commonly adopted model to describe such systems is the Linear Driving Force (LDF) model which lumps both diffusion mechanism contributions together and is given by EQ. 17 where  $k_{LDF}$  is the LDF mass transfer coefficient [111].

$$\frac{dq_t}{dt} = k_{LDF}(q_t - q_e)$$
 EQ. 17

Whilst the LDF model has found applications in the description of gas-solid adsorption processes, in practise this requires an experimental dataset with which to refine the value of  $k_{LDF}$  for best fit. This dataset is typically a breakthrough curve which represents the adsorptive concentration in the fixed-bed columns exhaust stream as a function of time, or occasionally bed height. The shape of this curve provides insight into the mass transfer within the system with those approaching ideal behaviour characterised by rapid mass transfer exhibiting rapid breakthrough with sharp, near vertical increases in the outlet concentration from the minimum to feed concentration. In reality, the curve is often more drawn out due to the existence of mass transfer limitations within the gas-solid system. A common approach to designed adsorption systems exploits the use of the mass transfer zone (MTZ) within the bed. The MTZ describes the region of a bed in which a concentration gradient exists in the adsorbed

phase. The length of the MTZ is dependent on both external and internal mass transfer resistance and the adsorption kinetics; in systems where mass transfer is hindered, the MTZ is extended resulting in inefficient utilisation of adsorption bed. The MTZ can be controlled by optimising particle size, flow rate, and the process conditions. As mentioned, a reduction in particle enhances both film and intraparticle diffusion effectively reducing the MTZ length. Improvements to diffusion can also be achieved by tailoring pore structures of the adsorbent.

# 2.2.5.2. Heat Transfer

Heat transfer in fixed-beds is also of importance considering the potential for significant heat evolution during the adsorption process. The driving force for this being the adsorption enthalpy which can introduce localised temperature gradients within the bed. Of the three fundamental heat transfer mechanisms, conductive and convective are the primary contributors. Convective heat transfer occurs between the feed gas and the adsorbent particles; as the adsorptive is adsorbed heat is released and exchanged with the gaseous medium. This heat transfer is primarily dependent on the gas flow rate, gas heat capacity and thermal conductivity of the gas-solid interface. Conductive heat transfer occurs within the individual adsorbent particle and those in the immediate vicinity. Largely influenced by the thermal conductivity of the adsorbent particle heat dissipation is relatively slow owing to the low thermal conductivity of zeolite adsorbents as a result of their innate porosity. This materialises as temperature gradients through the bed. In the intraparticle context, heat generated from the adsorption phenomenon is dissipated through the adsorbent particle by conduction, reliant upon the solid's thermal conductivity and internal pore structure. This process is somewhat limited and may lead to significant heat accumulation. That said, the adsorption enthalpies are often relatively low limiting the negative impacts of inefficient heat transfer, for this reason, most researchers assume heat effects to be negligible and consider the fixed beds as operating in the isothermal regime. This may become more of an issue in large-scale systems where heat effects are more significant, here the temperature gradients could impact the bed capacity and kinetics by modifying the local equilibrium conditions. That said, for low temperature, low pressure applications such as PCCC, the modest heat generation coupled with sufficient zeolite particle thermal conductivity usually dissipate most localised temperature increases.

# 2.2.5.3. Pressure Drop

The key challenge for fixed-bed adsorption systems is the associated pressure drop across the bed as this dictates the magnitude of work required to facilitate flow through the bed, affecting the system's energy consumption, operational efficiency and process viability. Minimisation of pressure drop across the bed is key for maximising the system's efficiency. The pressure drop arises due to resistance to gas flow. The magnitude of such dependent on particle size, bed height, gas velocity and the physical properties of both the gas and solid mediums. The relationship between these is often described by Ergun's equation which for fixed beds is given by EQ. 18 [112] where  $\mu$  is the fluid's dynamic viscosity,  $\varepsilon$  is the bed's void fraction,  $\rho_g$  is the gas density,  $d_p$  is the effective particle size and  $\Delta P/L$  is the pressure

drop per unit bed length. The Ergun equation accounts for both viscous (first term) and inertial (second term) contributions to pressure drop, with the relative importance of each term depending on the flow regime (laminar or turbulent) with the former becoming most significant at low velocities, *i.e.* laminar regimes and the latter most significant at high velocities, *i.e.* turbulent regimes.

$$\frac{-\Delta p}{L} = \frac{150\mu(1-\varepsilon)^2 u_g}{\varepsilon^3 d_p^2} + \frac{1.75\rho_g(1-\varepsilon)_\rho u_g}{\varepsilon^3 d_p}$$
EQ. 18

Considering the above equation, the pressure gradient across the bed can be seen to be dependent on both the bed properties and fluid properties, with the relative contribution dictated by the flow regime. Of the bed properties, particle size and shape, bed void fraction and bed height are key factors whereas gas viscosity and density are the primary fluid properties of concern. As such, mitigations for elevated pressure drops across fixed beds include optimisation of particle size, improved adsorbent bed packing and optimisation of the operating conditions such as feed flow rate and temperature [113,114].

# 2.2.5.4. Dispersion

Dispersion which refers to the spreading of gas-phase components (in this case, CO2) as they move through a fixed bed is also of importance as it leads to deviations from ideal plug flow behaviour. Nonideal flow patterns caused by dispersion reduce the steepness of concentration gradients negatively impacting breakthrough behaviour and hence overall efficiency of the adsorption process. In fixed-beds, axial and radial dispersion are the primary contributors to overall dispersion and lead to a diffuse concentration front vs the ideal plug flow system. Although axial is typically more significant, both are influenced by molecular diffusion, flow maldistribution and bed tortuosity leading to the spreading of gaseous components along the flow path and across the bed. Axial dispersion is of primary concern and will materialise in the shape of the breakthrough curve. Similarly to the bed's pressure drop, dispersion is influenced by several factors including particle size and shape, gas velocity and bed packing and void fraction. While radial dispersion is generally less significant, its effect can become apparent for largediameter adsorption beds which may present radial concentration gradients particularly near the column wall reducing the efficiency of bed utilisation. For lab-scale and pilot-scale demonstrations, radial dispersion is considered negligible [58]. In ideal gas-solid adsorption systems with minimal dispersion effects, the breakthrough curve would tend towards the ideal S shape implying effective utilisation of the bed. When dispersion becomes significant the breakthrough phenomenon is drawn out and often results in an early breakthrough and an extended stoichiometric time. Axial dispersion increases the length of the MTZ which results in underutilisation of the bed. Several strategies exist for minimising dispersion effects including reducing particle size and size distribution to limit channelling and flow maldistribution, optimising the gas velocity and appropriate design of the column's geometry.

#### 2.3. Biomass Combustion Products

The combustion of biomass for energy production results in a variety of by-products, many of which can pose significant challenges or offer potential opportunities for reuse and valorisation. In Bioenergy with Carbon Capture and Storage (BECCS), these combustion processes are integrated with carbon capture technologies to achieve negative emissions, making it an attractive option for mitigating climate change. However, the by-products of biomass combustion, such as ash, flue gases, and other particulates, must be managed carefully due to their environmental and operational impacts. Drax Power Station in the UK, one of the largest BECCS facilities, has transitioned from coal-fired to biomass-fuelled generation and is at the forefront of BE and soon (BE)CCS implementation. The facility burns millions of tonnes of sustainably sourced biomass, primarily in the form of wood pellets, to produce electricity. Biomass combustion generates significant quantities of ash, comprising fly ash (captured from flue gases) and bottom ash (collected from the combustion chamber). The quantity and composition of ash depend on the type of biomass used. Unlike coal, biomass ash typically contains higher levels of alkali metals (e.g., potassium, sodium), which can cause operational issues such as slagging, fouling, and corrosion in boilers. Fly ashes are typically dominated by a mixture of silica, alumina and ferric oxide; the relative proportion of these oxides amassing to over 50 wt% for class C and F fly ashes and to over 70 wt% for class N. Class C and F fly ashes differ with regards to their calcium oxide concentrations - over 18 wt% for class C. These classifications are defined by ASTM C618 [115] and are based on the FA's pozzolanic properties. For class C ashes, the elevated presence of calcium (compared to that of coal's) suggests their potential applicability for carbonation/mineralisation under conditions beyond those of post-combustion (i.e. elevated temperature (> 600 °C) and/or pressure such as in calcium looping). Class F and Class N ashes are candidates for inorganic adsorbent synthesis such as zeolites or porous silicas. The relative ratio of the three oxide components within FA (mentioned above) dictate the intended structure; zeolites as crystalline aluminosilicates would favour similar ratios of silica and alumina, whereas for porous silica, the presence of alumina would introduce additional challenges.

## 2.4. Zeolite Synthesis and Development

The synthesis of zeolites from biomass fly ash is an emerging field [40,116] that offers a pathway for the conversion of waste products into valuable materials. As a product of biomass combustion, biomass fly ash, is composed of predominantly silica and alumina, which are the primary precursors for zeolite formation. Industrial utilisation of biomass fly ashes can act to both mitigate the waste disposal challenge (economical and environmental) and produce adsorbents with good potential for applications in gas separation, water treatment, and catalysis; the focus of this work being the separation of CO<sub>2</sub> from large point source flue gases. This section provides an overview of zeolite synthesis from biomass fly ash, the types of zeolites that can be produced, the preparation methods, and the associated challenges, costs, and environmental considerations.

Zeolites are microporous aluminosilicate materials with well-defined microporous crystalline structures, known for their excellent adsorption, ion-exchange, and catalytic properties [71]. Conventionally, the synthesis of zeolites employs hydrothermal treatment of pristine precursors and is described simply as the mixing of silica, alumina and a source of cations under high pH before heating in a sealed autoclave [117]. In turn, this initiates spontaneous nucleation and crystallisation processes; the overall mechanism of zeolitisation is commonly described in four stages: 1) dissolution, 2) condensation, 3) nucleation and 4) crystallisation [116]. The dissolution of aluminosilicate phases results in monomeric tetrahedra (TO<sub>4</sub>, where T = Si or Al) often defined as the primary or basic building units. These then condense and form localised areas of supersaturation typically around cations such as sodium often described as an aluminosilicate gel where the tetrahedrons share oxygen atoms and can form multi-element rings. From this, various multi-element rings nucleate producing 3-dimension polyhedrons such as sodalite/alpha cages and double 6-rings, which are often described as the secondary or composite building units (CBU). Combinations of these CBUs are what facilitate nucleation of specific crystal structures which is then followed by crystal growth after the integration of subsequent CBUs onto the surface of the zeolite nuclei [118]. When considering the gas separation application, two structures are most commonplace: Linde Type A (LTA) and Faujasite (FAU) zeolites. Type A zeolites often present Si/Al ratios of 1 implying their construction is that of alternating primary building units (Si or Al). They exhibit a cubic arranged with connected cage topology, built from sodalite cages linked by double 4-rings (D4R) [119]. Contrastingly, whilst FAU zeolites are also cubic structures, they belong to a different space group or class and present hexoctahedral arrangements (vs LTA's orthombic) [120]. The CBUs of FAU zeolites are sodalite cages linked by double 6-rings (D6R) [119]. Whilst fly ashes may act as sources of both aluminium and silicon and to some extent, the cations for subsequent zeolitisation, pre-treatment is often necessary to improve the availability of the primary building units in solution. This is a result of fly ashes presenting both crystalline and amorphous aluminosilicate species with differing degrees of reactivity in alkaline mediums [121]. This is most often mitigated through alkaline-fusion of the fly ash precursor to produce more soluble sodium aluminosilicates [40,122]. The fused product is then what is taken for subsequent hydrothermal treatments [123]. A number of comprehensive reviews on this topic are available [40,124–126]. A summary of the synthesis methods for zeolitisation of fly ash is provided in the subsequent sections.

# 2.4.1. Fly Ash Zeolites

Whilst biomass fly ash (BFA) is a product of combustion much in the same way as coal fly ash, the composition of BFA is rarely consistent and exhibits significant heterogeneity owing to variations in biomass sources, combustion conditions and the differences in biomass composition [44]. This leads to extensive implications for any downstream processing such as zeolitisation. The challenges associated with BFA utilisation for zeolite synthesis are provided in the following section.

# 2.4.2. Biomass Combustion Fly Ash Utilisation Challenges

The composition of biomass fly ash can vary significantly depending on the type of biomass burned, combustion conditions, and ash collection methods. This variability can lead to inconsistent zeolite formation and difficulties in controlling the final product's purity and physicochemical properties. Biomass ash often contains impurities such as unburned carbon, alkali and alkaline earth phases, and trace metals, all of which can impinge on the synthesis of zeolite. Of note in the context of composition variability are the relative concentration of SiO<sub>2</sub>, Al<sub>2</sub>O<sub>3</sub>, Ca containing species, and both K and Ph species. It is well known that SiO<sub>2</sub> and Al<sub>2</sub>O<sub>3</sub> vary quite drastically in biomass fly ashes [127], which makes formation of specific zeolite frameworks which form in a narrow range of Si/Al ratios challenging. This can be mitigated to some extent by dosing additional SiO<sub>2</sub> or Al<sub>2</sub>O<sub>3</sub> sources although this adds both cost and complexity and may require the continuous monitoring and adjustment of additives as the BFA composition varies. Elevated concentrations of Ca in BFAs is a result of the biogenic nature of the source, Ca is fundamental for growth, especially in the case of woody biomasses [128]. These species, when present in the hydrothermal mixture can interfere with crystallisation due to the competing formation of calcium silicate or aluminate phases [129,130]. The presence of K and Ph in the BFA precursor also promote the formation of insoluble compounds which can interfere with nucleation and growth of zeolite crystals [131]. This is true for other impurities such as Mg, Fe, and Ti species; there is however, evidence in the literature that these can be incorporated into the zeolite structure thereby altering its properties beneficially [28,132,133]. Mineralogically, whilst the elemental composition varies, so too does the ratio of amorphous and crystalline phases [134], with the former being vastly more reactive under high pH than the latter [135]. This differing in reactivity leads to variation in how the BFA components dissolve and hence leads to inconsistency in the product [136]. The variation in BFA batches limit the ability to standardise synthesis procedures without some level of BFA pretreatment.

Pretreatments to mitigate the effect of BFA variation often feature thermal or chemical processes. For the former, the as-received BFA residue can be calcined to remove any residual carbonaceous species [137]. For the differences in minerology (*e.g.* crystalline/amorphous), the BFA is fused with an alkali, typically NaOH [135,138,139] although other mineralising agents can also be used to differing degrees of success [140]. This fusion process produces far more soluble sodium (in the case of NaOH) silicates and aluminates improving availability of these species in the subsequent hydrothermal reactions [141,142]. This however entails heating the BFA and NaOH to temperatures above 500 °C where the eutectic mixture melts/fuses. Although extremely beneficial for the subsequent hydrothermal zeolitisation, it increases the syntheses energy demand significantly. Chemical processes seek to remove or leach away any of the inactive BFA components [141] however this is associated with additional wastewater treatment making the improvements to product purity/quality difficult to justify.

Environmentally, the synthesis of zeolites from BFA is also associated with significant challenges. Regardless of the pretreatments, the hydrothermal synthesis of zeolites which is the basis of most research works in this field produces a large volume of alkaline waste streams [143]. Whilst it is known that this still has value in terms of subsequent syntheses [144], it will ultimately require neutralisation/treatment prior to disposal. The high energy costs for pretreatments such as alkaline fusion may add quite significantly to the cost and if low-carbon or renewable energy sources are not incorporated, the embedded emissions in the BFA-derived zeolites may limit their environmental 'benefit'. That said, the environmental 'benefits' associated with BFA valorisation are of vast potential. Whilst current production of biomass ash residues is already high, the anticipated increase in the share of BECCS power generation is associated with an increase in the generation of BFAs. Zeolitisation offers a pathway for waste mitigation and valorisation. The absence of BFA landfilling limits the potential for environmental contamination which is known to plague the disposal routes for fly ashes, of both coal and biomass origin [145]. If the BFA-derived zeolites are suitable for implementation in PCCC technologies, this pathway can also contribute positively to the reduction and CO<sub>2</sub> emissions and aid the journey to net-zero GHG emissions.

# 2.4.3. Biomass Fly Combustion Fly Ash Zeolites in CO<sub>2</sub> Capture

Although literature exists for the synthesis of zeolites from fly ashes, most is focussed on coal fly ash (CFA). Even less is associated with the application of fly-ash derived zeolites for CO<sub>2</sub> separation; examples do exist for gas separation in the broader sense. A summary of fly ash derived zeolites and their respective performance (equilibrium CO<sub>2</sub> adsorption capacity and selectivity) is given in Table 2. All of the zeolites have been produced through either hydrothermal (HT) or alkaline fusion assisted hydrothermal (AFHT).

Table 2: Ash-derived zeolites in the published literature and their CO<sub>2</sub> adsorption capacities. \*Capacity estimated from isotherm plot; reproduced from [71].

Precursor	Synthesis Method	Zeolite Type	Degassing Conditions	CO <sub>2</sub> Adsorption Capacity	Ref
Coal Fly Ash	AFHT	X	260 °C Helium	3.21 (0 °C, 1 bar)	[120]
Coal Fly Ash	AFHT	X	300 °C Vacuum	3.25* (50 °C, 1 bar)	[146]
Coal Fly Ash	AFHT	A	300 °C Vacuum	2.47* (50 °C, 1 bar)	[146]
Coal Fly Ash	AFHT	X	260 °C Helium	3.1 (0 °C, 1 bar)	[147]
Coal Fly Ash	AFHT	X	400 °C Nitrogen	3.03 (0 °C, 1 bar)	[132]
Coal Fly Ash	AFHT	X	450 °C	2.43 (40 °C, 1 bar)	[148]
Coal Fly Ash	AFHT	X	300 °C	3.23* (50 °C, 1 bar)	[149]
Coal Fly Ash	AFHT	A	300 °C	2.42* (50 °C, atm)	[149]
Coal Fly Ash	AFHT	X	500 °C Argon	3.3 (25 °C, 1 bar)	[150]
(gasification)					
Palm Oil Fly Ash	AFHT	X		4.47* (32 °C, 1 bar)	[151]
Rice Husk Ash	HT	X	250 °C Vacuum	4.7 (40 °C, 1 bar)	[152]
Rice Husk Ash	HT	X	350 °C	3.12 (0 °C, 1 bar)	[153]
Rice Husk Ash	HT	A	350 °C	1.46 (0 °C, 1 bar)	[153]

# 2.5. Synthesis of Zeolitic Materials from Biomass Combustion Fly Ash

As with the conventional synthesis of zeolites, those derived from BFA are too produced primarily using hydrothermal techniques although after a variety of pretreatments. Often, these pre-treatments are high temperature fusion with NaOH. That said, the scientific community has been progressing with novel techniques to alleviate some of the issues with more conventional synthesis such as alkaline waste, energy intensity and product quality/yield [154]. Although alternatives to the hydrothermal procedure exist, such as in the work of Park et al. [155] the complexity of the process outweighs the utility of the zeolite product. Most of the novel methodologies seek to build upon simpler techniques, i.e. hydrothermal. Hydrothermal synthesis involves dissolving the fly ash in alkaline solutions (e.g. NaOH and KOH) to extract silicate and aluminate species prior to heat treatment. In the context of BFA this method's efficacy is limited when considering that large portions of the aluminosilicate species in BFA are crystalline, such as mullite which is relatively inert under hydrothermal conditions [40]. Alkaline fusion with the solid feedstocks above 500 °C produces sodium silicate and aluminate species which are extremely soluble in alkaline solutions and hence result in zeolite products with improved yield and crystallinity [135]. Multi-step treatments are typically combinations of both hydrothermal and alkaline fusion, generally characterised by increased availability of Al and Si in solution engendering an increased product purity whilst introducing additional cost and complexity [126]. More recently, microwave irradiation and ultrasonication procedures have been investigated [40]. Whilst the former has not been demonstrated above the lab-scale, it is known to accelerate the dissolution of aluminosilicate species through rapid and homogenous heating, shrinking the overall synthesis duration [156] although some authors have reported retardation of subsequent crystallisation [157]. Similarly, whilst sonication has been found to increase the supersaturation of Al and Si in solution during the dissolution of amorphous FA thus reducing reaction times and temperatures, it has not been demonstrated above the lab-scale [123].

# 2.5.1. Hydrothermal Synthesis

Hydrothermal synthesis is the most commonly used method for converting fly ash into zeolites. This method involves mixing fly ash with an alkaline solution, typically sodium hydroxide (NaOH), and heating the mixture at moderate temperatures (80 °C – 200 °C) in an autoclave [117]. Under these conditions, the available species of silica and alumina in the fly ash dissolve, and zeolite crystals gradually form. This method allows for the synthesis of a wide variety of zeolites depending on the temperature, time, and concentration of the alkaline solution amongst other things. The method requires a sealed vessel to provide autogenous pressures usually comprised of a stainless-steel vessel lined with polypropylene or PTFE [126]. Among the factors which exhibit the influence on zeolite product, the hydrothermal time, Si/Al ratio, hydrothermal temperature and NaOH concentration are the primary contributors [143].

#### 2.5.2. Alkaline Fusion

Alkaline fusion-assisted hydrothermal synthesis incorporates a thermal pretreatment entailing the fusion of fly ash with an alkaline agent (commonly NaOH) at elevated temperatures (typically 500°C – 700°C). This initial stage facilitates the decomposition of relatively inert aluminosilicate species in the BFA precursor, forming sodium silicates and aluminates with an increased solubility of silica and alumina for subsequent hydrothermal steps [40,122,123]. After the fusion procedure, the material is dissolved in water and subjected to hydrothermal treatment as in the basic hydrothermal method. This two-step process enhances the efficiency of zeolite formation and can result in higher purity and better crystalline zeolites compared to hydrothermal synthesis alone [40,124–126].

# 2.6. Key variables in Alkaline Fusion Assisted Hydrothermal Synthesis

The impact of reaction conditions on the zeolite quality is of significant importance. The zeolite product purity, quality, composition and *etc.* have significant implications on the downstream application, in this case CO<sub>2</sub> adsorption. There is vast evidence in the literature that suggests through optimisation of the synthesis conditions, the product can be somewhat tailored towards a specific application or property such as CO<sub>2</sub> adsorption, increased crystallinity and purity, surface area or pore volume, cation coordination and *etc.* The following discussion will highlight the key factors in the synthesis of zeolites from BFA such as the NaOH to BFA weight ratio, the hydrothermal temperature, the hydrothermal time and the liquid to solid weight ratio.

# 2.6.1. NaOH to Fly Ash Ratio

As a factor in both the hydrothermal and alkaline fusion assisted hydrothermal synthesis procedures, the proportion of NaOH in the reaction mixture is a key parameter. Whilst this would entail defining the molarity of solution for conventional hydrothermal syntheses, during alkaline fusion the reactants are mixed in the dry phase. The significant influence of this factor was identified in the work of Sivalingam *et al.* [158] when optimising for product crystallinity. Verrecchia *et al.* also investigated NaOH/CFA ratios along with hydrothermal temperature and time [150]. They found that higher ratios led to the formation of stable zeolites such as sodalite or cancrinite (and also LTA). For the formation of type X, a ratio of 1.2 was required (at a hydrothermal temperature of 90 °C). Molina and Poole in their work revealed that an increase in the NaOH/FA ratio, promotes improved crystallinity and product purity [129]; this is somewhat contrasting to Verrecchia *et al.* where higher ratios formed denser phases such as sodalite and cancrinite [150]. Interestingly, Lie *et al.* identified the selective formation of A (over X) at higher NaOH/FA ratios [159]. These seemingly contradictory findings are likely a result of the variation between fly ash precursors, highlighting the importance for synthesis optimisation based on resource.

# 2.6.2. Hydrothermal Temperature

The conditions the mixture is exposed to during hydrothermal treatment are also of importance. In this case the hydrothermal temperature is known to present significant influence on the rate of zeolite crystallisation, the structure type and the crystal size. Yang et al found that at a temperature of 40 °C, the degree of crystallisation is minimal resulting in primarily amorphous aluminosilicates [160]. Increasing the temperature acts to increase the pressure in the vessel increasing the dissolution and hence crystallisation rates during syntheses, at 90 °C LTA zeolites with high crystallinity were achieved. This observation was also observed when studying temperatures in the range of 90 to 120 °C for the synthesis of type X; for type A no significant impact was observed [161]. That said, a lower hydrothermal temperature is known to reduce the crystallinity of the product along with the crystal size and yield [158]. A temperature of 80 °C was identified as the optimum when optimising for crystallinity (58 – 72%), associated with an increase in crystal size from 22.6 to 33.3 nm. Faujasitic zeolites were observed to form more readily at 90 and 100 °C, with the latter producing type X with an 88% product yield. It has been postulated that formation of zeolite X is often favoured under milder conditions however, such as a reduced temperature, pH and synthesis time [120,162,163]. Bai et al. identified 80 °C to be the optimum for type X crystallisation [164]. Ojha et al. identified correlations between the hydrothermal temperature and product surface area [141] with a maximum identified at 6 h (vs 10 h). As with the previous factor (NaOH/CFA) there appears to be some conflicting information in the literature although there is consensus that type X zeolites form more favourably at lower hydrothermal temperatures  $(80 - 90 \, ^{\circ}\text{C})$ .

# 2.6.3. Hydrothermal Time

The other factor of importance in the hydrothermal treatment is duration or time. It is commonly understood that type X zeolites often require a longer time to be fully formed when compared with Na-A, even up to 24 h as it has more complex and larger polymeric silicate units than A thus it could be more difficult to nucleate leading to lower crystallisation rate [134,161]. Yang *et al.* [160] during their study into CFA-derived zeolites identified important effects on the crystal morphology, size and crystallinity when vary hydrothermal time. This period involves dissolution of Al and Si sources, by increasing duration from 4 to 6 h, relativity crystallinity increased from 44.5% to 72.4% for Na<sub>2</sub>CO<sub>3</sub> fused CFA. The optimum point for NaOH fused fly ash, was 4 h which produced a 68.2% crystallinity; above 4 h, sodalite was observed in the product. An increase in hydrothermal time was also observed to improve both yield and crystallinity by Sivalingam [158]. In this work, the hydrothermal times were varied between 5, 7.5 and 10 h increasing yield from 59 to 88%. Hong *et al.* revealed that when modifying conditions with influence on the rate of crystallisation, such as NaOH/FA ratio or the hydrothermal temperature, the hydrothermal time must be adjusted in order to target phases such as type A and type X due to the metastable nature [165]. In their work, an optimum LTA product was identified at an NaOH/CFA ratio of 1.5, a hydrothermal temperature of 100 °C and a duration of 12 h.

The hydrothermal duration of the syntheses was also revealed to be of importance by Bai *et al.* [164] where prolonging the time was found to improve the type X product's crystallinity, at 24 h the crystallinity was 82.5%. This was attributed to the crystallisation process comprising both induction and growth periods, in the absence of sufficient time, crystallisation is rarely complete [166]. Whilst the literature is less conflicting for this factor, it does appear to be contingent on the other factors at play such as temperature and NaOH concentration. Any increase to the latter may result in reduced product quality for the same durations.

# 2.6.4. Liquid to Solid Ratio

In conventional hydrothermal synthesis the liquid to solid ratio directly correlates to the solution pH or basicity, in the case of alkaline fusion assisted hydrothermal, this variable refers to the ratio of water to alkali fused fly ash. Whilst direct correlation with pH is difficult, this factor plays a key role during the hydrothermal component of an alkaline-fusion assisted hydrothermal scheme. A wide range of ratios are often investigated and are usually optimised to specific fly ash precursors owing to their inherently variable composition. At a liquid to solid ratio of 8, Yang *et al.* produced a zeolite with the highest purity and crystallinity, albeit type 4A (LTA), at lower ratios (3) only sodalite was formed [160]. This was attributed to the metastable nature of LTA's ring skeleton having a higher structural energy than that of the sodalite [167]. Similarly, when Bai *et al.* [164] studied the effect of liquid to solid ratio, they revealed that at high liquid to solid ratios, low quality type X formed. At low liquid to solid ratios, crystallinity was observed to reduce due to the successive dissolution of crystalline species in the presence of excess hydroxyl ions [168]. There is a definite requirement for optimising the liquid to solid ratio in order to produce zeolites suitable for their desired application.

## 2.6.5. Other Factors

Whilst the aforementioned factors present significant influence in the synthesis of zeolites from fly ashes, other factors are also often considered. These include modification to the mixtures Si/Al ratio (or oxide ratio) as well as the ratio of other species such as Na<sub>2</sub>O or H<sub>2</sub>O. Whilst these are key when tailoring to specific crystal structures, they require the addition of pure feedstocks or extraction of components from the fly ash, adding complexity and cost and detracting from the effective utilisation of the bulk waste residue. With a view to produce zeolites for specific gas adsorption applications (*e.g.* CO<sub>2</sub> adsorption) knowledge of appropriate Si/Al ratios are still of value as this can be useful when characterising the precursor feedstocks. With that in mind, an Si/Al of around 1.8 (molar) is often identified as suitable for type X formation. above this and type P1 co-crystallises and lower than this type A co-crystallises [161,169]. Whilst not the focus of this work, the fusion conditions are also of importance but most work identifies an optimum at 550 °C, with negligible differences in efficacy for durations over 1 h [165]. Additionally, aging of the mixture after the addition of the fused solid is also important as it is related to the development of zeolite nuclei. Studies have shown that aging can reduce the required crystallisation duration at high temperatures; an optimum aging duration was identified at

18 by Ojha *et al.* [141]. That said, most studies employ stirred aging of between 10 and 16 h. In the remit of aging, some work has also sought to filter any solid residue post-aging to remove any solid particulates during hydrothermal processes [161,170]. Whilst there may be benefit in doing this it produces an additional waste stream and adds both cost and complexity.

# 2.7. Statistical Design of Experiments

Design of experiments (DoE) plays a crucial role in optimising engineering processes and material synthesis, providing a systematic and both cost and time efficient approach to experimentation. Unlike parametric studies or the traditional one-factor-at-a-time (OFAT) method, DoE permits the simultaneous exploration of multiple variables affording a comprehensive understanding of complex systems. This is of particular importance in engineering and materials science where interactions between variables often present significant influence over the outcome. By considering these interactions, DoE reduces the total number of experiments required to achieve optimisation, leading to time and resource efficiency. The robust statistical framework of DoE enables more reliable conclusions about the effects of experimental variables by maximising the amount of information which can be extracted from a specific campaign [171], improving the decision-making process and building confidence in the optimisation. Thus, DoE is widely favoured for its efficiency, effectiveness, and ability to handle complex, multi-factorial systems which are often found in the engineering and material science domains.

Commonly, individual factors are studied by varying them independently via OFAT [172]. Whilst the OFAT approach can reveal effects of single variables on the investigated output, it's lacking when considering any synergistic or antagonistic interactions between factors due to the inherent isolation of variables, ultimately restricting the investigated design space. In order to investigate the impact of factor interactions, advanced experimental campaigns require the adoption of statistical DoE which defines the framework for simultaneous modification of factor levels which also acts to reduce the total number of required experiments improving cost and time efficiency. Commonly adopted DoE techniques include factorial designs and Response Surface Methodology (RSM) designs, both of which systematically vary factor inputs to facilitate regression analysis and hence the prediction of optimal factor and level configurations whilst also identifying those factors of statistical significance. The correct implementation of DoE provides opportunity for optimisation of process performance, efficiency, material properties and product quality amongst other things, making it an invaluable tool in both the engineering and scientific communities. In the context of this work, DoE can be used for the investigation and optimisation of both the zeolite synthesis from BFA and the fixed-bed TSA process in which they will be applied.

# **2.7.1. Designs**

Within the field of DoE a range of techniques exist, selection of which depends upon the desired outcome from the experimental campaign. In general, designs are suited to the screening of factors for those with statistically significant impact on the dependent variable. Alternately, designs can be employed for statistically informed optimisation so as to maximise or minimise an objective function or aim for a specific value; this is often achieved through mapping the response surfaces within an experimental design space. With that said, some experimental designs find use in both applications simultaneously.

The simplest designs involve the evaluation of all possible combinations of input factors. These factorial designs are vastly informative but can be burdensome when the number of investigated factors increases as the number of possible combinations grows exponentially. Factorial designs due to this however, provide insight into both the main and interaction effects for each factor. Whilst this is beneficial, study of the complete design space is inefficient, *e.g.* a 3-factor full factorial would require 2<sup>3</sup> runs for completion. Their fidelity however is vast, so they're often utilised in small-scale campaigns where a comprehensive understanding of interactions is the objective [172]. With a view to reduce the overall resource intensity (time and cost), fractional factorial design study the experimental domain by systematically selecting combinations of factors and levels [173]. These designs are well poised for campaigns concerned with a large number of factors. This is made possible by assuming interactions of higher order between factors are negligible whilst priority is given to the factor's main effects and low order interactions. Higher order interactions are rarely significant, fractional factorials whilst they have less fidelity still provide efficient insight into those factors with the greatest significance [172].

Beyond this, fractional factorial designs are the basis for advanced DoE methodologies including the frameworks proposed by Taguchi and Central Composite Designs (CCD) [174]. The latter falls within a broader set of Response Surface Methodology (RSM) designs which also includes Box-Behnken Designs (BBD). As the name implies, these methodologies are better suited to systems where the relationship between dependent and independent variables is not adequately described by a linear model. The CCD is defined through the addition of experimental runs at the axial and centre points to an existing factorial design [175] facilitating the inclusion of quadratic terms in the regression analysis. This enables any higher-order effects to be revealed improving the response surface mapping and optimisation [172,176]. These designs have a good degree of flexibility and fidelity in the context of interactions; therefore, they lend themselves to complex systems with a large potential for interactions. The disadvantage of CCD designs, however, relates also to the axial points, these tend to be at the upper range of factor and level configurations, if the system is sensitive to this such as in material syntheses, the information obtained from the experiments is of limited use. For this reason, BBD designs are often selected; these typically require slightly fewer experimental runs (for the same number of factors/levels)

and they avoid the upper range of the experimental domain mitigating certain concerns around the impracticality or even safety [177,178].

When the intent is to optimise for system robustness, the Taguchi method is often more applicable. Here the focus is to improve product or process quality by increasing the resilience to external variation, *i.e.* increasing the signal to noise ratio of the response [179,180]. The basis of Taguchi designs are orthogonal arrays; these overlay two factorial designs as an inner array of control factors and an outer array of noise factors. This enables Taguchi DoEs to evaluate a system's robustness under simulated controlled and random variation [172,181]. This consideration for noise and an ability to isolate individual factor's main effects and some two-way interactions make Taguchi designs extremely efficient and reliable [172]. The inclusion of both qualitative and quantitative factors is relatively simple and hence these designs often find application in industrial applications, much in the way Taguchi himself intended.

The selection of a DoE design depends on the specific goals of the experimental campaign, whether screening factors for statistical significance or optimising a process by mapping the response surface. Factorial designs, including full and fractional factorials, are effective for screening and studying interactions between factors, while RSM designs (CCD and BBD) are ideal for optimisation tasks where non-linear relationships take precedence. The Taguchi method stands out for its ability to tailor for robustness, reducing variability in the presence of noise factors.

## 2.7.2. Statistical Analysis

Post-completion of any suitably designed experimental campaign, a series of statistical analyses are required to determine significance of the factors and their interactions. Of the analysis techniques, Analysis of Variance (ANOVA) is commonly employed as it allows for the evaluation of multiple factors and multiple levels (> 3) [182] and their statistical significance on the response. The technique was originally developed by Sir Ronald Fisher to provide a way to interpret simulation results by breaking variation up into accountable sources [183]. For ANOVA to be applicable however, a number of assumptions must be satisfied and these include: randomisation of the experimental runs, full independence between replicates and the results must follow a normal distribution [184]. The effective output of ANOVA includes the relative contribution to the response and both p- and F- statistics, with the former often set at a 95% confidence level. For a factors to be defined as statistically significant, the p-value must be sufficiently small so as to reject the null hypothesis, that the response variation is a result of noise. Contrastingly, the F-value is indicative of the variation between means, with a higher number suggesting a stronger influence on the dependent variable. For the analysis of CCD or BBD designs, the RSM approach aims to approximate the relationship between dependent and independent variables through a surrogate/empirical statistical model [185]. The response is often mapped in three (surface) or two (contour) dimensions for those factors identified with statistical significance. For Taguchi designs, the analysis often involves ANOVA and analysis of the factors main effects and Signal-to-Noise (SNR) ratios on the response. The latter is utilised for determination of the optimum factor and level configuration which satisfy the objective based on the SNRs. The SNRs are calculated using one of three equations, selection of which relies on the aim to minimise the SNR, maximise the SNR or nominal is best [179,180].

# 2.7.3. Design Of Experiments in the Synthesis of Biomass Combustion Fly Ash Derived Zeolites

In the context of BFA zeolitisation and subsequent applications of these products, DoE techniques have found some use. A fractional factorial design was adopted by Kastanaki *et al.* [186] to investigate the influence of 5 factors on the conversion of lignite (CFA) ash to zeolites:  $SiO_2/Al_2O_3$  ratio (4.31 – 6.27), solid/liquid ratio (1/2 – 1/4), crystallisation temperature (90 – 150 °C) and crystallisation time (2 – 6 h). Whilst the intent was to maximise yield, the author's identified the temperature to be statistically significant with the primary contribution to the response coming from the crystallisation temperature, time and the interaction between the  $SiO_2/Al_2O_3$  and S/L ratios.

A CCD was adopted by Verrechia et al. [187] to investigate the impact of NaOH/CFA weight ratio (0.87 - 1.53), crystallisation temperature  $(73 - 107 \, ^{\circ}\text{C})$  and crystallisation time  $(4.3 - 7.7 \, \text{h})$  on the zeolite product's adsorptive performance. All three factors were identified as statistically significant with the optimum values of 1.4, 80 °C and 7 h resulting in a type X zeolite with an amorphous constituent (no other crystalline species were identified). The authors identified that any indefinite increase to the factor's levels results in the formation of more stable (and less useful) zeolites such as sodalite. Chansiriwat et al. also investigated the zeolitisation of CFA via CCD [188]; in this work two factors were studied, the hydrothermal temperature  $(105 - 195 \, ^{\circ}\text{C})$  and hydrothermal time  $(12 - 84 \, \text{h})$ . The impact was evaluated on the bases of product specific surface area (BET), both factors were identified as statistically significant with an optimum at 105 °C and 12 h. Both a factorial and CCD design was implemented by Doumit et al. [175]. In this work, the factorial design (centrally weighted design, CWD) investigated five factors temperature (75 - 105 °C), time (24 - 72 h), NaOH concentration (3-5 M), S/L ratio (1:5-1:3) and Al/Si ratio (1:5-2:1). The optimisation revealed the optimum point to be close to outside the edge of the matrix, reducing reliability. The CCD was then incorporated by studying the most important variables: temperature (60 - 80 °C), NaOH concentration (4-6 M) and Al/Si ratio (2:5-4:5). The optimum zeolite presented a crystalline yield of 38.3% and a BET surface area of 228 m<sup>2</sup>·g<sup>-1</sup> with a hydrothermal temperature of 72.5 °C, 5M NaOH solution and an Al/Si ratio of 3:5

Taguchi designs have seen more application in the field of fly ash derived zeolites such as in the work of Tirva *et al.* [189] where an L9 OA was employed for the investigation of the impact of fusion temperature ( $500-600\,^{\circ}$ C), fusion time ( $9-15\,\text{h}$ ), liquid/solid ratio (L/S =  $1.1-1.5\,\text{ml}\cdot\text{g}^{-1}$ ) and alkaline solution concentration (NaOH =  $1-1.3\,\text{M}$ ) to maximise Na-X yield. The author's identified strong

main effects for all factors but fusion temperature and L/S were identified as the greatest contributors. The zeolitisation of fumed silica and CFA has also been investigated via Taguchi DoE [190]. Here the  $SiO_2/Al_2O_3$  ratio (4 – 6), NaOH concentration (1 – 2 M), synthesis time (12 – 36 h) and hydrothermal temperature (100 – 140 °C) were investigated in an L9 OA to study their impact on product crystallinity. The hydrothermal temperature and NaOH concentration had the main contribution to crystallinity (58.7% and 32.8%, respectively) based on the ANOVA of the SNRs. Larger Taguchi methods have also been employed in alkaline fusion hydrothermal conversion of CFA [191]. This L27 design studied 6 factors at 3 levels: NaOH/FA ratio (1.1 – 1.4), fusion temperature (300 – 650 °C), fusion time (0.5 -2 h), aging time (0.5 - 24 h), crystallisation temperature (60 - 110 °C) and crystallisation time (4 - 16 m)h). The response in this work was the product's BET surface area. The optimum factor level configuration was NaOH/FA = 1.2, fusion temperature = 550 °C, fusion time = 0.5 h, aging time = 24 h and crystallisation time = 16 h. The most significant factor was identified as the crystallisation temperature; the optimum product was approximately 90 % type X zeolite based on CEC and surface area with a 65 % product yield. An L27 OA was also employed by Medina et al. [192] however in this case, the alkaline source (NaOH/KOH/LiOH), weight percent of alkaline, crystallisation time (8 – 24 h), crystallisation temperature (120 – 175 °C) and stirring speed (100 – 600 RPM) were investigated on the percentage crystallinity of the product. The author's identified the most statistically significant factor to be the alkaline type (with 73% contribution to the response) attributed to the activation degree of the mineralising agent on the FA since this leads to nucleation and zeolite growth. Whilst crystallinity and quality can be used as responses, so too can adsorptive/catalytic properties. In the work of Haghjoo et al. [193], Austrian CFA was investigated for zeolitisation in the context of glyphosate removal efficiency. Here an L9 OA was used to investigate the impact of SiO<sub>2</sub>/Al<sub>2</sub>O<sub>3</sub> ratio, alkaline concentration, crystallisation time and crystallisation temperature. In the work of Tabit et al. [194], hydrothermal temperature (100 – 150 °C), hydrothermal time (12 – 48 h), NaOH concentration (0.5 – 3.0 mol·L<sup>-1</sup>) and L/S ratio (ml·g<sup>-1</sup>) were investigated for their impact on product crystallinity. The hydrothermal temperature had the greatest contribution to the response (43 %) followed by NaOH concentration (29%) and L/S ratio (28%).

## 2.8. Research Gap

Whilst a good body of research exists in the literature pertaining to the synthesis of zeolites from BFA, very little exists that focusses on industrially produced residues and even less for the synthesis of zeolites for selective separation of CO<sub>2</sub>. A large portion of the literature is actively seeking high purity zeolites, but this is often associated with a significant degree of experimental complexity or erroneous conditions. Tailoring any BFA treatments to facilitate improved zeolite synthesis whilst possible, may limit the potential for scaling up. It is highly likely that the BFA precursor will present variation such that any optimised pretreatment for a specific batch may be inapplicable for another. Whilst tailoring to specific batches is technically feasible, it is likely unviable. Feedstock quality is inherently variable so

any pretreatment should be robust to this. With the view to mitigate fly ash disposal and potentially reveal the feasibility for zeolitisation as a pathway to remediation, this work seeks to maximise the utilisation of BFA by employing the bulk residue in the synthesis of zeolites. To do so, statistical design techniques should be incorporated to ensure suitable optimisation and reliability, something often not considered in the literature. In the interest of combatting waste variation, Taguchi techniques are well suited to reduce the variability in the product by optimising the input conditions. Whilst most research stops here, investigation of the zeolite product's potential for CO<sub>2</sub> separation is only truly possible through representative application in a reaction vessel such as a fixed-bed adsorber. The design, build and commissioning of such has been in the remit of this thesis. Investigation of the parameters which influence the BFA-derived zeolites performance for CO<sub>2</sub> capture in fixed-bed is also required to reveal the actual potential for these materials in post-combustion CO<sub>2</sub> capture.

## 3. Characterisation Methods

#### 3.1. Material Characterisation

The characterisation of adsorbents is necessary for both understanding and describing the adsorption properties they have as well as for their comparison. Various techniques can be used to generate a comprehensive picture of the adsorbent's physicochemical properties and characteristics.

# 3.2. Scanning Electron Microscopy and Energy Dispersive X-ray Spectroscopy

The morphological characteristics of both fly ash precursor and zeolite product specimens can be identified through the use of a Scanning Electron Microscope (SEM) which can elucidate to the topographical nature of the materials. When coupled with the Energy Dispersive X-ray Spectroscopy (EDS), identification of the distribution of elements present in the adsorbents can be achieved [195].

Morphological analysis of the as-received biomass combustion fly ashes and the produced specimens has been completed by employing Scanning Electron Microscopy (SEM). As a non-destructive technique this instrument directs a focussed beam of electrons onto the surface of a specimen. The electrons interact and produce secondary electrons, backscattered electrons and X-rays, all of which can be detected to produce detailed images. The secondary electrons are produced during inelastic scattering of the primary electrons and afford the visualisation of the specimen's topology. Contrastingly, backscattered electrons are those produced during elastic scattering, these high energy electrons originate from deeper in the specimen and result in brighter imagery for atoms of higher atomic number due to increase scattering. Operationally SEM instruments typically require high vacuum chambers and an electron gun with an accelerating voltage up to 20 kV. Sample preparation involves affixing the specimen to an aluminium stub either through dispersion in isopropanol or a conductive adhesive (carbon tape or silver paint). Both fly ash and zeolite specimens are non-conductive and therefore require sputter coating with gold to minimise localised charging.

Energy Dispersive X-Ray Spectroscopy (EDS) is an analytical technique used in conjunction with SEM to determine the surface elemental composition of materials. When subjecting a specimen to an electron beam, characteristic X-rays are emitted from elements present in the sample. Through determination of the X-ray energy and their number, the sample's elemental composition can be estimated. That said, for elements with an atomic mass below that of Na, EDS often fails to accurately quantify. This is attributed to the emission of longer wavelength X-rays providing weaker signals which can be absorbed in the specimen [196]. This technique also facilitates visualisation of the distribution of elements across the specimen by allowing mapping of the characteristic X-rays providing insight into any localised concentrations of elements. This corroborates morphological analysis between various species present in the samples (*e.g.* crystalline or amorphous).

# 3.3. Fourier Transform Infrared Spectroscopy

Fourier Transform Infrared Spectroscopy (FTIR) is an analytical technique used to identify and characterize chemical substances based on their molecular vibrations. By measuring how a material absorbs infrared radiation at different wavelengths, FTIR provides a unique spectral fingerprint that reveals information about the functional groups and molecular structures present. This technique whilst able to identify various bonds present in crystalline zeolites (both framework and non-framework Si-O and Al-O vibrations) the information you can draw from this is limited as most unit cells exhibit vibrations at similar wave numbers. For fly ashes, whilst their inorganic composition may limit the interaction with IR due to the lack of strong excitation upon exposure to IR spectra [197] it can be used to corroborate findings from other techniques such as EDS and XRD. Samples are prepared by mixing trace amounts of specimen with KBr to dilute the specimen and increase the detectability of the IR radiation. This preparation method suits the transmission methodology of FTIR as KBr does not present any absorption bands above 400 cm<sup>-1</sup>. That said, the compression of the mixture into a disc can induce structural changes in the specimen; KBr is also extremely hygroscopic resulting in large O-H bands in the absence of dehydration prior to analysis. For this reason, FTIR has only been employed for analysis of the fly ash precursor.

# 3.4. X-ray Diffraction

Identification of phases present in both the fly ash precursors and zeolite products has been achieved through analysis of X-ray Diffraction (XRD) patterns. As an extremely powerful technique, XRD can identify the presence of specific crystalline phases of materials through the diffraction and scattering of X-rays due to interactions with the sample's atomic lattice. This can afford information around crystallinity, structure quality and composition often achieved through software which can facilitate both quantitative and qualitative assessments of the mineralogic content in adsorbents [146]. The XRD instrument features an X-ray source where high-energy electrons are accelerated and collide with a metal target, often copper which causes the emission of X-rays with characteristic wavelengths. Diffraction occurs when light is scattered by a periodic array which possesses long-range order, this can produce constructive interference at various angles. The electrons of an atom scatter light coherently, the strength of which is directly related to the number of electrons around the atom. In crystalline structures, the atoms are present in an array with periodicity and hence they can diffract light. The scattering of X-rays in a crystalline specimen will produce a diffraction pattern that contains information about the crystal's atomic arrangement. The position of these diffraction peaks is determined by the distance between parallel planes of an atom as the condition for constructive interference is described by Braggs Law, EQ. 19, where  $\lambda$  is the X-ray wavelength,  $d_{hkl}$  is the interplanar spacing. The intensity of the diffraction peaks is dictated by the location of atoms in a crystal structure and what they are (i.e. how well they scatter X-rays). When a crystal structure with multiple diffraction peaks is analysed, the produced diffraction pattern/diffractogram is characteristic to that phase, allowing for accurate phase

determination based on existing datasets. When multiple phases are present the diffractogram is a composition of these. If amorphous phases exist, while these will not produce sharp diffraction peaks, broad peaks are produced often centred at specific angles allowing for an approximate identification.

$$\lambda = 2d_{hkl}\sin\theta$$

In this work, powder X-ray diffraction or more aptly polycrystalline diffraction has been employed due to the nature of the investigated specimens, fine powders. The instruments used for this application often use Bragg-Brentano geometry. In this configuration the diffraction vector, the angle which bisects the angle between the incident and scattered beam is always normal to the specimen surface and hence parallel to the plane normal (hkl). Polycrystalline samples contain a large number of crystallites, meaning all possible diffraction peaks should be observed permitting these are randomly oriented. To facilitate this, the powder specimen must be produced with a small and narrow size distribution before lightly pressing into a corundum sample holder.

# 3.5. Particle Size Analysis

Particle size analysis of the fly ash precursor has been achieved through laser diffraction techniques. The particle size distribution of the fly ash is of importance due to the influence on a material properties and reactivity during the alkaline fusion required prior to the hydrothermal synthesis of ash derived zeolites. It is suitable for particles with a broad size range and types, such as powders, suspensions and emulsions. The principle relies on the scattering of light through a suspension whereby the scatter angle is inversely proportional to the particle size, *i.e.* larger particles scatter light at small angles and viceversa. Detectors measure the intensity of the scattered light, and the size distribution is determined through mathematical models such as Mie theory. In this work, a Beckman Coulter LS230 Particle size analyser was employed. Samples were prepared by dispersing the fly ash (< 0.2 g) in 50 ml of 4% sodium hexametaphosphate solution prior to ultrasonic disaggregation for 10 min. The distribution width is defined by the  $D_{V0.9}$ ,  $D_{V0.1}$ ,  $D_{V0.5}$  values, which represent the diameter where 90 %, 10 % and 50 % of the population lies below this value. The volume mean diameter is defined by  $D_{[4,3]}$ , EQ. 20.

$$D[4,3] = \frac{\sum_{i=1}^{n} D_i^4 v_i}{\sum_{i=1}^{n} D_i^3 v_i}$$
 EQ. 20

## 3.6. Surface Area and Porosity

In the context of gas adsorption, textural properties are also of significant importance. The porosity and external surface area of a material are largely responsible for its ability to facilitate the adsorption of adsorbates. Measurement of these properties is most often achieved through analysis of experimental adsorption isotherms. The initial analysis involves qualitatively assessing the isotherm shape and features such as hysteresis. The isotherms are then fit with an isotherm model which can facilitate determination of the external surface area. The Brunauer-Emmet-Teller or BET model is a popular choice and employs the adsorption isotherms of nitrogen at 77K (the boiling point of N2) [198,199].

Other gases are too employed such as Ar or Kr, however these are more costly than  $N_2$  [59]. The isotherm is measured after the adsorbent specimen is suitably degassed, in this work the degassing procedure has been aligned to ASTM D4365 [200] featuring a vacuum degassing temperature of 350 °C (1 °·min<sup>-1</sup>) for 12 h. The external surface area is determined *via* the BET equation (EQ. 21) in the  $P/P_0$  range which satisfy the criteria defined by Rouquerol [201]; traditionally this linear region was taken between 0.05 – 0.35 however this has limited applicability when the specimen presents microporosity. In EQ. 21, v is the specific adsorbed volume at relative pressure  $P/P_0$ , C is the BET constant and  $v_m$  is the specific monolayer adsorbed volume.

$$\frac{p}{\nu(p_0 - p)} = \frac{1}{\nu_m C} + \frac{C - 1}{\nu_m C} \left(\frac{p}{p_0}\right)$$
 EQ. 21

Total pore volume and pore size distribution of FA and zeolite samples in this work have also been estimated *via* analysis of the N<sub>2</sub> isotherm at 77K. For FA this was achieved by applying the Barrett-Joyner-Halenda (BJH) method. This method is considered a classical approach and combines the Kelvin equation with a cylindrical pore model to determine the distribution of pore sizes and the pore volume of a porous material in the mesopore range [202]. The applicability of this method to zeolitic materials is limited as they fail to satisfy the assumption of a cylindrical pore shape. In this case, Density Functional Theory methods have been applied to estimate the total pore volume as this is often considered more reliable due to their ability to capture micropore and mesopore filling and hysteresis [203,204]. Both methods (BJH and DFT) have been implemented in the Kaomi software provided by Anton Paar. The micropore volume of the samples in this work has been estimated through the t-plot method. Whilst other methods exist, the t-plot method is widely used due to its versatility. The technique relies on the estimation of surface area through the thickness of the adsorbed layer, t. The value *t* is referred to as the statistical thickness [205]. The adsorbed volume is plotted against the adsorbed layer's statistical thickness which is given by the de Boer equation, EQ. 22 [206,207].

$$t(\text{Å}) = \left[\frac{13.99}{\log\left(\frac{p_0}{p}\right) + 0.034}\right]^{\frac{1}{2}}$$
 EQ. 22

#### 3.7. Thermogravimetric Analysis

Thermogravimetric Analysis (TGA) is an analytical technique that measures the change in mass of a material as it is heated or cooled over time. This method provides critical insights into the thermal stability, composition, and decomposition processes of substances by recording weight changes associated with physical and chemical transformations. Whilst not conventionally used for the assessment of adsorption/desorption, the instrument facilitates precise control of both temperature and chamber atmosphere whilst recording sample mass to high accuracy. In this work a Mettler Toledo TGA 2 system has been employed for proximate analyses and investigation into the adsorptive performance of both ash precursor and zeolite product specimens.

# 3.7.1. Proximate Analysis and Decomposition

Proximate analyses have been carried out aligned with ASTM D7582 [208] to determine the quantity of moisture, volatile organic compounds (VOCs), fixed carbon and ash that is present in the biomass combustion fly ash precursor and derived adsorbents. The procedure follows placing the sample into an alumina crucible and exposing this to a series of thermal treatments. The first assesses the moisture content by heating to 107 °C under N<sub>2</sub> (22 ml·min<sup>-1</sup>) for 1 h. The temperature is then increased to 950 °C (30 °C·min<sup>-1</sup>) under N<sub>2</sub> for 7 minutes to determine VOC content. The sample is then cooled to 600 °C under N<sub>2</sub> before the gas is switched to an oxidising gas (air, 22 ml·min<sup>-1</sup>) and then heated to 950 °C (6 °C·min<sup>-1</sup>) where it is held for 3 h leaving the ash residue; the fixed carbon content is calculated as the mass loss during this final heating stage.

# 3.7.2. Adsorption and Desorption Analysis

The adsorption of CO<sub>2</sub> has also been evaluated through the use of a TGA by simulating a TSA cycle with pure component gases. In this context, the sample is loading into an aluminium crucible before it is degassed at 150 °C (10 °C·min<sup>-1</sup> from ambient) under N<sub>2</sub> (50 ml·min<sup>-1</sup>) for 2 h to remove any preabsorbed species; the lower degassing temperature is employed here to simulate conditions more representative of the post-combustion capture scenario, *i.e.* regeneration conditions of approximately 150 °C correlating with low-grade steam availability. After degassing, the sample is cooled to the adsorption temperature where after settling, the gas flow is switched to 100 mol% CO<sub>2</sub> (50 ml·min<sup>-1</sup>) and held until equilibrium has been achieved. In screening assessments, the adsorption time was fixed at 2 h however equilibrium is defined in this work as a mass change of less than 0.005 mg·min<sup>-1</sup>. This final mass value is used to determine the equilibrium adsorption capacity measured gravimetrically. The dataset of adsorbed amount vs time has been used to investigate the kinetics of CO<sub>2</sub> adsorption at the small scale. A typical TGA programme employed for analysis of adsorption and desorption is provided in Figure 3.1.

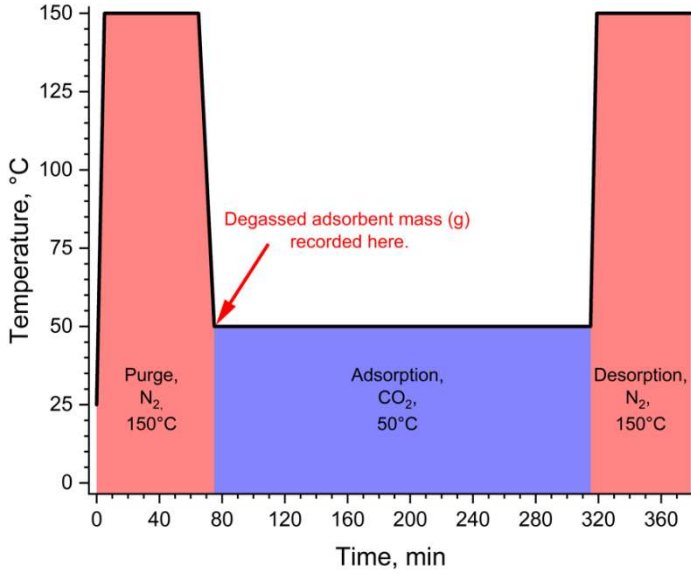


Figure 3.1: A typical programme sequence employed to analyse the adsorption of CO<sub>2</sub>via TGA.

## 3.8. Adsorption Kinetics

With the adsorption data from the TGA, the kinetics have been investigated by fitting the adsorbed amount against time to various kinetic models. In this work four kinetic models have been evaluated for quality of fit, these are given in Table 3-1.

Table 3-1 Kinetic models investigated for quality of fit in this thesis.:

Model	Differential Equation		
Pseudo First Order, PFO	$\frac{dq_t}{dt} = k_1(q_e - q_t)$		
Pseudo Second Order, PSO	$\frac{dq_t}{dt} = k_2 (q_e - q_t)^2$		
Elovich	$\frac{dq_t}{dt} = \alpha e^{-\beta q_t}$		
Intraparticle Diffusion W&M	$q_t = k_{IPD} \cdot t^{1/2} + C$		

## 3.9. Volumetric Equilibrium Gas Adsorption

As an alternative to gravimetric techniques, volumetric gas adsorption has been the traditional method owing to its relative simplicity [53,209]. This technique is that which is employed by most commercially available BET surface area analysers and relies on the measurement of changes in pressure in a calibrated volume at a constant temperature. Gas is normally dosed from a vessel of known/calibrated volume to another containing the adsorbent. The dosed amount should correlate to an increase in pressure in the second vessel; any deviation from this is a result of adsorption onto the adsorbent. By plotting the adsorbed amount vs absolute pressure an equilibrium adsorption isotherm is produced. This isotherm can be fit with theoretical or empirical models to reveal the adsorption mechanisms. In this work, five isotherm models have been investigated for quality of fit, these are given in Table 3-2. All samples in this thesis were degassed under high vacuum at 350 °C prior to analysis; the instrument employed was an Anton Paar NOVA 600 instrument. The sample bulb dead volumes were corrected by helium expansion.

 ${\it Table 3-2 \ Equilibrium \ adsorption \ models \ investigated for \ quality \ of fit \ in \ this \ thesis.}$ 

Model	Equation			
Langmuir	$\theta = \frac{q}{q_m} = \frac{k_L P}{1 + k_L P}$ $q = k_F P^{\frac{1}{n_F}}$			
Freundlich				
Sips	$\theta = \frac{q}{q_m} = \frac{(k_S P)^{n_S}}{1 + (k_S P)^{n_S}}$			

Toth	$\theta = \frac{q}{q_m} = \frac{k_T P}{\left[1 + (k_T P)^{n_T}\right]^{\frac{1}{n_T}}}$
Multiple Site Langmuir	$q = \sum_{i=1}^{n} \frac{q_{m(i)} k_{L(i)} P}{1 + k_{L(i)} P}$

## 3.10. Adsorbent Selectivity

Pure component adsorption comprises a significant portion of both academic and industrial research in the field of adsorptive separations. It is however, extremely uncommon for feed gases to be of pure components. In the case of post-combustion  $CO_2$  capture the feed gas is composed in the simplest sense of  $N_2$ ,  $O_2$ ,  $CO_2$  and  $H_2O$ . The adsorption of  $CO_2$  then requires the adsorbent to be selective towards this adsorptive. Assessment of adsorbate selectivity, commonly  $CO_2/N_2$  due to  $N_2$  being the bulk of the feed gas, is inherently challenging in gas mixtures due to experimental requirements [210]. Selectivity can be estimated *via* breakthrough tests using gaseous mixtures although this requires significant capacity to measure each gas concentration and the total flow rate, pressure, temperature and etc. Estimation of the selectivity can be made through analysis of the pure component isotherms. Pure component selectivity in a binary mixture requires evidence of an adsorbent's equilibrium capacity for each gas [211]. It is estimated at a given pressure and temperature based on EQ. 23., where  $n_{CO2}$  and  $n_{N2}$  represent the equilibrium adsorption capacities at the same pressure and temperature.

$$\alpha_{P(CO2/N2)} = n_{CO2}/n_{N2}$$
 EQ. 23

Selectivity can also be estimated using the adsorbent-adsorbate Henry's constants which gives an indication of the selectivity in the initial adsorption stage (typically below 0.15 bar(a)) which is often what dictates the breakthrough performance of a specific system. Equilibrium selectivity is calculated as the ratio of Henry's Law constants according to EQ. 24 [212]. Henry's Law constants can be estimated *via* fitting the experimental uptake data to the virial expansion as per EQ. 25 with  $K_H$  given by EQ. 26. Here  $\alpha_{E(CO2/N2)}$  is the equilibrium selectivity (CO<sub>2</sub>/N<sub>2</sub>),  $A_i$  are the virial coefficients, p is the equilibrium pressure, q is the adsorbed amount at that pressure and  $K_{H,I}$  is Henry's Law constant for species i. [213,214].

$$\alpha_{E(CO2/N2)} = K_{H,CO2}/K_{H,N2}$$
 EQ. 24

$$\ln\left(\frac{p}{q}\right) = A_0 + A_1 q + A_2 q^2$$
EQ. 25

$$K_H = e^{-A_0}$$

Additionally, the separation factor has also been estimated for the FA-derived zeolites at typical post-combustion conditions ( $CO_2/N_2 - 15 \text{ kPa/85 kPa}$ ) through EQ. 27 where y is the molar fraction of gases in the gas phase and x is the molar fraction of gases in the adsorbed phase [215].

$$S_{CO2/N2} = \frac{y_{CO2}/y_{N2}}{x_{CO2}/x_{N2}}$$
 EQ. 27

# 3.11. Enthalpy of Adsorption

The isosteric enthalpy of adsorption has been estimated in this work via the Clausius-Clapeyron approach. The equation for this is provided in EQ. 28 where T is absolute temperature, p is vapour pressure and the molar enthalpy of adsorption is  $\Delta H_{ads}$ . This property indicates the strength of the interaction between adsorbent-adsorbate and typically varies as a function of both temperature and adsorbent loading. The method involves fitting multiple empirical isotherms ( $\Delta 10 - 20$  K) with continuous functions (e.g. Langmuir, Toth or Sips model) whose constants are used to predict data pairs comprising the adsorbent loading and adsorbate partial pressure [216]. The isosteric method is based on the integrated version of EQ. 28 assuming the enthalpy of adsorption is constant over small temperature intervals ( $T_1 - T_2$ ), given by equation EQ. 29 [53,216]. Given that most adsorbents present different adsorption sites and surface energies, their adsorption enthalpies will vary according to the surface coverage. The variation of  $\Delta H_{ads}$  can be seen when plotted against the adsorbent loading indicating the energetic heterogeneity of the adsorbent-adsorbate pair.

$$\frac{dp}{dT} = \frac{p \cdot \Delta H_{ads}}{-RT^2}$$

$$ln\frac{p_2}{p_1} = \frac{\Delta H_{ads}}{R} \left(\frac{1}{T_2} - \frac{1}{T_1}\right)$$
 EQ. 29

# 3.12. Compressive Strength

The primary mechanical property of an adsorbent pellet is its' compressive strength. The common failure mode for extrudates is a brittle fracture [217] along its radius and hence characterisation of a pellets radial crush strength is recommended for mechanical stability investigations [218]. In this work, the radial crush strength has been estimated *via* ASTM D6175 [219] using a Mecmesin MultiTest-dV. Briefly, this procedure loads individual pellet samples of aspect ratio (defined as the ratio of pellets length to diameter) than 1 at a rate of between 4 and 20 N·s<sup>-1</sup> until failure is observed. The peak force and length of the pellet then provides a crush strength in the form N·mm<sup>-1</sup>. All materials were conditioned at 150 °C for 12 h to remove free water before testing.

## 3.13. Design of a Fixed-bed Reactor

Materials prepared for the selective capture of  $CO_2$  require comprehensive testing to identify their suitability for various applications. In the context of PCC the typical flue gas conditions are 40 - 60 °C,  $CO_2$  partial pressures are normally in the region of 4 - 16 mol% with the upper representative of coal fired stations and the lower natural gas, the mid-range is typical for biomass fired stations and other less conventional fuels [33,220]. Whilst the TGA is often used due to the simplicity and speed with which data can be collected, the value of this data is dwarfed by that produced through breakthrough apparatus. These systems are much more representative of the configuration in which adsorbents will be applied.

In the literature, there appears to be a consensus in the design fixed bed reactors among researchers in this field, column geometry is often constrained to internal diameter of between 0.01 m and 0.02 m, and a height of between 0.13 and 0.18 m [221–223] (column height and not bed length) fabricated from stainless steel. Typical column specifications and process conditions used for the evaluation of ash derived adsorbents are given in Table 3-3.

Table 3-3: Existing fixed-bed reactors used for the evaluation of ash-based sorbents.

Colu	umn	Gas		Adsorption		Desorption			
H (m)	ID (m)	CO2/H2O/N2 (mol%)	(L/min)	Superficial (m/s)	T (°C)	P (barg)	T (°C)	P (barg)	Source
-	0.05	5/5/90	1.0	0.0085	60	0	120	0	[224]
0.1	0.02	5-20/0/95-80	0.2-1.2	0.0106-0.0637	50-90	0	90-150	0	[225]
0.16	0.02	5-20/0/95-80	0.4-1.2	0.0212-0.0637	40-80	0	105	0	[222]
0.13	0.02	15/15/60	1.0	0.0531	30-60	0	-	-	[221]
-	0.02	14/0/86	1.0	0.0531	650	0	900	0	[226]
0.16	0.02	10/8-16/82-74	0.16-0.83	0.0085-0.0440	60-100	0	120-200	0	[227]
0.18	0.01	0.08/10/89.92	0.3-1.0	0.0637-0.2122	-20-40	0	-	-	[223]

## 3.13.1. Design Intent

The design intent of any process is key in order to be able to adequately and satisfactorily assess and mitigate any of the associated hazards to ultimately improve the inherent safety of the process. The fixed-bed reactor is designed to capture 30-90% of the  $CO_2$  from a synthetic flue gas. The composition of the simulated flue gas will be 4-20 mol%  $CO_2$  in a nitrogen balance; the gas will pass through the reactor at a total flow rate of 1-10 L·min<sup>-1</sup>. Prior to any experiment the equipment will be calibrated. During adsorption the operating conditions within the reactor will be a pressure of 1.3 bara and a temperature of  $40^{\circ}$ C maintained by a pressure control valve (PCV-1) and two electric heaters (E-1 and E-2) which will be regulated by a temperature controller. The adsorption regime will continue until the concentration of  $CO_2$  in S-7 is identical to S-6 and the column is saturated. Upon the saturation condition being met, the bed will be regenerated by passing a hot purge  $N_2$  stream through the column. Desorption will take place at a maximum of  $180^{\circ}$ C and 1 bara; the temperature of the column will be maintained by the two electric heaters (E-1 and E-2) with temperature controllers. The high temperature  $CO_2$  rich gas will be cooled passively by an air-cooler (E-3) to room temperature prior to passing through the gas analyser. The desorption regime will continue until the concentration of  $CO_2$  in the effluent stream is equal to the ambient level.

# 3.13.2. Final Design

The final design can be seen in Figure 3.2 which exhibits the schematic of the developed process, instrumentation, and control methods. This design was the result of comprehensive risk assessments including HAZID and What-if? analyses.

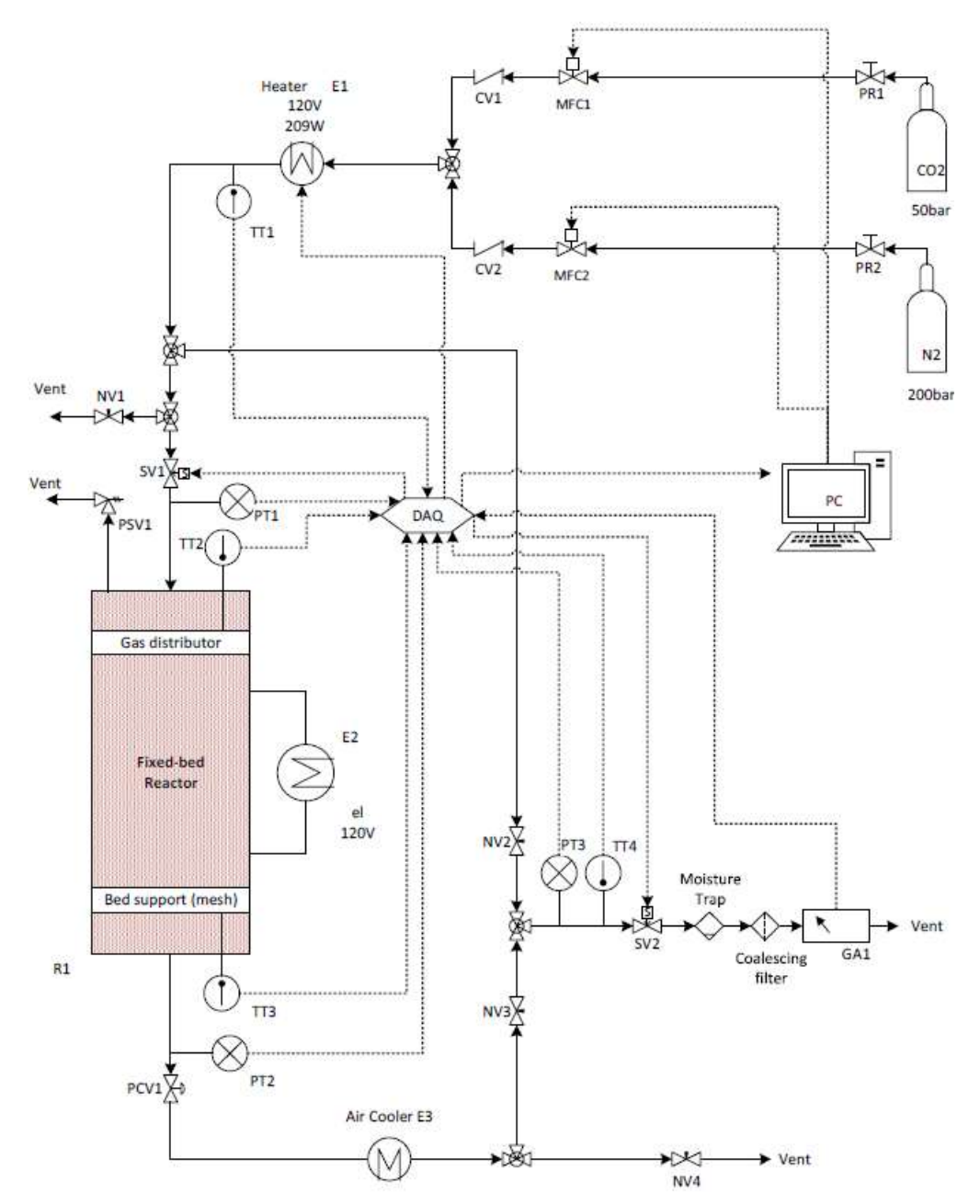


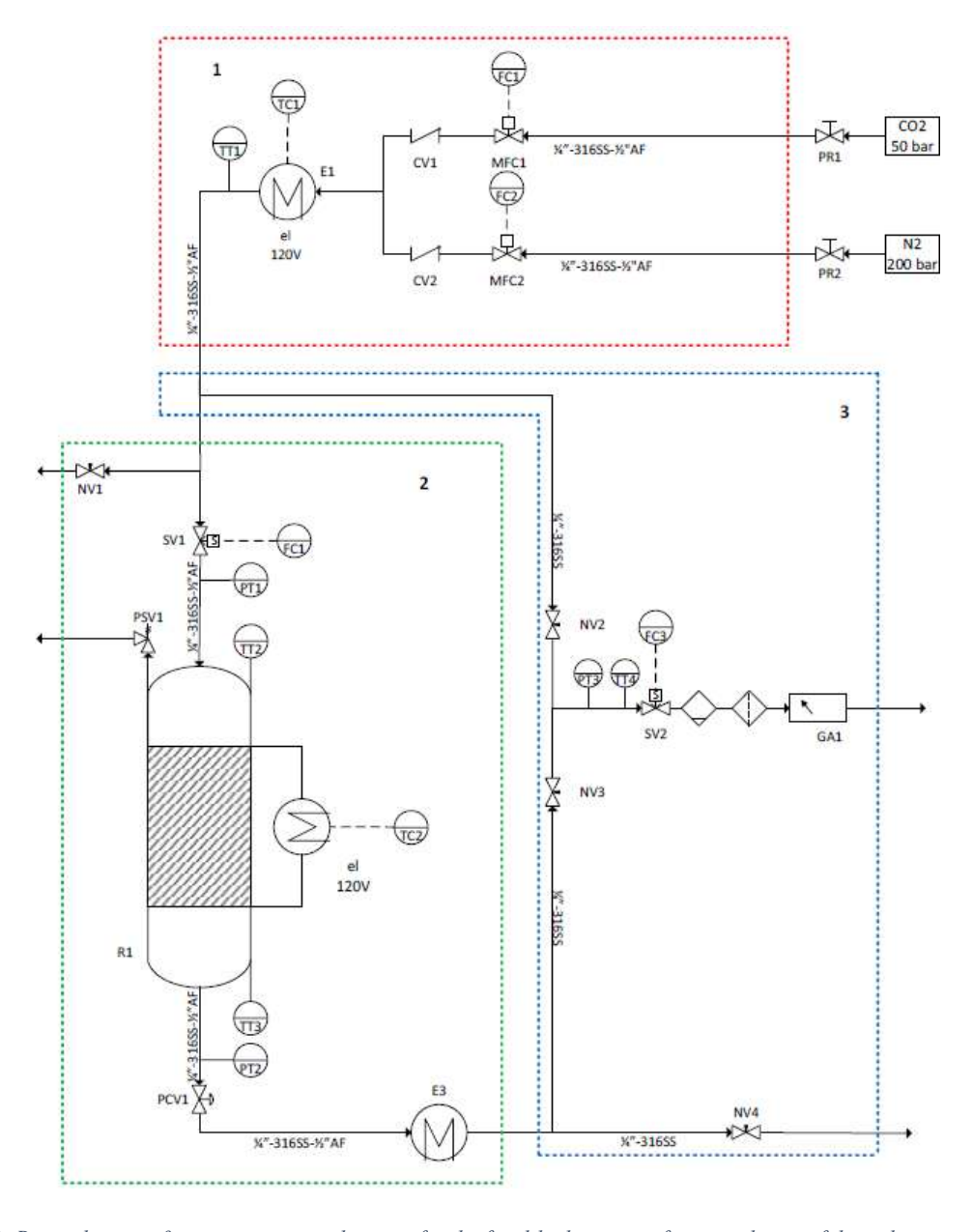
Figure 3.2: Final process design schematic of the fixed-bed reactor designed, built, commissioned and tested in this work.

# 3.13.3. Piping & Instrumentation Diagram

# 3.13.3.1. Node 1 – Synthesising Simulated Flue Gas

The first node comprises the two gas cylinders (CO<sub>2</sub> and N<sub>2</sub>), two mass flow controllers (MFC1 and MFC2), two check valves (CV1 and CV2) and an electric resistance heater with temperature controller (E1). The CO<sub>2</sub> and N<sub>2</sub> feed streams are provided from compressed gas cylinders (BOC) and PR1 and PR2 represent the two stage pressure regulators in the laboratory. All piping is seamless ½" OD 316

stainless steel (Swagelok). The two mass flow controllers have been sized to be capable of supplying the reactor with between 1 and 10 L·min<sup>-1</sup> synthetic flue gas of between 4 and 20 mol% CO<sub>2</sub> carried in an N<sub>2</sub> balance. Given that the pressure in the CO<sub>2</sub> and N<sub>2</sub> cylinders is 50 and 200 bar respectively, there will be a significant drop in temperature as the pressure reduces to the line pressure after the regulators c1.3bara. This effect is known as the Joule-Thomson effect which describes the isenthalpic reduction in gas pressure, resulting in either an increase or decrease in temperature. Estimations of this effect have been carried out and elucidated to CO<sub>2</sub> and N<sub>2</sub> gas temperatures of -63 °C and -16 °C, respectively at the regulator outlets (V-1 and V-2, respectively). By conducting heat balances across the pipe's inlet to the two MFCs, it was clear that the low heat capacities of the gas meant that the gas temperature would normalise extremely quickly and thus no heater is required prior to the MFCs. Gas supply to the reactor at a desired temperature for both adsorption (~40 °C) and desorption (150 °C) requires the addition of



Figure~3.3:~Revised~piping~&~instrumentation~diagram~for~the~fixed-bed~reactor~after~completion~of~the~risk~assessment~process.

heat in S-3 by the heater E1. The heater is of resistance type and features full PID control. The heater has been sized through estimated of the overall heat transfer coefficient  $h_a$ . Different correlation are required for laminar, transition or turbulent flow, the correlation for laminar flow is given EQ. 30 where D = pipe diameter, L = pipe length before mixing occurs in the pipe in m,  $\mu_b = \text{fluid}$  viscosity at bulk average temperature in Pa·s,  $\mu_w = \text{viscosity}$  at the wall temperature,  $c_p = \text{heat}$  capacity in J/kg·K, k = thermal conductivity in W/m·K,  $h_a = \text{average}$  heat-transfer coefficient in W/m², and  $N_{Nu} = \text{dimensionless}$  Nusselt number. All physical properties are evaluated at the bulk fluid temperature except  $\mu_w$ .

$$(N_{Nu})_a = \frac{h_a D}{k} = 1.86 \left(N_{Re} N_{Pr} \frac{D}{L}\right)^{\frac{1}{3}} \left(\frac{\mu_b}{\mu_w}\right)^{0.14}$$

The Reynolds number is given by EQ. 31 and the Prandtl by EQ. 32

$$N_{Re} = \frac{Dv\rho}{u}$$
 EQ. 31

$$N_{Pr} = \frac{c_p \mu}{k}$$
 EQ. 32

The viscosity of the mixture can be calculated at both the bulk and wall temperature. For viscosity calculations Schmik's equation for binary mixtures can be used shown in EQ. 33 although approximate values can also be found using mass fraction averaged calculations. Wilke's equation can also be used although this can lead to significant errors in real gases [228].

$$\mu_{mix} = \frac{\sum \mu_i x_i \sqrt{M_i}}{\sum x_i \sqrt{M_i}}$$
 EQ. 33

The area of pipe required to be at the wall temperature can be found using the equation detailed in EQ. 34 where  $T_w$  = wall temperature in K,  $T_{bi}$  = inlet bulk fluid temperature and  $T_{bo}$  = outlet bulk fluid temperature in K.

$$q = h_a A \Delta T_a = h_a A \frac{(T_w - T_{bi}) + (T_w - T_{bo})}{2}$$
EQ. 34

# 3.13.3.2. Node 2 – Fixed-bed Reactor

The second node comprises the fixed-bed reactor, R1, a needle valve (NV1) to vent to atmosphere during calibration, a solenoid valve (SV1) to contain the system in the event of failure or incorrect flow, a pressure relief valve (PSV1) to ensure the pressure within reactor would be released in the event of excessive fluid pressure increase, a back pressure regulator (PCV1) to regulate pressure in the vessel and a cooling system (E3) to reduce the gas temperature during desorption prior to entering the gas analyser in node 3. The reactor itself features a second electric heater (E2) of the resistance type controlled *via* full PID with feedback from the column wall temperature and/or top/bottom fluid temperature. Given the reactor vessel is classified as a pressure vessel there are requirements for the

material specifications outlined by various organisations, for example the American Society of Mechanical Engineers (ASME) [229,230] or the British Standards Institution [231]. Using these standards and design specifications for the reactor of a maximum 150 °C and 8 bar the minimum wall thickness would be 0.3mm with an internal diameter of 50 mm. The connection fittings for the reactor and process piping are provided by Swagelok. Swagelok specify that a 2" OD pipe must have a minimum thickness to ensure a leak-tight connection. For gas service this thickness is 0.188" or 4.76mm [232] far exceeding that of the minimum requirement. Cooling requirements for E3 were estimated using the equations detailed in the previous section. The pressure drop through the column can be estimated using the Ergun equation for fixed beds and is given in EQ. 35 where  $\Delta P$  = pressure drop,  $L_b$  = length of bed of solids,  $\varepsilon$  = void fraction,  $\mu$  = fluid viscosity, u = superficial velocity,  $d_p$  = particle effective mean diameter and  $\rho_f$  = fluid density. The pressure drop is estimated for a range of effective particle diameters, bed heights, void fractions and feed conditions.

$$\frac{\Delta P}{L_b} = 150 \frac{(1-\varepsilon)^2 \mu \cdot u}{\varepsilon^3 d_p^2} + 1.75 \cdot \frac{(1-\varepsilon)\rho_f u^2}{\varepsilon^3 d_p}$$
 EQ. 35

# 3.13.3.3. Node 3 - Gas Analysis

The third node encompasses the gas analysis section and includes three needle valves (NV2, NV3 and NV4) to meter the gas flow to the analyser (GA1) for the calibration, adsorption and desorption regimes, an N/C solenoid valve (SV2) which would stop flow to the analyser if the gas stream is at an extreme temperature or pressure that exceeds the limits of the analyser, a particulate filter and moisture trap. The gas analyser is a Gascard NG sourced from Edinburgh Sensors with a CO<sub>2</sub> measuring range of 30 mol% CO<sub>2</sub>. The needle valves are required to ensure appropriate flow distribution so that the correct flow rate of gas passes through the analyser (~ 1 L·min<sup>-1</sup>).

#### 3.13.1. Reactor Control

The reactor has been designed to run with near complete autonomy, requiring only the selection of set temperatures and pressures and their tolerable range during operation. This has been achieved by developing a control architecture for each of the operating schemes in LabVIEW. The control architecture employs a state-machine with both error control/handling and emergency shutdown procedures. All of the control systems including the two heating PID control loops, MFC control loops and gas conditioning and analysis systems are software based whilst the emergency shutdown procedures are both hardware and software-based. The state diagram is provided in Figure 3.4

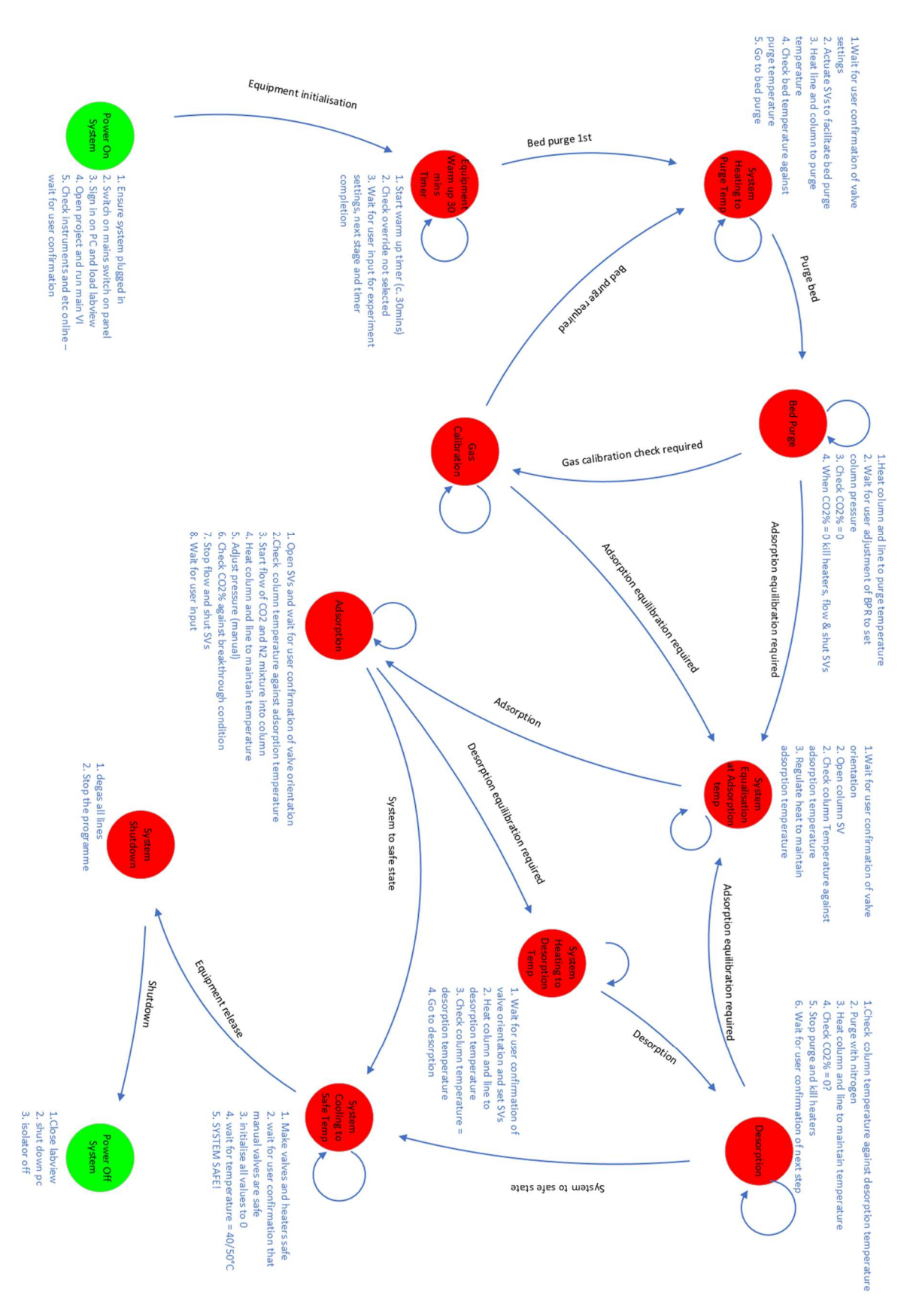


Figure 3.4: State machine schematic for the developed fixed-bed reactor control system.

# 4. Characterisation of Biomass Combustion Fly Ash

#### 4.1. Introduction

Utilisation of BFA requires knowledge of composition and physicochemical properties, without which selection of an application will likely be misplaced. Vassilev *et al.* state that the two fundamental aspects connected with the use of biomass ashes are: 1) to extend and improve the basic knowledge on composition and properties; and 2) to apply this knowledge for the most innovative and sustainable utilisation and/or environmentally safe disposal [233]. Initial characterisation of BFA is critical for determining an end use. To that end, this chapter presents the comprehensive characterisation of BFA sourced from Drax Power Station, Selby.

The biomass fuel used at Drax power plant is typically wood and woody biomass pellets; the ash formed from its combustion tends to have some of the lowest ash yields when compared to other variants such as animal or agricultural biomass [39] with ash yield increasing as you move vertically away from the stems/stumps toward foliage. Wood grown in hotter climates tend to produce more ash although this is also dependent on the age and type (hardwood has higher ash content than soft) [234–236]. Even with a basic understanding of the origin of the biomass and its growing conditions, the thermochemical conversion processes and any downstream gas processing can significantly alter the final ash properties.

Drax Power Station comprises four individual biomass boilers which were originally intended for the combustion of pulverised coal. A number of factors can influence the fly ash properties and introduce heterogeneity, including combustion efficiency and plant load. Ash heterogeneity is problematic for any secondary applications. Characterisation of fly ash provided by Drax Power Station provides insight to their associated properties, informing the pathway to ash valorisation and application in CO<sub>2</sub> capture. In this context, four separate fly ash samples collected at different times from Drax have been characterised in terms of surface morphology and elemental composition, phase composition, proximate analyses, particle size and adsorption of N<sub>2</sub> (77 K) and CO<sub>2</sub> (273 K). Evaluation of the ashes is made in the context of their direct application in post-combustion CO<sub>2</sub> capture and alternately, their use as a precursor for zeolitic adsorbents.

# 4.2. Surface Morphology Analyses

The surface morphology of the raw BFA from Drax was evaluated using SEM which can be seen in Figure 4.1 to Figure 4.3. Given the nature of biomass FA *i.e.* non-conductive, the samples were gold coated prior to analysis which involved fixing the sample on conductive carbon tape to the sample stub followed by deposition of a thin layer of gold *via* the gold sputtering technique.

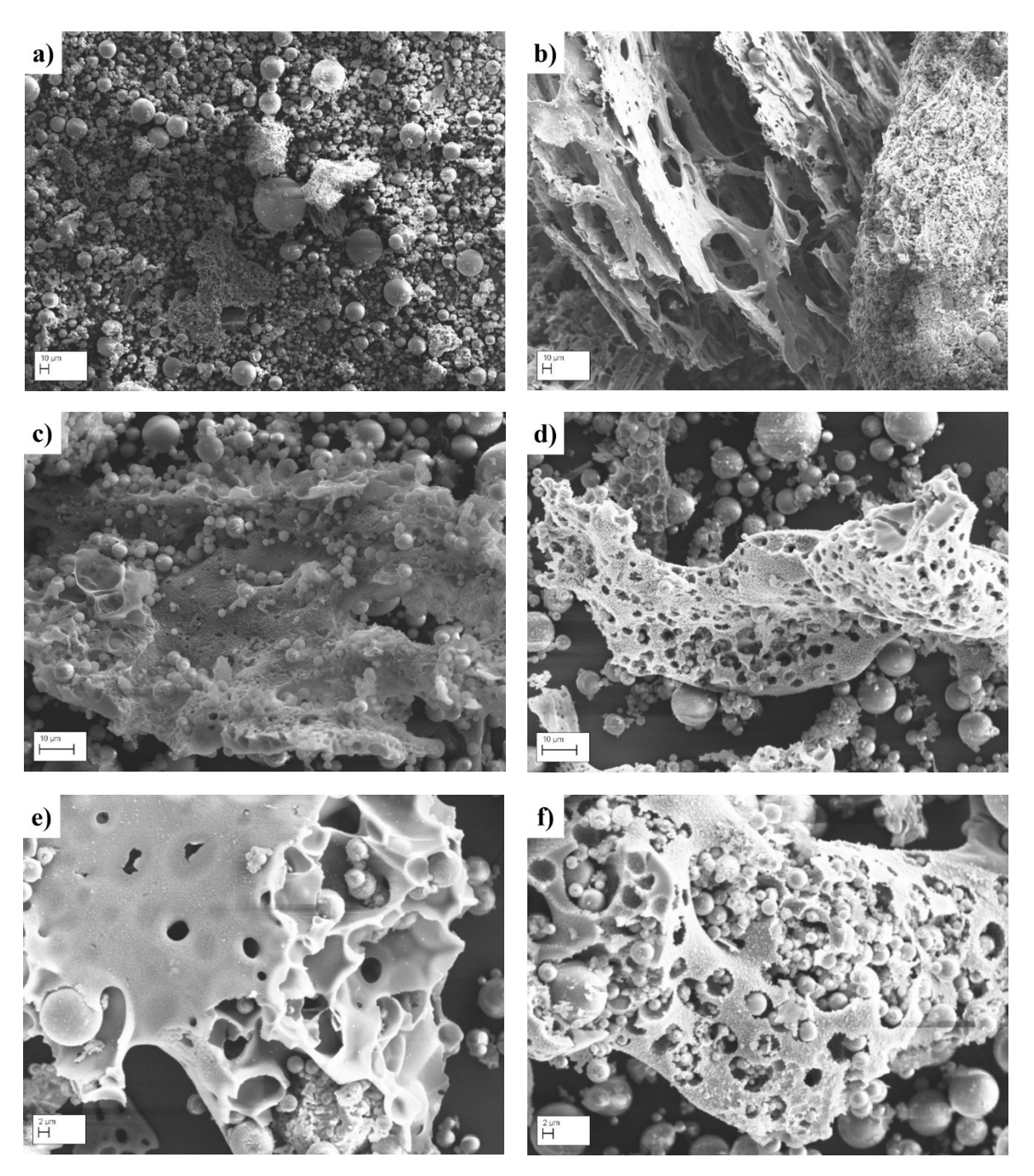


Figure 4.1:BFA SEM: a) 10kV, 500pA and 0.5kX magnification; b) 10kV, 500pA and 0.5kX magnification; c) 20kV, 500pA and 2kX magnification; d) 10kV, 500pA and 2kX magnification; e) 10kV 500pA and 1kX magnification; f) 10kV, 500pA and 3kX magnification.

The ash is comprised of multiple morphologies including spherical particles with wide size variation; particle agglomerates and a selection of porous elements, as can be seen in Figure 4.1.a). The spherical particles are typical of fly ash and can be attributed to their amorphous/glassy outer layer formed as a result of relatively abrupt cooling directly after combustion [237]; these particles will often have a varying wall thickness as a result of this. Fly ash particles can also present as hollow particles, consisting of aluminosilicate shells having inclusions of crystalline phases such as quartz or mullite [238,239], examples of these albeit non-spherical can be seen in Figure 4.2 and Figure 4.3. The broad range of morphologies can be seen clearly in Figure 4.1.b) along with evidence of porosity. The porous particles can be seen more clearly in Figure 4.1.c) through f), although these pores are within the macroporous region and of limited value in the context of CO<sub>2</sub> adsorption.

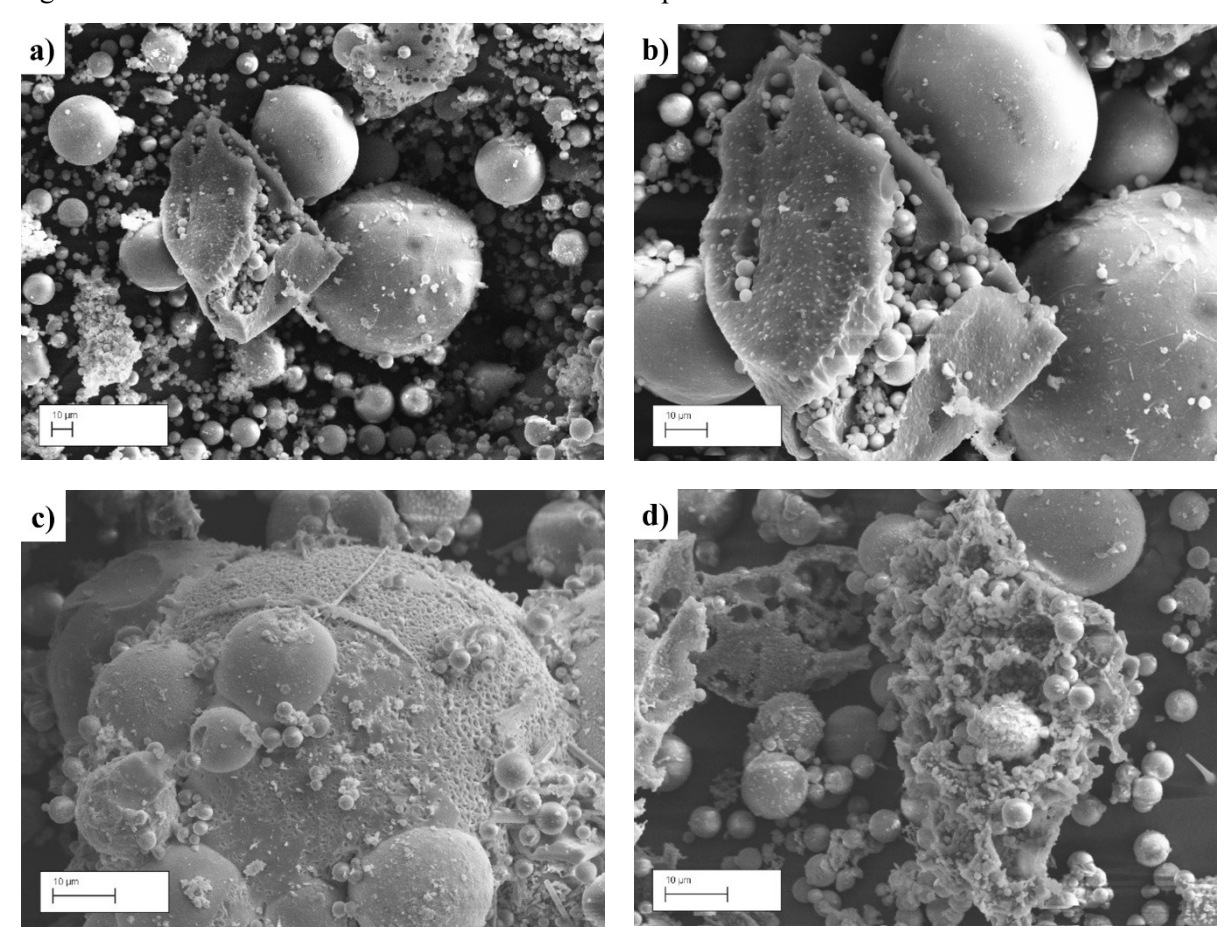


Figure 4.2: BFA SEM: a) 20kV, 300pA and 1kX magnification; b) 20kV, 300pA and 2kX magnification; c) 10kV, 50pA and 3kX magnification; d) 10kV, 100pA and 3kX magnification.

Figure 4.2.a) through d) show similar characteristics *i.e.* a wide size distribution of spherical particles, agglomerations of these and a select number of porous elements, the exception being Figure 4.2.c). The EDS analysis of this image elucidated to the presence of a significant amount of O (41wt%), Ca (25wt%) and Si (15wt%) as well as Al, Fe, Mg, and K. This particle will be an aluminosilicate sphere with inclusions of various other elements. Irregularly shaped particles can be seen in Figure 4.2.d) perhaps elucidating to the accumulation of various similar elements. When increasing the magnification shown in Figure 4.3.a) and b), it can be seen that on the surface of the irregular and slightly porous

elements there exists a rough surface or the attachment of non-spherical features. When increasing the magnification further in Figure 4.3.c) and d) the tetrahedral indentations seen in Figure 4.2.c) can be seen more clearly and occur in various sizes. Surface inclusions of crystalline phases can also be seen due to their non-spherical morphology. For example, hematite can present as small crystalline inclusions [240].

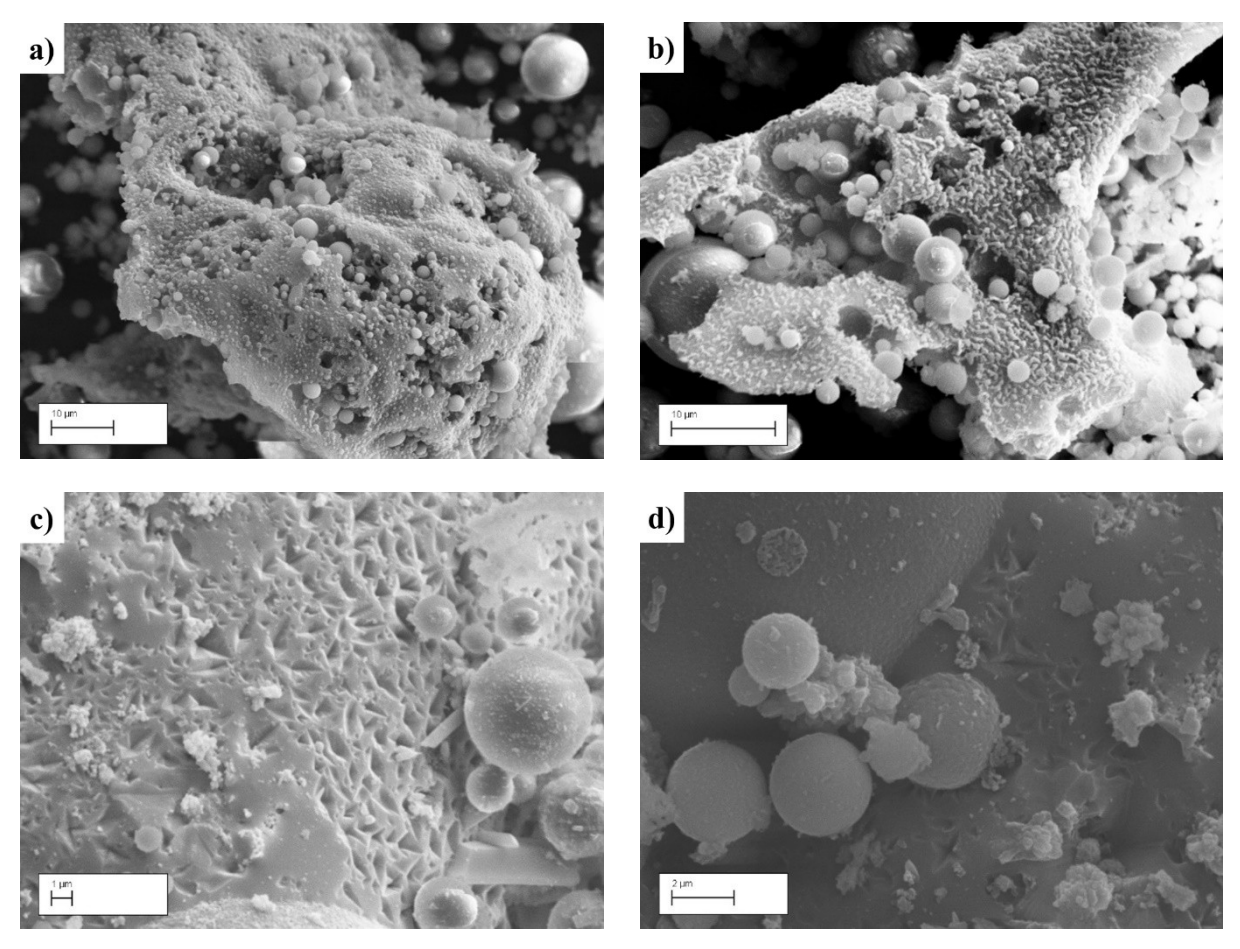


Figure 4.3: BFA SEM: a) 20kV, 300pA and 3kX magnification; b) 20kV, 300pA and 5kX magnification; c) 10kV, 50pA and 10kX magnification; d) 20kV, 50pA and 15kX magnification.

Owing to their intrinsic variability, the ashes produced from biomass combustion will present a more diverse range of morphologies than their coal analogues. For wood and woody biomasses, there is often a prevalence of calcium rich particles that present as irregularly shaped, loosely bound, and sub-micron salt particles [241]. An elevated presence of calcium in a biomass feedstock is known to reduce ash melt/fusion by the increasing the temperature required for such, by between 100 and 200 °C, this however is also dependent on the other components present in the ash [242]. In this case, particles which do not undergo complete melt/fusion processes will exhibit angular rather spherical morphologies and owing to their high melt temperatures, will often be quartz or feldspar phases [243].

#### 4.1. Elemental Analysis

The specific elemental composition of fly ash is primarily a function of the biomass feedstock as the inorganic matter within the biomass comprises the bulk of the ash residue [242]. The combustion

process is often dynamic with fluctuations in gas velocity, pressure and temperature influencing the ash formation mechanisms. This can alter the distribution of elements within the residue and when coupled with variations in the inorganic constituents of biomass, ultimately leads to heterogeneity [244]. This heterogeneity makes accurate measurement of bulk fly ash elemental composition challenging. Fly ashes are also a relatively complex matrix of phases both crystalline and amorphous phases. Commonly employed techniques such as XRF and EDS exploit the characteristic X-rays emitted from individual elements to quantitatively assess elemental composition. As a technique, the accuracy of XRF is heavily dependent on the availability of referenceable standards; the heterogeneity of biomass fly ashes and the complexity of them as a matrix of different phases, limit the applicability of this technique as accurate standards are unavailable [245]. Although EDS is considered a surface level analysis only, it can be successfully used to semi-quantitatively characterise the elemental composition.

*Table 4-1: Surface elemental composition of the four fly ash batches evaluated via* EDS.

	FA	1	FA	.2	FA	.3	FA	4	Relative Standard Deviation
	wt	%	wt	%	wt	%	wt	%	
Element	<del>-</del>	S	<del>x</del>	S	<del>x</del>	S	<del>x</del>	S	$\frac{S}{\overline{x}} \times 100$
Na	0.7	0.6	1.5	0.4	1.9	0.2	1.3	0.6	36.7 %
Mg	2.4	1.5	2.1	0.4	2.2	0.1	2.2	0.3	7.4 %
Al	10.7	0.8	7.9	3.0	9.9	0.9	9.6	0.5	12.4 %
Si	17.8	2.7	17.5	3.7	16.8	1.4	17.6	0.7	2.6 %
P	0.5	0.4	0.9	0.5	0.7	0.5	0.8	0.3	27.4 %
S	1.2	1.1	2.1	0.6	1.5	0.4	1.4	0.2	25.1 %
K	10.5	1.7	9.7	1.8	10.2	1.0	9.6	0.5	4.3 %
Ca	10.0	2.4	11.7	1.9	10.1	1.5	10.2	0.9	7.8 %
Fe	4.1	0.4	5.0	2.4	5.2	0.5	5.0	0.4	9.9 %
0	42.1	1.1	41.7	1.0	41.5	0.6	42.4	0.7	1.0 %

The elemental composition of the four fly ash batches, measured via EDS by averaging 10 areas of the sample, is provided in Table 4-1 where  $\bar{x}$  and S are the mean value and standard deviation, respectively. The relative standard deviation (RSD) has been calculated by dividing the mean by the standard deviation and is provided as a percentage. The analysis has revealed the fly ash to be primarily comprised of Si, Al, Ca and K with significant quantities of Fe. Sodium, Mg, P and S have also been identified but in smaller concentrations and associated with a larger degree of variability. The largest variation is observed with Na; however, this, to some extent, can be attributed to limitations with the EDS technique as it fails to accurately quantify elements with low atomic numbers such as those including and below Na. This is due to the absence of core electrons for the generation of any X ray (e.g. hydrogen), or, as a result of too low-intensity of the emitted X ray for reliable detection and

measurement (e.g. lithium). Phosphorus and Sulphur are commonly observed in biomass ash residues due to their presence in soils and fertilisers [246]. These elements when present in the ash are mostly secondary (i.e formed during combustion) and as such heavily influenced by the combustion conditions resulting in a large standard deviation [233]. Less variation is observed in elements at greater concentration such as Si and Ca. Aluminium is an exception to this and whilst comprising approximately 10 wt% of the FA, the samples present a 12.4 % relative standard deviation. This is due to the low concentration measured in FA2; this fly ash also presents a slightly higher Ca content than the other batches. The oxygen content for all samples is calculated assuming oxide stoichiometry. The silicon to aluminium weight ratio based on the EDS analysis is 1.67, 2.22, 1.70 and 1.83 for FA1, FA2, FA3 and FA4, respectively. Faujasite and LTA zeolites are commonly synthesised with Si/Al ratios of 1.5 and 1, respectively [247] which suggests these FAs may not be entirely suitable for their synthesis without provision of aluminium. Synthesis of these phases however, has been reported for fly ash precursors with wide ranging Si/Al ratios including beyond those typical for synthetic zeolites A and X [120,146,147,149,160,165,187,248–250]. During the combustion process, sulphur, phosphorous and to a lesser extent, sodium, magnesium, potassium and calcium can vaporise after which they will recondense and form aerosols as the temperature decreases downstream of the combustion reaction [241]. Normal biomass boiler furnace temperatures are typically between 800 - 900 °C with exit gas temperatures often higher than this [251]. This can promote slag formation and fouling on heat transfer surfaces due to condensation of gaseous sulphates and chlorides. The presence of potassium in the biomass fuel is the primary concern as these species promote lower temperature melting of siliceous species further promoting slag formation and fouling; the incorporation of additional alkali and alkaline earth metals usually lowers the melting point further. In the context of zeolitisation, sodium is the common cation selection and facilitates the formation of common CBUs such as sodalite cages and D4Rs; calcium and potassium however, can exhibit structure breaking effects [131]. High concentration of calcium is very common to biomass ashes and it has been reported that its inclusion within zeolitic phases can also promote CO<sub>2</sub> adsorption by enhancing the acid-base interactions [140]. Iron is also common in biomass fly ashes and although less reported in terms of CO2 adsorption on zeolites, as a charge compensating cation, it enhances the catalytic performance of FA-derived zeolites [132]. That said, oxides of both iron and calcium can hinder the nucleation rate during fly ash-zeolitisation [116]. The bond length of Fe-O (1.9 Å) is greater than that of Ca-O's, which increases strain in the lattice, whereas calcium often preferentially reacts with silicates to form hydrated calcium silicates rather than crystalline zeolite phases [129,130].

# 4.2. Proximate Analysis

Proximate analysis is used to estimate the relative percentage of moisture, VOC, fixed carbon and ash within a specific material. Although typical for organic or carbonaceous substances owing to their composition, as a tool it is still useful for bulk characterisation of fly ashes. In this case, it can facilitate

a first estimation of the variation that exists within the fly ash between sample batches. In this work, the analysis has been conducted aligned with ASTM D3172 which is the standard for proximate analyses of coal and coke. Of the four fly ash batches based on the RSD for each component, a degree of variation does exist. This can arise from both the mechanism of production (i.e. differences in the combustion, transportation or storage of the ash) and the heterogeneity in the biomass feedstock. The tabulated results are provided in Table 4-2. Moisture content between the four batches does vary between FA1, FA2 and FA3, FA4; however, this can be attributed to FA1 and FA2 being collected from the production site earlier than FA3 and FA4, whilst the analysis was conducted at the same time. Additionally, fly ashes are generally hygroscopic so the weight percent of moisture is expected to increase during storage. Denoting the fly ash weight loss during heating to 950 °C under N<sub>2</sub> as volatile organic compounds (VOCs) is potentially misleading as this will possess contributions from both VOCs (from incomplete combustion) and the decomposition of inorganic phases [252]. Given the composition of the FA, the mass loss during this step is more easily attributed to the decomposition of various alkaliand alkaline earth metal-based compounds, including carbonates [253]. The presence of fixed carbon in all samples is relatively consistent for all batches and is expected, given their grey colour. This carbon is a result of incomplete combustion of biomass in the boiler [254]. Ash content sits at around 90 wt% for all samples bar FA2; this batch exhibits the highest content of volatile compounds and the lowest ash content. This could be a result of an increased calcium content which exists in its carbonate form in the fly ash which is subsequently calcined, increasing the weight loss during volatile determination and hence reducing the final ash weight.

Table 4-2: Proximate analysis as per ASTM D3172.

Fly Ash	Moisture, wt%	VOC, wt%	Fixed Carbon, wt%	Ash, wt%
FA1	0.57	5.20	3.20	91.03
FA2	0.49	6.09	4.45	88.97
FA3	0.15	3.42	4.45	91.98
FA4	0.14	3.48	4.59	91.79
RSD	67.1 %	28.9 %	15.6 %	1.5 %

# 4.3. Phase Identification

With inorganic elements comprising the majority of the fly ash; the nature of the inorganic phases which contain these elements is of equal importance. The inorganic phases in FA can present as amorphous, semi-crystalline or crystalline constituents [233,246,255], identification of which can inform subsequent valorisation and application methods. Depending on the phases present, the degree of reactivity which could be expected from alkaline hydrothermal procedures is variable, with crystalline phases such as mullite considered inert in the context of fly ash zeolitisation [40]. The four fly ash batches have been characterised by powder X-ray diffraction to identify which crystalline phases are present, these are provided in Figure 4.4; the PDF numbers are provided for all identified phases in

Table 4-3. The diffractograms corroborate the results of the EDS analysis with each of the elements evidenced in the crystalline phases, specifically, quartz, mullite, hematite, portlandite and calcite. All of the fly ash batches present a broad ridge on their diffractograms centred at a  $2\theta$  of approximately  $30^{\circ}$ . This ridge is a result of the lack of long-range order in amorphous phases and potential scattering as a result of this disorder; the position of this peak is related to the average interatomic distances within the material and hence can still elucidate to the material type. In this case, centred at  $30^{\circ}$  the amorphous constituent is likely a complex mixture of glassy aluminosilicate phases [256,257] formed during the abrupt cooling after combustion [246,258,259].

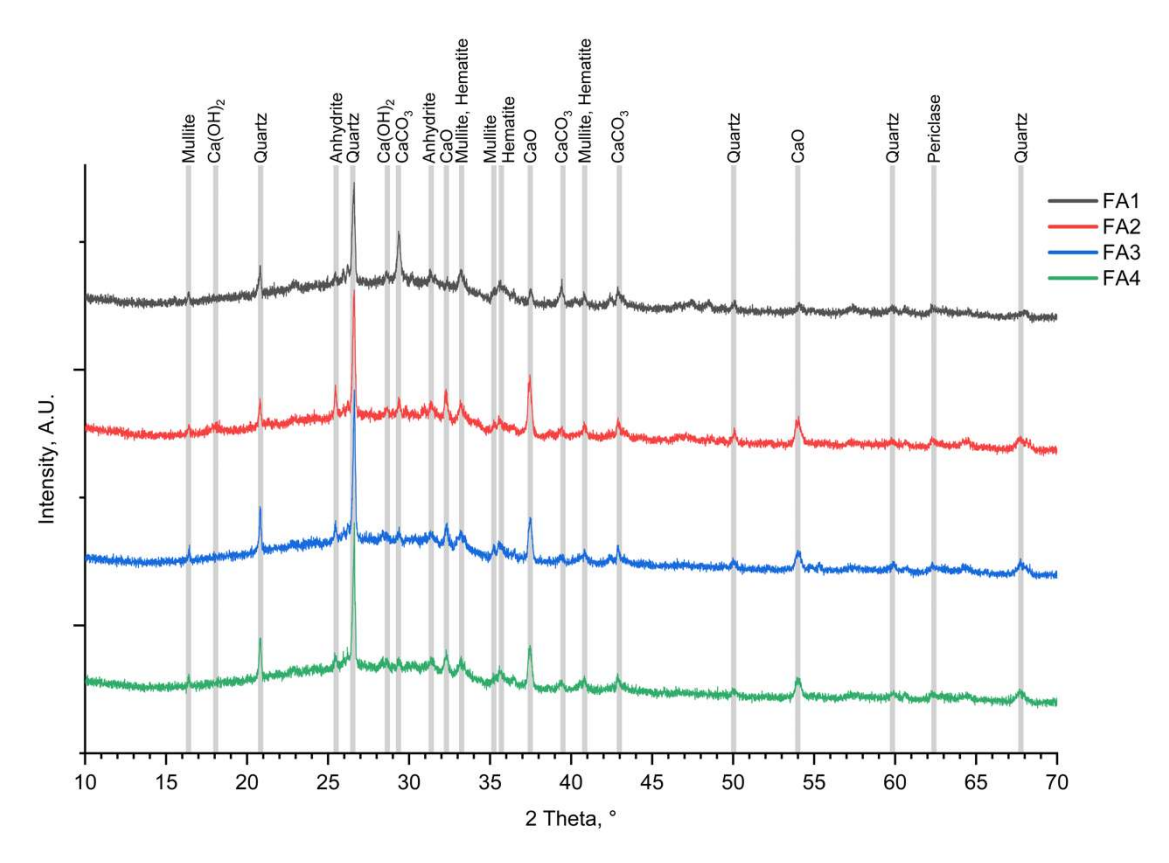


Figure 4.4: Powder X-ray Diffractograms of the four fly ash batches.

Calcium is essential for plant growth and exists in biomass in various forms including calcium oxalate and calcium carbonate [128]; the high temperature thermochemical conversion of biomass can lead to decomposition of these phases forming CaO. In oxide form, calcium has good potential for direct carbonation although this is typically carried out at elevated temperatures (*e.g.* 650 °C); less likely is the application of these oxides for post-combustion capture due to the high temperature requirements for carbonation and regeneration and/or the slow kinetics of the carbonation process when carried out at low temperatures [260]. Portlandite has also been identified in the fly ash batches and is likely a derivative of calcium oxide. The formation of portlandite occurs during the transport and storage of fly ash hence, it's considered a tertiary phase forming *via* hydration of CaO with ambient moisture [42]. Portlandite will react with CO<sub>2</sub> at much lower temperatures than CaO, typically from ambient to below 100 °C after which dehydration occurs [261,262]. That said, formation of CaCO<sub>3</sub> would still require

extremely high regeneration temperatures. Considering the high combustion temperatures and elevated concentration of CO<sub>2</sub> within a boiler, it is to be expected that calcium carbonate exists in the ash residues. Calcium is present in woody biomass at naturally high concentrations and presents as calcite in the ash due to exposure to high temperatures and high CO<sub>2</sub> partial pressures [263].

Magnesium is also present in the diffractogram in periclase (MgO). Periclase can be formed by similar mechanisms to CaO [242]. Although a minor constituent in the fly ashes based on the measured EDS quantity, periclase requires lower temperatures for carbonation reactions ( $100-300\,^{\circ}$ C) and calcination ( $<500\,^{\circ}$ C) [264]. The presence of anhydrite further confirms the presence of sulphur identified in small quantities *via* EDS. Anhydrite is anhydrous calcium sulphate which forms through oxidation of sulphur contained in the biomass and the subsequent reactions with calcium-species [265]. This chemical reaction is used to reduce  $SO_x$  emissions in flue gases and is employed by Drax Power Station. In the FGD process a scrubber introduces the gas to  $CaCO_3$  and/or  $Ca(OH)_2$  sorbents which react with  $SO_2$  in the flue gas to form Ca-S compounds such as gypsum [266]. In the case of Drax however, FGD is downstream of the FA collection, so anhydrite in the ash suggests this is formed in the boiler. Some traces of hematite can be observed in the diffractogram; however, this is assumed to be of limited quantity owing to the relatively low concentration of iron in the fly ash and the low peak intensity (at 20=33.2 and  $35.6\,^{\circ}$ ). Hematite can form *via* decomposition on pyrite and other iron containing compounds such as iron sulphides through thermal decomposition and subsequent oxidation or direct oxidation [267].

Table 4-3: Powder Diffraction Files (PDF) of the phases identified.

Phase	PDF
CaO	01-070-4068
Ca(OH) <sub>2</sub>	01-070-5492
CaCO <sub>3</sub>	01-071-3699
Hematite	01-073-8431
Mullite	01-074-4145
Periclase	01-076-3013
Anhydrite	01-080-0787
Quartz	01-089-1961

Mullite is a stable aluminosilicate mineral and is often found in fly ash due to the exposure of clay-type minerals (*e.g.* kaolinite) to temperatures of approximately 1000 °C during combustion forming crystalline mullite [268,269]. Properties of mullite include high thermal, mechanical and chemical stability, with the latter reducing efficacy of any alkaline treatments in view of zeolitisation [40]. The presence of mullite however, proves this biomass fly ash as a candidate for such. Conversion of mullite and other stable crystalline phases through high temperature alkali activation/fusion increases the

availability of Si and Al containing species by forming soluble sodium silicates and aluminates [135]. Traditional hydrothermal procedures are often unable convert phases such as mullite, limiting the zeolite yield and leaving unreacted ash particles as product impurities [40]. Based on the EDS analysis, silicon is the primary constituent of the fly ash, with crystalline silica (quartz) observed in each of the fly ash diffractograms. The sharp and angular morphology of quartz has also been observed in the SEM [270]. Although quartz may remain unchanged through combustion it can also form through various conversion mechanisms, one being the conversion of kaolinite to mullite and amorphous quartz at approximately 900 °C [243].

# 4.4. Thermogravimetric Analysis

As a complement to the previous analyses, thermogravimetric analysis (TGA) can further the understanding of the specific phases present by observing the fly ashes behaviour at elevated temperatures. When used in conjunction with derivative thermogravimetry (DTG) these analyses can facilitate determination of specific decomposition reactions and their associated temperatures. Curves (TGA and DTG) are provided for all fly ash batches in Figure 4.5 under three different gases, air, nitrogen and carbon dioxide.

Evaluation of the fly ashes under air provides insight into the potential for any combustion or oxidation reactions. Given that volatile compounds and carbon have been identified in all of the four fly ash batches (Table 4-2), mass loss in the region of 400 – 600 °C is expected. Under air, the largest mass loss for all fly ashes occurs at approximately 460 °C. This is typical of residual carbon oxidation forming CO<sub>2</sub> [271], with FA1 presenting the least mass loss and FA2 the greatest. Based on the proximate analyses, FA1 presents the lowest fixed carbon content and highest VOC, decomposition of the volatiles can be observed in a gradual mass loss prior to the significant drop at 466 °C likely owing to the slower decomposition of volatiles. In the 650 – 700 °C region, the mass loss can be attributed to dehydration of hydroxides and/or decomposition of carbonates; variation in the specific temperature is influenced by differences in the four FAs mineralogical composition and structural or phase differences [255,272,273]. Residual ash content largely agrees with the proximate analyses, with FA2 exhibiting the lowest ash content vs FA1, FA3 and FA4. Under a nitrogen atmosphere, the fly ashes present between 3 (FA1, FA3 and FA4) and 4 (FA2) distinct mass losses. At approximately 400 °C, FA1 and FA2 exhibit a minor mass loss due to dehydration of such as portlandite [274] which may not have been observed under air due to the overlap of oxidation reactions. Mass losses above 600 °C are attributed to decomposition of carbonates such as calcite [272]. Although not a conventional assessment, TGA under CO<sub>2</sub> can further the insight into the composition of the fly ashes as any species with potential for carbonation will be calcined and subsequently exposed to a high temperature CO<sub>2</sub> environment. A mass increase for FA2 can be observed at 470 °C owing to the carbonation reactions of either CaO or Ca(OH)<sub>2</sub> [275]. The relative intensity of CaO in the diffractograms was highest for FA2 than the other batches; however, FA3 and FA4 also possess these peaks. The lack of mass increase for the other ashes may be due to differences in the fly ash matrix; the mass change is relatively small and may therefore, not be observed in the other FAs. The accessibility of CaO and Ca(OH)<sub>2</sub> depends on its distribution in the FA, upon initial carbonation reactions, a surface layer of carbonate can form which limits accessibility to the particle's core limiting subsequent carbonation reactions [276,277]. A small mass loss at 730°C is observed for FA2, FA3 and FA4 which would suggest decomposition of calcite phases; however, this may be the onset of the largest mass loss at approximately 880 °C for all ashes. The decomposition temperature is shifted upward due to the presence of CO<sub>2</sub> in the furnace [278,279]. Mass loss in this region may also be due in part to CO<sub>2</sub>-gasification of any residual carbon [279]. This mass loss appears to be the greatest of all experiments which can be attributed to the calcination of all pre-existing and *insitu* (formed during the ramp up of temperature) carbonate species. No calcium hydroxide is observed as the carbonation reaction will occur at similar temperatures obscuring decomposition; a greater degree of decomposition is observed at higher temperatures due to the subsequent decomposition of the carbonate. Mullite and quartz are typically stable above 1100 °C hence no decomposition has been observed under any of the gases [280].

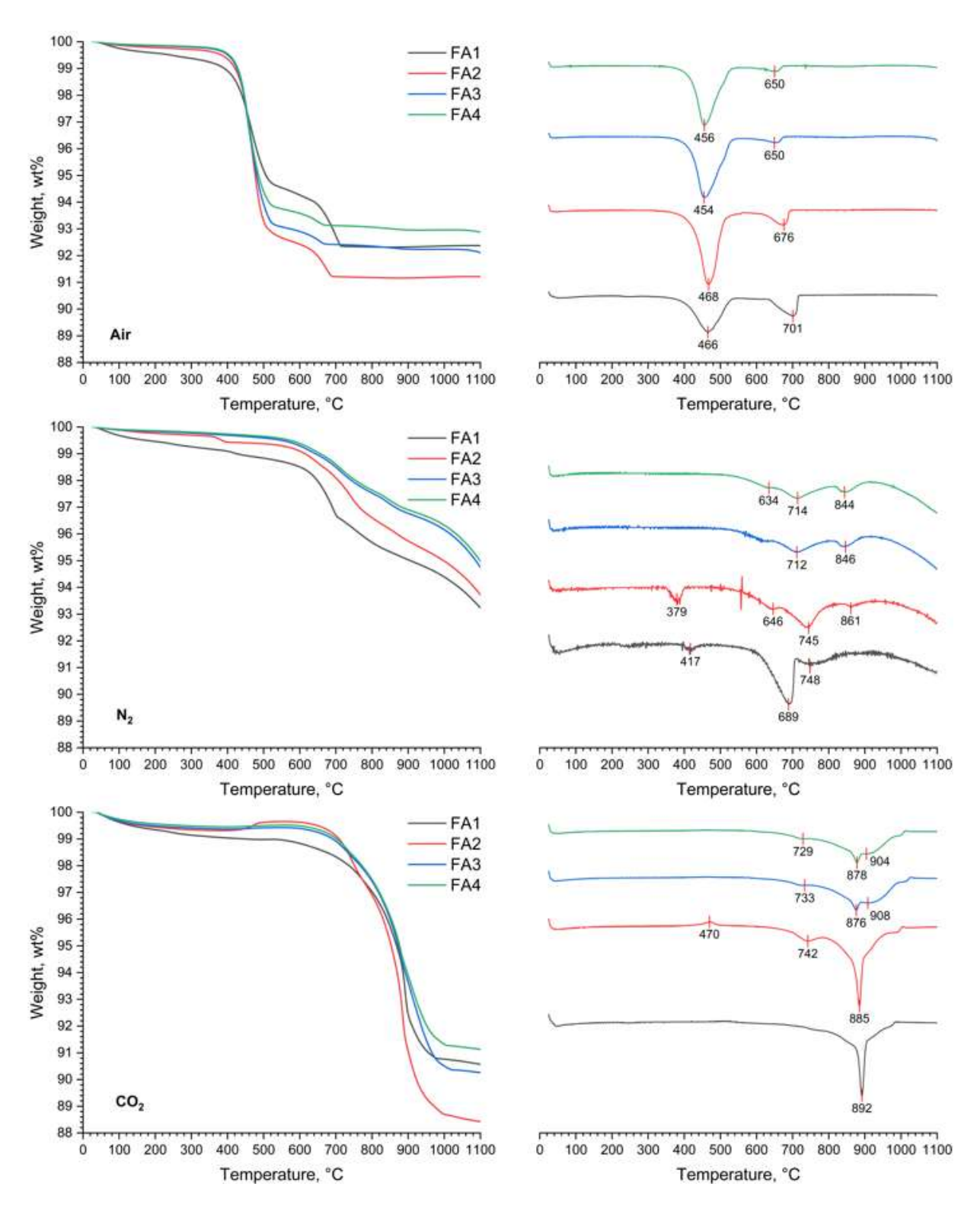


Figure 4.5: Thermogravimetric analysis and derivative thermogravimetric curves of the four fly ash batches. Tests conducted with a ramp rate of 10 °C/min from 25 to 1100 °C. Gas atmospheres air (top), nitrogen (middle) and carbon dioxide (bottom).

## 4.5. Fourier Transform Infrared Spectroscopy

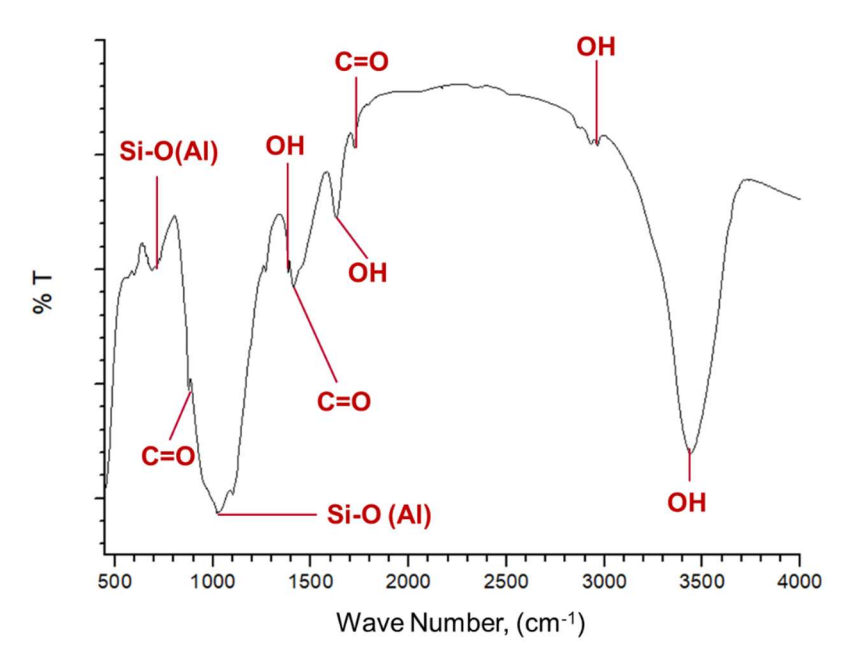


Figure 4.6: FTIR spectrum of biomass combustion fly ash (FA1).

An FTIR spectrum of FA1 is provided in Figure 4.6 which was measured in the region of 500 – 4000 cm<sup>-1</sup>. Although not a technique commonly employed for the analysis of inorganic materials, FTIR can still be used to confirm the presence of bonds in phases identified by other characterisations such as XRD. In the spectra, a band in the 3000-3500 cm<sup>-1</sup> region can be seen which is ascribed to OH functional groups belonging to metal alkoxides in the sample and physisorbed moisture [281,282]. These same functional groups can also be observed at approximately 1630 and 1385 cm<sup>-1</sup> which arise due to the stretching and bending vibrations of the OH bond [197,281]. Carbonyl groups (C=O) have also been identified at bands 876 and 1410 which can be assigned to the bending vibration and asymmetric tensile stretching of the double bond, respectively [283,284]. These groups can exist in the FA as carbonyl functionalities but are more likely a result of metal carbonates [197,284,285]. Confirmation of Si-O bonds is also found at the bands 1020 and 689 cm<sup>-1</sup> which are typical of aluminosilicate structures [197,286,287] due to a shift of the vibration band. Substitution of Si atoms with Al in tetrahedral formations will decrease the binding energy (T-O, where T = Si or Al) which in turn decreases the asymmetric stretching band from 1100 cm<sup>-1</sup> observed in pure Si-O-Si compounds [288].

## 4.6. Particle Size Analysis

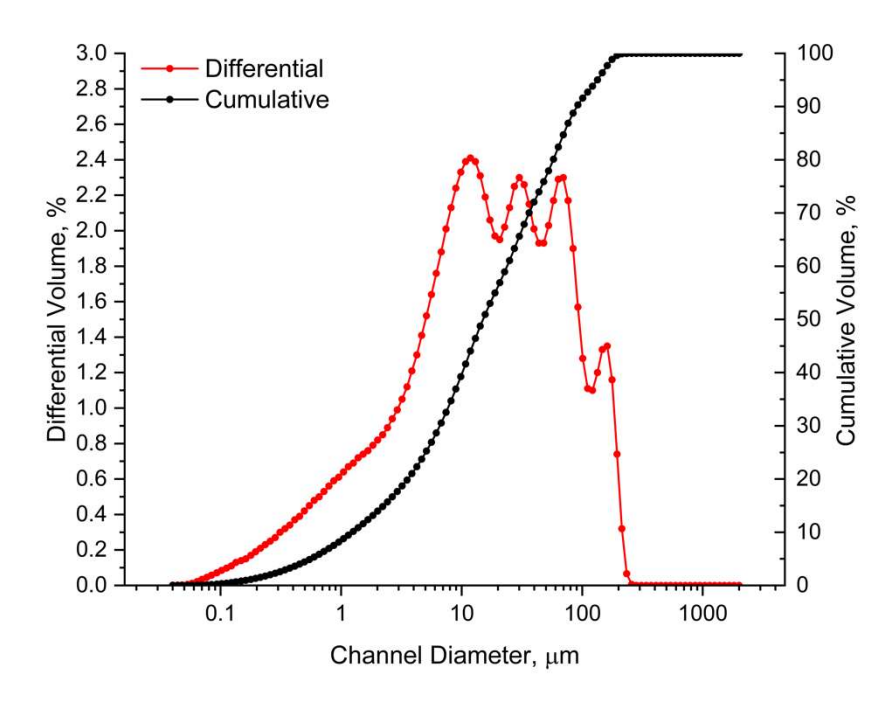


Figure 4.7: Particle size analysis of the as-received fly ash measuring using a Beckman Coulter LS230. Red line representing the differential volume (left y-axis); black line representing the cumulative volume (right y-axis).

Particle size analysis of fly ashes in general is key for their utilisation as structural fill in industries such as construction. In this application, success is reliant upon adequate compaction, which is primarily a function of the particle size but also the sphericity [124]. Although spherical morphology is dominant in these fly ashes as per the SEM, a very broad range of sizes exist as well as many non-spherical particles. The particle size distribution of the BFA is provided in Figure 4.7 in both differential and cumulative volume %. The analysis indicates four distinct regions in the differential volume with local maxima at approximately 12, 30, 70 and 161 µm. These peaks corroborate the broad size distribution or multimodal distribution observed in the SEM due to complex morphology and agglomeration within the fly ash particles. Although deconvolution of the distribution could facilitate determination of the specific aspect ratio, most of the particles within the FA are indeed spherical as observed in from SEM. As such, the FA presents a wide distribution of spherical particles with a median diameter (D<sub>v50</sub>) of 15.7  $\mu$ m, whilst the lower and upper percentile  $D_{v10}$  and  $D_{v90}$  values are 1.3  $\mu$ m and 92.1  $\mu$ m. The volume mean, D [4,3] is calculated to be 157.4 μm. The high value of D [4,3] being greater than D<sub>v90</sub> suggests there is a highly skewed distribution. This can result from the presence of very large particles as seen in the SEM, which influence volume-mean calculations especially for laser diffraction instruments [289]. This influence is less apparent when considering the 90<sup>th</sup> percentile value of 92.1 µm.

# 4.7. Pore Structure and Surface Area

The external surface area ( $S_{BET}$ ) of the BFA has been estimated through analysis of the materials nitrogen adsorption and desorption isotherms measured at 77 K in the relative pressure range of 0 to

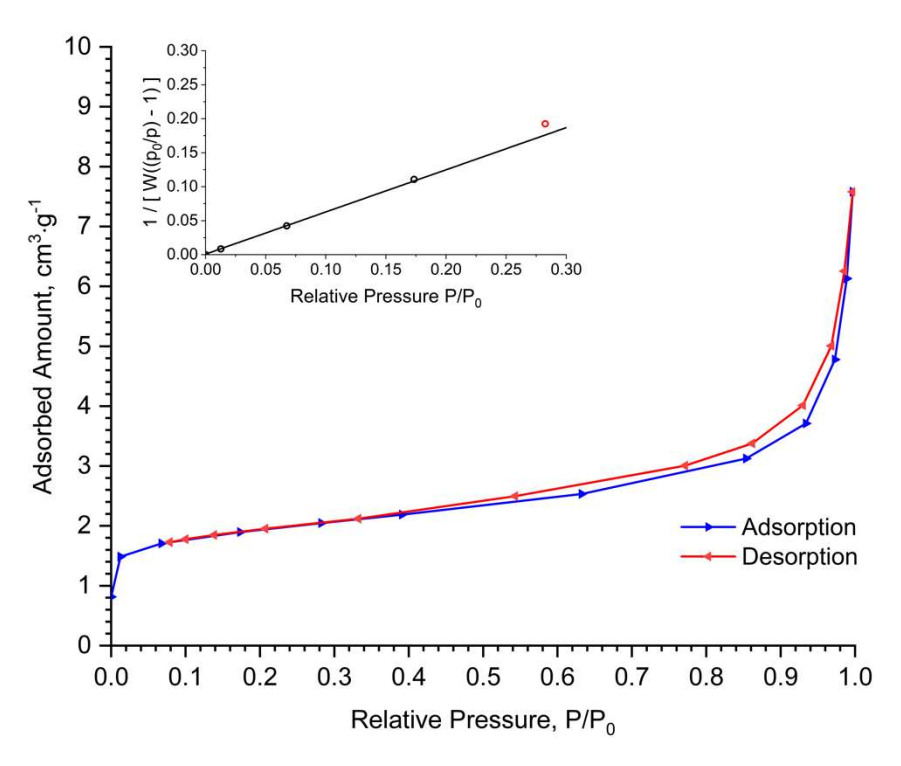


Figure 4.8: Nitrogen adsorption/desorption isotherms measured at 77K; linear BET plot provided as an inset, datapoints coloured red are not included in the model fitting.

0.99. The isotherm appears to be of the type II IUPAC classification which is common for non-porous or macroporous materials, the shape (i.e. a knee at low  $P/P_0$ ) signifies completion of monolayer coverage and the onset of multilayer adsorption [59]. Thickness of the multilayer is generally unbounded at  $P/P_0 = 1$  as can be seen in Figure 4.8. A mild H3 hysteresis is observed on the desorption branch of the isotherm which closes in the P/P<sub>0</sub> range of 0.35 to 0.4 indicative of macroporous networks which failed to fill completely during adsorption [59]. The external surface area was calculated as 7.06 m<sup>2</sup>·g<sup>-1</sup> in the P/P<sub>0</sub> range 0.013 to 0.173 so as to satisfy the criteria proposed by Rouquerol [201]. The linear plot fit which is provided as an inset to Figure 4.8 results in a C value of approximately 750. A value this high can limit the validity of the calculated S<sub>BET</sub> as any value over 150 is considered to suggest either strong localised adsorption or contribution from micropore filling [53]. Total pore volume has been calculated as  $0.006 \text{ cm}^3 \cdot \text{g}^{-1}$  at  $P/P_0 = 0.95$  due to the unbounded adsorption above this. The t-plot micropore area and volume were calculated as 2.93 m<sup>2</sup>·g<sup>-1</sup> and 0.002 cm<sup>3</sup>·g<sup>-1</sup>, respectively, suggesting approximately 40% and 33% contributions to S<sub>BET</sub> and total pore volumes from micropores. Assessment of the fly ashes pore size distribution can provide further detail on the ashes textural properties and corroborate the qualitative assessments above. Pore size has been determined by applying the BJH methodology to the desorption branch of the N<sub>2</sub> isotherm with the distribution provided in Figure 4.9. The most frequent pore width being 1.42 nm, whereas the median pore width was identified at 17.85 nm. The presence of micropores in the BJH distribution supports the assessment of micropore contribution to the total pore volumes. That said, both the S<sub>BET</sub> and micropore volumes are relatively low. Direct application of these ashes in an adsorption-based separation process is unlikely to be cost

effective. These results however, are well aligned with the values reported in the literature for both biomass and coal fly ashes [244].

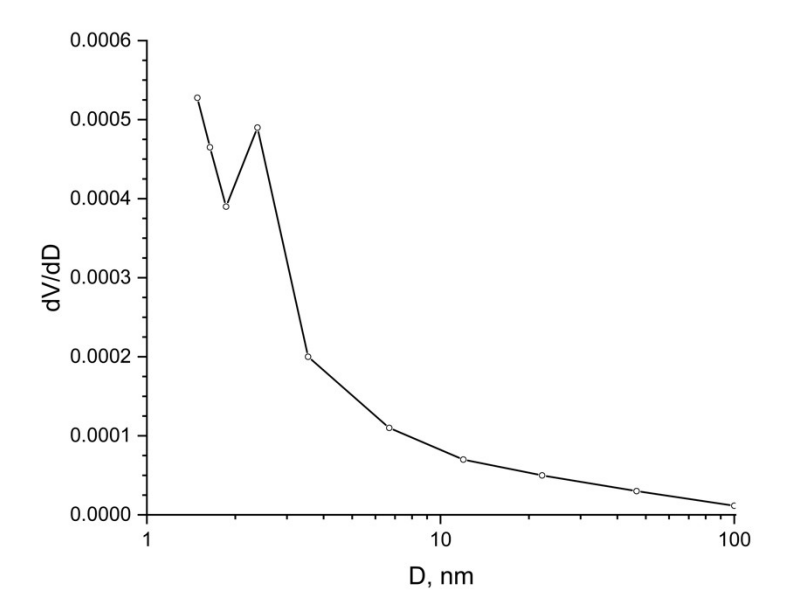


Figure 4.9: Pore size distribution plot of FA1.

# 4.8. Carbon Dioxide Adsorption

Up to now, discussion of the potential application of fly ash for carbon dioxide removal has been exclusive to mineral carbonation. Adsorption of CO<sub>2</sub> on the four fly ash batches has been evaluated by means of static/volumetric adsorption methods. Namely, isotherms measured at 273 K up to 1 bar in order to quantify the as-received fly ashes innate capacity for CO<sub>2</sub>. The isotherms are provided in Figure 4.10. Adsorption capacities for the fly ash at these conditions are in the region of 0.14 to 0.20 mmol·g<sup>-1</sup>, with FA2 presenting the highest, and FA1 the lowest. Variation in capacity between each FA is

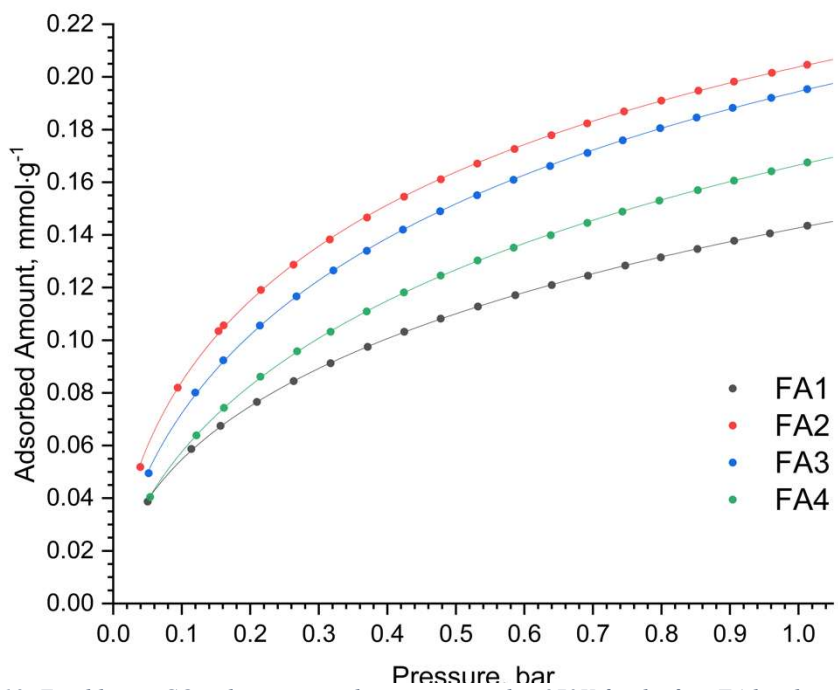


Figure 4.10: Equilibrium CO<sub>2</sub> adsorption isotherms measured at 273K for the four FA batches, with the Sips isotherm model fit.

expected given the previous characterisations. The adsorption fits within the type I IUPAC classification due to its concave nature. Although the capacity is low, fitting of the experimental isotherm to conventional isotherm models provides insight into  $CO_2$  adsorption equilibria. Quality of fit has been estimated *via* the coefficient of determination adjusted for predictors (adj-R<sup>2</sup>) and the root mean squared error (RMSE), results are provided in Table 4-4. Both the Sips and Toth isotherm models have been shown to fit the data well with the Toth model marginally better based on the RMSE. These models each possess three fitting parameters including one to account for heterogeneity. The Sips model often describes heterogenous systems at low pressure that tend towards Langmuir behaviour at higher pressures (*i.e.* monolayer sorption) [74,290]; the Toth model is used broadly across both high and low pressure ranges, to describe adsorption systems which present significant heterogeneity [72]. The model fit parameters are provided in Table 4-4. The Toth model appears to overestimate  $q_m$  for FA1 (1.26 mmol·g<sup>-1</sup>) when compared to the other FAs. Model parameters for the Sips isotherm are more consistent hence their presentation in Figure 4.10. Based on the Sips model fit, all FAs present similar degrees of heterogeneity with FA2 presenting the highest adsorption affinity ( $k_s = 0.013$ ).

Table 4-4: Equilibrium isotherm model fitting via non-linear regression results.

	FA1		FA2		FA3		FA4	
<b>Isotherm Model</b>	Adj-R <sup>2</sup>	RMSE						
Langmuir	0.9787	0.0045	0.9836	0.0056	0.9875	0.0047	0.9887	0.0040
Freundlich	0.9980	0.0014	0.9930	0.0037	0.9943	0.0032	0.9960	0.0024
Sips	0.9999	0.0002	0.9999	0.0004	0.9999	0.0004	0.9999	0.0002
Toth	0.9999	0.0002	0.9999	0.0002	0.9999	0.0003	0.9999	0.0002

	FA1	FA2	FA3	FA4
G.	$q_{\rm m} = 0.415$	$q_{\rm m} = 0.380$	$q_{\rm m} = 0.392$	$q_{\rm m} = 0.380$
Sips	$k_{\rm S} = 0.003$	$k_{\rm S} = 0.013$	$k_{\rm S} = 0.010$	$k_S = 0.007$
	$n_s = 0.538$	$n_s = 0.608$	$n_s = 0.639$	$n_s = 0.641$
	$q_{\rm m} = 1.261$	$q_{\rm m} = 0.550$	$q_{\rm m} = 0.596$	$q_{\rm m} = 0.676$
Toth	$k_T = 0.166$	$k_T = 0.127$	$k_T = 0.07$	$k_T = 0.051$
	$n_T = 0.205$	$n_T = 0.349$	$n_T = 0.360$	$n_T = 0.329$

## 4.9. Conclusions and Potential Routes for Application in CO<sub>2</sub> Separation

Four individual batches of biomass combustion fly ash sourced from Drax Power Station have been comprehensively characterised to provide an understanding of their physicochemical properties. The fly ashes present as predominately inorganic matter with a combination of both amorphous and aluminosilicate phases. These phases contain a large proportion of alkali and alkaline earth metals, specifically calcium, and potassium. Silicon and aluminium content of approximately 17 and 10 wt%, respectively, with calcium and potassium present at approximately 10 wt% each. The content of Si and Al (average Si/Al weight ratio = 1.86) suggests these fly ashes may be candidates for subsequent zeolitisation. The presence of crystalline mullite and quartz, however, would require an additional ash

pretreatment such as alkaline-fusion in order to maximise availability of Si and Al species for crystallisation. Adsorption analysis with both  $N_2$  and  $CO_2$  suggest the fly ashes possess a minor degree of porosity, likely contributed by the minor component of carbon present in each. Adsorption capacities for  $CO_2$  at 273K and 1 bar are between  $0.14-0.20~\text{mmol}\cdot\text{g}^{-1}$  which is significantly lower than commercially available adsorbents. Direct application of these ashes in adsorption-based post-combustion  $CO_2$  removal, therefore, would not be cost-effective. Similarly, direct carbonation of these ashes would be of limited value at post-combustion conditions due to the high temperature requirements for cyclic operation. In terms of exploiting the bulk of the FA, utilisation of these FAs as a precursor for an adsorbent such as zeolites would enable this to a larger degree than the carbonation of certain inorganic species (e.g. Ca or K) or the physical adsorption of  $CO_2$  through modification of the residual carbon (e.g. activation or surface functionalisation).

# 5. Synthesis, Characterisation and Performance Evaluation of Biomass Combustion Fly Ash Derived Zeolites in CO<sub>2</sub> Adsorption

#### 5.1. Introduction

The pathway to development of a sorbent from FA, is dependent on the ash classification. Based on the characterisation of the BFA in the previous chapter, the ash can be considered to sit within the F class of fly ash with a combined silica, alumina and ferric oxide of around 62 wt% although CaO content is near to the C classification at 15 wt%. The molar ratio of silica/alumina of the BFA used in this work has been estimated at approximately 3 which is within the range for low-silica zeolites such as type X [291]. Additionally, in the context of CO<sub>2</sub> adsorption, mesoporous silicas are typically used as aminefunctionalised supports and hence require post-synthesis modification with amines [292,293], this would introduce additional cost and concerns around secondary/residual waste and/or emissions.

Zeolite synthesis can be described in the most rudimentary sense as the dissolution of silicates and aluminates from a precursor, followed by condensation of these monomers to form polymeric silico-aluminate species which then act as nucleation sites for zeolite crystal growth. This can be achieved in myriad ways: the conventional hydrothermal protocol [294]; alkaline fusion assisted hydrothermal [135]; microwave [295]; multistep treatments [170,296]; the sonication approach [297]; and the molten salt method [155]. There are crossovers between these methods as a result of attempts to improve individual procedures by incorporating aspects from others. Evaluation of the different protocols is provided in a previous chapter but if we consider that the issues with traditional hydrothermal zeolite synthesis from FA arise due to the slow rate of dissolution or lack thereof from crystalline aluminosilicate phases [40], it is clear why novel methodologies intend to mitigate this. Whether it be by focussing on local temperatures and pressure through ultrasound induced-cavitation or rapid and homogenous microwave-heating; similar effects can be achieved by fusing the FA with NaOH [144]. As such and in the interest of potential scalability and robustness, the alkaline-fusion hydrothermal protocol has been adopted in this thesis.

This synthesis procedure has been reported consistently in the field of coal fly ash zeolites which seek to utilise the bulk of the fly ash [129,238] and is often studied through variation of: mixture ratios such as FA/NaOH, liquid/solid and silica/alumina [160,250]; aging/homogenisation: stirring speed, duration and temperature [120,163]; and crystallisation conditions: temperature, temperature profile and durations [120,187]. Additives are also often considered with a view to optimise the oxide ratios for synthesis of specific/pure phases [146,298]. This work seeks to optimise the synthesis from the bulk FA as-received to maximise CO<sub>2</sub> adsorption uptake. To support this optimisation, the work initially sought to identify fusion conditions which facilitate synthesis of crystalline products by considering the fusion conditions and applying ranges provided in the literature. Subsequently the synthesis is optimised *via* a Taguchi DoE, investigating the FA/NaOH ratio, liquid/solid ratio, crystallisation temperature and

time. This is followed by examination of the influence of FA batch on the zeolite product. The optimum zeolite produced in this work based on equilibrium CO<sub>2</sub> adsorption capacity measured gravimetrically is then characterised in terms of material properties and adsorption equilibria and kinetics.

#### 5.2. Influence of NaOH/FA Ratio

The initial work acts as a proof-of-concept for the synthesis of zeolitic CO<sub>2</sub>-adsorbents from industrial BFA produced in the UK. This is necessary as there is limited evidence in the literature that industrial biomass combustion residues can be used for the selective separation of CO<sub>2</sub>. The range of synthesis conditions is also broad and identification of the applicable range in this case requires preliminary assessment. Due to the varied phase composition of this FA and the lack of comparable data in the literature, an assessment of the NaOH/FA ratio was made by considering three separate ratios as well as two different fly ash batches (FA1 and FA2). The two FAs were selected as they represent the minimum and maximum Si/Al ratios. The range in which the FA/NaOH was studied was selected as 1.2 - 2.0 based on the values studied in similar works investigating zeolitisation of coal or biomass ashes [147,150,158,165,238]. The procedure employed in these syntheses entails grinding/mixing 10 g FA and 1.2/1.6/2.0 g NaOH in a pestle and mortar. The ground mixture is then fused in a nickel crucible at 550 °C for 1 h in a muffle furnace (10 °C·min<sup>-1</sup> ramp rate). After cooling to ambient temperature, the fused product is removed and pulverised in a pestle and mortar before dispersing the fused product into a fixed 100 ml deionised water in a TFM (modified-PTFE) vessel (250 ml). The mixture is then mechanically stirred (magnetic stirrer) at 300 RPM and room temperature for 16 h. Subsequently, the magnetic stirrer is removed, and the TFM vessel inserted into a stainless-steel jacket for hydrothermal treatment in a conventional oven at 90 °C for 4 h (0.5 °C·min<sup>-1</sup> ramp rate). Finally, the solids are separated via vacuum filtration and washed with DI water until a pH of 9 is measured in the filtrate. Experimental conditions are provided in Table 5-1.

Table 5-1: Experimental conditions employed in the initial alkaline fusion assisted hydrothermal study. Uptake measured at 50 °C, 1 bar(a) measured via TGA.

Comple	NaOH/FA	HT Time	HT Temp	FA1	FA2	NaOH	Yield	Uptake
Sample	w/w	h	°C	g	g	g	%	mmol·g <sup>-1</sup>
ZF1-1.2/4/90	1.2	4	90	10.00	0	12.00	43.1	0.52
ZF2-1.2/4/90	1.2	4	90	0	10.07	12.09	42.2	0.43
ZF1-1.6/4/90	1.6	4	90	10.01	0	16.01	39.1	0.57
ZF2-1.6/4/90	1.6	4	90	0	10.03	16.05	43.5	0.55
ZF1-2.0/4/90	2.0	4	90	10.01	0	20.03	40.1	1.66
ZF2-2.0/4/90	2.0	4	90	0	10.03	20.06	40.9	0.96

Product yield is calculated on the basis of the fly ash amount added prior to fusion and appears to be relatively consistent at approximately 40% across the three NaOH/FA ratios. The lowest yield is observed for ZF1-1.6/4/90 at 39.1 % with the FA2 analogue presenting the highest yield. This variation

is minor but is likely due to the variations identified between FA1 and FA2 in the previous section. Fly ash 1, however, does not provide the lowest yield consistently which may suggest that the fluctuations in yield may be a result of heterogeneity in the bulk ashes. The adsorption capacity for each of the products has been estimated via TGA at 50 °C, 1 bar(a) after degassing under N2 at 150 °C, 1 bar(a) for 1 h. The uptakes for ratios 1.2 and 1.6 are relatively consistent between 0.43 and 0.57 mmol·g<sup>-1</sup>, i.e. 0.3 mmol·g-1 more than the raw FAs. At the higher NaOH/FA ratio of 2.0, capacities are improved significantly. The ZF1-2.0/4/90 sample presented a capacity of 1.66 mmol·g<sup>-1</sup> and the FA2 analogue 0.96 mmol·g<sup>-1</sup>. The increase here can be associated with the production of a crystalline phase with improved porosity that can facilitate the adsorption of CO<sub>2</sub>. The FA1 batch can be seen to facilitate improved CO<sub>2</sub> adsorption at all NaOH/FA ratios than for FA2. The larger amount of Ca and lower amount of Al identified in FA2 may be reducing the efficacy of the synthesis procedure limiting purity/crystallinity of the product. Calcium can influence zeolite synthesis by competing with sodium (Na) during crystallisation. High concentrations of Ca in the reaction mixture is associated with structure breaking properties, as such this leads to suppression of zeolite crystallisation [299]. With the fundamental role Al plays in facilitating zeolite crystallisation, a lower weight percentage suggests that the degree of zeolitisation would be reduced as less is available for conversion.

#### **5.2.1.** Phase Identification of Initial Products

The improved  $CO_2$  adsorption capacity of ZF1-2.0/4/90 suggests that this product may be of greater crystallinity than its counterparts. Confirmation of crystallinity has been achieved through powder-XRD with subsequent identification of crystalline phases. The diffractograms measured in the  $2\theta$  range 5-50° are provided in Figure 5.1 for each product. Of the six samples, ZF1-2.0/4/90 can be clearly seen as distinctly crystalline due to the well-defined peaks characteristic of primarily LTA but also FAU zeolites. Interestingly, most of the pattern is typical of LTA zeolites with the peak centred below  $7^\circ$  corresponding to the (200) lattice plane. Linde Type A and FAU diffraction patterns have a number of overlaps; however, the first peak at around  $6^\circ$  (111) is specific to the FAU unit cell. The presence of this suggests the co-crystallisation of LTA and FAU. The sample produced at the same conditions with FA2 does not feature any indication of FAU. Evidently, the presence of LTA in this sample is reduced due to the decreased peak intensity in the diffractogram. Of the other two ratios, we can see that no clear crystalline phase has been formed, there is however broad ridge centred at around  $30^\circ$  which indicates the presence of amorphous aluminosilicate species in the product. A small peak can be seen at a ratio of 1.6 for both FA1 and FA2 derived samples, although these cannot be confirmed as a specific phase. Potentially, a slightly longer hydrothermal step may have facilitated zeolite crystallisation.

Although unsuccessful in producing crystalline zeolites at each of the ratios, we have confirmed that the fusion successfully converts all crystalline phases present in the precursor FA as none of the patterns identified in the FA XRD persist. By maintaining the hydrothermal conditions and water addition whilst varying the NaOH/FA ratio, the mixture liquid/solid ratio has inevitably varied between samples. This will lead to variations in the solution y which can have significant effects on the product. Study of this and the hydrothermal conditions needs to be conducted simultaneously to better understand the synthesis. Solution pH will have a large impact on Si and Al species solubility and hence the degree of saturation in the solution prior to gel condensation [300]. Variation of the hydrothermal conditions can modify this further hence identification of the optimum configuration is necessary. Before doing so, the products produced during this initial study have been characterised by XRD, SEM and EDS.

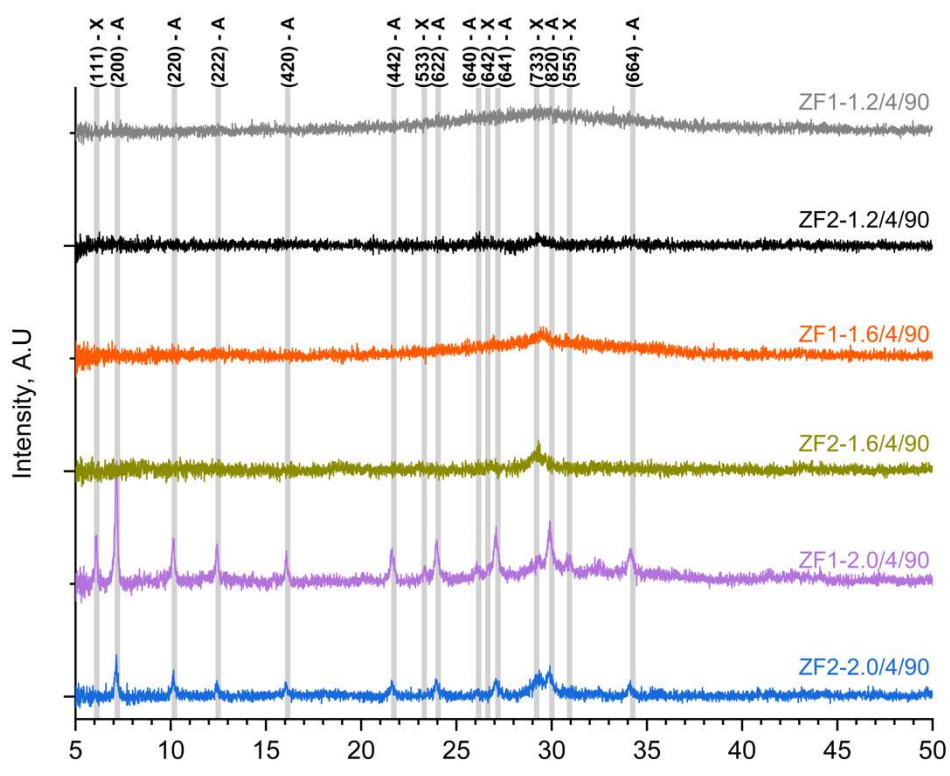


Figure 5.1: Diffractograms of the products produced during the initial NaOH/FA ratio study.

# 5.2.2. Product Morphology – Initial NaOH/FA Ratio Investigation

Crystalline and amorphous phases are often extremely dissimilar morphologically and with the presence of both crystalline and amorphous components, ZF1-2.0/4/90 has been studied *via* SEM to reveal the samples morphology. Given that this sample has the highest capacity, crystallinity should be observable in the SEM. Images are provided in Figure 5.2. In the left image the solid can be seen as a heterogenous solid with distinct sharply faceted morphologies attributed to type A and type X zeolites. Amorphous components are also present evidenced by irregular particles with disorder. The crystalline components have formed from the amorphous gel which still remains after the hydrothermal treatment. The right image exhibits less crystallinity and a larger mass of amorphous components, evidencing a degree of

heterogeneity in the bulk product. The presence of residual amorphicity around crystalline particles suggest an incomplete crystallisation [162]. A longer hydrothermal time may have facilitated an improvement in crystallisation as kinetics are a key component of zeolite crystallisation [301]; however, this can also be due to impurities as non-aluminosilicates species can also influence the product crystallinity and purity [123,161]. The SEM images show no unreacted FA-particles, corroborating the XRD result in which no crystalline FA-phases were detected. The persistence of amorphous material indicates that the fixed synthesis conditions were insufficient for complete crystallisation. As hydrothermal time was not varied here, its' influence cannot be isolated from that of possible impurities; that said, this data suggests complete crystallisation may not be required for high CO<sub>2</sub> uptakes.

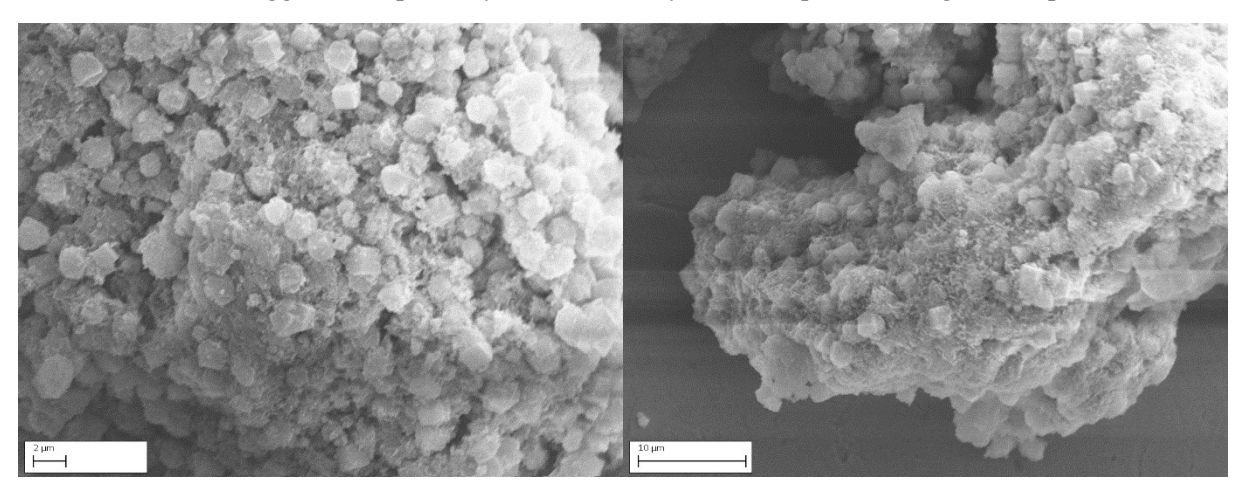


Figure 5.2: SEM images of ZF1-2.0/4/90 produced with an accelerating voltage of 15 kV.

# 5.2.3. Elemental Composition Estimated via EDS – Initial NaOH/FA Ratio Investigation

Having established the coexistence of both LTA and FAU type structures in the XRD and SEM, an analysis of the surface composition further demonstrates the change in composition (from the FA). Cation exchange in zeolite is common and with the presence of a significant quantity of Ca and K in the FA used in this work, there is potential for the zeolite to have either formed or exchanged with cations present in the mixture. The diffractogram can provide indication to the presence of specific cations due to the differences in scattering power for each and levels of site occupation as these influence peak intensities and angle shifts [302,303]. That said, due to the limited crystallinity, refinement of the XRD will be of limited accuracy. The composition, therefore, has been estimated by analysing a minimum of ten areas of a sample stub and the results are provided in Table 5-2. Based on these averages, the adsorbent has an average Si/Al weight ratio of 1.46 which is lower than the fly ash precursor (1.67 for FA1). This implies that Al has been concentrated in the zeolitic product or Si species have been lost in the supernatant. There is a significant quantity of calcium present in the sample although associated with a large RSD. Similarly, Na content demonstrates a large RSD. The low concentration of Na, suggests the type A present in the sample may be of the type 5A, as calcium ions can take place as charge compensators in the LTA [120]. Some of the Ca present (and K) in the bulk

solid can also exist in the amorphous component of the sample, as an unused product of the alkalifusion due to incomplete crystallisation.

Table 5-2: Surface elemental composition of ZF1-2.0/4/90 evaluated via EDS (averaged over 10 different surface areas).

Element	ZF1-2.0/4/90 wt%	Relative Standard Deviation %
Na	4.5	34.5
Mg	2.5	55.7
Al	12.7	16.0
Si	18.5	11.5
K	0.7	43.5
Ca	8.9	44.4
Fe	5.5	51.7
0	46.7	9.7

# 5.3. Taguchi Optimisation

After identifying the NaOH/FA ratio of 2.0 as suitable for producing crystalline zeolites for  $CO_2$  adsorption, optimisation of the hydrothermal conditions is required. A randomized Taguchi (L9) DoE has been employed to study the impact of NaOH/FA ratio (NaOH/FA), hydrothermal time ( $t_{cry}$ ), hydrothermal temperature ( $T_{cry}$ ) and the liquid/solid ratio (L/S) on the product's equilibrium  $CO_2$  adsorption capacity measured via TGA (at 50 °C, 1 bar(a)). The factors and levels for this design are provided in Table 5-3 and have been informed by the previous study (NaOH/FA) and literature values for synthesis of LTA and FAU zeolites from fly ash [71,119,147,238]. The results are provided in

Table 5-4, the adsorption capacities are clearly positioned around 0.6 and 1.7 mmol·g<sup>-1</sup>. This may indicate that the former is amorphous and the latter crystalline; this has been confirmed by powder XRD. Analysis of the signal-to-noise ratios facilitates identification of the factor levels that minimise response variation, *i.e.* improving robustness. With a view to maximise adsorption capacity, the "larger-the-better" SNR equation is employed (see EQ. 36).

Table 5-3: Factor and level configuration of the Taguchi L9 DoE.

Factors		Levels	
NaOH/FA, w/w	1.8	2.0	2.2
Hydrothermal Time, h	2	6	10
<b>Hydrothermal Temperature</b> , °C	50	70	90
Liquid/Solid, w/w	5	6	7

Table 5-4: Experimental conditions employed in the Taguchi L9 DoE. Uptake measured at 50 °C, 1 bar(a) measured via TGA.

Sample	NaOH/FA	HT Time	HT Temp	Liquid/Solid	Yield	Uptake	
Sumpre	1 (4 0 11, 1 11	111 11110	111 10111	=iquia/20114	11010	Сриши	

	w/w	h	°C	w/w	%	mmol·g <sup>-1</sup>
Z-1.8/2/50/5	1.8	2	50	5	70.8	0.65
Z-1.8/6/70/6	1.8	6	70	6	75.3	0.61
Z-1.8/10/90/7	1.8	10	90	7	80.9	1.51
Z-2/2/70/7	2.0	2	70	7	71.4	0.56
Z-2/6/90/5	2.0	6	90	5	71.5	1.67
Z-2/10/50/6	2.0	10	50	6	73.5	0.56
Z-2.2/2/90/6	2.2	2	90	6	71.4	0.59
Z-2.2/6/50/7	2.2	6	50	7	72.3	0.49
Z-2.2/10/70/5	2.2	10	70	5	72.9	1.70
S 10 1	$\frac{1}{2}$					EO 26

$$\frac{S}{N} = -10 \cdot \log \left( \sum \left( \frac{1}{v^2} \right) / n \right)$$
 EQ. 36

The response table for the SNRs is provided in Table 5-5 which provides both the delta and rank of each factor. The *delta values* describe the magnitude of variation existing within a factor across the studied levels; rank provides an indication to the relative importance of each factor on the equilibrium  $CO_2$  uptake within the design space [304]. The results demonstrate a sequence of importance that follows  $L/S > T_{cry} > t_{cry} > NaOH/FA$ . A graphic representation of the factors relative importance is provided in a main effects plot for both the SNRs and data means (Figure 5.3). The magnitude of variation between the SNRs and means suggest the factor to be a significant contributor to the dependent variable [305]. This is observed in the gradient of the main effect plot for each factor. It can be seen that the NaOH/FA ratio has little effect on the SNR or mean. The three remaining factors all exhibit strong main effects on both the SNR and means, in agreement with the SNR response table. Optimisation based on the main effects plots depends on the objective, either to minimise variability (SNR) or to simply maximise the response (mean). In this case and based on the main effects plot for the means, the optimum configuration of factors and levels would be: NaOH/FA ratio of 2.2,  $t_{cry}$  equal to 10 hours,  $T_{cry}$  equal to 90 °C, and L/S equal to 5 [71].

Table 5-5: Response table for the signal to noise ratios.

Level	NaOH/FA	HT Time	HT Temp	Liquid/Solid
Level	w/w	h	°C	w/w
1	-1.485	-4.454	-4.991	1.774
2	-1.873	-2.012	-1.574	-4.638
3	-2.057	1.041	1.15	-2.551
Delta	0.571	5.504	6.142	6.411
Rank	4	3	2	1

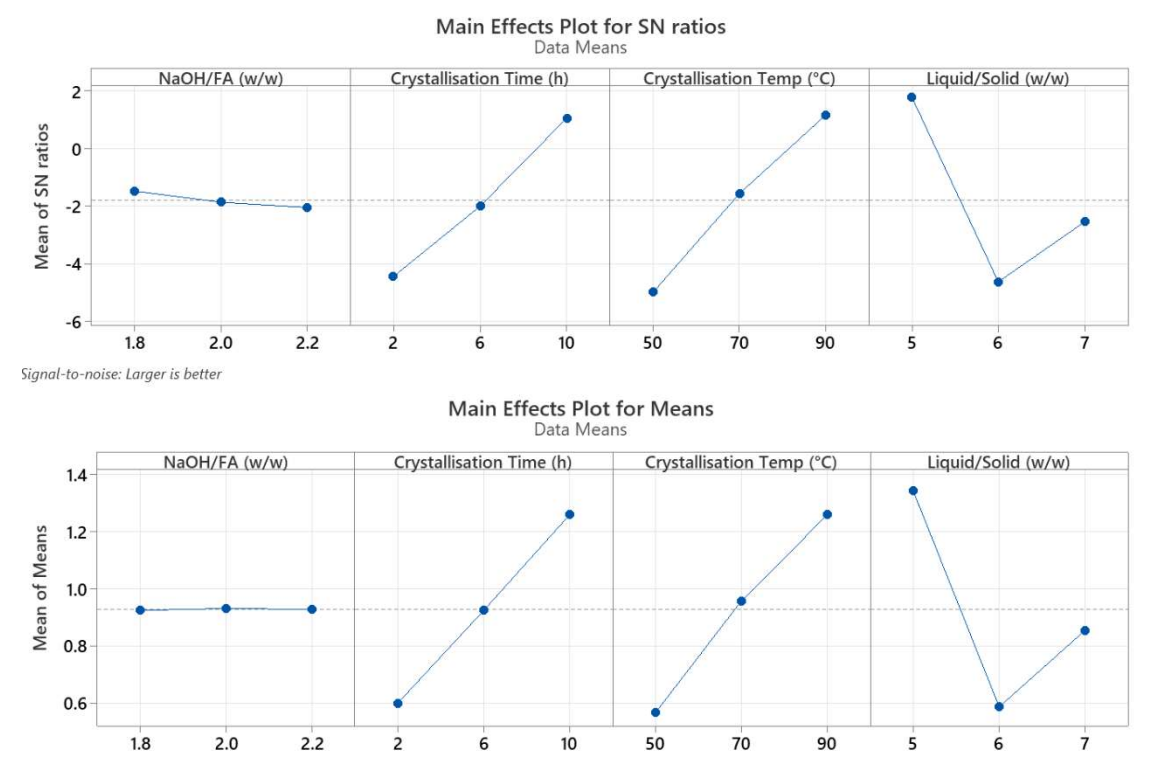


Figure 5.3: Main effects plots for SNRs and data means from the Taguchi L9 DoE.

Upon completing the confirmation experiment, the predicted optimum (ZOPT-2.2/10/90/5) presented an adsorption capacity of 1.84 mmol·g<sup>-1</sup> or 0.14 mmol·g<sup>-1</sup> higher than the highest from the L9 design. A significant limitation can arise when analysis an L9 Taguchi DoE due to the potential for model overfitting. This occurs when there are more fitting terms than there are observations, *i.e.* degrees of freedom [306]. Terms which are not considered significantly influential on the dependent variable, such as the NaOH/FA ratio, can be removed. With this factor removed, ANOVA has been conducted on the design with results provided in Table 5-6. Each of these factors present a p-value far below 0.05 with significantly large F-values. The most statistically significant factor within the design space is identified as the L/S ratio. The L/S ratio determines the water content in the mixture and hence basicity of the solution. These are key considerations when synthesising zeolites [126] and can have significant impact on the product's quality (*i.e.* crystallinity) as well as the structure type [307]. The percentage contribution to the equilibrium uptake for each factor is also provided at approximately 30% for T<sub>cry</sub> and t<sub>cry</sub>, whilst L/S represents 39% contribution in agreement with the response tables ranking.

Table 5-6: ANOVA results for the Taguchi L9 design.

Factor	Percentage Contribution (%)	F- value	p-value	Order of Significance
Crystallisation Time	29.49	5721.91	0.000	3
(tery)				
<b>Crystallisation Temp</b>	31.87	6183.58	0.000	2
(Tcry)				
Liquid/Solid Ratio	38.63	7495.90	0.000	1
(L/S)				

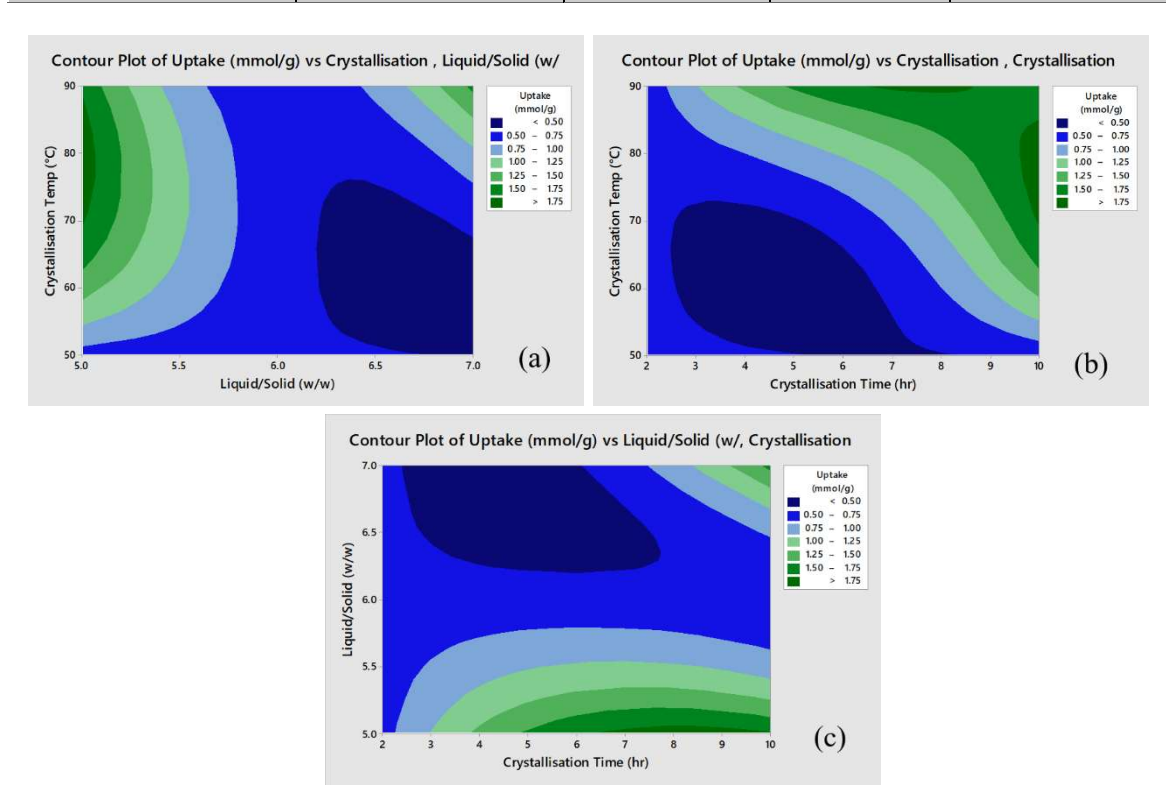


Figure 5.4: Contour plots of CO<sub>2</sub> uptake for a) L/S vs T<sub>cry</sub>; b) t<sub>cry</sub> vs T<sub>cry</sub>; c) t<sub>cry</sub> vs L/S.

Contour plots which illustrate the effect of the statistically significant factors on the CO<sub>2</sub> adsorption uptake are provided in Figure 5.4. Considering Figure 5.4.a), there are two ranges of the predictors ( $T_{cry}$  and L/S) which would result in products with improved adsorption capacity. At lower L/S ratios, there is a broad range of  $T_{cry}$  at which crystalline zeolites will form. When increasing the L/S ratio, however, the high-capacity products are only achievable at elevated  $T_{cry}$ . At lower temperatures the capacity decreases significantly indicating synthesis conditions unsuitable to facilitate zeolitisation Figure 5.4.b) illustrates the effect of  $T_{cry}$  and  $t_{cry}$  on the CO<sub>2</sub> adsorption capacity. At both lower durations and temperatures, the predicted adsorption capacity is at a minimum. The large region indicative of synthesis conditions which do not facilitate zeolitisation/development of uniform microporosity and hence result in a poor adsorption capacity likely a result of the phase's amorphicity. At the other

extreme, it is clear that elevated temperatures and durations produce phases with increased capacity. Interestingly, the two regions of highest capacity form either side of the maximum ( $T_{cry}$  and  $t_{cry}$  at +1), suggesting that at the extreme of each of these factors, the product actually sees a decrease in CO<sub>2</sub> capacity. This is assumed to be a result of the generation of more stable and denser zeolite phases with less suitable pore structures for CO<sub>2</sub> separation [187]. The improved capacity will be a result of the development of crystalline phases which possess a uniform micropore structure providing sites for the adsorption of CO<sub>2</sub>. The two distinct regions in the contour plot clearly demonstrate there is a minimum energy requirement whether through extended exposure or intensity of heating which if not met will be insufficient to overcome the energy barrier and facilitate zeolite formation [117]. Figure 5.4.c) plots the effect of  $t_{cry}$  and L/S on the CO<sub>2</sub> adsorption capacity. As in the previous case (Figure 5.4.a)) at low L/S ratios there is a broad range of durations which result in improved adsorption performance; at elevated L/S ratios this is exclusive to the extended durations. This is likely a result of a reduction to the degree of saturation during the aging step reducing the crystallisation kinetics [308,309]. Lower L/S ratios will simultaneously increase the degree of saturation whilst reducing the energy requirement for the synthesis by minimising the mass within the system.

# 5.3.1. Phase Identification from the Taguchi Optimisation

Comparison of the nine samples CO<sub>2</sub> adsorption capacity has highlighted that three (Z-1.8/10/90/7, Z-2.0/6/90/5 and Z-2.2/10/70/5) may be distinctly crystalline. Identification of which crystalline phases exist requires analysis of the powder X-ray diffractograms. The diffractograms are provided for the crystalline phases in Figure 5.5. The remaining samples (not shown) all present a broad peak centred at 30 ° 20 typical of amorphous aluminosilicates [256,257]. This ridge also exists in the crystalline samples which indicates the persistence of amorphous components that have failed to produce crystalline zeolites [119]. The peaks observed in all of the crystalline samples are characteristic of LTA and FAU zeolites. Owing to the similarity of the CBU's which comprise these phases there is some overlap in the patterns, that said, each presents a number of characteristic peaks. Product Z-2.0/6/90/5 exhibits the greatest relative intensities to the other two produced in the campaign (not ZOPT) which corroborates the findings from the contour plots, in that elevated hydrothermal temperatures will produce zeolites with improved CO<sub>2</sub> adsorption capacity. The improved adsorption capacity can be correlated with the relative intensity of peaks characteristic of certain phases in the products. The highest capacity sample presents a peak at approximately  $6 \circ 2\theta$  due to the (111) lattice plane of FAU zeolites. At a  $2\theta$  of  $7 \circ$ , a peak indicative of LTA zeolites (200) lattice plane can be seen in all of the products. The uptakes of the samples suggests that those with peaks typical of FAU zeolites have a higher capacity. Zeolite 13X or NaX, a commercial FAU zeolite presents a larger capacity than commercially available LTA zeolites [211]. Powder diffraction files of the zeolites identified in Figure 5.5 are for FAU: PDF: 01-070-2168 and for LTA PDF: 01-089-8015. The optimum sample exhibits a well-defined pattern of increased

relative intensity compared to the other three samples, a result of improved crystallinity in ZOPT. The conditions employed are clearly more favourable for zeolite crystallisation as is evidenced by the reduced intensity of the amorphous ridge at 30 ° 20. The improved crystallisation consumes more of the amorphous aluminosilicates in the fused fly ash. For all syntheses in this campaign, none have any indication of phases present in the fly ash precursor. Interestingly for the four diffractograms in Figure 5.5, the peak positions for LTA appear to be shifted slightly to lower Bragg angles whilst for FAU slightly higher. This is typically indicative of unit cell expansion (lower angles) or contraction (higher angles). Given both LTA and FAU are cubic structures, a unit cell expansion implies an increase to the lattice parameter whilst contraction the opposite. The unit cell parameter can be directly correlated to the phase's Si/Al ratio due to the differing bond length of Si-O and Al-O [310–312]. This suggests the LTA present in the products may present slightly lower Si/Al ratios than in the example pattern whilst the FAU may present slightly higher Si/Al ratios. The presence of additional cations not present in the example patterns along with differences in moisture content, can also modify the unit cell [313] and hence complicate determination of the zeolite product's Si/Al ratio owing to the sample's heterogeneity.

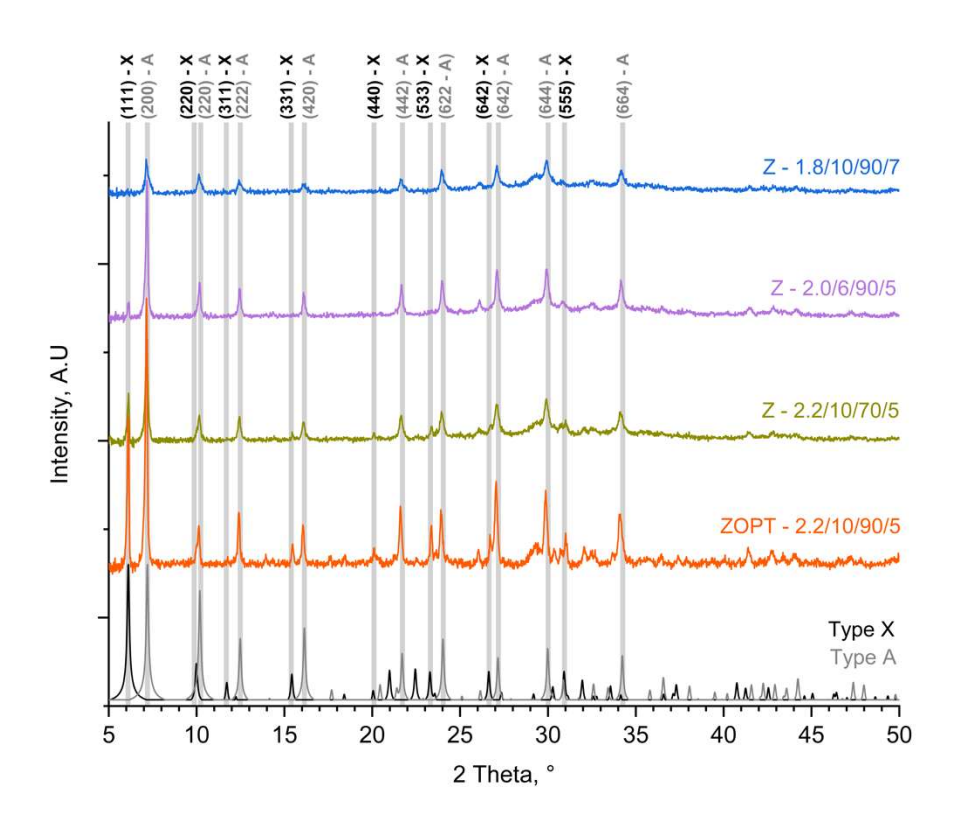


Figure 5.5: Powder x-ray diffractogram for crystalline zeolites produced in the L9 OA and the predicted optimum, ZOPT. Diffractograms provided for type X and type A zeolites adjacent to the x-axis.

## 5.3.2. Product Morphology – Taguchi Optimisation

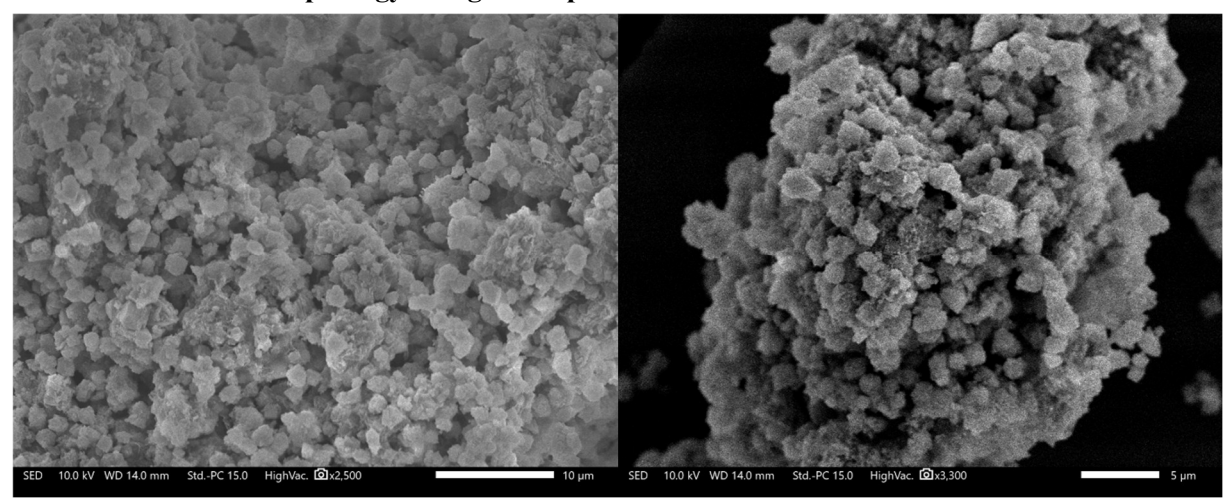


Figure 5.6: SEM images of ZOPT-2.2/10/90/5 at 2500x (left) and 3300x (right) magnification.

During the previous study, the SEM images of the crystalline products indicated poor crystallinity and a diverse range of morphologies. Optimisation of the hydrothermal conditions has facilitated an improvement to CO<sub>2</sub> adsorption capacity which has been attributed to the formation of crystalline zeolites, both LTA and FAU. Given the adsorption capacity of zeolites is largely influenced by available pore volume and composition, an increase in capacity implies either an increase in pore volume or compositional variation, such as the Si/Al ratio or exchanged cations. Pore volume would increase if the degree of crystallisation improves, which itself would be observed *via* SEM as morphological regularity and less disorder. Additionally, exchange of Na cations with Ca in LTA (and other small-pore) zeolites is known to increase pore volume and hence CO<sub>2</sub> capacity due to the lower number of multivalent cations required to balance framework charge [26,28,211]. Two pairs of images are provided in Figure 5.6 and Figure 5.7, with the latter at a higher magnification. The particles observed in Figure 5.6 indicate a greater proportion of crystalline phases vs amorphous than the sample produced in the initial study (Figure 5.2). This suggests the synthesis is improved as already evidenced by XRD and CO<sub>2</sub> adsorption capacity. Similarly, crystal size remains consistent at approximately 2 μm with

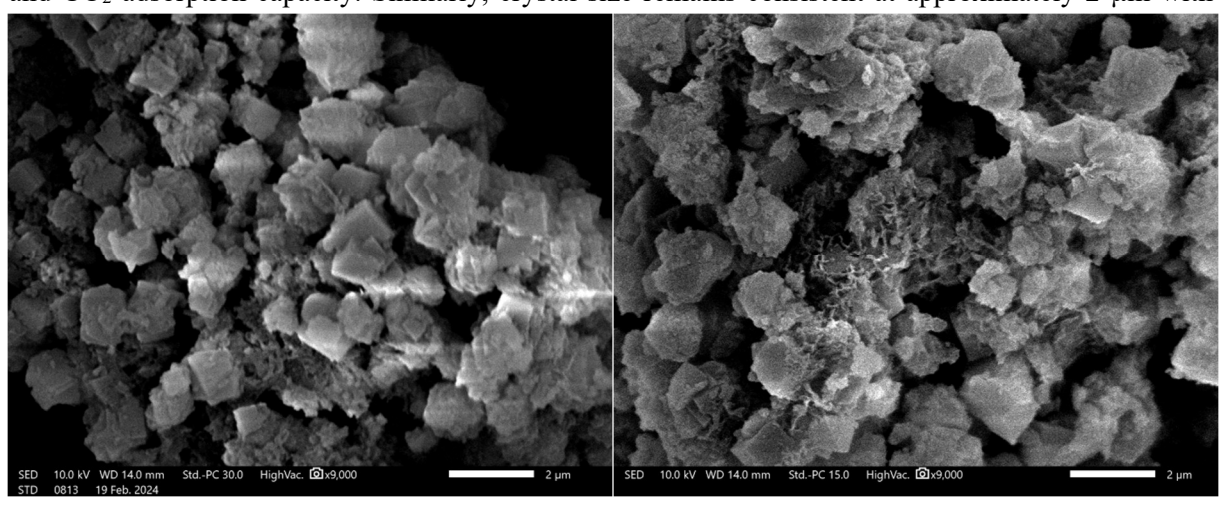


Figure 5.7: SEM images of ZOPT-2.2/10/90/5 at higher magnification.

most presenting as agglomerations of both crystalline and amorphous masses. This amorphous mass will comprise all unreacted fly ash species such as aluminosilicates and alkali and alkaline earth metals. At higher magnification (Figure 5.7) both cubic and octahedral morphologies are observed in the sample indicating that both LTA and FAU unit cells exist [164,314]. The quality of the zeolite crystals is still relatively low owing to the presence of disorder and irregularities in the crystal structures and intergrowth.

## 5.3.3. Elemental Composition Estimated via EDS – Taguchi Optimisation

With primarily LTA and some FAU identified in the zeolitic products, EDS can complement both the XRD and SEM analyses by elucidating the presence of certain cations in the frameworks and amorphous constituents. An assessment of the crystalline phase composition has been achieved by averaging EDS data across ten areas of the sample which present a clearly crystalline morphology, results of which are provided in Table 5-7 for ZOPT-2.2/10/90/5. In this sample, Ca was identified in most of the crystalline morphologies and typically at greater quantities than Na. The results suggest the crystalline component in ZOPT presents a Si/Al weight ratio of approximately 1.71 which is higher than found in the previous zeolite study (1.46) and the fly ash precursor (1.67). This increase could be a result of a larger proportion of FAU zeolites which typically form at higher Si/Al ratios than LTA [149]. Higher quantities of calcium have also been identified (14.6 wt% vs 8.9 wt%) in ZOPT than ZF1-2.0/4/90; however, Fe content is slightly lower (3.9 wt% vs 5.5 wt%). That said, both elements demonstrate a lower RSD in ZOPT. The presence of calcium further suggests that the LTA in the sample may be calcium-exchanged [315]. Type X is also known to exchange Na for Ca and may even feature Mg as compensating cations [238,316]. The RSD of both Al and Si has increased in ZOPT from 16.0 and 11.5 % to 18.6 and 25.4 %, respectively. An increase in the variation could indicate a varying Si/Al ratio of the crystalline components. The existence of variation between the Si/Al ratio could be attributed to there being both LTA and FAU zeolites, which often present dissimilar Si/Al ratios both in pure form and FA-derived.

Table 5-7: Surface elemental composition of ZOPT-2.2/10/90/5 evaluated via EDS averaged over 10 distinct sample areas.

Element	ZOPT-2.2/10/90/5 wt%	Relative Standard Deviation %
Na	3.9	18.2
Mg	1.4	54.5
Al	11.3	18.6
Si	19.3	25.4
K	0.6	41.8
Ca	14.6	25.9
Fe	3.9	23.3
0	44.9	17.7

## 5.4. Impact of Fly Ash on Zeolite Product

With the common understanding that fly ash is inherently heterogenous coupled with the measured variation in both the fly ash batches and the zeolite products produced from FA1 and FA2, an investigation into the effect of each FA on the zeolite product is required. Using the optimum point identified via Taguchi optimisation, four samples have been produced using the same conditions but differing fly ash batches (FA1/FA2/FA3/FA4). The equilibrium CO<sub>2</sub> adsorption has also been estimated via TGA at 50 °C, results are provided in Table 5-8. The sample produced from FA1 is the second produced at these conditions, so it should be considered a repeat batch of ZOPT-2.2/10/90/5. An assessment of sample variation is provided in the next chapter. The yield from the four individual fly ashes is higher than that in the original confirmation experiment. Fly ash batch 1 presented the lowest yield during this study at 76.70%, FA3 had the largest yield at 87.85 %. Adsorption capacities for the FA1 precursor are consistent with the FA3-derived sample even with the variation between FA1 and FA3. Conversely, FA2 and FA4 both present lower capacities, with FA2 at 1.14 mmol g<sup>-1</sup>. This can be explained in part by the elevated concentration of Ca in FA2. Calcium present during synthesis can reduce the efficacy of zeolitisation by acting as a "structure-breaking" cation [131]. Two roles exist for the alkali-metal cations in zeolite synthesis: provision of OH- required to solubilise silicate and aluminate species; and a limited structure directing role [317]. The structure directing role of the hydrated alkali-metal cations involves the ordering of H<sub>2</sub>O molecules around the cations, these H<sub>2</sub>O molecules are then displaced by silicate and aluminate species forming small nucleation centres for CBUs [317–319]. The aluminium content in FA2 was also lower than the other batches which can limit the extent of zeolitisation. With FA4 possessing similar properties to FA3, a reduced capacity is unexpected and may arise due to heterogeneity in the fly ash batches themselves. That said, the yield for both FA3 and FA4 is higher (16%) than the original ZOPT (FA1).

Table 5-8: Yield and uptake of samples produced at conditions 2.2/10/90/5 using FA1, FA2, FA3 and FA4.

Sample	Yield	Uptake
Sample	%	mmol·g <sup>-1</sup>
ZOPT-2.2/10/90/5	71.07	1.84
ZF1-2.2/10/90/5	76.70	1.80
ZF2-2.2/10/90/5	82.72	1.14
ZF3-2.2/10/90/5	87.85	1.80
ZF4-2.2/10/90/5	82.76	1.66

## 5.5. Porosity and Surface Area Analysis

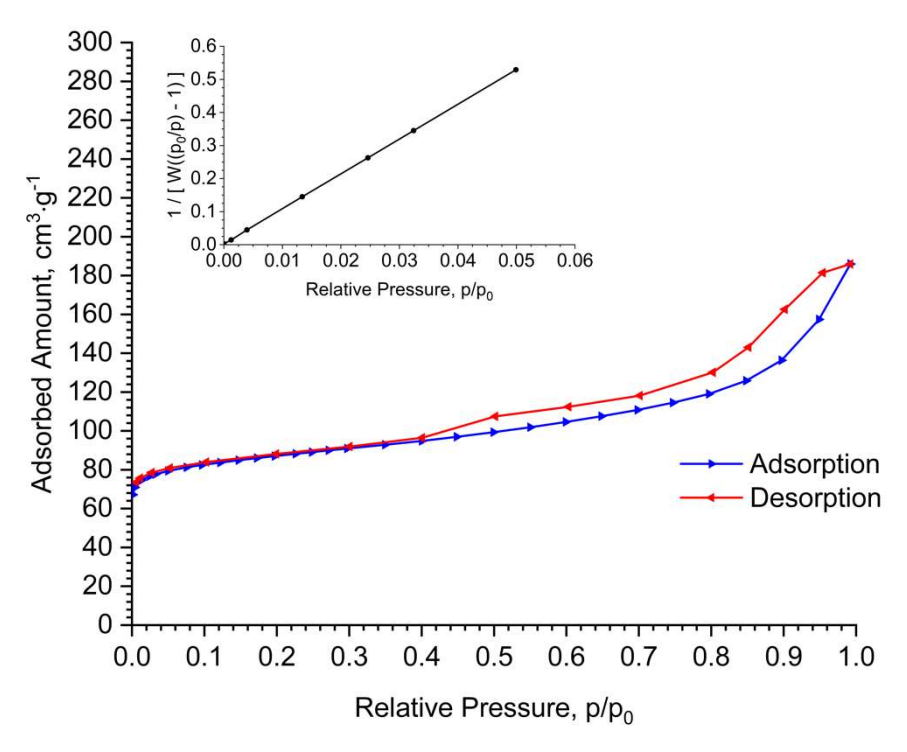


Figure 5.8: N2 adsorption/desorption isotherm measured at 77 K (BET) with the linear BET plot (inset).

A nitrogen isotherm measured at 77 K is provided in Figure 5.8 for ZOPT. Visually the isotherm presents type IV (IUPAC) characteristics defined by the sharp rise in adsorbed amount at low  $p/p_0$  due to micropore filling [320], followed by formation of a multilayer and onset of capillary condensation in larger pores [165]. The hysteresis loop suggests the adsorbent possesses mixed micro-mesoporosity which in this case can be attributed to either formation of mesoporosity via aggregation of zeolite crystals/crystallites or the presence of an amorphous impurity likely composed of residual sodium silicate and aluminate species[120,148,321]. As the adsorption isotherm presents a composite of type I and II shapes (i.e. type IV), the hysteresis can be defined as a type H4 [59] which is typical for mixed micro-mesoporous materials and is likely a result of the aggregation of the individual zeolite crystals [71,120,148,321]. Type IV isotherms typically show an adsorption plateau towards the saturation pressure and the absence of this in ZOPT suggests a lack of saturation, this can be attributed to the presence of pores in the macropore domain [322]. This causes a near limitless increase in adsorbed amount as there is no (theoretical) restriction of the multilayer. Framework defects in the crystalline phases can create microporosity as can the aggregation of larger crystals [323]. The linear region which satisfies Rouquerol's criteria [201] was identified between p/p<sub>0</sub> of 0.0012 and 0.05, facilitating estimation of the external BET surface area as 329.89 m<sup>2</sup>·g<sup>-1</sup>. The linear BET plot is provided as an inset of Figure 5.8. The total pore volume has been estimated via DFT as 0.225 cm<sup>3</sup>·g<sup>-1</sup>. Analysis of the micropore contribution has been achieved by t-plot analysis (Table 5-9). The micropore contributes to 71.67 % & and 41.86 % of the total surface area and pore volumes, respectively.

*Table 5-9: Textural properties of ZOPT estimated via the N*<sub>2</sub> *adsorption/desorption at 77K.* 

BET Surface Area m <sup>2</sup> ·g <sup>-1</sup>	Micropore Area m <sup>2</sup> ·g <sup>-1</sup>	Micropore Volume cm <sup>3</sup> ·g <sup>-1</sup>	Total Pore Volume cm <sup>3</sup> ·g <sup>-1</sup>	
329.89	236.42	0.094	0.225	
$p/p_0$ : $0.0012 - 0.050$	p/p <sub>0</sub> : 0.07	$p/p_0 = 0.95$		

# 5.6. Adsorption Equilibria

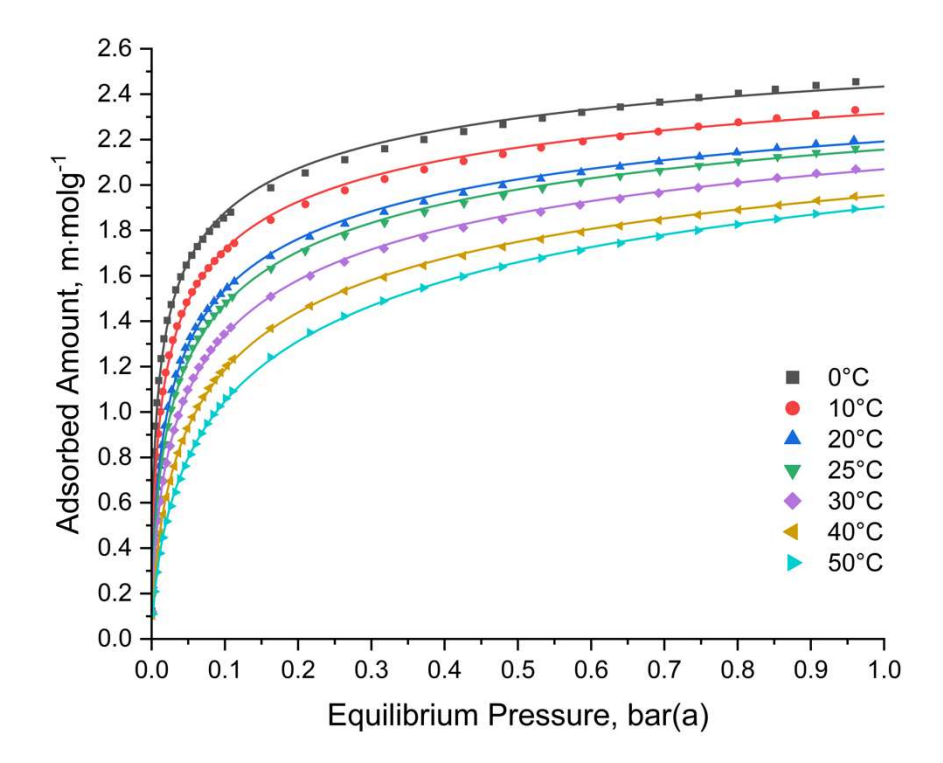


Figure 5.9: Equilibrium CO<sub>2</sub> adsorption isotherms (discrete) and the fitted Toth isotherm model (continuous line).

Equilibrium  $CO_2$  adsorption isotherms have been generated for the optimum zeolite, i.e. ZOPT. The experimental data have been modelled *via* non-linear regression analysis with the fit-quality data for four models provided in Table 4-4. Across the studied temperatures, the Toth isotherm model presents the best fit based on the adj- $R^2$  and RMSE values. The isotherm plots are provided in Figure 5.9. Visually, the fits corroborate the statistical results and display typical type I IUPAC traits. The large increase in adsorbed amount in the low pressure region is primarily influenced by a zeolite's Si/Al ratio as this dictates the site occupation of framework cations [324,325]. The presence of different cations and multiple zeolite phases will lead to heterogeneity in the adsorbent's overall matrix. This is evidenced by the Toth constant,  $n_T$ ; when below one the adsorbent is considered heterogeneous. Table 5-11 exhibits the isotherm constants estimated through non-linear regression with their associated

standard error. For all temperatures,  $n_T$  can be seen to be below 1, reaching a minimum of 0.36 at 0 °C. This suggests a significant degree of heterogeneity in the adsorbent which can be attributed to the presence of multiple crystalline phases (LTA and FAU) and amorphous constituents, each of which facilitate CO<sub>2</sub> adsorption mechanisms and affinities [326]. The difference in both pore size and adsorption enthalpy between LTA and FAU could also result in significant adsorbent heterogeneity. Additionally, with potential for cation exchange, even pure crystalline zeolites can present multiple adsorption sites with varied energetics due to the distribution and position of framework cations [211] as well as the varying levels of occupation arising due to the size and charge of the cation and the frameworks Si/Al ratio [247], leading to heterogeneity of gas distribution [327]. The Toth constant is temperature dependent and typically seen to approach 1 (homogeneity) as temperature increases [73]. For ZOPT, a general trend is observed which sees  $n_T$  tend towards 0.44 at 40 °C; however, at 50 °C it drops to 0.41. A general reduction in heterogeneity can be explained by an increase in adsorbate mobility promoting lateral interactions [328]. This would in turn narrow the range of adsorption site energies [329]. As the temperature increases further, low energy sites reliant on van der Waals dispersion interactions (i.e. Debye, London and Keesom) are no longer viable, decreasing site heterogeneity. An increase in site heterogeneity between 40 °C and 50 °C, and albeit small, 25 °C and 30 °C as evidenced by  $n_T$ , implies its dependence on temperature to be non-linear and non-monotonic, potentially due to modification of the adsorption mechanisms as temperature increases.

Table 5-10: Equilibrium isotherm model fitting via non-linear regression results.

Isotherm Model	Langmuir		Freundlich		Sips		Toth	
Temperature	Adj-R <sup>2</sup>	RMSE						
0 °C	0.9413	0.1675	0.9452	0.1619	0.9970	0.0379	0.9988	0.0241
10 °C	0.9541	0.1386	0.9485	0.1468	0.9960	0.0407	0.9993	0.0177
20 °C	0.9653	0.1152	0.9578	0.1270	0.9989	0.0203	0.9996	0.0129
25 °C	0.9689	0.1081	0.9609	0.1214	0.9990	0.0190	0.9996	0.0127
30 °C	0.9735	0.0973	0.9686	0.1059	0.9992	0.0169	0.9996	0.0117
40 °C	0.9813	0.0780	0.9712	0.0968	0.9996	0.0120	0.9998	0.0087
50 °C	0.9831	0.0737	0.9801	0.0799	0.9998	0.0086	0.9998	0.0072

Table 5-11: Toth fitted isotherm model constants.

Temperature	q	m	k k	Γ	$\mathbf{n}_{\mathrm{T}}$		
°C	Val	SE	Val	SE	Val	SE	
0	3.028	0.044	10.375	1.219	0.360	0.010	
10	2.907	0.035	4.496	0.376	0.389	0.009	
20	2.855	0.032	2.327	0.149	0.402	0.008	
25	2.854	0.034	1.784	0.109	0.407	0.008	
30	2.884	0.041	1.228	0.076	0.404	0.009	
40	2.751	0.033	0.612	0.025	0.441	0.008	
50	3.039	0.045	0.413	0.015	0.415	0.007	

# 5.7. Adsorption Kinetics

The adsorption kinetics of ZOPT have been estimated *via* modelling of the adsorption uptake data produced *via* TGA at 50 °C. In total, four kinetic models were evaluated, the results of which are provided in Table 5-12. Based on adj-R<sup>2</sup> and RMSE, the best fit would be the Elovich kinetic model. The Elovich model often describes heterogeneous gas-solid systems or those exhibiting chemisorption interactions [330].

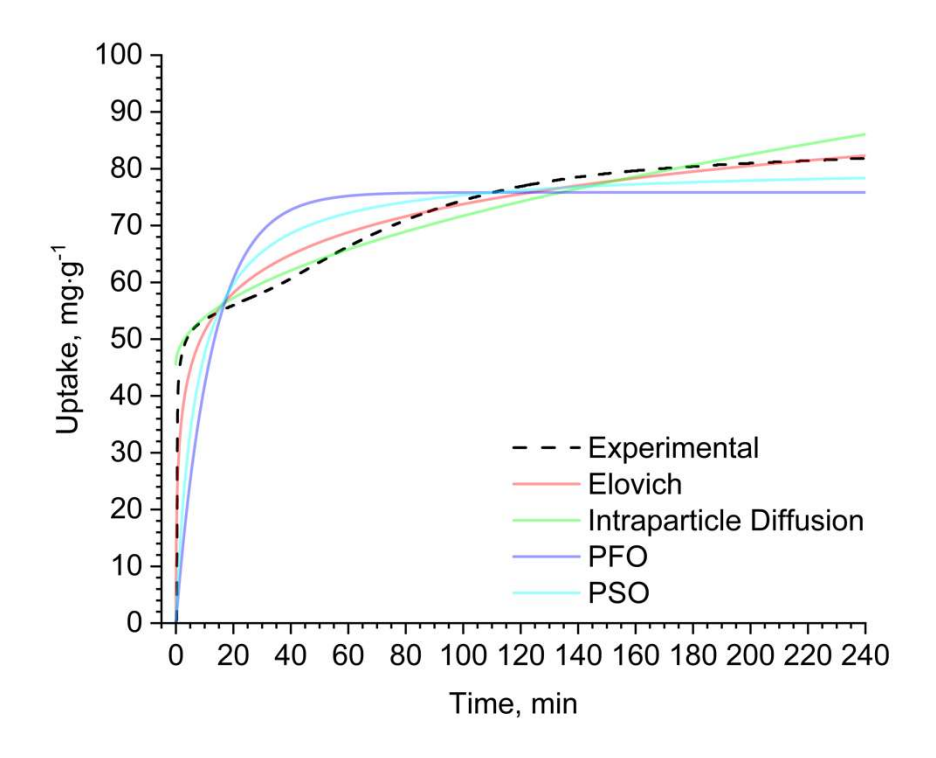


Figure 5.10: ZOPT CO<sub>2</sub> adsorption kinetic model fitting; PFO, PSO, Elovich and W&M Intraparticle Diffusion model shown.

Table 5-12: Adsorption kinetic model fitting via non-linear regression results.

Pseudo-first Order		Pseudo-second Order		Elovich		W&M Intraparticle Diffusion	
Adj-R <sup>2</sup>	RMSE	Adj-R <sup>2</sup>	RMSE	Adj-R <sup>2</sup>	RMSE	Adj-R <sup>2</sup>	RMSE
0.3694	7.904	0.6955	5.492	0.9430	2.376	0.9212	2.794

As an empirical model, the parameters have limited physical implications [331], although the derivation considers both the dependency of adsorption energies and adsorption rate on the surface coverage [332,333]. The four kinetic models can be seen in Figure 5.10 and visually, all fail to represent the data accurately. One cause for this would be the presence of multiple rate or diffusion mechanisms influencing the overall rate of adsorption (i.e. adsorption kinetics) [334]. Confirmation of this is achieved by plotting  $q_t$  vs  $t^{1/2}$  which identified three separate linear regions. Wang and Guo have successfully modelled similar systems by fitting individual Intraparticle Diffusion (IPD) functions to each region, doing so ensures consistency with the IPD theory [84]. As such, the ZOPT kinetic data has been fitted to three IPD functions (EQ. 37 to EQ. 39) where The fitted plot is provided in Figure 5.11.

$$q_t = k_{IPD1} \cdot t^{1/2}$$
 $q_t - q_{t1} = k_{IPD2}(t - t_1)^{1/2}$ 
EQ. 38

$$q_t - q_{t2} = k_{IPD3}(t - t_2)^{1/2}$$
 EQ. 39

The adsorption kinetics of ZOPT can be described by three primary diffusion-controlled steps connected by transient regions with a clear decrease in the rate constant such that  $k_{IPD1} < k_{IPD2} < k_{IPD3}$ . This indicates the reduction adsorption rate due to an increase of diffusional resistance [148]. The adsorption capacity was estimated at 1 minute as 1.2 mmol·g<sup>-1</sup> which results in a significant initial rate of adsorption due to strong adsorbent-adsorbate interactions [335].

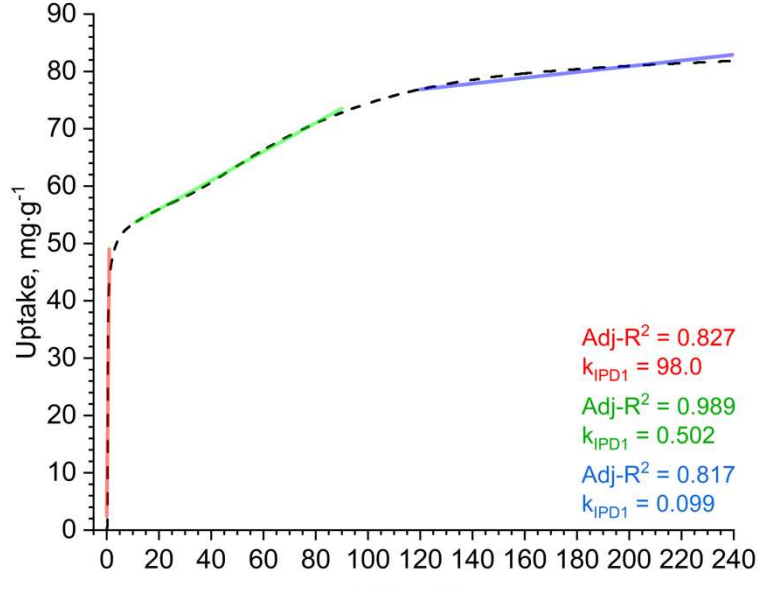


Figure 5.11:CO<sub>2</sub> adsorption kinetics (ZOPT) at 50 °C and 1 bar fitted with three Intraparticle Diffusion model functions.

#### 5.8. Enthalpy of Adsorption

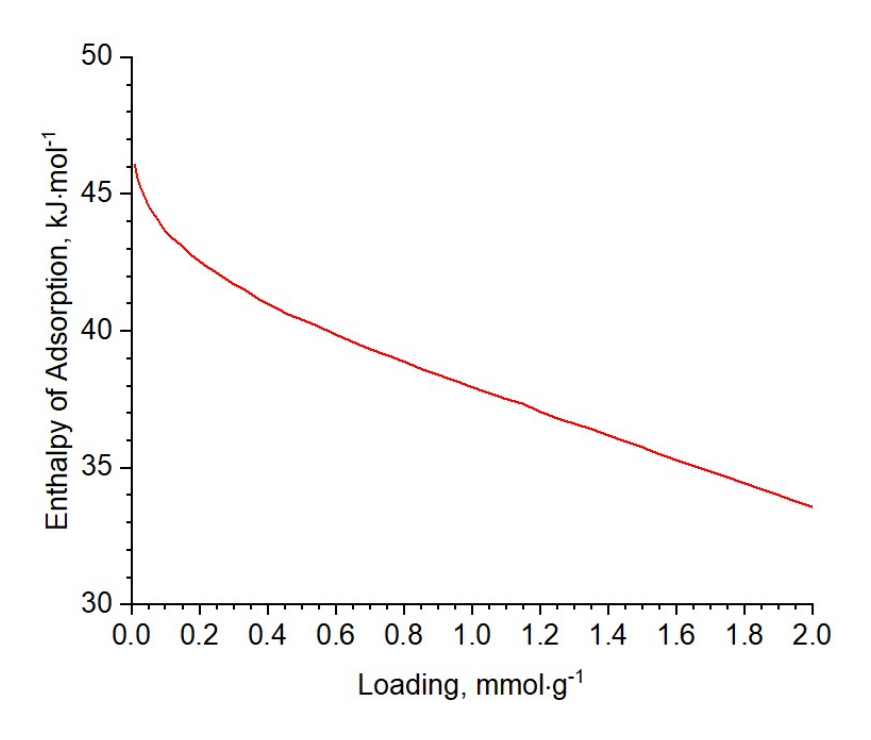


Figure 5.12: Adsorption enthalpy ZOPT-CO2 estimated using Toth isotherm model fit.

Adsorption enthalpy has been estimated from the equilibrium isotherms between 0 and 50 °C and has been provided in Figure 5.12. This can facilitate estimation of regeneration energy requirements which for TSA translates to the heat demand during desorption. The absolute value of isosteric enthalpy of adsorption has been calculated for ZOPT to be 33.7 kJ·mol<sup>-1</sup>. It can be seen to increase at lower CO<sub>2</sub> loadings, with a maximum estimated at zero coverage of 46 kJ·mol<sup>-1</sup>. This occurs due to heterogeneity of adsorption sites, and with the highest energy sites occupied first, the adsorption enthalpy is expected to be larger [216]. In the case of zeolites, the high energy sites are those closest to the framework cations which have been associated with adsorption enthalpies in the region of 30 to 90 kJ·mol<sup>-1</sup> [211]. The general trend indicates a decrease in adsorption enthalpy, this is expected as coverage increases to the maximum loading. Here, the interactions between CO<sub>2</sub> and the framework oxygen become more prevalent [336]. The interaction between CO<sub>2</sub> and framework oxygen is comparatively weaker to those with framework cations as it is primarily a product of van der Waals dispersion interactions.

## 5.9. Working Capacity

An initial estimate of the sorbents working capacity under typical adsorption/desorption conditions (50°C/150°C) has been provided in Figure 5.13 where fractional coverage (θ) is based on the initial uptake during the very first adsorption cycle. This was measured *via* TGA by simulating a TSA process by repeating desorption (150 °C, 1 atm N<sub>2</sub>, 1 h) and adsorption (50 °C, 1 atm CO<sub>2</sub>, 2 h) steps for a total of 40 complete cycles. The five cycles occurring after cycle 1 demonstrate a general decline in capacity

to approximately 90% of the initial. Relative stability is achieved after cycle 6 whereby capacity fluctuates minimally around a median value of 0.87. Given most adsorbents are expected to have a (theoretical) lifetime of multiple thousands of cycles (in the absence of any deactivating impurities in the inlet gas stream), this reduction is quite substantial after 40. The cause of this is likely an insufficient desorption step in the context of either time or temperature. Without sufficient degassing between each cycle, adsorptive will remain in the adsorbent and reduce the availability of adsorption sites, reducing the uptake during the next adsorption cycle. With hysteresis often reported for LTA zeolites, this is to be expected as desorption is controlled by the adsorbent's effective pore aperture which is smaller than the adsorption rate-controlling diameter, the LTA  $\alpha$ -cage [337] i.e. the  $\alpha$ -cage diameter is approximately 11.4 Å [338] vs an effective pore aperture of 4.3 Å [247].

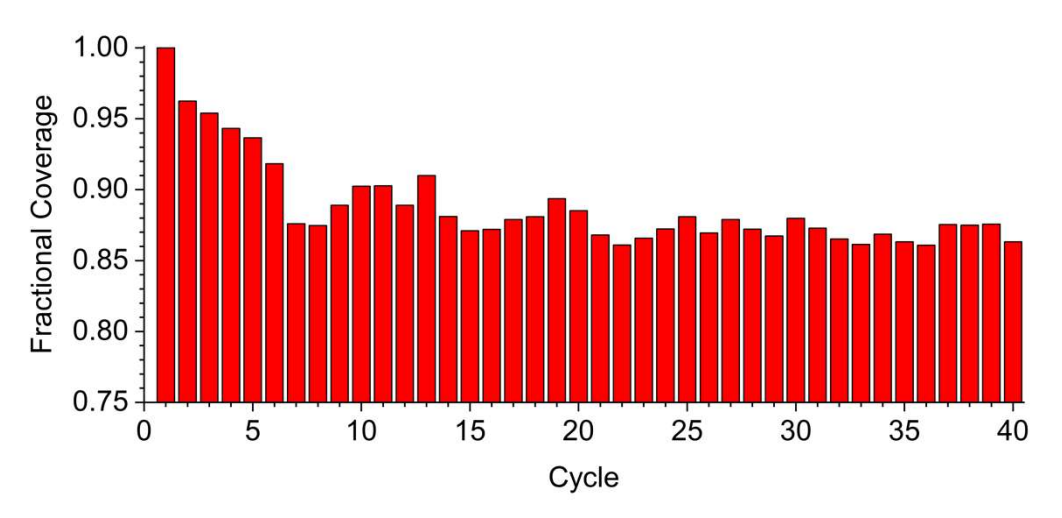


Figure 5.13: Working  $CO_2$  adsorption capacity of the optimised BFA-derived zeolite. Adsorption at 50 °C, 100 mol% $CO_2$  at 1 atm for 2 h; desorption at 150 °C, 100 mol% $N_2$  at 1 atm for 1 h.

# 5.10. Conclusion

Industrial biomass combustion fly ashes produced at Drax power station in the UK have been successfully employed as a precursor for the synthesis of LTA and FAU zeolites. The zeolitic product has been synthesised *via* an optimised alkaline fusion assisted hydrothermal protocol. The Taguchi optimisation employed an L9 orthogonal array to study the impact of NaOH/FA ratio, hydrothermal temperature, hydrothermal time and liquid/solid ratio on the equilibrium CO<sub>2</sub> adsorption capacity at 50 °C and 1 atm. The optimum zeolite, ZOPT, exhibited an improved adsorption capacity of 1.84 mmol·g<sup>-1</sup> at 50 °C, 1 atm or approximately 1.6 mmol·g<sup>-1</sup> higher than the FA from which it was derived. The net improvement in capacity from the initial NaOH/FA study is 0.18 mmol·g<sup>-1</sup>. Three of the four studied factors in the L9 were identified as statistically significant within the design space: the hydrothermal time, hydrothermal duration and liquid/solid ratio. Crystalline zeolites however were produced at all of the investigated NaOH/FA ratios demonstrating the statistical insignificance when varying between 1.8 and 2.2. The optimum sample has been comprehensively characterised to reveal the product's phase

composition, morphology and surface elemental composition. Results suggest both LTA and FAU type zeolite structures have co-crystallised with evidence of the amorphous gel from which they formed also present. Evaluation of pure component N2 and CO2 adsorption has shown that ZOPT has an external BET surface area of 330 m<sup>2</sup>·g<sup>-1</sup>, of which, 72% is contributed by microporosity. This suggests the adsorbent possesses both micro and mesoporosity due to structural defects and residual amorphous aluminosilicates. The generation of crystalline and microporous zeolitic phases promotes CO2 adsorption which was evidenced by analysis of the adsorption equilibria and kinetics. The Toth equilibrium isotherm model was identified as the best fit for the data highlighting significant heterogeneity in the adsorbent. Additionally, the kinetic data was fitted with a piece-wise intraparticle diffusion model further corroborating the notion of mixed porosity and sample heterogeneity. Adsorption enthalpy was identified as coverage dependent, reducing to approximately 33.7 kJ·mol<sup>-1</sup> at a loading of 2 mmol·g<sup>-1</sup>. An initial estimate of the adsorbent's working capacity was made via TGA which demonstrated a reduction in capacity to 87% after 40 cycles however, this significant drop was attributed to insufficient desorption cycle time. This work has identified that industrial-grade biomass combustion fly ashes are potential feedstock candidates for the synthesis of zeolites LTA and FAU. An investigation is now required to understand the variability and repeatability in the optimised synthesis procedure and requirements for powder structuring to facilitate representative mass transfer studies in a fixed-bed adsorber to reveal the potential of biomass FA-derived zeolites for selective CO<sub>2</sub> separation.

# 6. Scale-up and Structuring of Fly Ash Derived Zeolites

#### 6.1. Introduction

Considering the variation identified in the fly ash precursor, an evaluation of the variation present in the derived zeolite is required. Confirmation of replicability will provide confidence in both the adsorption performance and pathway for fly ash valorisation. Of equal importance is the potential deployment of this technology which is currently associated with a lengthy synthesis time (> 24h). The aging of the mixture takes 16 h, and reductions to this would reduce the overall synthesis time significantly. Water usage is also non-negligible due to washing the produced zeolites. In this work, the average water consumption per synthesis is primarily driven by the washing water post-separation of the solid product, each synthesis using approximately 5-8. If washing to a lower degree, *i.e.* a higher supernatant pH then less water is required reducing the overall cost and inherent waste production.

Effective utilisation of waste fly ash derived zeolites demands macroscopic structure and form compatible with the intended application. Fixed-bed adsorption processes often require particle sizes above that of powders for avoidance of excessive pressure drops and operational issues within the reactor vessel. Mechanically, these particles need to maintain and preserve their physical form across the operating envelope. This typically involves the production of pellets or granules achieved *via* extrusion, granulation or casting. Naturally, zeolite powders do not retain structured form without the aid of binders. To overcome this and increase the mechanical strength of the adsorbents, binders such as kaolin or boehmite are added [339–342]. This unfortunately reduces the performance of the adsorbent as the additives in most cases do not contribute positively to CO<sub>2</sub> adsorption.

This chapter seeks to identify synthesis improvements to reduce both total time and water usage whilst maintaining the adsorption performance. Variation present in the ash derived zeolites is quantified through analysis of the 35 batches produced for the fixed bed adsorption experiments. Finally, the zeolites are evaluated for extrusion with and without the addition of kaolin binder to determine the optimum mixture ratio which permits sufficient mechanical strength and minimal impact to performance. Production of a suitable particle size is achieved through wet granulation of the best mixture before a comparative characterisation of the powder and pellets.

#### 6.2. Impact of Stirring Conditions

Utilising the optimised synthesis conditions from the previous chapter, the influence of stirring rate and duration is evaluated with the intention of reducing the total synthesis time. Each sample is produced as per the methodology defined previously but with different stirring speeds and durations as outlined in Table 5-8. Stirring rate was initially increased to 500 RPM and the duration halved, after which it was increased until the produced zeolite presented a capacity consistent with ZOPT. The adsorption

capacities have been estimated *via* TGA at 50 °C, 100 mol% CO<sub>2</sub> at atmospheric pressure after degassing at 150 °C under 100 mol% N<sub>2</sub> for 1 h.

Table 6-1: Stirring conditions, yield and uptake of samples produced during synthesis method adjustments. ZOPT provided in row 1 for comparison.

Sample	Stirring Speed RPM	Stirring Duration h	Yield %	Uptake mmol·g <sup>-1</sup>
ZOPT-2.2/10/90/5	300	16	71.07	1.84
ZOPT-ST8	500	8	82.79	1.68
ZOPT-ST10	500	10	79.14	1.83

The table above presents the results of increasing the stirring rate and reducing the stirring duration. Upon reducing the total stirring duration to 8 h, the yield can be seen to increase by over 11% whereas the capacity is reduced. At a stirring duration of 10 h, the capacity of the produced zeolite is consistent with the optimum produced in the previous chapter suggesting the stirring duration can be reduced by 6 h without significant impact to product quality or performance. Interestingly, the yield of sample ZOPT-ST10 is 8% greater than the previously produced optimum. Although this yield may be the result of precursor heterogeneity, the increase stirring rate (500 RPM vs 300 RPM) may have improved the dissolution of aluminosilicate species [343]. Stirring during aging facilitates the dissolution of silica and alumina species [317,343]; any reduction in this may limit subsequent nucleation and crystallisation reactions as less precursor species are available. Reductions in Al and Si species availability during zeolite crystallisation often extends the required crystallisation time as the crystallisation rate is heavily dependent on the quantity and composition of the amorphous aluminosilicates formed during aging as these serve as nuclei precursors that induce subsequent crystallisation [344,345].

# **6.2.1.** Analysis of Surface Morphology

Given the products produced in the previous subsection exhibit CO<sub>2</sub> adsorption capacities consistent with the optimum, it is assumed that they possess a crystalline structure which are confirmed in the next section. Morphologically, adjustments to synthesis conditions such as aging can result in marked differences, primarily in zeolite crystal size distribution [346,347]. The two samples, ZOPT-ST8 and ZOPT-ST10 have been evaluated *via* SEM (IT200) after gold-coating *via* the sputtering technique (Figure 6.1). The morphology of ZOPT-ST8 is significantly dissimilar to ZOPT-2.2/10/90/5 due to the presence of layered-like crystalline structures which have not been observed in previous analyses. These structures are likely alternate crystal structures such as cancrinite or sodalite [348,349], both are denser zeolitic phases with less applicability for CO<sub>2</sub> adsorption without significant modification [350]. Faujasite zeolites such as 13X is known to crystallise as an intergrowth of FAU and EMT in the form of layered-like zeolites which can introduce a degree of inter-crystalline macro and mesoporosity in the material [323] and hence enhance transport of CO<sub>2</sub> into the pore system by reducing the diffusional path length [108]. Quantification of the ratio of the two is difficult as they often form as an intergrowth introducing overlaps within the diffractogram [351] and with EMT often presenting only a minor

contribution further adding complexity. Wang et al. reported a 7% EMT contribution in their FAU/EMT intergrowth estimated via analysis of relative peak intensities  $(5 - 7 \circ 2\theta)$  from high-resolution diffractograms [352]. The sphericity of the layered-like zeolites in ZOPT-ST8 would suggest these to be sodalite [353,354] although these were also absent in the diffractogram. Sample ZOPT-ST10 is also provided in Figure 6.1 (bottom) which is morphologically consistent with ZOPT-2.2/90/10/5 albeit with the addition of layered-like crystalline structures. Both cubic and hexagonal morphologies can be seen emerging from the amorphous constituents (left) with a larger particle exhibiting layers on the external surface appearing to have been deconstructed. This can occur by the process of Ostwald ripening whereby crystals formed early during the reaction will subsequently dissolve and recrystallise as a different structures [355,356]. The right-hand image of ZOPT-ST10 exhibits morphologies characteristic of FAU/EMT intergrowth due to their hexagonal, plate-like shape. This typically only occurs if templating techniques are employed which can involve inorganic salts (hard-templating) or surfactants (soft-templating) [323,357]. In this case and in the absence of templating agents, the presence of inorganic phases from the FA precursor may have similar effects, especially when considering calcium species are both present in the FA and are an example of hard-templating agent [358].

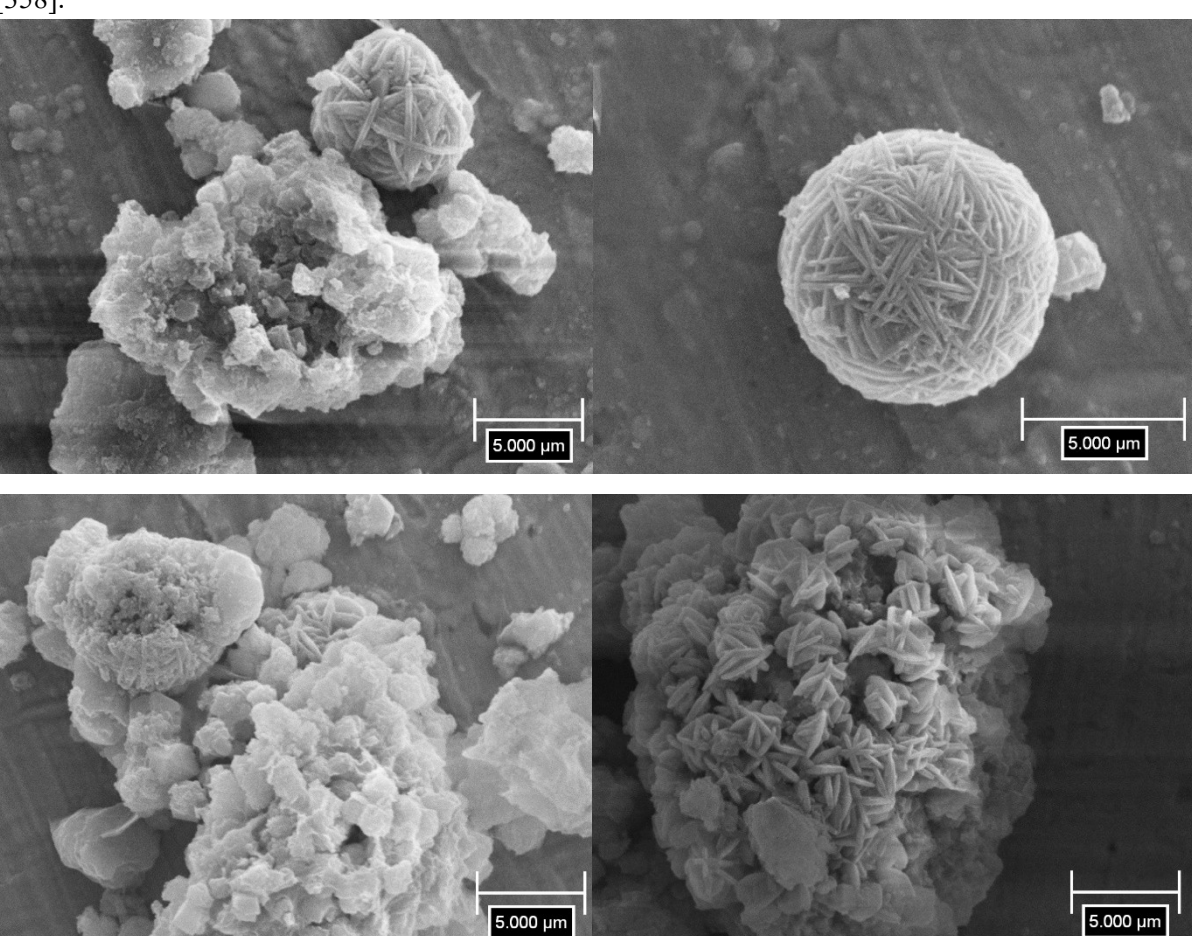


Figure 6.1: SEM images of ZOPT-ST8 (top) and ZOPT-ST10 (bottom); accelerating voltage 15kV.

#### **6.2.2.** Phase Identification

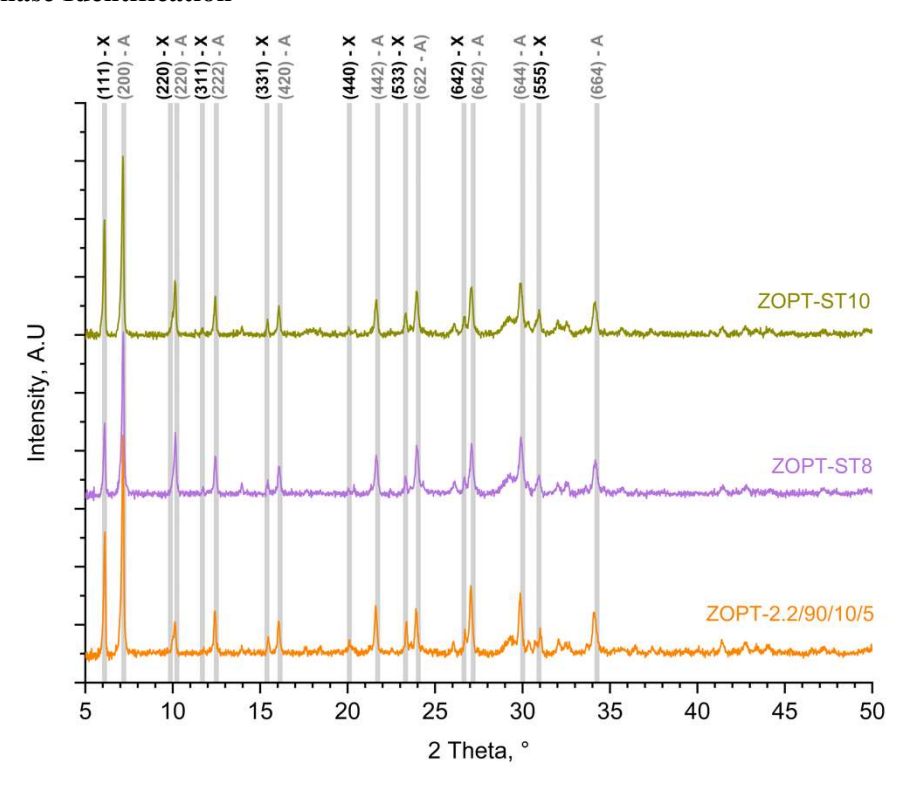


Figure 6.2: Powder x-ray diffractograms of samples produced during assessment of stirring conditions; ZOPT-2.2/90/10/5 provided for comparison.

Confirmation of the phases present in the ZOPT-ST8 and ZOPT-ST10 has been made *via* analysis of their powder X-ray diffractograms which are provided in Figure 6.2 with ZOPT-2.2/90/10/5 provided for comparison. Considering the primary peak characteristic of type X zeolites (111) a reduction in peak intensity is observed for ZOPT-ST8 compared to the original zeolite sample. The intensity at this Bragg angle for ZOPT-ST10 is more consistent with the original further suggesting that aging conducted by stirring for 8 h at 500 RPM is insufficient for replication of the original synthesis; however, at 10 h stirring the produced zeolite is comparable. When considering type A zeolite phases, both ZOPT-ST8 and ZOPT-ST10 appear to present stronger peak intensities than for the original ZOPT. This suggests a reduced stirring regime actually favours (slightly) the crystallisation of type A. Zeolite A (LTA) is known to crystallise in shorter times than type X (FAU) and if there was a reduction in nucleation rate as a product of the reduced stirring duration, the conditions for ZOPT-8ST were likely unsuitable for the crystallisation of the FAU zeolites present in ZOPT-ST10.

## 6.3. Impact of Degree of Washing

The previous method utilised vacuum filtration to both separate and wash the produced zeolites with a target supernatant pH of 9. Assessment of this property's impact on CO<sub>2</sub> adsorption should be quantified in order to identify if improvements can be made to the synthesis such as reductions in water usage. As such, a single batch produced at the same conditions as ZOPT-2.2/10/90/5 was separated into five individual samples prior to individual, post-synthesis washing. The samples and their final supernatant

pH are provided in Table 6-2. The uptakes are relatively consistent when completing the washing to a pH of between 7 and 10 and are aligned with the original ZOPT. When reducing the washing further to a pH of 11, a significant drop in capacity is observed. Sample ZOPT-PH11 presents a CO<sub>2</sub> adsorption capacity of 1.59 mmol·g<sup>-1</sup>, which is approximately 85% of both the original ZOPT and the other samples which have been washed to a greater degree.

Table 6-2: Washing conditions and uptake of samples produced during synthesis method adjustments. ZOPT provided in row 1 for comparison.

Sample	Supernatant pH	<b>Uptake</b> mmol∙g <sup>-1</sup>
ZOPT-2.2/10/90/5	9	1.84
ZOPT-PH7	7	1.81
ZOPT-PH8	8	1.83
ZOPT-PH9	9	1.80
ZOPT-PH10	10	1.80
ZOPT-PH11	11	1.59

Washing of the solid product after zeolitisation is applied to remove any residual and unreacted hydroxide, which in this case is NaOH. The reduction in capacity observed for ZOPT-PH11 is likely a result of pore blockage due to the presence of non-framework sodium species or other solid phases [359]. Thorough washing is key to ensure the availability of active sites for CO<sub>2</sub> adsorption; however, too intensive a washing may lead to removal of structural cations [360], negatively impacting CO<sub>2</sub> adsorption by reducing the intensity of its interaction with the ion-deficient framework. Based on this investigation, it is clear that a reduction in water usage is possible by reducing the number of washes (aiming for a supernatant pH of 10) without significant implications on the biomass fly ash derived zeolite.

#### 6.3.1. Analysis of Surface Morphology

Given the consistency in CO<sub>2</sub> adsorption capacities of samples washed to a pH of between 7 and 10, it is unlikely that significant differences in their morphology will be present. For ZOPT-PH11 though, the

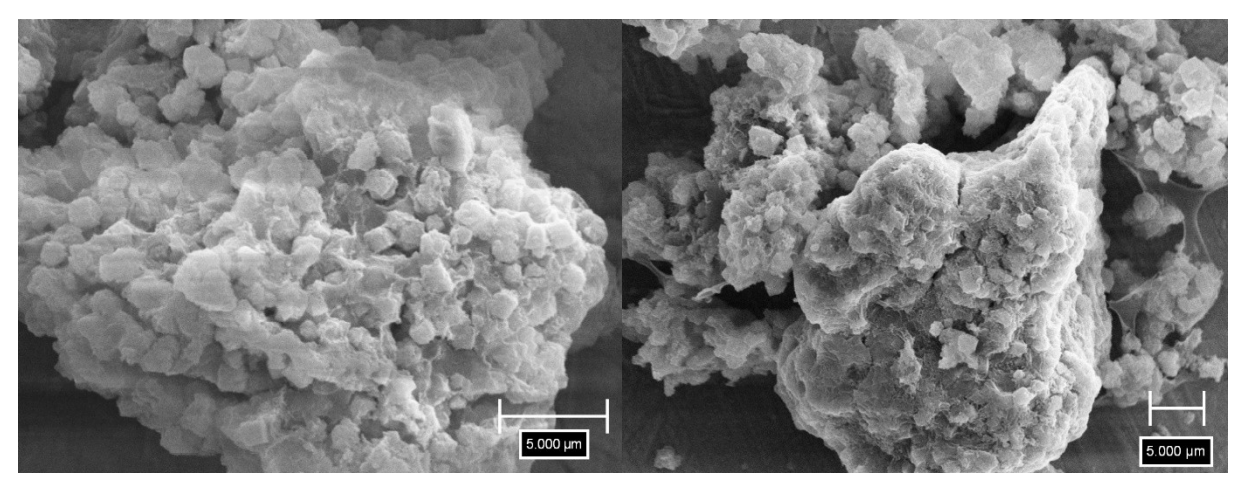


Figure 6.3: Scanning electron images of ZOPT-PH7 (left) and ZOPT-PH11 (right). Accelerating voltage of 10 kV.

reduction in capacity which has been attributed to blockage by residual sodium species, should be indicated by significant non-crystalline phases surrounding the crystalline frameworks. It is however, unlikely that these will look dissimilar to the amorphous component known to exist in ZOPT-2.2/90/10/5. Images of ZOPT-PH7 and ZOPT-PH11 are provided Figure 6.3. The SEM image of ZOPT-PH7 (Figure 6.3 left) exhibits both crystalline and amorphous morphologies in an agglomerated mass. This is also true for ZOPT-PH11 (Figure 6.3 right); however, there appears to be a greater degree of amorphous constituents evidenced by less pronounced crystalline geometries. This is likely a result of their being a greater relative proportion of amorphous components due to the residual and unreacted sodium aluminosilicate species which have not been removed *via* washing.

## 6.3.2. Phase Identification

With respect to crystallography of the samples produced at varying supernatant pH, the crystalline phases should be unchanged and consistent. The presence of an increased amorphous aluminosilicate component however, may reduce the relative intensity of the crystalline diffractograms as these too scatter x-rays, albeit broadly [256,257]. The results of the XRD are provided in Figure 6.4. For all samples washed to a pH of 10 or less, the diffractograms are extremely similar with regards to both peak positions and intensity. When washing to the lowest degree (*i.e.* ZOPT-PH11), the intensity of all peaks is reduced. This infers that this sample is less crystalline; however, given the nature of their preparation, this is a result of there being a greater degree of residual NaOH and other amorphous

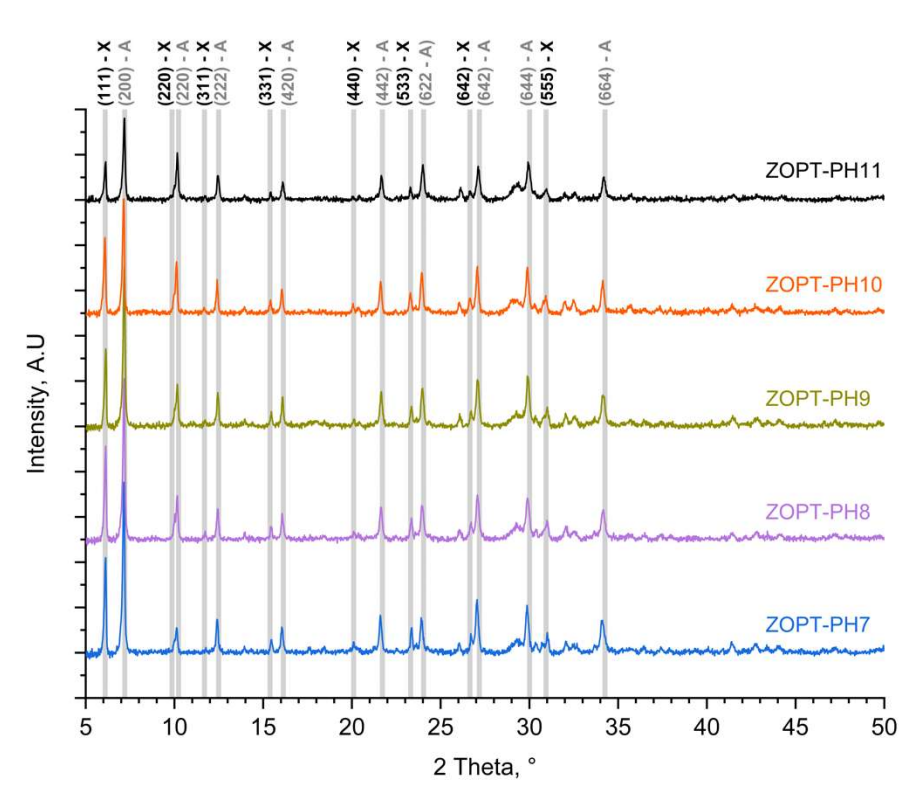


Figure 6.4: Powder x-ray diffractograms of samples produced during assessment of washing degree.

species in the solid product reducing the relative crystalline content. These findings further corroborate the potential to reduce the degree of washing during synthesis without significant change to adsorption performance or crystallinity.

## 6.4. Scale-up Quality

In order to produce sufficient volume of adsorbent to facilitate evaluation of the breakthrough performance and determine mass transfer properties of the fly ash derived zeolites in a fixed-bed column, a larger number of individual batch syntheses is required. Given the variation identified in the fly ash precursor it is highly likely that the subsequent zeolite is also associated with a level of heterogeneity, both in terms of structure and adsorption performance. Consequently, in total, 35 batches were produced during this work, totalling approximately 300 g of fly-ash derived ZOPT-2.2/10/90/5. Assessment of the variation has been achieved by analysis of the individual samples' CO<sub>2</sub> adsorption capacities and X-ray diffractograms Figure 6.5 details the adsorbed amounts measured via TGA at 50 °C and 1 bar pure CO<sub>2</sub> for the individual batches. The yields of the 35 individual batches represent an average of 88.34 %, the standard deviation is 3.69%. The CO<sub>2</sub> adsorption capacities however, exhibit a significant degree of variation between batch 5 and 10. This has been attributed to the presence of carbon in the biomass fly ash precursor which is understood to be associated with significant variability.

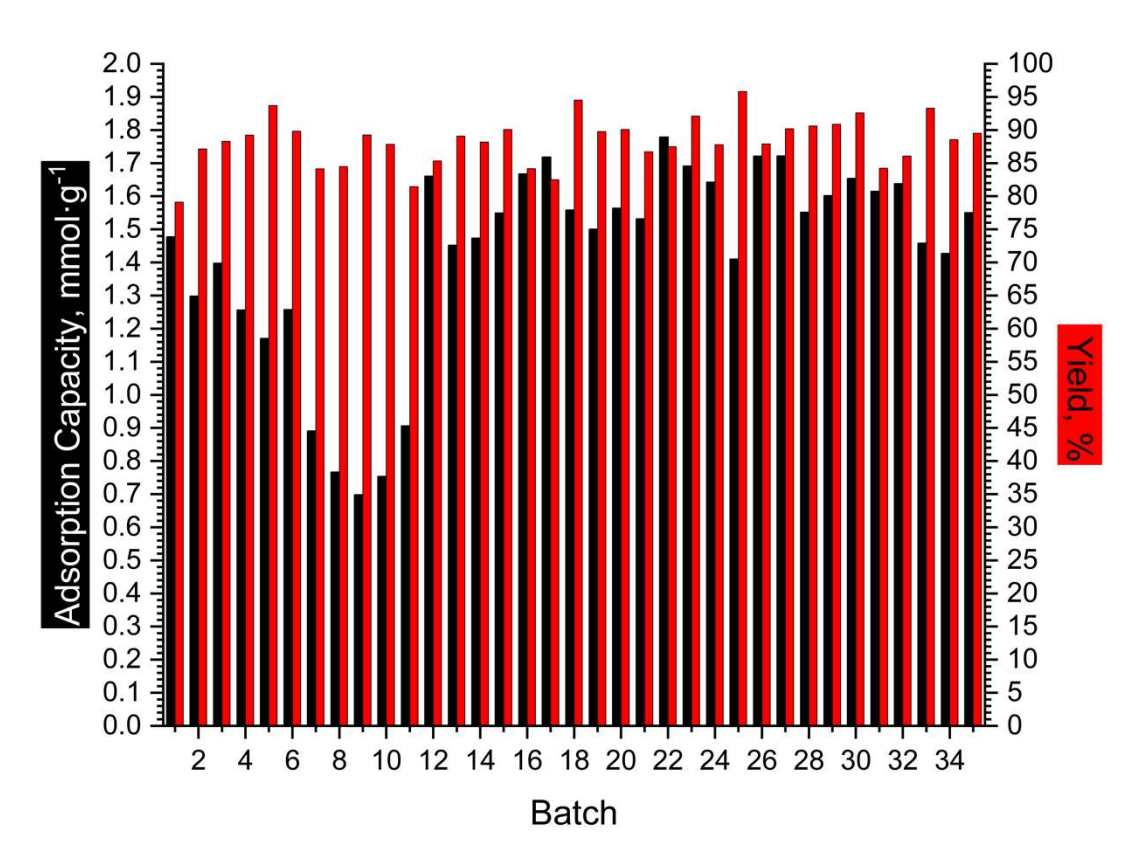


Figure 6.5: Yield and CO<sub>2</sub> adsorption capacity of the replicate ZOPT batches. Capacity estimated via TGA at 50 °C, 1 bar CO<sub>2</sub> after degassing for 1 under N<sub>2</sub>.

The presence of carbon in the hydrothermal mixture can negatively impact the alkaline fusion step through decomposition of the carbonaceous species [361] at the elevated fusion temperatures. Removal of the carbon was facilitated by heating the fly ash to 550 °C in the presence of air for 1 h. Equally this could be achieved through use of an ashing furnace which ensures adequate exchange of the furnace gas volume which is assumed to have been insufficient for batches 5 through 11. Employing the same conditions as those in the alkaline fusion step will minimise the additional energy expenditure for synthesis by combining the carbon removal and alkaline fusion steps.

Table 6-3: Synthesis yields and CO<sub>2</sub> adsorption capacities from the 35 individual batches.

	Mean mmol·g <sup>-1</sup>	Lower 95% CI of Mean	Upper 95% CI of Mean
CO <sub>2</sub> Adsorption Capacity	1.43	1.33	1.53
Predicted Canacity	1.90	1.21	2.59

Given these individual batches constitute subsequent repeats of the optimised synthesis from the Taguchi DoE further analysis of the experimental design can be made such as validation of the predicted uptake. The upper and lower 95% confidence intervals (CI) of the mean adsorption capacity of the 35 batches and the predicted value is provided in Table 6-3. The measured range of  $CO_2$  adsorption capacities at the 95% CI range (1.33 – 1.53) overlaps well with the 95% CI range of the predicted value identified during analysis of the Taguchi DoE (1.21 – 2.59). This suggests the data to be reproducible and well aligned to the analysis of the Taguchi DoE.

## 6.5. Thermal Stability of Fly Ash Zeolites

The intended application of these fly ash derived zeolites does not require significant thermal stability owing to the relatively mild temperature swing of 40 - 150 °C. Industrially however, structuring of zeolites to increase granulometry typically involves high temperature calcination which can induce interactions within the precursor matrix improving the mechanical stability [362] and influence the reactivity and selectivity [340]. It can also remove any residual water including framework water [363,364]. Given the requirement to increase particle size for fixed-bed experiments, an understanding of the thermal stability of the synthesised zeolites is key. As such, the bulk ZOPT adsorbent underwent a series of tests via TGA to investigate the impact of high temperature on the CO<sub>2</sub> capacity during subsequent adsorption cycles. In the absence of framework collapse, the capacity should be relatively repeatable. Commercial zeolites will often maintain their crystalline structures below temperatures of around 800-900 °C after which the framework collapses and the microporosity is lost and hence so too is the adsorption capacity [363,365,366]. The TGA procedure adopted to investigate intermediary high temperature desorption at increasing temperatures on structural stability can be seen in Figure 6.6 along with the experimental results for weight change of the sample. Briefly, the sample was degassed at 150 °C under N<sub>2</sub> flow before cooling to 50 °C where CO<sub>2</sub> was then introduced under isothermal conditions. Thereafter, the sample underwent subsequent desorption and adsorption cycles where the desorption

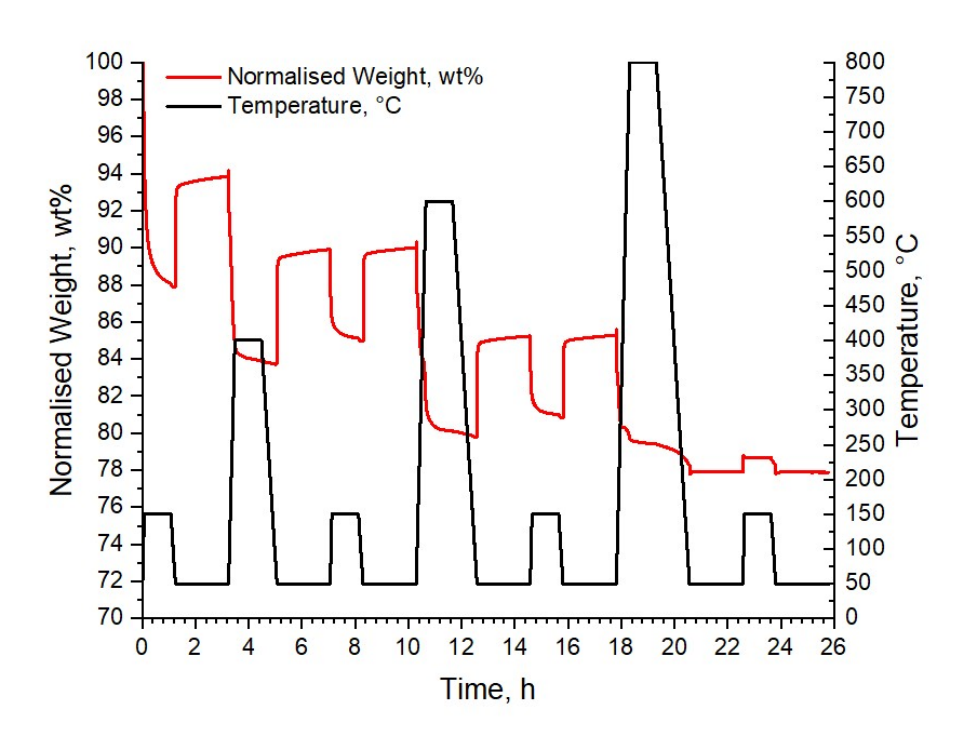


Figure 6.6: Weight change of the bulk ZOPT adsorbent during high temperature desorption and 50 °C adsorption.

temperature was increased to 400 °C to desorb and then cooled once more to 50 °C for adsorption. An additional desorption at 150 °C and adsorption at 50 °C cycle was evaluated before increasing the high temperature desorption again by 200 °C. This was repeated until a desorption temperature of 800 °C. The adsorption capacities calculated from the weight change are provided in Table 6-4 for the individual cycles. The adsorption capacity after high temperature desorption (below 800 °C) increase by 8.89 % and 0.42 % for 400 °C and 600 °C, respectively. This suggests that the higher temperatures are able to increase the availability of adsorption sites through an improved degree of desorption. Interestingly, the capacity after the subsequent 150 °C desorption is between 12 and 18 % lower than the initial cycle. This suggests that 150 °C may be insufficient to effectively remove all adsorbed gases or that the adsorbent has changed structurally such as through loss of framework water. Loss of framework water can damage the structure of zeolites due to the rapid expansion of vapour, i.e. self-steaming if the heating rate is too large [200]. The loss of this water can be seen at approximately 450 °C which is in agreement with the literature for FA-derived zeolites [339,367]. After increasing the temperature to 800 °C, a similar weight loss is observed to that during the 600 °C desorption; however, the subsequent adsorption step indicated zero adsorbed CO<sub>2</sub> suggesting a complete collapse of microporosity and therefore, the crystalline framework. This is slightly lower than for commercial zeolites; however, the presence of amorphous constituents and additional cations (e.g. Ca) instead of Na may have a pore filling effect [363]. Thermal stability of zeolites is often reported to be dependent on Si/Al ratio [368] and any dissimilarities in this ratio between FA-derived and commercial zeolites will result in modification to the zeolites' thermal stability. The results show that biomass combustion fly ash zeolites retain their adsorption capacity up to  $600\,^{\circ}$ C which increases the potential applications of this valorised waste.

Table 6-4: Adsorption capacities estimated via TGA after high temperature desorption. Adsorption at 50 °C, 100 mol%CO2 at 1 atm for 2 h.

Cycle	Desorption Temperature °C	Uptake mmol·g <sup>-1</sup>	Change from Initial %
1 (initial)	150	1.53	N/A
2	400	1.67	8.89
3	150	1.35	-12.28
4	600	1.54	0.42
5	150	1.25	-18.40
6	800	0	-100
7	150	0	-100

#### 6.6. Powder Extrusion with Kaolin Binder

Application of biomass fly ash derived zeolites in CO<sub>2</sub> separation requires material compatible with large scale processes. These processes traditionally employ fixed bed configurations although fluidised beds are becoming more commonplace. That said, investigation of the derived zeolites suitability for pelletisation is required to determine the potential improvements to mechanical stability by increasing granulometry. This also facilitates identification of performance implications and will reveal the potential for optimisation of binder ratios in the context of equilibrium CO2 adsorption capacity and mechanical crush strength. The extrusion process was conducted by first grinding and sieving the bulk ZOPT sorbent to ensure a consistent particle size of narrow distribution (< 70 μm). The fine powder was then mixed with varying amounts of kaolin binder as per the ratios defined in Table 6-5 before water was added until the mixture was "workable". Thereafter, the wet mixture was extruded manually through a syringe with a 1.5 mm die aperture. Two different thermal post-treatments were investigated to identify if any phase-change or interaction occurs with the kaolin binder and ZOPT adsorbent under calcination conditions. The two adopted procedures were a simple drying at 150 °C (using a 1°C·min<sup>-1</sup> ramp rate from ambient) for 1 h and a drying and calcination procedure. With the dried and calcined samples, drying remained unchanged and the subsequent calcination took place at 550 °C in a muffle furnace (5 °C·min<sup>-1</sup> ramp rate from ambient) for 1 h.

#### 6.6.1. Compressive Strength Testing

The compressive strength of the pellets produced in this work has been estimated *via* ASTM D6175 with a load rate of 4 N·s<sup>-1</sup> after conditioning of the materials at 150 °C for 12 h to remove free-water. To determine the pellet population's crush strength, a suitable sample size is required, in this case 30

samples were evaluated for each binder ratio and drying condition. The results are provided in Table 6-5.

Table 6-5: Samples produced during the pelletisation campaign investigating kaolin as binder for pellet extrusion and their associated radial crush strengths,  $N \cdot mm^{-1}$ .

Sample	Kao lin wt	Thermal Treatment °C	Mean Crush Strength N·mm <sup>-1</sup>	Crush Strength Std Dev N·mm <sup>-1</sup>	Relative Change % Strength
	%				
ZOPT-0K-D	0	150	1.08	0.35	N/A
ZOPT-15K-D	15	150	1.85	0.59	71.63
ZOPT-30K-D	30	150	1.67	0.38	54.81
ZOPT-45K-D	45	150	1.31	0.37	21.10
ZOPT-0K-C	0	150 & 550	1.22	0.58	N/A
ZOPT-15K-C	15	150 & 550	1.95	1.21	59.22
ZOPT-30K-C	30	150 & 550	2.47	1.02	101.37
ZOPT-45K-C	45	150 & 550	2.82	0.74	129.97

The compressive strength of the dried pellets does not increase monotonically with the increase in binder content. At binder ratios above 15 wt% the contribution of the kaolin binder negatively impacts the extrudate's mechanical stability. This can be attributed to an increase in the secondary pore dimension and a heterogeneous distribution of the binder [339,369]. At high concentrations, the kaolin binder's plate-like morphology may introduce areas within the matrix where force can concentrate, increasing the likelihood of mechanical failure. At ratios below 15 wt% the two morphologies may act to improve the mechanical stability by stopping lattice faults from propagating. The estimated compressive strength for the calcined pellet however, does increase monotonically with the addition of binder. The increase in crush strength can be attributed to the calcination step which facilitates dehydroxylation of the kaolin phase to metakaolin [282,370]. Metakaolin forms when kaolin is heated in air at around 550 °C [371], the amorphicity presented by the metakaolin increases the crush strength of the pellet by minimising the potential for fault propagation within the matrix. The crush strength's standard deviation is highest for samples ZOPT-15K-C and ZOPT-30K-C, suggesting a degree of variation in the prepared extrudates. This and the variation exhibited by the other samples can be attributed to irregularities in the extruded pellets which distribute the load non-uniformly [217,372]. Any heterogeneity in the extrudates will lead to deviation between an individual pellet's crush strength due to matrix defects, the distribution and orientation of bonds and pore size distribution [373]. Additionally, the extrusion method introduces additional inconsistencies due to the non-constant syringe pressure owing to the manual nature of the process. ZOPT-0K-D presents a crush strength of approximately 1.1 N·mm<sup>-1</sup> (0.46 MPa) which is significantly lower than for industrial catalysts/adsorbents but aligned with those produced experimentally in the published literature (0.22 – 0.54 MPa) [86,374–376].

#### 6.6.2. Pellet Adsorption Capacity

All samples have been evaluated for their equilibrium CO<sub>2</sub> adsorption capacity *via* TGA at 50 °C, 1 bar(a) pure CO<sub>2</sub> after an initial degassing at 150 °C, 1 bar(a) N<sub>2</sub> for 1 h. These adsorption tests were conducted in triplicate with the mean and standard deviation provided in Table 6-6. The adsorption capacities decrease close to linearly with the increase in binder addition due to the inert (in the context of CO<sub>2</sub> adsorption) nature of the kaolin binder. This is true for both the dried and dried/calcined samples. Interestingly, the capacity of the calcined samples is actually lower for all binder ratios than the samples produced with a simple drying. The reduction in capacity for the calcined samples can be attributed to potential pore blockage after the phase transformation of kaolin to metakaolin which would limit accessibility to the active sites [339,377,378]. The pure kaolin binder has been shown to exhibit a negligible CO<sub>2</sub> adsorption capacity (0.06 mmol·g<sup>-1</sup>) when compared with the 1.51 demonstrated by the ZOPT-bulk powder. The consistency in uptake between the pellets without binder and the bulk-powder suggest there is negligible impact on the average CO<sub>2</sub> uptake when forming 1.5 mm pellets *via* syringe extrusion.

Table 6-6: Samples produced during the pelletisation campaign investigating kaolin as binder for pellet extrusion and their associated equilibrium CO<sub>2</sub> adsorption capacities estimated via TGA at 50 °C, 1 bar(a).

Sample	Kaolin wt%	Thermal Treatment °C	Mean CO <sub>2</sub> Uptake 50°C 1 bar(a)	CO2 Uptake Standard Deviation
ZOPT-0K-D	0	150	1.53	0.03
ZOPT-15K-D	15	150	1.26	0.08
ZOPT-30K-D	30	150	1.08	0.07
ZOPT-45K-D	45	150	0.91	0.03
ZOPT-0K-C	0	150 & 550	1.28	0.04
ZOPT-15K-C	15	150 & 550	1.12	0.02
ZOPT-30K-C	30	150 & 550	0.91	0.02
ZOPT-45K-C	45	150 & 550	0.78	0.01
Kaolin	100	N/A – Powder	0.06	0.002
ZOPT-bulk	0	150	1.51	0.02
(powder)				

#### **6.6.3.** Pellet Adsorption Kinetics

The kinetics of CO<sub>2</sub> adsorption for each of the produced pellets have been investigated by fitting the uptake data estimated *via* TGA at 50 °C and 1 bar(a) CO<sub>2</sub>. The kinetic data has been fitted with the PFO, PSO, Elovich and W&M Intraparticle Diffusion kinetic models with the quality of fit determined *via* adjusted R<sup>2</sup> and RMSE values provided in Table 6-7. The Elovich kinetic model can be seen as the best fit with adj-R<sup>2</sup> values above 0.97 for all datasets. The experimental data and the fitted Elovich kinetic model are given in Figure 6.7 with the estimated model constants in Table 6-7. Visually the fitted model appears to describe the adsorption kinetics well. Previously, the Elovich model failed to capture the three distinct regions of the CO<sub>2</sub> adsorption kinetics for ZOPT-2.2/10/90/5. The decrease in

equilibrium capacity with increasing kaolin content can also be seen although the step change between the 30 and 45 wt% samples is less significant than for the 0 and 15 wt% samples.

Table 6-7: Results of the biomass combustion fly ash zeolite pellets kinetic modelling. Experimental data produced via TGA under at 50 °C, 1 bar CO2.

Sample	Pseudo-first Order		Pseudo-second Order		Elovich		W&M Intraparticle Diffusion	
	Adj-R <sup>2</sup>	RMSE	Adj-R <sup>2</sup>	RMSE	Adj-R <sup>2</sup>	RMSE	Adj-R <sup>2</sup>	RMSE
ZOPT-0K-D	0.5518	0.1223	0.8242	0.0766	0.9866	0.0212	0.8759	0.0643
ZOPT-15K-D	0.4303	0.1132	0.7376	0.0768	0.9706	0.0257	0.9186	0.0428
ZOPT-30K-D	0.5247	0.0876	0.8069	0.0558	0.9862	0.0149	0.8897	0.0422
ZOPT-45K-D	0.5241	0.0742	0.8050	0.0475	0.9864	0.0126	0.8958	0.0347
ZOPT-0K-C	0.6706	0.0860	0.8991	0.0476	0.9811	0.0206	0.8001	0.0670
ZOPT-15K-C	0.5325	0.0928	0.8072	0.0596	0.9857	0.0162	0.9046	0.0419
ZOPT-30K-C	0.4667	0.0797	0.7637	0.0531	0.9761	0.0169	0.9173	0.0314
ZOPT-45K-C	0.4535	0.0669	0.7568	0.0446	0.9764	0.0139	0.9143	0.0265
<b>ZOPT-bulk</b>	0.4740	0.1297	0.7701	0.0857	0.9769	0.0272	0.9121	0.0530
Powder								

The model constants estimated via non-linear regression also exhibit trends with the increasing kaolin content. The initial adsorption rate constant,  $\alpha$ , decreases with an increase in kaolin content for the dried samples but less so for the calcined samples; the value reaches a relatively stable 2.4 mmol·g<sup>-1</sup>·min<sup>-1</sup> for kaolin contents between 15 and 45 wt%. The desorption constant,  $\beta$ , is seen to decrease more consistently with the increasing kaolin content for both dried and calcined extrudates. The calcined pellets exhibit slightly higher desorption constants for all binder ratios due to the lower equilibrium capacity. The desorption constant, although without physical meaning, can be associated with a lack of available active sites which is attributed to the increase in relative proportion of inert kaolin binder.

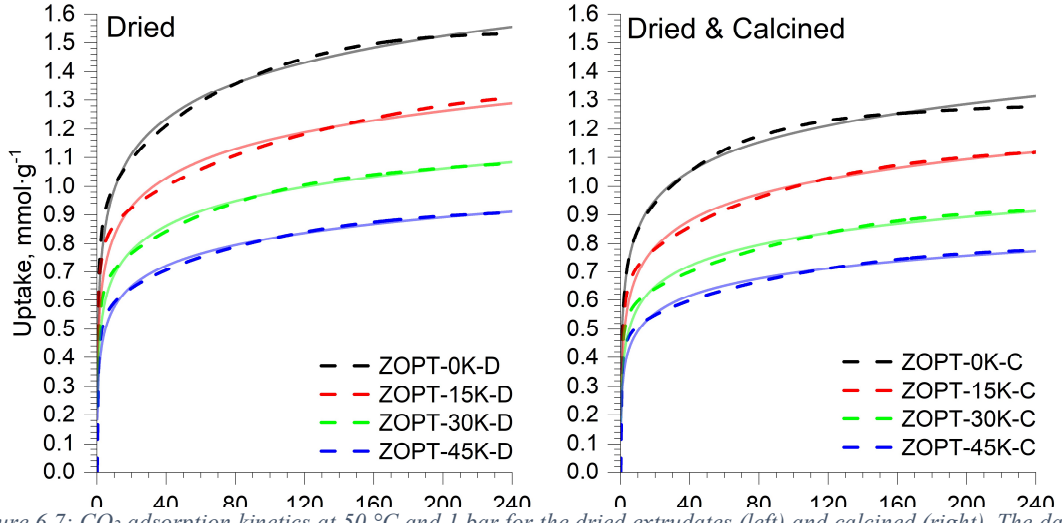


Figure 6.7: CO<sub>2</sub> adsorption kinetics at 50 °C and 1 bar for the dried extrudates (left) and calcined (right). The dashed line represents the experimental data and the solid line the fitted Elovich kinetic model.

Table 6-8: Elovich kinetic model constants estimated via non-linear regression.

Sample	$oldsymbol{lpha}$ mmol $\cdot$ g $^{-1}\cdot$ min $^{-1}$	β g·mmol <sup>-1</sup>
ZOPT-0K-D	4.47	5.59
ZOPT-15K-D	4.30	6.88
ZOPT-30K-D	3.17	8.04
ZOPT-45K-D	2.49	9.50
ZOPT-0K-C	4.93	6.86
ZOPT-15K-C	2.46	7.51
ZOPT-30K-C	2.33	9.40
ZOPT-45K-C	2.38	11.35
ZOPT-bulk Powder	3.78	5.74

# 6.6.4. Surface Morphology

The surface morphology of the produced extrudates has also been revealed *via* SEM (IT200). The samples produced at binder ratios of 0 and 45 wt% kaolin for both thermal post-treatments are provided in Figure 6.8 and Figure 6.9, respectively. The extrudates produced without the addition of kaolin binder (Figure 6.8) exhibit morphologies consistent with their powdered analogues which is to be expected. The differences between the dried (ZOPT-0K-D) and calcined (ZOPT-0K-C) samples are not distinct which suggests the high temperature (550 °C) treatment does not induce significant morphological changes of the bulk ZOPT adsorbent. As such the decrease in CO<sub>2</sub> adsorption capacity is likely due to slight modifications to the zeolite framework owing to the loss of framework water [379]. In both samples, a relatively broad size distribution is observed for both the crystalline constituents (LTA and FAU zeolites) and amorphous aluminosilicates. No unexpected morphologies have been observed as were in the stirring condition assessment. There is also an improved segregation of the amorphous and crystalline components when compared with the samples produced during the washing degree investigation. This is likely a result of the extrusion procedure which involved a significant degree of mixing. Figure 6.9 presents both ZOPT-45K-D (left) and ZOPT-45K-C (right). The morphologies are distinctly dissimilar to each other and those in Figure 6.8 with very limited evidence of crystalline

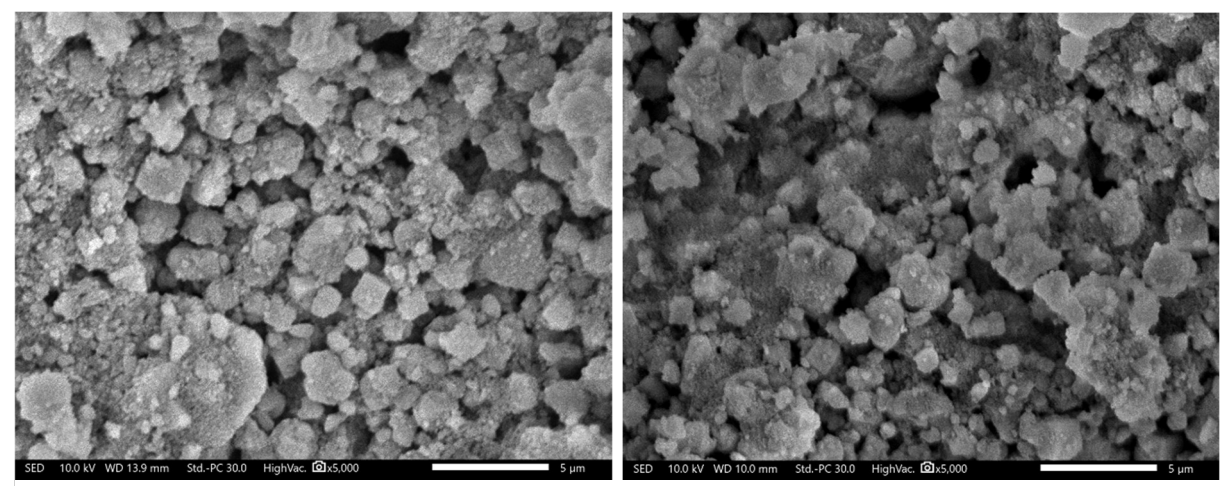


Figure 6.8: Scanning electron microscope images of ZOPT-0K-D (left) and ZOPT-0K-C (right).

morphologies. For the dried samples, the presence of kaolin binder is clear due to the plate-like and sharp morphology of the mixture. Due to this, a large number of voids and cracks can be seen which could decrease the adsorbent's mechanical stability during crush strength testing. For the calcined sample, the angular morphology is absent and has been replaced by a more continuous surface. This is due to the conversion of crystalline kaolin to amorphous metakaolin upon high temperature treatments. The amorphous nature of this additive will improve the mechanical stability of the extrudate which has been experimentally confirmed in section 6.6.1. That said, some porosity is observed; however, this presents more rounded morphology which will not concentrate internal stresses to the same degree as those seen in ZOPT-45K-0D. Given these findings, it is to be expected that the pellet mixed with 45 wt% kaolin and treated thermally at 550 °C would have the highest crush strength as per ASTM D6175.

#### 6.6.5. Elemental Composition – EDS

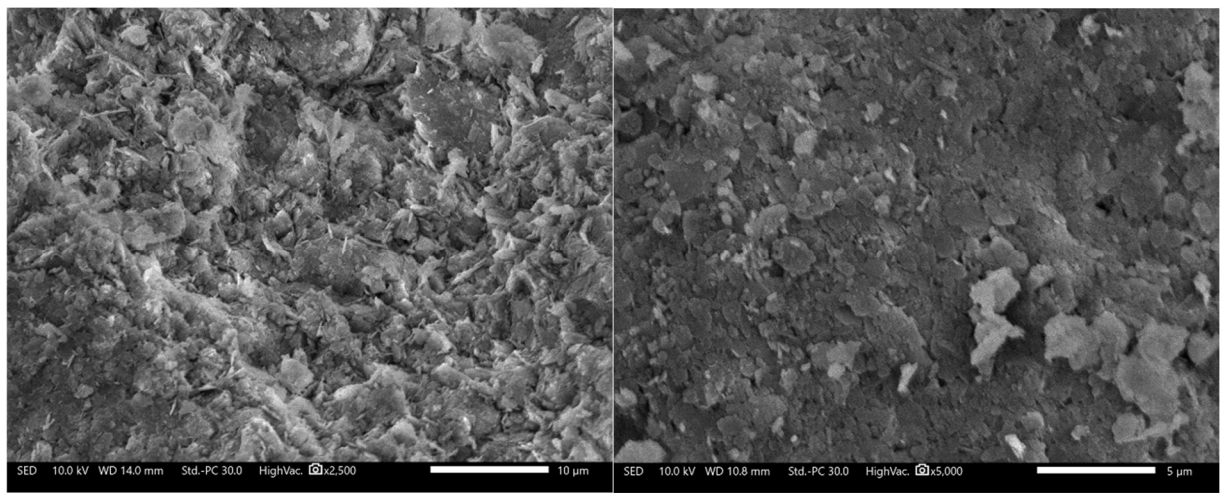


Figure 6.9: Scanning electron microscope images of ZOPT-45K-D (left) and ZOPT-45K-C (right).

The elemental composition of the produced extrudates has been estimated via EDS, the results of which are provided in Table 6-9 with both the mean value ( $\bar{x}$ ) and standard deviations (S) computed after analysis of 10 individual sites for each sample. Although semi-quantitative, this analysis allows for comparative assessment of the elemental composition of the pelletised samples produced with 0 and 45 wt% kaolin additions under the two thermal post-treatments. The addition of kaolin binder increases the relative composition of both Si and Al which appears to be independent of the thermal treatments. The phase change of kaolin to metakaolin produces water due to the loss of hydroxyl groups, a slight reduction in O content is observed in ZOPT-45K-C vs ZOPT-45K-D which further suggests phase transformation. The limitations of EDS limit confidence in this; however, XRD will confirm the presence of kaolin in the samples. These limitations can explain why calcium content drops from approximately 17 wt% for ZOPT-0K samples to 3 wt% for the ZOPT-45K samples; EDS being a surface level analyses will not quantify the pellets internal or bulk composition, rather the external surface. Visually, both ZOPT-45K-D and ZOPT-45K-C present primarily the binder's morphology and

so any calcium present in the ZOPT precursor is underestimated as kaolin/metakaolin is an aluminosilicate. The Si/Al weight ratios are also provided Table 6-9. The estimated Si/Al ratio for ZOPT-0K-D and ZOPT-0K-C are 1.88 and 1.95, respectively. For ZOPT-45K-D and ZOPT-45K-C, they are 1.10 and 1.16, respectively. The reduction in these ratios after adding 45 wt% binder is due to the chemical composition of the kaolin binder (Al<sub>2</sub>Si<sub>2</sub>O<sub>5</sub>(OH)<sub>4</sub>). Its prevalence in the pellets morphology likely underestimates the Si content of the ZOPT precursor, hence reducing the Si/Al ratio.

Table 6-9: Elemental composition of pelletised fly ash zeolites, estimated via EDS.

Element	ZOPT-0K-D wt%			ZOPT-0K-C wt%		ZOPT-45K-D wt%		ZOPT-45K-C wt%	
	x	S	x	S	x	S	x	S	
Na	3.5	2.5	2.8	1.0	2.9	2.2	3.6	0.9	
Mg	1.3	1.0	0.9	0.5	0.4	0.1	0.7	1.0	
Al	7.6	3.5	7.1	3.1	20.0	1.3	19.6	2.4	
Si	14.2	5.9	13.9	5.5	22.0	1.7	22.8	1.1	
P	0.1	0.1	0.1	0.1	0.1	0.1	0.1	0.1	
K	1.1	0.4	1.2	0.3	0.3	0.1	0.3	0.1	
Ca	16.7	7.6	17.7	5.3	3.2	1.5	2.5	1.9	
Ti	0.2	0.4	1.4	0.4	0.6	0.4	0.6	0.2	
Mn	0.9	1.0	2.3	1.4	0.1	0.2	0.2	0.2	
Fe	11.2	7.9	15.4	8.0	1.1	0.5	2.2	1.3	
0	43.2	17.2	37.9	5.7	49.1	2.3	47.4	1.3	
Avg. wt. Si/Al	1.	88	1.	95	1.	10	1.	16	

#### 6.6.6. Phase Identification

Given the nature of the two thermal post-treatments and the anticipated phase change during calcination at 550 °C, identification of crystalline phases *via* XRD has been completed for both the dried, and the dried and calcined extrudates (Figure 6.10). The dried pellets present diffractograms which appear as a superimposition of the individual precursors, kaolin and ZOPT. The peak intensity for those characteristics of kaolin becoming stronger as the relative concentration of kaolin increases from 15 to 45 wt%. This is also associated with a decrease in the peak intensity of ZOPT due to the decrease in its relative concentration. When considering the dried and calcined pellets, the addition of kaolin and subsequent high temperature calcination has induced certain interactions between the precursor matrix [340]. Additionally, kaolin is a crystalline phase and undergoes a series of de-hydroxylation reactions at elevated temperatures, resulting in disordered metakaolin [282,370]. This phase transformation typically improves the mechanical stability confirmed by the compressive strength testing and postulated in the morphological analysis. In the diffractograms for the calcined pellets, all characteristic peaks of kaolin are absent suggesting no kaolin remains in the pellets. The kaolin precursor has therefore, undergone dehydroxylation to form metakaolin which exhibits no distinct diffractogram. Although de-hydroxylation of kaolin typically occurs above 700 °C, kaolin phase transformation has

been reported at lower temperatures such as 550 °C with subsequent transformation to mullite at approximately 1050 °C [371].

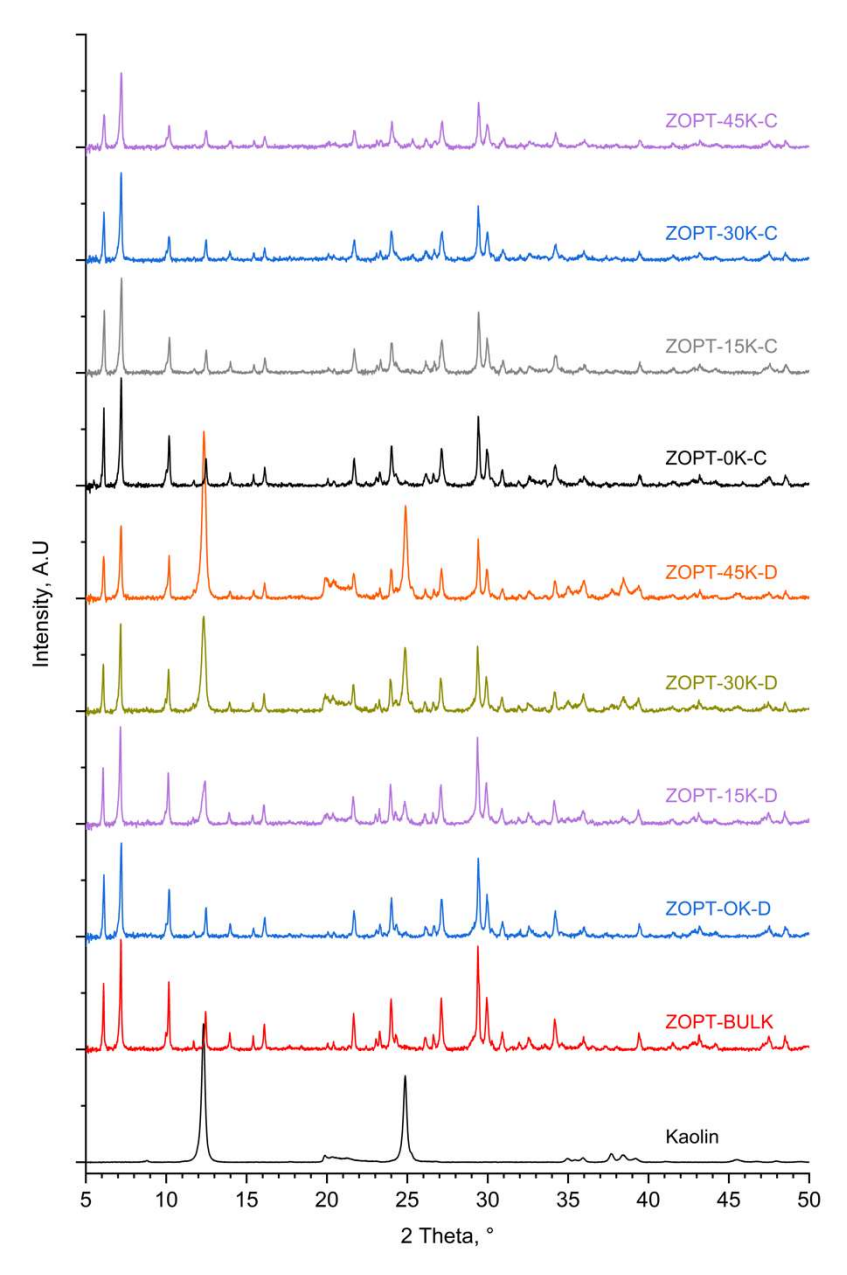


Figure 6.10: Powder x-ray diffractograms of the extruded biomass ash derived fly ash zeolite adsorbents; diffractograms of the bulk ZOPT sample and 100 wt% kaolin provided for comparison.

#### 6.7. Conclusion

In order to facilitate evaluation of the breakthrough performance of biomass combustion fly ash derived zeolites, 35 replicates at the optimum synthesis conditions have been carried out after an investigation into potential for method intensification. Slight modification was made to the synthesis procedure in order to minimise synthesis duration and water consumption. This was informed by an evaluation of the impact on both CO<sub>2</sub> adsorption capacity and zeolite quality. It was found that a reduction in washing

degree is realisable if targeting a supernatant pH of 10 without degradation of performance. Similarly, a reduction in the stirring step from 16 to 10 h was also realised. The bulk sorbent, a mixture of the 35 replicates then underwent a series of pelletisation experiments via extrusion to determine the optimum kaolin binder ratio which facilitates sufficient mechanical stability and maintained CO<sub>2</sub> capture performance. The results revealed that an addition of 45 wt% kaolin and subsequent calcination at 550 C produces a pellet with a crush strength exceeding 2.7 N·mm<sup>-1</sup>. This however was associated with a significant decrease in equilibrium uptake and adsorption kinetics, based on the kinetic modelling. Binderless zeolites prepared without calcination presented a crush strength above 1 N·mm<sup>-1</sup> whilst maintaining the powders adsorption capacity and kinetics. Thereafter the produced pellets were characterised via XRD and SEM for phase identification and analysis of surface morphology, respectively.

The ability to extrude biomass fly ash derived zeolites without the requirement to introduce CO<sub>2</sub> inert binder, is of significant importance as there is no net reduction in adsorption performance. The ability of the powder precursor to form pellets with sufficient strength has been attributed to the presence of mixed zeolite phases with broad size distribution and an amorphous constituent which acts as an inherent binding material after extrusion much in the same manner that the kaolin binder does. Implementation of binderless fly ash zeolite pellets in adsorption processes would mitigate potential reductions to performance often experienced when tailoring adsorbent particles towards specific mechanical requirements.

# 7. Lab-scale Fixed-bed Adsorption of CO<sub>2</sub> by Biomass Combustion Fly Ash Derived Zeolites

#### 7.1. Introduction

Development of zeolitic adsorbents from industrially produced biomass combustion fly ashes requires assessment of their performance in process configurations representative of those in which they would be deployed. In this work, a lab-scale fixed bed TSA system has been designed, built and tested to facilitate both the analysis and optimisation of process conditions representative of post-combustion  $CO_2$  capture. This is crucial for evaluating the efficacy of the proposed fly ash valorisation pathway and will provide insight into the key performance indicators characteristic of adsorption process such as bed capacity and breakthrough time. This information facilitates subsequent design of larger-scale systems as well as validation of adsorption process modelling.

This chapter presents a detailed investigation into the breakthrough performance of these zeolites under simulated biomass combustion flue gases using a lab-scale fixed bed reactor. The granulometry of the fly ash derived zeolites has been increase based on the work in the previous chapter. Due to the diameter of the fixed bed column, a particle size of around 1 mm is required, as such, the wet granulation technique has been employed to formulate binderless zeolite granules. The CO<sub>2</sub> adsorption equilibria and kinetics have been revealed *via* both volumetric and gravimetric adsorption techniques supported by modelling of the phenomenon to facilitate comparison between the original ZOPT adsorbent, the derivative bulk ZOPT and the granulated bulk ZOPT and ultimately provide the foundational data required for scale-up of this process technology. Through systematic variation of the adsorption process operating parameters by Taguchi DoE, this work has identified conditions which facilitate an improved adsorption efficiency defined by the bed's usable adsorption capacity. This offers insight into the dynamic behaviour of the adsorption process informing the design and scaling of an industrial scale post-combustion carbon capture system.

The data produced during these breakthrough investigations can facilitate an informed process design for a large-scale post-combustion CO<sub>2</sub> capture plant. The use of empirical techniques in the design of adsorption processes is often the quickest pathway as there is no requirement for identifying solutions to the array of governing heat and mass balances [58]. That said empirical routes are often plagued by inaccuracy and error; implementation of empirical methods within the framework of statistical Design of Experiments can further improve the time and cost efficiency for development of biomass fly ashderived zeolite adsorbents for post-combustion CO<sub>2</sub> capture.

#### 7.2. Binderless Wet Granulation

Confirmation of potential improvements to mechanical stability has been achieved through investigation of the impact of kaolin binder addition during extrusion. Although commercially viable, the lower limit for typical extrudate diameter is on the order of multiple millimetres [61,380]. The fixed-

bed reactor designed and built during this research has an internal diameter of approximately 40 mm (with the mesh adsorbent cartridge) and a maximum bed length of 250 mm. Particles with typical extrudate diameters of 3-5 mm would be outside of the conventional particle size to column ratio which minimises potential for wall channelling,  $d_c/d_p < 30$ , where  $d_c$  is the column diameter and  $d_p$  the particle diameter [381]. Considering the column diameter, the largest compatible particle size would be approximately 1.3mm. Additionally, it is desirable that the bed length be > 100 times the adsorbent particle diameter [381]. Formation of adsorbents with a diameter of around 1 mm to minimise potential for channelling and flow maldistribution typically requires granulation technologies. Wet granulation is an industrially employed process and has been used to increase the particle size of fly ash derived zeolites without the addition of kaolin due to the tolerable mechanical stability of the previous extrusion testing. The procedure involved wet massing the dried and sieved (70 µm) bulk ZOPT sorbent until the solids could be compressed by hand and retain their shape. This equated to a water addition approximately 50% of the adsorbent mass. Thereafter the wet mass was passed through a sieve granulator (Erweka FGS wet granulator coupled to Erweka AR 403 drive unit) with a mesh size of 1.4 mm. The granules were then dried in an oven at 110 °C overnight before loading into the fixed-bed reactor.

# 7.3. Surface Morphology – Comparison

Without the addition of kaolin binder and the relatively mild mechanical processing which is associated with wet granulation, the surface morphology of the powder and granules should have remained relatively unchanged. The bulk ZOPT powder can be seen in the left side Figure 7.1 at two magnifications, the granulated ZOPT adsorbent is provided in the right of Figure 7.1. As expected, limited morphological differences are seen between the two however the individual particles do appear to be more densely packed in the granulated form. This is apparent at both magnifications (top and bottom) suggesting that the wet granulation process has successfully bound ZOPT-BULK together through compaction [323,382]. At the higher magnification, the individual crystals are more dispersed within the sample suggesting the granulation technique has blended the crystalline and amorphous components to a higher degree than which exists in the ZOPT powder. This can explain the tolerable mechanical stability of the binderless FA-zeolites. The presence of large voids between the individual crystal structures provides a level of hierarchical porosity [383] which should promote the intercrystalline transport of CO<sub>2</sub> during the adsorption process [384] That said however, the irregular and rough surface may increase the thickness of the boundary layer at low flow rates reducing the rate of film diffusion from the bulk gas phase [334,385].

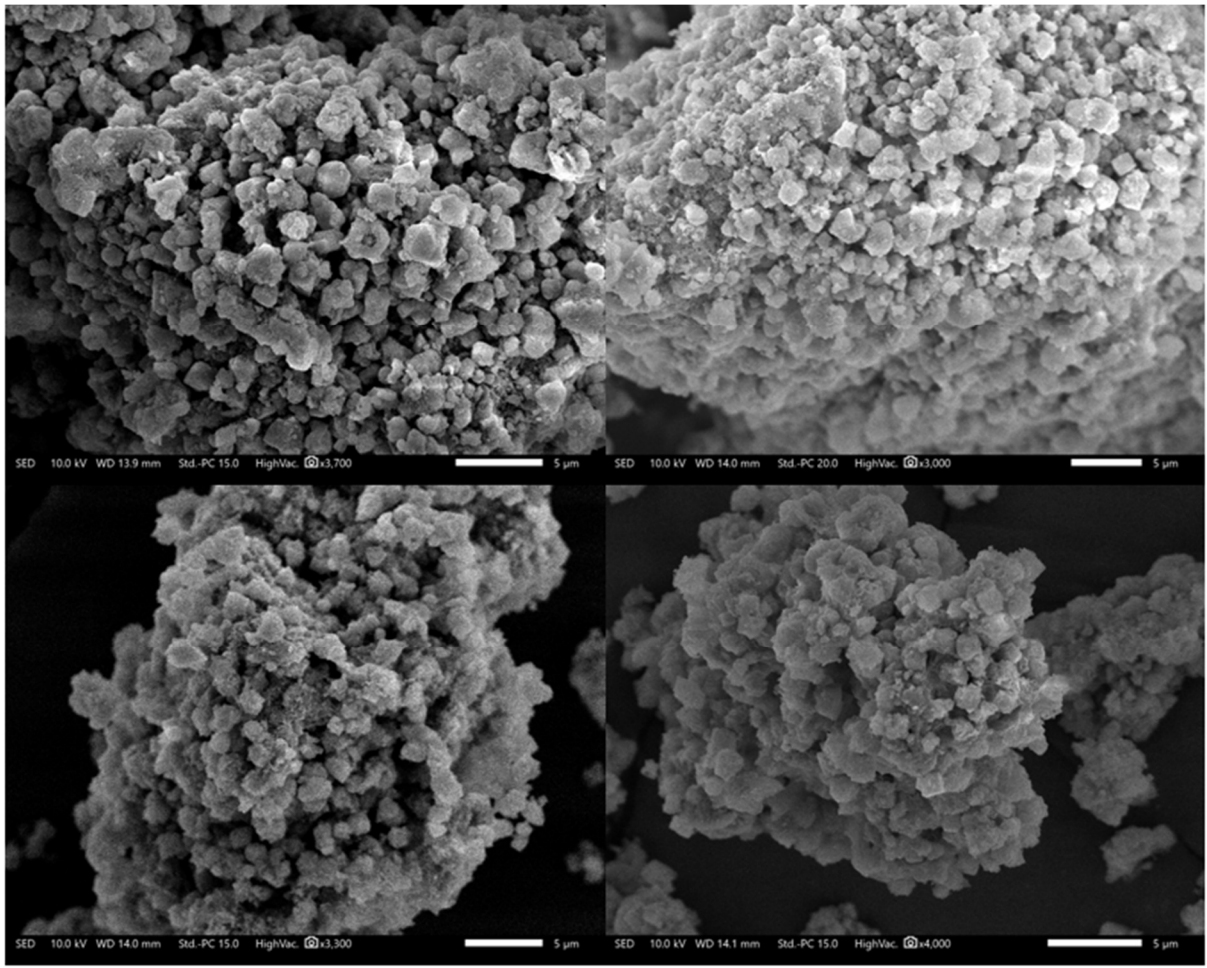


Figure 7.1: Scanning electron microscope images of the bulk ZOPT powder (left) and the bulk ZOPT granule (right).

#### 7.4. Elemental Composition via Energy Dispersive X-ray Spectroscopy - Comparison

The elemental composition of the bulk adsorbent (ZOPT-BULK) has been estimated *via* EDS, the results of which are provided in Table 7-1 along with the results for ZOPT-OG to facilitate comparison. The two samples differ primarily in the percentage weight of Na, Mg and Ca although the first two are relatively small components of the sample and are present with a significant degree of variation. The Ca content of the two samples differs by approximately 4 wt%, again both samples have a large degree of variation. This difference suggests that less Ca is present in the crystalline frameworks of ZOPT-BULK vs ZOPT-OG; the increased content of Na in ZOPT-BULK is present by way of compensation of the reduced Ca present in the crystalline frameworks are charge compensating cations. The Si content of ZOPT-OG presents a greater degree of variation (S = 4.9 wt%) compared with ZOPT-BULK (S = 1.5 wt%) which can be attributed to a larger proportion of LTA in ZOPT-BULK than ZOPT-OG as evidenced by the reduced intensities of the FAU-type XRD peaks. Type A and type X zeolites typically present dissimilar Si/Al ratios so a reduction in the relative proportion of one phase will reduce the bulk sample's Si/Al ratio variation as type X often form with higher Si/Al ratios than LTA [149]. The average Si/Al ratio for both is relatively consistent at between 1.66 for ZOPT-BULK and 1.71 for ZOPT-OG. Interestingly, the Si/Al ratio of ZOPT-BULK (1.66) is extremely close to the parent fly ash (1.67).

Table 7-1: Elemental analysis estimated via EDS for the original ZOPT sample and the bulk-ZOPT adsorbent.

	ZOPT wt		ZOPT-BULK wt%			
Element	- X	S	$\bar{\mathbf{x}}$	S		
Na	3.9	0.7	7.5	1.9		
Mg	1.4	0.8	2.4	1.7		
Al	11.3	2.1	11.7	3.1		
Si	19.3	4.9	19.4	1.5		
P	0.0	0.2	0.1	0.4		
K	0.6	0.3	0.8	0.4		
Ca	14.6	3.8	10.2	4.5		
Ti	0.0	0.0	0.5	0.5		
Fe	3.9	0.9	4.7	2.6		
0	44.9	7.9	43.2	2.3		
Avg. wt. Si/Al	1.7	<u>'1</u>	1.6	66		

#### 7.5. Apparent BET Surface Area – Comparison

As an additional quality metric, the apparent BET surface area can be used to compare the original (ZOPT-OG) and bulk adsorbent (ZOPT-BULK). Although not representative of actual external surface area as it is essentially erroneous to apply to microporous materials [201] as the assumption of monolayer coverage in a micropore has no clear physical or theoretical meaning. That said, the relative change in this metric can still be used as indication of quality deviation between samples or batches of the same mixture [60]. The BET surface area has been estimated *via* analysis of the N<sub>2</sub> adsorption isotherm at 77K. The samples were degassed prior to the isotherm measurement as per ASTM D4365 [200], by ramping the sample under vacuum from ambient to 350 °C at a ramp rate of 1 °C·min<sup>-1</sup> before holding at 350 °C for 12 h. The sample tube was backfilled with nitrogen before commencing the isotherm measurement.

Table 7-2: Textural properties of ZOPT estimated via the N2 adsorption/desorption at 77K.

Sample	BET Surface Area m <sup>2</sup> ·g <sup>-1</sup>	Micropore Area m <sup>2</sup> ·g <sup>-1</sup>	Micropore Volume cm <sup>3</sup> ·g <sup>-1</sup>	Total Pore Volume cm <sup>3</sup> ·g <sup>-1</sup>
ZOPT-BULK	163.96	43.62	0.019	0.185
	$p/p_0$ : $0.032 - 0.1716$	p/p <sub>0</sub> : 0.	$p/p_0 = 0.95$	
ZOPT-OG	329.89	236.42	0.094	0.225
	$p/p_0$ : $0.0012 - 0.050$	p/p <sub>0</sub> : 0.0	$p/p_0 = 0.95$	

The N<sub>2</sub> adsorption and desorption isotherm measured at 77K for ZOPT-BULK is provided in Figure 7.2 with the linear BET plot provided as an inset. The textural properties estimated *via* analysis of the N<sub>2</sub> adsorption isotherms at 77K for ZOPT-BULK and ZOPT-OG are provided in Table 5-9. The characteristics of the ZOPT-BULK isotherm are consistent with those of ZOPT-OG suggesting a similar pore structure in that a combination of both micro- and mesoporosity evidenced by the type IV (IUPAC) shape and type H4 hysteresis [59,165,320]. The hysteresis once more attributed to the formation of mesoporosity through individual crystal aggregation and the amorphous constituents [120,148,321].

The lack of an adsorption plateau at high relative pressures also indicative of microporosity [322]. in the bulk sample as for ZOPT-OG. There is however a significant difference between the estimated BET surface areas and pore volumes for the two samples. This is to be expected given the difference in both material characterisations and adsorption performance. The bulk adsorbent presents a BET surface area of approximately half the original sample (164 vs 330 m²·g¹). Total pore volume is slightly smaller for the bulk sample but the micropore contribution is only 20 % of that estimated for ZOPT-OG, 0.019 vs 0.094 m²·g¹. Although direct correlation between BET surface area and CO<sub>2</sub> adsorption capacity isn't possible, the decreased microporosity corroborates the decreased CO<sub>2</sub> adsorption capacity. A lack of microporosity is also evidenced by the position of the linear region which satisfy Rouquerol's criteria [201] identified during the model fitting; the relative pressure range for ZOPT-BULK was 0.03 – 0.17 (vs 0.001 – 0.05 for ZOPT-OG)) which is more typical of mesoporous materials [53].

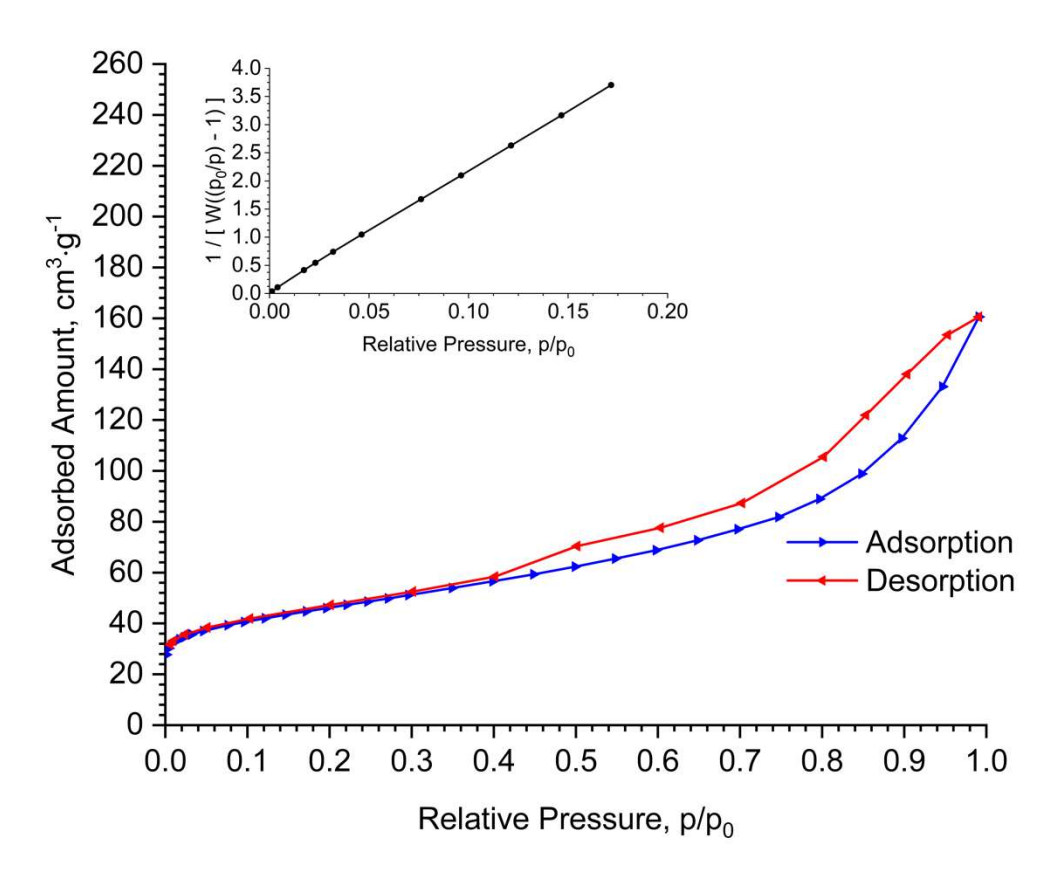


Figure 7.2: N<sub>2</sub> adsorption/desorption isotherm measured at 77 K; linear BET plot (inset). Produced for bulk ZOPT adsorbent.

# 7.6. Equilibrium CO<sub>2</sub> Adsorption

Equilibrium CO<sub>2</sub> adsorption isotherms have been estimated volumetrically between 0 and 1 bar(a) for between 0 and 50 °C. The samples were degassed prior to the isotherm measurement as per ASTM D4365 [200]. The equilibrium isotherms are provided in Figure 7.3 (discrete data points); the fitted curve is that defined by the Toth adsorption model which was identified as the best fit. The data was fit

with adsorption models via non-linear regression with the results provided in Table 7-3. For all of the investigated temperatures, the adj-R<sup>2</sup> and RMSE values are lowest for the Toth model. The model constants defined during the regression are given in Table 7-4. In general, both ZOPT-OG and ZOPT-BULK present similar adsorption characteristics but with a decrease in the equilibrium adsorption capacity for the latter (ZOPT-BULK). The degree of heterogeneity also appears to be greater for ZOPT-BULK,  $n_T$  was estimated as 0.21 [unit] for the 10 °C isotherm. Generally, the fitted  $q_e$  and  $K_T$  values decrease with an increasing temperature as the adsorption of CO<sub>2</sub> is less favourable [386]. Considering the adsorption mechanisms in the zeolite-CO<sub>2</sub> system, their temperature dependence is expected.

Table 7-3: Equilibrium isotherm model fitting via non-linear regression results.

Isotherm	Lang	muir	Freui	ıdlich	Si	ps	To	oth
Temperature	Adj-R <sup>2</sup>	RMSE						
0 °C	0.9058	0.1723	0.9787	0.0819	0.9972	0.0297	0.9987	0.0206
10 °C	0.9144	0.1539	0.9828	0.0691	0.9967	0.0303	0.9981	0.0228
20 °C	0.9327	0.1285	0.9845	0.0618	0.9981	0.0216	0.9992	0.0143
25 °C	0.9343	0.1221	0.9862	0.056	0.9981	0.0206	0.9992	0.0137
30 °C	0.9471	0.1074	0.9869	0.0535	0.9984	0.0187	0.9993	0.0119
40 °C	0.9572	0.0907	0.9873	0.0494	0.9984	0.0177	0.9993	0.0117
50 °C	0.9635	0.0785	0.9893	0.0426	0.9993	0.0111	0.9998	0.0058

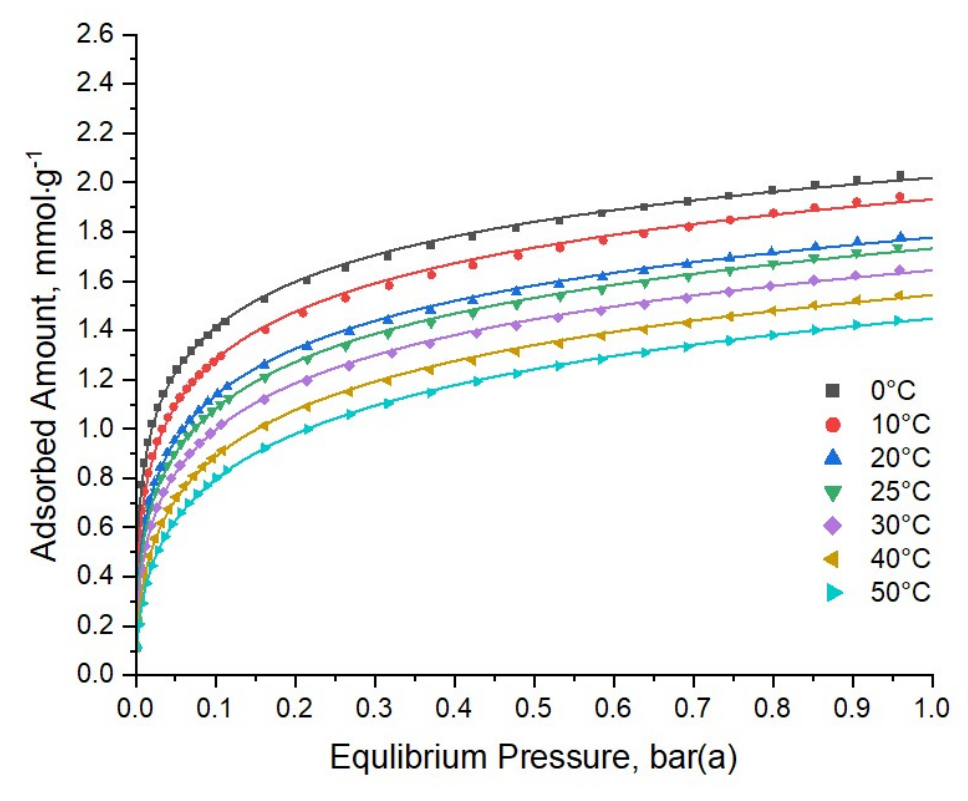


Figure 7.3: Equilibrium CO<sub>2</sub> adsorption isotherms measured volumetrically for ZOPT-BULK, with the Toth model fitted.

Table 7-4: Toth fitted isotherm model constants estimated via non-linear regression for ZOPT-BULK.

Temperature	q <sub>m</sub>	$\mathbf{k}_{\mathrm{T}}$	$\mathbf{n}_{\mathrm{T}}$
°C	mmol·g <sup>-1</sup>	bar <sup>-1</sup>	
0	3.835	2.648	0.210
10	4.111	2.262	0.208
20	3.825	1.936	0.222
25	3.998	1.847	0.217
30	3.734	1.618	0.233
40	3.474	1.300	0.259
50	3.482	1.159	0.262

## 7.7. Adsorption Kinetics - Comparison

Increasing the scale of granulometry of zeolitic adsorbents can significantly influence the adsorption kinetics for adsorbates. Zeolites present a number of diffusion mechanisms which are often the rate-determining step during the adsorption phenomenon [387]. This is especially true in the case of LTA zeolites due to their relatively small alpha cages. By increasing particle size, the contribution to adsorption kinetics from intra-particle and intra-crystalline diffusion can become greater and hence decrease the overall kinetics [388]. As such, the CO<sub>2</sub> adsorption kinetics have been estimated *via* nonlinear regression of typical adsorption kinetic models for both the bulk ZOPT sorbent and the bulk ZOPT granules, these are provided in Table 7-5. The uptake data which has been modelled was measured *via* TGA at 50 °C under pure CO<sub>2</sub> after an initial degassing at 150 °C under 100 mol% N<sub>2</sub> for 1 h. Although not representative of a typical adsorption process this analysis facilitates a comparative assessment of adsorption kinetics when increasing particle size. The Elovich kinetic model has been identified as the best fitting with the highest adj-R<sup>2</sup> and RMSE values.

Table 7-5: Results of the adsorption kinetic modelling for the bulk ZOPT adsorbent (powder) and the derived bulk ZOPT granules; the model constants from the original ZOPT sample is provided for comparison.

Sample		o-first der	Pseudo-second Order		Elovich		W&M Intraparticle Diffusion	
	Adj-R <sup>2</sup>	RMSE	Adj-R <sup>2</sup>	RMSE	Adj-R <sup>2</sup>	RMSE	Adj-R <sup>2</sup>	RMSE
Powder	0.4740	0.1297	0.7701	0.0857	0.9769	0.0272	0.9121	0.0530
Granule	0.7256	0.0882	0.9173	0.0484	0.9481	0.0384	0.7309	0.0873

The Elovich constants determined *via* non-linear regression analysis are provided in Table 7-6 for the granulated and powder ZOPT-BULK zeolite. The observed values of  $\alpha$  and  $\beta$  are higher in the granulated form than powder. During granulation and in the absence of binders, particle agglomeration may improve active site accessibility by making the geometry more favourable for gas diffusion through introducing hierarchical porosity and hence improve the overall adsorption kinetics [383,389,390].

When considering the gravimetric method, the granulated form provides a better surface area to volume ratio compared to the powder which should promote the adsorption kinetics when passing the adsorptive over a crucible containing the adsorbent.

Table 7-6: Elovich kinetic model constants estimated via non-linear regression for powdered and granulated ZOPT-BULK..

_	Sample	α mmol·g <sup>-1</sup> ·min <sup>-1</sup>	β g∙mmol <sup>-1</sup>
Ī	Powder	3.78	5.74
_	Granule	5.99	6.21

The uptake curves are provided in Figure 7.4. along with the fitted Elovich kinetic model for both powder and granulated forms of ZOPT-BULK. The powdered adsorbent exhibits a marginally higher initial adsorption rate reaching 0.8 mmol·g<sup>-1</sup> within the two and a half minutes (vs 5 for the granulated form). That said, the granulated form reaches an adsorption plateau albeit at a reduced capacity than the powdered adsorbent in around half the time. For the powdered adsorbent, the adsorption of CO<sub>2</sub> appears to be more drawn out than the granulated form likely due to the diffusional resistance as the adsorptive migrates from the top surface of the crucible to the bottom. This phenomenon while still existent in the granulated form represents a smaller contribution as the diffusional distance is smaller.

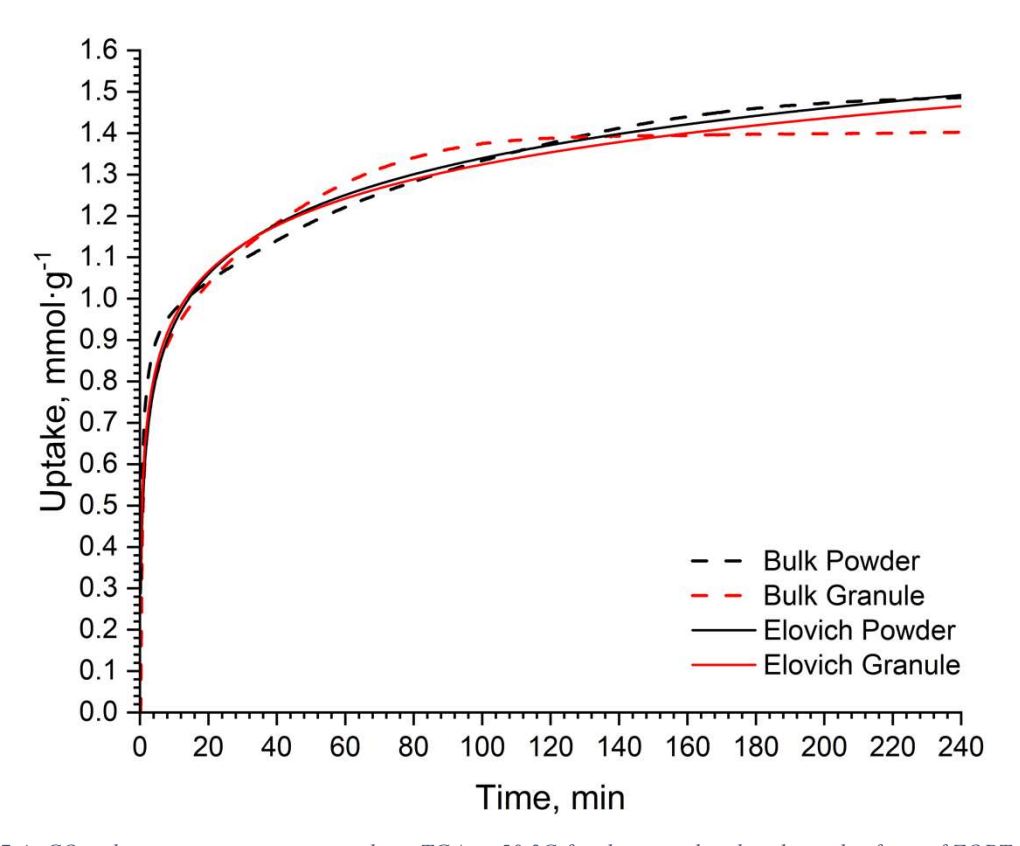


Figure 7.4: CO<sub>2</sub> adsorption vs time measured via TGA at 50 °C for the granulated and powder form of ZOPT-BULK. The dashed line represents the experimental data and the solid line the fitted Elovich model.

# 7.8. Enthalpy of Adsorption

The adsorption enthalpy has been estimated from the Toth equilibrium adsorption model for ZOPT-BULK between 0 and 50 °C. This facilitates a comparison between the original sample (ZOPT-OG) and the bulk adsorbent used in this chapter. The value for ZOPT-BULK, 32.4 kJ·mol<sup>-1</sup> represents a 3.9% decrease from 33.7 kJ·mol<sup>-1</sup> estimated for ZOPT-OG. Whilst this is a minor difference, at higher loadings, it is generally accepted that the zeolitic framework oxygen become the dominant adsorption site [336] and with similar Si/Al ratios, it is to be expected that ZOPT-BULK and ZOPT-OG would present similar CO2 adsorption enthalpies. Interestingly, at zero loading ZOPT-BULK presents a maximum enthalpy of adsorption at 54 kJ·mol<sup>-1</sup> vs 46 kJ·mol<sup>-1</sup> for ZOPT-OG. This suggests that at low loading, the strength of the interaction between ZOPT-BULK and CO<sub>2</sub> is greater than for ZOPT-OG. This can be explained when considering that at CO<sub>2</sub> loadings below 1 molecule per unit cell, the predominant adsorption sites are those in the vicinity of a compensating framework cation [389]. Given the likelihood that ZOPT-BULK presents a greater proportion of both LTA zeolites and Na-type cations, the strength of interaction between the adsorbent and CO<sub>2</sub> is larger than for ZOPT-OG, at low loadings due to the smaller charge-to-size ratio of the Na cation [391]. This in turn induces a greater charge, i.e. structural Lewis basicity in the zeolite framework due to the smaller electronegativity of Na vs Ca creating stronger framework interactions with CO<sub>2</sub> [392–394]; Pauling's electronegativity for Na is 0.9 and for Ca, 1.0 [395,396]. That said, a higher proportional of Al in the zeolite framework also contributes to an increased basicity [397,398].

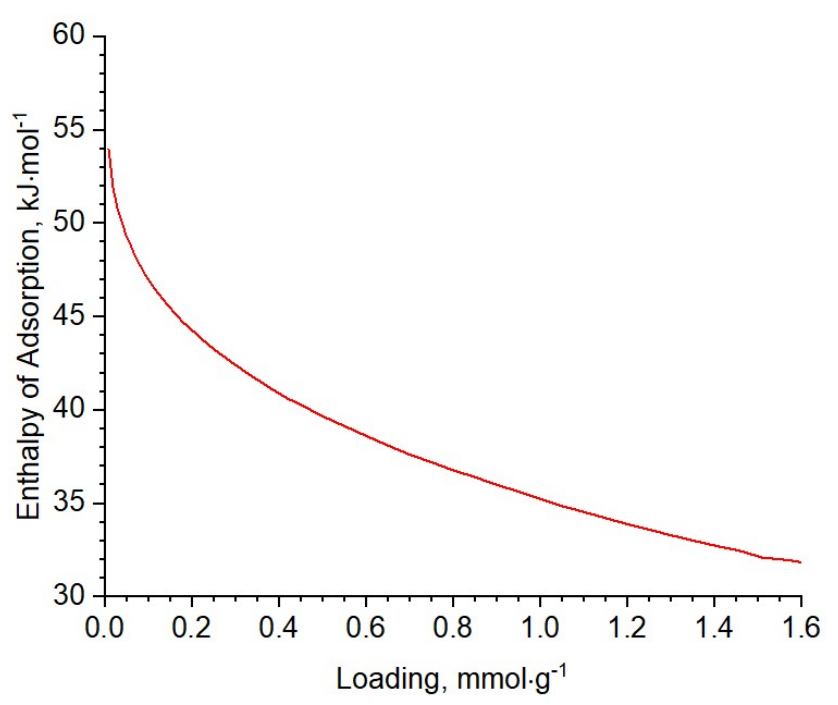


Figure 7.5: The enthalpy of adsorption determined between CO2 and ZOPT-BULK via analysis of the equilibrium adsorption isotherms (Toth) between 0 and 50  $^{\circ}$ C up to 1 bar(a).

#### 7.9. Working Capacity

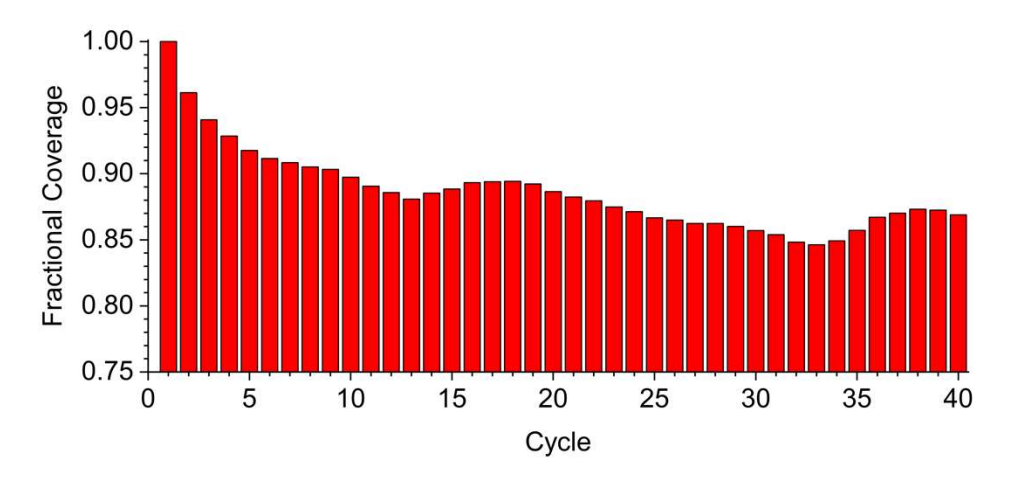


Figure 7.6: Working capacity of ZOPT-BULK estimated via TGA simulating a TSA cycle in the temperature range of 50(CO2) and 150 °C (N2) at 1 bar(a).

The working capacity of ZOPT-BULK has been estimated by the same method as that for ZOPT-OG, through a simulated TSA process at similar temperatures to that of post-combustion CO<sub>2</sub> capture, 50 °C adsorption (50 °C, 1 atm CO<sub>2</sub>, 2 h) and 150 °C desorption (150 °C, 1 atm N<sub>2</sub>, 1 h). After 40 cycles, the working capacity is approximately 90% of the initial after cycle 1 (*i.e.* 0.97 after cycle 1 and 0.88 after cycle 40). Much in the same way as ZOPT-OG the working capacity stabilises after between 5 and 10 cycles. This reduction can be attributed to the investigated conditions of temperature and cycle time. Improvements to the working capacity could be achieved by modifying the desorption conditions during the adsorbent's operational life such as extended degassing cycles or increasing the regeneration temperature. This may incur additional energy penalties but would improve the available working capacity between cycles.

## 7.10. Adsorbent Selectivity – $CO_2/N_2$

Table 7-7: Adsorption selectivity for ZOPT-OG and ZOPT-BULK at three temperatures. Pure selectivity has been estimated at 1 bar(a) and the separation factor at 1 bar(a) adsorption pressures 15 mol% CO<sub>2</sub>.

Tr. 4	Pure S	Selectivity	Equilibriu	ım Selectivity	Separation Factor		
Temperature °C	$(\alpha_{P(CO2/N2)})$		$(\alpha_{E(i)})$	co <sub>2/N2)</sub> )	$S_{CO2/N2}$		
	ZOPT-OG	ZOPT-BULK	ZOPT-OG	ZOPT-BULK	ZOPT-OG	ZOPT-BULK	
0	7.83	9.59	1788	4769	33.8	48.3	
25	15.36	13.01	1588	2354	66.3	72.8	
50	21.05	18.97	901	993	84.1	91.8	

Nitrogen isotherms have been measured at 0 °C, 25 °C and 50°C between 0 and 1 bar(a) in order to provide approximations for the  $CO_2/N_2$  selectivity of the fly-ash derived zeolites. The equilibrium  $CO_2$  adsorption isotherms are given in Figure 7.3 and those for  $N_2$  in Figure 7.7.

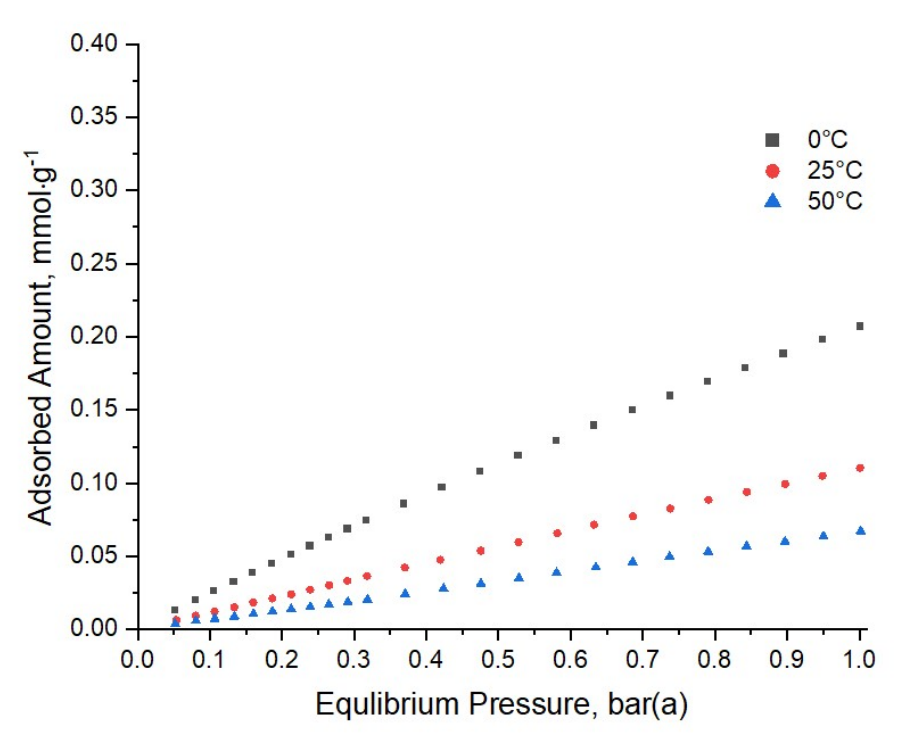


Figure 7.7: Equilibrium N2 adsorption isotherms for ZOPT-BULK.

Pure component equilibrium selectivity is the simplest estimation of selectivity and requires knowledge of an adsorbent's equilibrium adsorption capacity for each gas in a binary mixture [211]. In this case the equilibrium CO<sub>2</sub> and N<sub>2</sub> capacities have been used to estimate the pure component selectivity, results of which are provided in Table 7-7, in this case, 1 bar(a) and 0, 25 and 50 °C have been estimated. A general trend is observed in an increase in the pure component selectivity for both ZOPT-OG and ZOPT-BULK with an increase in temperature. Given that most separation process employing zeolites are kinetic rather than equilibrium-based operations, utilisation of the equilibrium capacities to estimate selectivity is likely conservative. The initial adsorption phenomena for CO<sub>2</sub> is rapid whereas for N<sub>2</sub> the increase in adsorbed amount is close to linear. The equilibrium selectivity is observed to decrease with an increase in temperature for both ZOPT-OG and ZOPT-BULK, with the latter demonstrating a greater selectivity for CO<sub>2</sub> over N<sub>2</sub>. The separation factor has also been estimated for the CO<sub>2</sub>/N<sub>2</sub> system at typical post combustion conditions (CO<sub>2</sub>/N<sub>2</sub> - 15 kPa/85 kPa) for ZOPT-OG and ZOPT-BULK. The separation factor is seen to increase with an increase in temperature for both adsorbents, with ZOPT-BULK presenting between 10 and 40% higher than ZOPT-OG. This suggests that the bulk adsorbent may have an improved selectivity for CO<sub>2</sub> vs the original ZOPT-OG.

#### 7.11. Assessment of Operating Variables on Adsorption Breakthrough

The breakthrough performance of biomass fly ash derived zeolites has been evaluated using the fixed bed reactor designed in this work. The column features an internal diameter of 40.25 mm and a

maximum bed length of 250 mm. The same adsorbent bed was employed for each of the experimental design points. The bed was filled to a total bed height,  $H_T$  of 240mm which equated to 100g. The weight loss during desorption was observed at approximately 14 wt% and therefore the adsorbent fill weight can be taken as 86g. Prior to each of the breakthrough experiments, the column was heated via resistance heaters surrounding the external bore. The initial purge sequence follows an initial pre-heating of the column to a surface temperature of 180 °C prior to supply of a 100 mol% N<sub>2</sub> purge at a total flow rate of 3 L·min<sup>-1</sup>. The purge stream was preheated to a set temperature of 150 °C before injection into the column. These conditions were held until an outlet CO<sub>2</sub> concentration of < 0.16 mol% and an exhaust gas temperature of >150 °C was observed consistently for 5 minutes. After this, the bed was allowed to cool under isolated conditions (i.e. no gas flow, with the column filled with  $N_2$ ). After cooling, the column was preheated to the defined adsorption temperature (measured at the column surface) before introducing a feed stream of pure N<sub>2</sub> at the desired total flow rate. After adjustment and stabilisation of column pressure the CO<sub>2</sub> was introduced to the feed stream in the appropriate concentration (reducing the N<sub>2</sub> flow). All adsorption experiments were performed at a column pressure of 1.3 bar(a), desorption was performed at atmospheric pressure. After each adsorption cycle an extended desorption was carried out to ensure as near complete removal of any adsorbed gas before the next cycle to minimise the impact of capacity loss due to cycling. An estimate of working capacity has been achieved via completion of 40 adsorption/desorption cycles via TGA (see 7.9, above) which revealed a 15% reduction in the working capacity at temperatures and cycle times of 150 °C, 1 h and 50 °C 2 h for desorption and adsorption, respectively under pure N<sub>2</sub> and pure CO<sub>2</sub>.

## 7.11.1. Taguchi L9 OA

The experimental design adopted for this work was an L9 Taguchi OA that investigated 3 factors at 3 levels. The factors were selected with a view to focus the investigation on parameters which are possible to modify without significant implications to both upstream and downstream processes. The factors and their associated levels are provided in Table 7-8 with the individual experiments and results in Table 7-9. The DoE was randomised prior to commencement. The superficial velocity range has been selected to ensure the mass transfer zone is retained in the bed whilst also ensuring typical fixed bed superficial gas velocities were considered; the normal range is between 15 and 45 cm·s<sup>-1</sup> [399] although a number of publications at lab-scale utilise velocities much lower than this including from below 1 cm·s<sup>-1</sup> and up to 50 cm·s<sup>-1</sup> [221,222,224–227,400,401]. The feed stream  $CO_2$  concentration,  $C_0$  varies between a range representative of gas-fired power stations utilising exhaust gas recirculation (~ 7 mol%) [402], biomass combustion facilities (~ 12 mol%) [403] and traditional coal-fired plants (~ 16 mol%) [404]. The breakthrough time, the has been estimated assuming a breakthrough condition of  $C/C_0 = 0.05$ . Approximation of the equivalent usable bed time, tu and the equivalent stoichiometric, ts has been achieved through integration of the 1- $C/C_0$  curve between  $t_o$  (adjusted for system deadtime) and  $t_b$  or  $t_s$ ,

respectively as per equations EQ. 40 and EQ. 41. The height of unused bed has been estimated as per EQ. 42.

Table 7-8: Factors and levels employed in the Taguchi L9 OA investigating the adsorption process configurations impact on bed adsorption capacity.

Factor Level	Superficial Velocity, v <sub>s</sub> cm·s <sup>-1</sup>	CO <sub>2</sub> Concentration, C <sub>0</sub> mol%	Adsorber Temperature, T <sub>A</sub> °C
1	2	8	40
2	7	12	50
3	12	16	60

$$t_s = \int_0^\infty \left(1 - \frac{C}{C_0}\right) dt$$
 EQ. 40

$$t_u = \int_0^{t_b} \left(1 - \frac{c}{c_0}\right) dt$$

$$LUB = \left(1 - \frac{t_u}{t_s}\right) \times H_T$$
 EQ. 42

Fraction of Bed Used 
$$=\frac{t_u}{t_s}$$

Table 7-9: Experimental design (Taguchi L9) with factor configurations for each run and associated results from analysis of the breakthrough curves.

	$\mathbf{v_s}$			Brea	kthrough	Stoic	hiometric	Bed	
	m·s-	C <sub>0</sub>	$T_A$	Time	Capacity	Time	Capacity	Utilization	LUB
<b>Experiment</b>	1	mol%	°C	min	mmol·g-1	min	mmol·g-1	%	mm
1	2	8	40	3.50	0.277	7.37	0.585	47.33	131
2	2	12	50	3.04	0.340	5.75	0.642	52.74	118
3	2	16	60	0.23	0.208	0.71	0.634	58.96	168
4	7	8	50	0.63	0.350	1.54	0.855	33.99	148
5	7	12	60	2.87	0.403	4.85	0.679	38.62	102
6	7	16	40	0.32	0.133	1.28	0.539	40.14	188
7	12	8	60	0.60	0.220	1.55	0.572	25.46	154
8	12	12	40	0.78	0.205	2.31	0.602	32.72	165
9	12	16	50	0.41	0.291	1.29	0.922	34.45	171

The measured breakthrough curves produced during this DoE are provided in Figure 7.8 with the inset graph providing a higher time resolution for experiments with a shorter breakthrough time. The observed breakthrough times vary between 0.23 and 3.50 minutes whilst the equivalent stochiometric times vary between 0.71 and 7.37 minutes. The length of the bed left unused at breakthrough varies between 102 and 188 mm which corresponds to a bed utilisation of between 25 to 59%, this can be considered an efficiency estimation based on column capacity [401]. The estimated equilibrium capacities are in agreement with those measured volumetrically in section 7.6. The extent to which a bed's adsorption capacity is usable can be inferred to some extent by the shape of the breakthrough curve. This is representative of the mass transfer taking place within the adsorbent bed, the width of the breakthrough curve being indicative of the width of the mass transfer zone; longer breakthrough curves

indicative of inefficient bed utilisation. An ideal breakthrough curve would be a steep symmetrical S-shape, with the outlet adsorptive concentration tending from zero to the feed concentration almost instantly, approaching a vertical line with suppressed mass transfer resistance. As can be seen in Figure 7.8, all the breakthrough curves exhibit distinct S-shaped curves. That said, those measured with the lowest superficial gas velocity (2 cm·s<sup>-1</sup>) present a flattening of the breakthrough curve from  $C/C_0 = 0.9$  to 1.0.

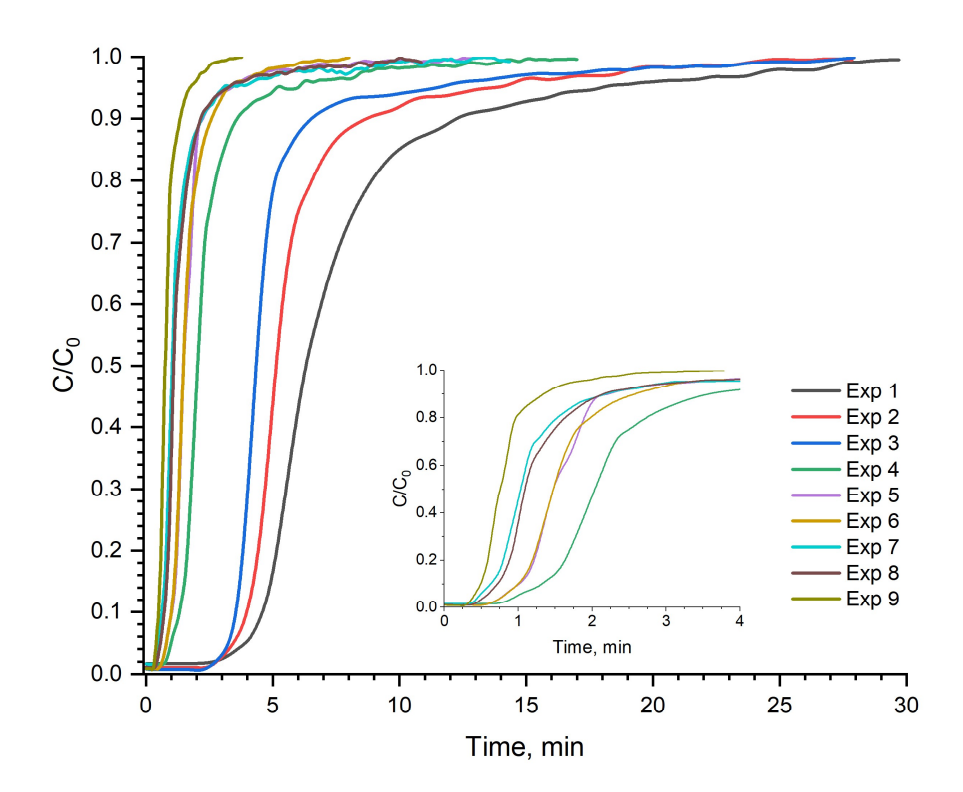


Figure 7.8: Experimentally determined CO2 fixed-bed adsorption breakthrough curves as per the Taguchi L9 DoE. The inset graph is of the same datasets.

#### 7.11.2. Breakthrough Optimisation and Statistical Analysis

Optimisation of the breakthrough experiments requires analysis of the main effects on the dependent variable. Depending on the intention to maximise the usable bed capacity or bed utilisation, the optimum factor configuration may differ. The SNRs have been calculated using the 'larger-the-better' equation

$$\frac{S}{N} = -10 \cdot \log \left( \sum \left( \frac{1}{y^2} \right) / n \right)$$
 EQ. 44

The main effects plots for the SNRs are given for both maximisation of the breakthrough or usable bed adsorption capacity (Figure 7.9) and of the bed utilisation efficiency (Figure 7.10). The usable bed capacity is impacted by all three of the studied factors within the studied levels. The impact of  $T_A$  is less pronounced than both  $v_s$  and  $C_0$  and this is evidenced by the reduced variation in the mean SNR values for that factor. Additionally, the response table given in Table 7-10 details  $T_A$  to be the lowest ranked

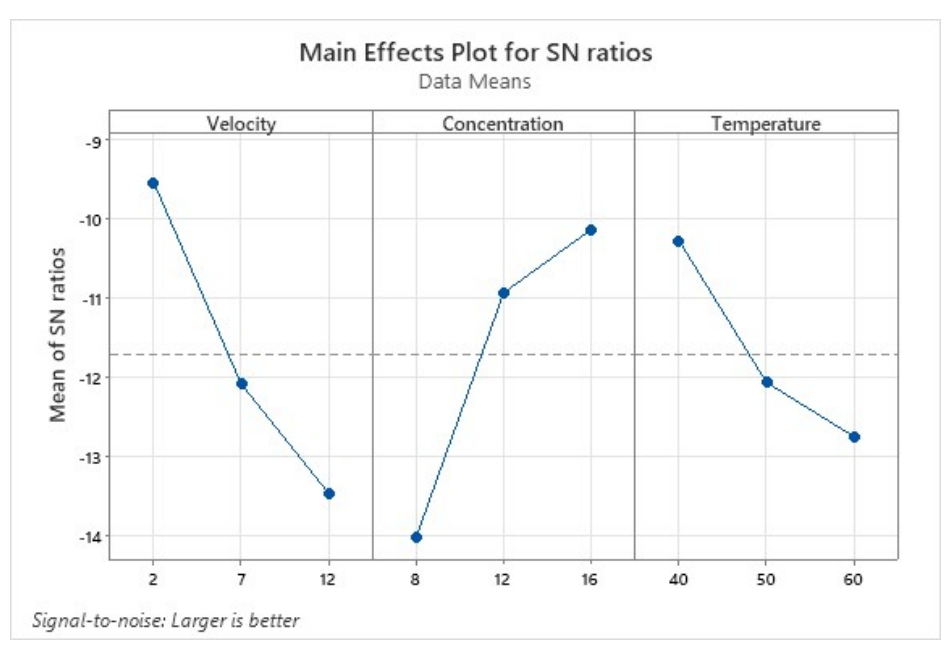


Figure 7.9: Main effects plots for the SNR ratios with the objective of maximising usable bed adsorption capacity.

factor indicating a smaller influence on the dependent variable. The superficial velocity was identified as the factor with the greatest impact on the usable bed adsorption capacity however, the feed concentration is only marginally different. Both factors can be seen to have huge influence on the working performance of the adsorbent bed under the studied conditions. Based on the main effects plot, if intending to maximise the usable bed adsorption capacity, the factor/level configuration would be  $v_s = 2 \text{ cm} \cdot \text{s}^{-1}$ ,  $C_0 = 16 \text{ mol}\%$  and  $T_A = 40 \text{ °C}$ .

Table 7-10: Response table for the SNR ratios with the objective of maximising usable bed adsorption capacity.

Level	Superficial Velocity, v <sub>s</sub> cm·s <sup>-1</sup>	CO <sub>2</sub> Concentration, C <sub>o</sub> mol%	Adsorber Temperature, T <sub>A</sub> °C
1	-9.547	-14.036	-10.284
2	-12.091	-10.938	-12.071
3	-13.472	-10.137	-12.755
Delta	3.924	3.899	2.471
Rank	1	2	3

When considering the bed utilisation efficiency, the main effects for the SNR ratios suggest the magnitude of the factor impacts on the dependent variable to be slightly different. In this case,  $v_s$  exhibits a far greater effect on the dependent variable than both  $C_0$ , and  $T_A$  within the studied factor levels. The adsorption temperature has been shown to have a relatively small effect on the bed utilisation efficiency as evidenced by the flatness in the mean SNR values. The superficial gas velocity is known to impact bed utilisation significantly due to its direct relationship with both residence time and mass transfer [405]. A higher velocity implies a larger volumetric flow rate and therefore reduced residence time for the gas in the column which can lead to reduced breakthrough times as insufficient time is provided to facilitate equilibrium between the adsorbent and  $CO_2$  [114,406]. Additionally, high flow rates may

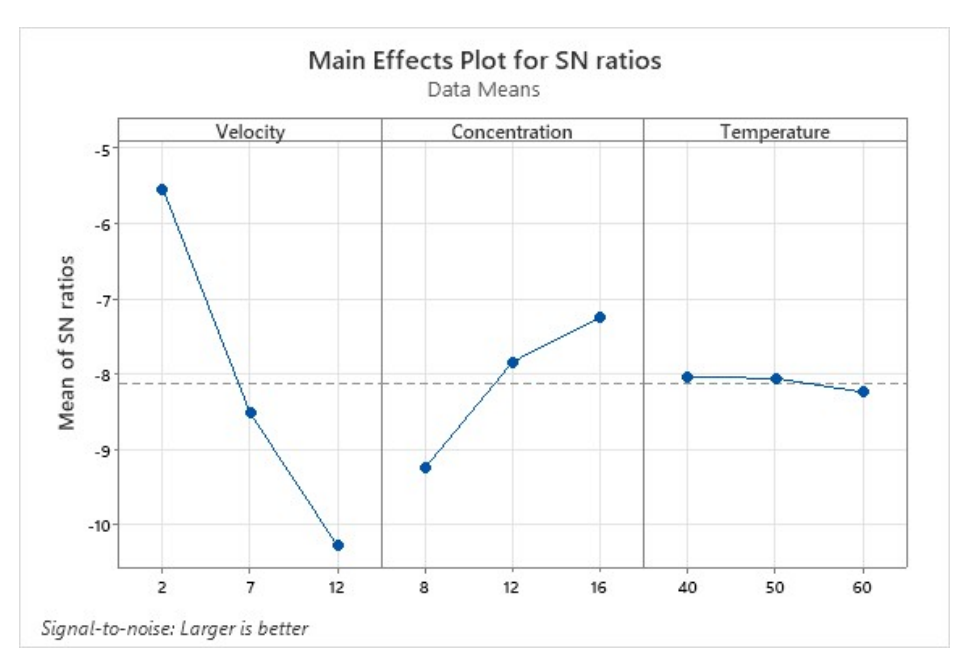


Figure 7.10: Main effects plots for the SNR ratios with the objective of maximising bed utilisation.

promote channelling of the gas at the column wall leading to immature breakthrough times and hence lower usable capacities [381]. Mass transfer on the other hand is often improved with an increase in superficial velocity due to increases in the Reynolds numbers which reduces the time to for an adsorbent to reach saturation which in turn can decrease the time to breakthrough. The response table given in Table 7-11 corroborates the main effects plot, the ranking of factor impact on the dependent variable is consistent for both dependent variables albeit with a greater impact of  $C_0$  and  $T_A$  on the usable capacity than bed utilisation. This suggests strong reliance on the operational parameters such as superficial velocity and feed concentration for both the usable bed capacity and bed utilisation efficiency. Based on the main effects plots, if intending to maximise the bed utilisation efficiency the factor/level configuration would be  $v_s = 2 \text{ cm} \cdot \text{s}^{-1}$ ,  $C_0 = 8 \text{ mol}\%$  and  $T_A = 40 \text{ °C}$ . This suggests that maximisation of either the usable capacity or bed utilisation may be detrimental to the other.

Table 7-11: Response table for the SNR ratios with the objective of maximising bed utilisation.

Level	Superficial Velocity, v <sub>s</sub> cm·s <sup>-1</sup>	CO <sub>2</sub> Concentration, C <sub>0</sub>	Adsorber Temperature, T <sub>A</sub> °C			
1	-5.548	-9.251	-8.044			
2	-8.522	-7.842	-8.062			
3	-10.280	-7.258	-8.245			
Delta	4.732	1.994	0.201			
Rank	1	2	3			

# 7.11.3. Analysis of Variance

As a complement to analysis of the SNR main effects, Taguchi DoE can employ analysis of variance (ANOVA) to determine which factors are statistically significant by modelling the experimental domain. In this case, modelling of the 3 factors from the L9 array requires 6 degrees of freedom (DoF),

leaving 2 to estimate error. This is because the three factor, three level DoE contributes 2 DoF (the number of levels minus 1); and the total DoF in the L9 array is 8 (the number of observations – 1) [182]. Without the remaining two DoF it would be impossible to allocate variability estimate error variance or assess significance [182]

As such, ANOVA for the mean factor values and the fraction of the bed which is utilised up to breakthrough (EQ. 43) is provided in Table 7-12. The linear model analysis is summarised in

Table 7-13, the adj- $R^2$  value is approximately 95.8% and pred- $R^2$  is 78.7%. This seemingly suggests that the linear model fit is somewhat adequate when considering the three investigated factors. That said only one of the factors has been identified as statistically significant, the superficial velocity. This is somewhat contradictory to the analysis of the SNR main effects, in that both the superficial velocity and adsorptive concentration influenced the dependent variable when compared with the adsorption temperature. Additionally, the distribution of residuals does not appear to be of the normal type based on the normal probability plot, *i.e.* the plot could not be approximately described by a straight-line suggesting overfitting. Removal of the least impactful factor (adsorption temperature,  $T_A$ ) from the model has resulted in an improved fit quality.

Table 7-12: Results of the ANOVA for the bed utilisation efficiency data means with three factors.

Source	Source DF Seq SS		Contribution	Adj SS	Adj MS	F-	P-
		_				Value	Value
Velocity	2	0.077276	85.23%	0.077276	0.038638	81.06	0.012
Concentration	2	0.012294	13.56%	0.012294	0.006147	12.90	0.072
Temperature	2	0.000140	0.15%	0.000140	0.000070	0.15	0.872
Error	2	0.000953	1.05%	0.000953	0.000477		
Total	8	0.090663	100.00%				

Table 7-13: Linear model analysis of the bed utilisation efficiency and the main effects of all three factors.

R-sq	R-sq(adj)	PRESS	R-sq(pred)
98.95%	95.79%	0.0193052	78.71%

The results of the ANOVA for two factors are given in Table 7-14 with the linear model analysis provided in

Table 7-15. There is a clear improvement in the model fitting quality based on the adj- $R^2$  and pred- $R^2$ , at 97.6% and 93.9% respectively. Additionally, both superficial velocity ( $v_s$ ) and adsorptive concentration ( $C_0$ ) have been identified as statistically significant, with the former responsible for over 85% of the contribution to the dependent variable, compared with 13.6% for the latter. The normal probability plot is also given which suggests there is a normal distribution of the residuals, see Figure 7.11.

Table 7-14: Results of the ANOVA for the bed utilisation efficiency data means with two factors.

Source DF		Seq SS Contribution		Adj SS	Adj MS	F-	P-
	-					Value	Value
Velocity	2	0.077276	85.23%	0.077276	0.038638	141.31	0.000
Concentration	on 2 0.01229		13.56%	0.012294	0.006147	22.48	0.007
Error	4	0.001094	1.21%	0.001094	0.000273		
Total	8	0.090663	100.00%				

Table 7-15:Linear model analysis of the bed utilisation efficiency and the main effects with two factors.

S	R-sq	R-sq(adj)	PRESS	R-sq(pred)
0.0165356	98.79%	97.59%	0.0055369	93.89%

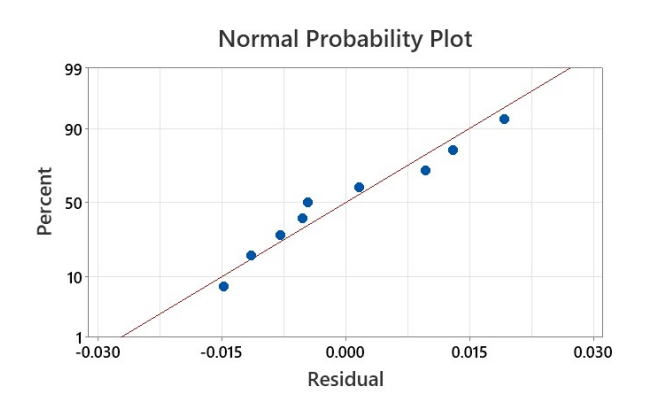


Figure 7.11: Normal probability plot of residuals for the 2 factor ANOVA.

### 7.11.4. Validation Experiments

After determining which of the investigated independent factors (*i.e.*  $v_s$ ,  $C_0$  and  $T_{Ads}$ ,) and have a statistically significant effect on the dependent variable, the fraction of the bed used up to breakthrough (*i.e.* the column utilisation efficiency), a series of confirmation experiments are required to determine if the predicted factor and level configuration results in improvement/optimisation of the dependent variable. Four confirmation experiments were completed at the optimum configuration of  $v_s = 2 \text{ cm} \cdot \text{s}^{-1}$ ,  $C_0 = 16 \text{ mol}\%$ , and  $T_A = 40 \,^{\circ}\text{C}$ , (Error! Reference source not found.); four experiments have been carried out to provide three replicates for the original confirmation. This will allow an improved determination of the predicted optimum's accuracy. All the confirmation experiments present characteristically similar profiles, with a steep increase in outlet CO<sub>2</sub> concentration after the breakthrough time to the feed concentration. The results from the confirmation experiments are given in Table 7-16 with the estimated mean response values and standard deviations. The mean breakthrough capacity has been identified as 0.591 mmolg<sup>-1</sup>, with an associated equivalent stoichiometric capacity of 0.951 mmolg<sup>-1</sup>. These values both represent the maximum which has been observed during this campaign. The highest breakthrough and equilibrium capacities were identified as 0.403 mmolg<sup>-1</sup> and 0.922 mmolg<sup>-1</sup> for experiments 5 and 9, respectively. The computed standard deviations suggest a

relative standard deviation for all KPIs of between 1 and 2%. Which suggests good consistency in the breakthrough adsorption performance, albeit between four cycles.

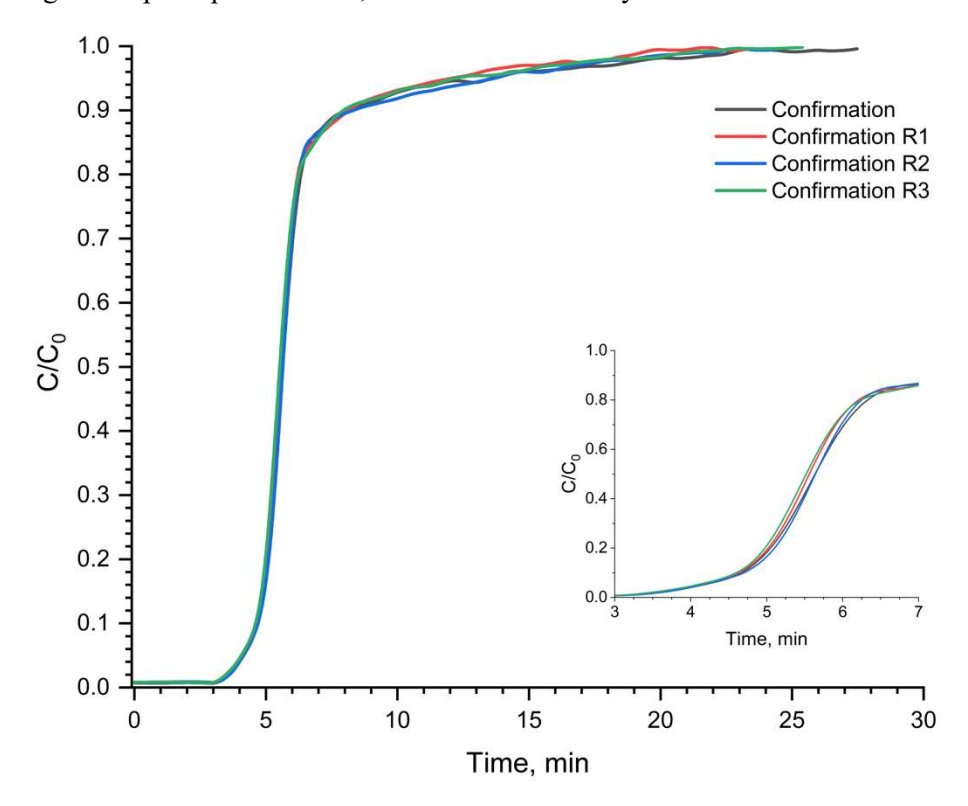


Figure 7.12: Breakthrough curves for the confirmation experiments conducted at factor and level configurations of vs = 2 cm·s-1; C0 = 16 mol%; TA = 40 °C.

Table 7-16: Confirmation experiments conducted at the optimum design point which maximises the adsorption bed's usable capacity. The mean response and the associated standard deviation are also given.

		$\mathbf{v_s}$			Breakthrough		Stoichiometric		Bed	
		m·s-	Co	T <sub>A</sub>	Time	Capacity	Time	Capacity	Utilization	LUB
	Experiment	1	mol%	°C	min	mmol·g <sup>-1</sup>	min	mmol·g <sup>-1</sup>	%	mm
	Confirmation	2	16	40	3.77	0.598	6.09	0.966	61.90	95
	Confirmation R1	2	16	40	3.70	0.587	5.89	0.934	62.85	93
	Confirmation R2	2	16	40	3.76	0.596	6.07	0.963	61.90	95
	Confirmation R3	2	16	40	3.68	0.584	5.92	0.939	62.22	95
	Mean	-	-	-	3.73	0.591	6.0	0.951	62.2	95
	Std. Deviation	-	-	_	0.043	0.0067	0.10	0.0163	0.4446	1.1

An average length of unused bed of 95 mm correlates to a bed utilisation efficiency of 62.2%. An increase in the utilisation of the bed suggests the mass transfer zone to be narrower for the investigated factor and level configuration in the confirmation experiments. When considering the three individual factors, a reduction in superficial velocity provides an increased residence time within the column facilitating additional diffusion during the gas-solid contact time [407]. That said, the effective thickness of the concentration boundary layer around the adsorbent particle is typically higher at lower superficial gas velocities [61] as viscous forces dominate, this decreases the rate of mass transfer from the bulk gas phase to the solid phase [408]. It is however, common for mass transfer to be limited primarily in the porous particle (vs the external film), heat transfer is often limited by the external

film/boundary layer [381]. Additionally, an increased adsorptive concentration in the feed gas increases the concentration gradient in the mass transfer zone [409]. Given that adsorption is an exothermic reaction a reduction in the adsorber temperature is expected to improve both the breakthrough and stoichiometric capacities and the LUB. Adsorption is more favourable at lower temperatures, that said however, the relative impact of the adsorption temperature was identified as lower than the other two factors. This may be due to the narrow range of adsorption temperatures investigated, whilst they represent a range of post-combustion scenarios, they are all still within typical ranges for gas adsorption with physisorbents. An additional consideration is the influence of temperature on the diffusion of CO<sub>2</sub> through the adsorbent particle, elevated temperatures promote molecular collisions and hence improves gas diffusion [410]. The fact that within the investigated range, the impact is negligible suggests that fly ash-derived zeolites are robust to a range of post-combustion flue gas temperatures.

#### 7.12. Conclusion

The bulk fly ash derived zeolite has been characterised in the context of both material and textural properties with a view to compare the adsorbent in both the powdered and granulated forms. Minimal differences have been identified in terms of material properties with marginal differences between surface morphologies and elemental analyses. That said, the differences between the original and bulk adsorbent are more pronounced, this was identified in the elemental analyses but more drastically in the textural properties estimated by N<sub>2</sub> adsorption at 77K. The bulk adsorbent was shown to have around half of the apparent BET surface area compared to the bulk and with even larger reductions to the micropore volume. Even with this, the adsorption performance was still shown to be of good quality for the bulk adsorbent when compared with the original. Whilst reductions in the equilibrium capacity were observed, they are not proportional to the reductions in BET surface area. Additionally, a greater degree of LTA is observed in the bulk adsorbent which resulted in variations of the CO<sub>2</sub> adsorption enthalpy and the adsorption kinetics. The working capacity of the bulk adsorbent was slightly reduced vs the original, but the final coverage was still approximately 0.85.

The granulated bulk adsorbent was then investigated *via* Taguchi L9 DoE in a fixed-bed adsorption column. The design studied the impact of superficial gas velocity, adsorptive concentration and adsorption temperature on the usable or breakthrough capacity and the bed utilisation efficiency. For both KPIs, the superficial gas velocity was identified as the most influential factor, with adsorbate concentration second and the adsorption temperature third. The superficial velocity and adsorptive concentration were both identified as statistically significant factors within the design space. Optimisation of the breakthrough experiments based on analysis of the SNR main effects resulted in a breakthrough capacity of 0.591 mmol·g<sup>-1</sup>, a LUB of 95 mm, equivalent stoichiometric capacity of 0.951 mmol·g<sup>-1</sup> and a bed utilisation efficiency of 62.2%. This was achieved with a factor and level configuration of:  $v_s = 2 \text{ cm·s}^{-1}$ ,  $C_\theta = 16 \text{ mol}\%$ , and  $T_A = 40 \text{ °C}$ . Biomass combustion fly ash derived

zeolites have been employed in a laboratory-scale fixed-bed adsorption column operating *via* TSA to selectively remove CO<sub>2</sub> at post-combustion concentration levels in a simulated flue gas. This highlights their potential application for post-combustion flue gas treatment.

#### 8. Conclusions & Future Work

#### 8.1. Conclusions

Whilst concerns around climate change are significant and alternative forms of energy are prioritised, dispatchable power generation is necessary to balance renewable intermittency. Traditionally this is met with fossil-fuels but to meet ambitions for net zero and ultimately net-negative GHG emissions, CCS and BECCS are poised for significant growth. The combustion of biomass fuels results in the cogeneration of waste ash such as fly ashes. The remediation of this waste is of key importance to both the economic and environmental feasibility of large-scale BECCS implementation. This work sought to reveal the potential for conversion of industrial-grade biomass combustion fly ash (BFA), sourced from Drax Power Station in the UK, into effective carbon dioxide (CO<sub>2</sub>) adsorbents.

This first entailed the comprehensive characterization of four batches of FA to satisfy objective one. This revealed their predominantly inorganic nature, composed of both amorphous and aluminosilicate phases enriched with alkali and alkaline earth metals, specifically calcium and potassium at approximately 10 wt% each. The silicon and aluminium contents presented an average Si/Al weight ratio of 1.86 indicating potential for subsequent zeolitisation. The presence of crystalline mullite and quartz phases necessitated an alkaline-fusion pretreatment to liberate Si and Al for subsequent crystallisation. The relatively poor CO<sub>2</sub> adsorption performance of the as-received fly ashes (0.14 - 0.20 mmol·g<sup>-1</sup>) further demonstrated the need for zeolitisation.

The second objective was satisfied in chapter 5 through optimisation of an alkaline fusion-assisted hydrothermal synthesis protocol. Implementation of an L9 Taguchi orthogonal array to systematically investigate and enhance the key parameters: NaOH/FA ratio, hydrothermal temperature, time, and liquid/solid ratio. Characterisation of ZOPT confirmed the co-crystallization of LTA and FAU zeolite structures alongside residual amorphous aluminosilicates, contributing to a mixed micro- and mesoporosity with a BET surface area of 330 m<sup>2</sup>·g<sup>-1</sup>, 72% of which is microporous.

Objective three was fulfilled by the comprehensive thermogravimetric and volumetric analyses in chapters 5, 6 and 7. These revealed the favourable adsorption equilibria and kinetics for the optimum materials prepared in this work including the original optimised sample and bulk analogue in powdered, pellet and granulated forms. The equilibria was best described by the Toth isotherm model indicating significant adsorbent heterogeneity. The adsorption enthalpy was coverage-dependent, decreasing to approximately 33.7 kJ·mol<sup>-1</sup> at a loading of 2 mmol·g<sup>-1</sup>. Initial cyclic testing showed a capacity retention of 87% after 40 cycles, suggesting good stability pending optimization of desorption conditions.

The fourth objective was realised in chapter 6 which involved assessing the transition from laboratory synthesis to practical application. Adoption of various method intensification strategies demonstrated

reductions to both synthesis duration and water consumption without compromising performance. A bulk sorbent was produced from 35 replicate syntheses, and pelletisation experiments explored the formation of mechanically robust granules. Notably, binderless pellets achieved a crush strength exceeding 1 N·mm<sup>-1</sup> while maintaining their adsorption equilibrium capacity and kinetics, attributed to the inherent binding properties of the amorphous phases and mixed zeolite structures within the FA-derived material. This eliminated the need for additional binders, which often diminish adsorption performance.

The final chapter sought to fulfil the final objective of this research through evaluation of the BFA-derived zeolite in an experimental fixed-bed reactor using a Taguchi L9 design of experiments. This DoE optimised the operational parameters of the adsorption process. Under optimal conditions (2 cm·s<sup>-1</sup> gas velocity, 16 mol% CO<sub>2</sub> concentration, and 40 °C temperature), the adsorbent achieved a breakthrough capacity of 0.591 mmol·g<sup>-1</sup> and a bed utilization efficiency of 62.2%. These results underscore the potential of biomass FA-derived zeolites for effective CO<sub>2</sub> capture in post-combustion scenarios.

This thesis demonstrates the pathway for industrial biomass fly ash valorisation and application in CO<sub>2</sub> separation from flue gas. The work shows that a high-volume biomass combustion by-product can be remediated into a functional CO<sub>2</sub> capture medium with measurable and optimisable performance. The combined use of alkaline fusion and statistically guided hydrothermal synthesis optimisation, and subsequent process intensification significantly improved the path from waste ash to cost-effective and performant adsorbents. The successful production of binderless granules mitigated the dilution penalties typical of binder addition and improves sustainability by reducing reliance on additional/secondary feedstocks. Finally, dynamic breakthrough experiments conducted under well-defined hydrodynamic conditions afforded correlation of intrinsic material characteristics (e.g. BET surface area, adsorption equilibria, kinetics and adsorption enthalpy) with process metrics such as breakthrough capacity and bed-utilisation efficiency, thereby providing a full assessment of the produced materials potential application for post-combustion CO<sub>2</sub> separation.

## 8.2. Future Work

The present study demonstrates that biomass fly ash (BFA) can be converted into structurally robust zeolitic sorbents with meaningful CO<sub>2</sub>-capture performance. Nevertheless, full industrial deployment requires a deeper understanding of feedstock variability, multicomponent adsorption behaviour and process integration/scale-up. The following research directions are proposed.

The physicochemical properties of the BFA depend heavily on the biomass type, boiler type/design and combustion conditions. Whilst the synthesis developed here was demonstrated for four batches, a wider compositional envelope should be studied to guarantee reproducibility both for Drax ash but also for

the wider BECCS fleet in the UK and internationally. Further to this, the mechanisms by which the BFA undergoes zeolitisation should be studied to generate an improved understanding of the solution chemistry, nucleation rates and competitive formation of LTA and FAU phases with respect to the experimental conditions and ash feedstock composition. This would allow for predictive models that tailor synthesis protocols for a robust product quality in light of ash variation.

Whilst the presence of the mixed porosity in the BFA-derived zeolite was identified in this thesis, the contribution of this hierarchical porosity to the overall performance of the material in both static and dynamic analyses should also be investigated. Further to this, if the synthesis procedure could be tailored to modify the distribution of pore sizes within the sample this would enable tailored adsorbent designs for specific process configurations and geometries.

Performance and selectivity of the BFA-derived zeolite should also be investigated under real flue-gas conditions and compositions. Both moisture and acid gases are ubiquitous in biomass combustion gases; this necessitates investigation of the adsorption equilibria and kinetics of gaseous mixtures to assess potential for competitive adsorption and adsorbent poisoning. Alongside this, alternative process configurations should also be investigated in order to optimise the energy intensity of the capture process. Both pressure and vacuum swing often feature heavily in industrial-scale adsorber design and the impact of these regeneration regimes and their hybrids should be investigated systematically to optimise the BFA-derived adsorbent's working capacity and specific energy consumption.

Whilst this work endeavoured to assess the separation performance of BFA-derived zeolites at representative scales and conditions, further scale-up would be necessary before translation to tonne-scale adsorption process deployment. Pilot-scale demonstrations should be sought to generate both an improved understanding of the adsorbent's performance but also elucidate the long-term cyclic stability of the adsorbent. This should then be supported by a full process model incorporating overall mass transfer kinetics, full energy balances for gaseous and solid phases, momentum balances and column-specific heat-loss terms. This would provide a means for full process optimisation at the cycle level rather than individual column level.

Finally, a comprehensive assessment of the prepared adsorbent's life cycle should be made supported by a full technoeconomic assessment of the adsorbent and applied process should be completed. This would facilitate comparison between commercially available adsorbents and these waste-derived alternatives in the context of net-emission benefits and both economic and environmental considerations. Addressing these questions would position BFA-derived zeolites as a circular, low-cost option for large-scale implementation of BECCS and other post-combustion carbon capture applications.

#### 9. References

- 1. Rafiee A, Rajab Khalilpour K, Milani D, Panahi M. Trends in CO<sub>2</sub> conversion and utilization: A review from process systems perspective. J Environ Chem Eng. 2018;6(5):5771–94.
- 2. Brown P, Broomfield M, Buys G, Cardenas L, Kilroy E, MacCarthy J, et al. UK Greenhouse Gas Inventory, 1990 to 2018. Annual Report for Submission under the Framework Convention on Climate Change. Science Research Programme of the Department of Energy and Climate Change. London; 2020.
- 3. Committe on Climate Change, Change C on C. Net Zero: The UK's contribution to stopping global warming. Committe on Climate Change. 2019.
- 4. Brown P, Cardenas L, Del Vento S, Karagianni E, MacCarthy J, Mullen P, et al. UK Greenhouse Gas Inventory, 1990 to 2023. Annual Report for Submission under the Framework Convention on Climate Change. 2025.
- 5. Commission E, European Commission. Paris Agreement | Climate Action [Internet]. European Commission Climate Action. 2015. Available from: https://ec.europa.eu/clima/policies/international/negotiations/paris en
- 6. Van Vuuren DP, Stehfest E, Gernaat DEHJ, Van Den Berg M, Bijl DL, De Boer HS, et al. Alternative pathways to the 1.5 °c target reduce the need for negative emission technologies. Nat Clim Chang. 2018;8(5):391–7.
- 7. Bui M, Adjiman CS, Bardow A, Anthony EJ, Boston A, Brown SF, et al. Carbon capture and storage (CCS): The way forward. Energy Environ Sci [Internet]. 2018;11(5):1062–176. Available from: http://eprints.whiterose.ac.uk/126186/
- 8. Fuss S, Lamb WF, Callaghan MW, Hilaire J, Creutzig F, Amann T, et al. Negative emissions Part 2: Costs, potentials and side effects. Environ Res Lett. 2018;13(6).
- 9. Li JR, Ma Y, McCarthy MC, Sculley J, Yu J, Jeong HK, et al. Carbon dioxide capture-related gas adsorption and separation in metal-organic frameworks. Vol. 255, Coordination Chemistry Reviews. 2011. p. 1791–823.
- 10. Masoudi Soltani S, Lahiri A, Bahzad H, Clough P, Gorbounov M, Yan Y. Sorption-enhanced Steam Methane Reforming for Combined CO<sub>2</sub> Capture and Hydrogen Production: A State-of-the-Art Review. Carbon Capture Sci Technol [Internet]. 2021;1(August):100003. Available from: https://doi.org/10.1016/j.ccst.2021.100003
- 11. United Kingdom HM Government. The Ten Point Plan for a Green Industrial Revolution. Dep

- Business, Energy Ind Strateg. 2020; (November).
- 12. Karimi F, Khalilpour R. Evolution of carbon capture and storage research: Trends of international collaborations and knowledge maps. Int J Greenh Gas Control [Internet]. 2015;37:362–76. Available from: http://dx.doi.org/10.1016/j.ijggc.2015.04.002
- 13. Koytsoumpa EI, Bergins C, Kakaras E. The CO<sub>2</sub> economy: Review of CO<sub>2</sub> capture and reuse technologies. J Supercrit Fluids. 2018;132(July 2017):3–16.
- 14. Samanta A, Zhao A, Shimizu GKH, Sarkar P, Gupta R. Post-combustion CO<sub>2</sub> capture using solid sorbents: A review. Vol. 51, Industrial and Engineering Chemistry Research. 2012. p. 1438–63.
- 15. Stadler H, Beggel F, Habermehl M, Persigehl B, Kneer R, Modigell M, et al. Oxyfuel coal combustion by efficient integration of oxygen transport membranes. Int J Greenh Gas Control. 2011;
- 16. Mukherjee A, Okolie JA, Abdelrasoul A, Niu C, Dalai AK. Review of post-combustion carbon dioxide capture technologies using activated carbon. J Environ Sci (China) [Internet]. 2019;83:46–63. Available from: https://doi.org/10.1016/j.jes.2019.03.014
- 17. Hossain MM, de Lasa HI. Chemical-looping combustion (CLC) for inherent CO<sub>2</sub> separations-a review. Vol. 63, Chemical Engineering Science. 2008.
- 18. Wang X, Song C. Carbon Capture From Flue Gas and the Atmosphere: A Perspective. Front Energy Res. 2020;8(December).
- 19. Adelodun AA, Kim KH, Ngila JC, Szulejko J. A review on the effect of amination pretreatment for the selective separation of CO<sub>2</sub>. Appl Energy [Internet]. 2015;158:631–42. Available from: http://dx.doi.org/10.1016/j.apenergy.2015.08.107
- 20. Ahmed R, Liu G, Yousaf B, Abbas Q, Ullah H, Ali MU. Recent advances in carbon-based renewable adsorbent for selective carbon dioxide capture and separation-A review. J Clean Prod [Internet]. 2020;242:118409. Available from: https://doi.org/10.1016/j.jclepro.2019.118409
- 21. Raganati F, Miccio F, Ammendola P. Adsorption of Carbon Dioxide for Post-combustion Capture: A Review. Vol. 35, Energy and Fuels. 2021.
- 22. Gomez-Rueda Y, Verougstraete B, Ranga C, Perez-Botella E, Reniers F, Denayer JFM. Rapid temperature swing adsorption using microwave regeneration for carbon capture. Chem Eng J. 2022;446.
- 23. Bae YS, Snurr RQ. Development and evaluation of porous materials for carbon dioxide

- separation and capture. Angew Chemie Int Ed. 2011;50(49):11586–96.
- 24. Ding M, Flaig RW, Jiang HL, Yaghi OM. Carbon capture and conversion using metal-organic frameworks and MOF-based materials. Chem Soc Rev. 2019;48(10):2783–828.
- 25. Bae YS, Farha OK, Spokoyny AM, Mirkin CA, Hupp JT, Snurr RQ. Carborane-based metalorganic frameworks as highly selective sorbents for CO<sub>2</sub> over methane. Chem Commun. 2008;
- 26. Zhang J, Singh R, Webley PA. Alkali and alkaline-earth cation exchanged chabazite zeolites for adsorption based CO<sub>2</sub> capture. Microporous Mesoporous Mater. 2008;111(1–3):478–87.
- 27. Kim J, Lin LC, Swisher JA, Haranczyk M, Smit B. Predicting large CO<sub>2</sub> adsorption in aluminosilicate zeolites for postcombustion carbon dioxide capture. J Am Chem Soc. 2012;
- 28. Bae TH, Hudson MR, Mason JA, Queen WL, Dutton JJ, Sumida K, et al. Evaluation of cation-exchanged zeolite adsorbents for post-combustion carbon dioxide capture. Energy Environ Sci. 2013;6(1):128–38.
- 29. Kumar S, Malik MM, Purohit R. Synthesis Methods of Mesoporous Silica Materials. In: Materials Today: Proceedings. 2017.
- 30. Lee SY, Park SJ. A review on solid adsorbents for carbon dioxide capture. J Ind Eng Chem. 2015;23:1–11.
- 31. McDonald TM, D'Alessandro DM, Krishna R, Long JR. Enhanced carbon dioxide capture upon incorporation of N,N'- dimethylethylenediamine in the metal-organic framework CuBTTri. Chem Sci. 2011;2(10):2022–8.
- 32. Nie L, Mu Y, Jin J, Chen J, Mi J. Recent developments and consideration issues in solid adsorbents for CO<sub>2</sub> capture from flue gas. Chinese J Chem Eng [Internet]. 2018;26(11):2303–17. Available from: https://doi.org/10.1016/j.cjche.2018.07.012
- 33. Chiang YC, Juang RS. Surface modifications of carbonaceous materials for carbon dioxide adsorption: A review. J Taiwan Inst Chem Eng [Internet]. 2017;71:214–34. Available from: http://dx.doi.org/10.1016/j.jtice.2016.12.014
- 34. Heinimö J, Junginger M. Production and trading of biomass for energy An overview of the global status. Biomass and Bioenergy. 2009;
- 35. Demirbaş A. Biomass resource facilities and biomass conversion processing for fuels and chemicals. Energy Convers Manag. 2001;
- 36. Vassilev S V., Baxter D, Andersen LK, Vassileva CG. An overview of the composition and

- application of biomass ash. Part 1. Phase-mineral and chemical composition and classification. Fuel [Internet]. 2013;105:40–76. Available from: http://dx.doi.org/10.1016/j.fuel.2012.09.041
- 37. Demirbas MF, Balat M, Balat H. Potential contribution of biomass to the sustainable energy development. Energy Convers Manag. 2009;
- 38. Creutzig F. Economic and ecological views on climate change mitigation with bioenergy and negative emissions. GCB Bioenergy. 2016;8(1):4–10.
- 39. Vassilev S V., Baxter D, Andersen LK, Vassileva CG. An overview of the chemical composition of biomass. Fuel. 2010.
- 40. Belviso C. State-of-the-art applications of fly ash from coal and biomass: A focus on zeolite synthesis processes and issues. Prog Energy Combust Sci [Internet]. 2018;65:109–35. Available from: https://doi.org/10.1016/j.pecs.2017.10.004
- 41. Srivastava VC, Mall ID, Mishra IM. Equilibrium modelling of single and binary adsorption of cadmium and nickel onto bagasse fly ash. Chem Eng J. 2006;
- 42. Vassilev S V., Vassileva CG. A new approach for the classification of coal fly ashes based on their origin, composition, properties, and behaviour. Fuel. 2007;
- 43. Wang P, Guo Y, Zhao C, Yan J, Lu P. Biomass derived wood ash with amine modification for post-combustion CO<sub>2</sub> capture. Appl Energy [Internet]. 2017 Sep;201(2):34–44. Available from: http://dx.doi.org/10.1016/j.apenergy.2017.05.096
- 44. Zając G, Szyszlak-Bargłowicz J, Gołębiowski W, Szczepanik M. Chemical characteristics of biomass ashes. Energies. 2018;11(11):1–15.
- 45. Blissett RS, Rowson NA. A review of the multi-component utilisation of coal fly ash. Fuel. 2012;97:1–23.
- 46. (UKQAA) UQAA. Ash Utilisation Data [Internet]. 2018. Available from: http://www.ukqaa.org.uk/
- 47. Vassilev S V., Baxter D, Andersen LK, Vassileva CG. An overview of the composition and application of biomass ash.: Part 2. Potential utilisation, technological and ecological advantages and challenges. Fuel [Internet]. 2013;105:19–39. Available from: http://dx.doi.org/10.1016/j.fuel.2012.10.001
- 48. Drax group. Drax Annual Reports and Accounts. 2019;
- 49. UK Committee on Climate Change. Biomass in a low-carbon economy [Internet]. 7 Holbein

- Place London SW1W 8NR: Veille énergie climat; 2018. p. 161. Available from: https://www.theccc.org.uk/wp-content/uploads/2018/11/Biomass-in-a-low-carbon-economy-CCC-2018.pdf
- 50. Li J, Zhuang X, Querol X, Font O, Moreno N. A review on the applications of coal combustion products in China. Int Geol Rev. 2018;60(5–6):671–716.
- 51. Theo WL, Lim JS, Hashim H, Mustaffa AA, Ho WS. Review of pre-combustion capture and ionic liquid in carbon capture and storage. Appl Energy. 2016;183:1633–63.
- 52. Chen L, Yong SZ, Ghoniem AF. Oxy-fuel combustion of pulverized coal: Characterization, fundamentals, stabilization and CFD modeling. Progress in Energy and Combustion Science. 2012.
- 53. Rouquerol J, Rouquerol F, Llewellyn P, Maurin G, Sing KSW. Adsorption by Powders and Porous Solids: Principles, Methodology and Applications: Second Edition. Adsorption by Powders and Porous Solids: Principles, Methodology and Applications: Second Edition. 2013. 1–626 p.
- 54. Nakao S, Yogo K, Goto K, Kai T, Yamada H. Advanced CO<sub>2</sub> capture technologies: Absorption, adsorption, and membrane separation methods [Internet]. Book. Cham: Springer International Publishing; 2019. p. 1–90. Available from: http://link.springer.com/10.1007/978-3-030-18858-0
- 55. Nollet H, Roels M, Lutgen P, Van Der Meeren P, Verstraete W. Removal of PCBs from wastewater using fly ash. Chemosphere. 2003;53(6).
- 56. McGlashan ML. Manual of symbols and terminology for physicochemical quantities and units. Pure Appl Chem. 1970;21(1):1–44.
- 57. Li JR, Kuppler RJ, Zhou HC. Selective gas adsorption and separation in metal-organic frameworks. Chem Soc Rev. 2009;38(5):1477–504.
- 58. Knaebel KS. Albright's Chemical Engineering Handbook [Internet]. Albright L, Albright L, editors. Albright's Chemical Engineering Handbook. CRC Press; 2008. 1120–1170 p. Available from: https://www.taylorfrancis.com/books/9780429135866
- 59. Thommes M, Kaneko K, Neimark A V., Olivier JP, Rodriguez-Reinoso F, Rouquerol J, et al. Physisorption of gases, with special reference to the evaluation of surface area and pore size distribution (IUPAC Technical Report). Pure Appl Chem. 2015;87(9–10):1051–69.
- 60. Sing KSW, Everett DH, Haul RAW, Moscou L, Pierotti RA, Rouquerol J, et al. Reporting

- Physisorption Data for Gas/Solid Systems with Special Reference to the Determination of Surface Area and Porosity. Pure Appl Chem. 1985;57(4).
- 61. Suzuki M. Adsorption engineering, Chemical engineering monographs: Vol. 25. Elsevier Science. 1991. 278 p.
- 62. Everett DH. The thermodynamics of adsorption: Part II. Thermodynamics of monolayers on solids. Trans Faraday Soc. 1950;46.
- 63. Barrer RM (Richard M. Zeolites and clay minerals as sorbents and molecular sieves [Internet]. Academic Press; 1978 [cited 2024 Apr 14]. Available from: https://cir.nii.ac.jp/crid/1130282270656369536.bib?lang=en
- 64. Sips R. On the structure of a catalyst surface. J Chem Phys. 1948;16(5).
- 65. Hubbard A. Adsorption: Theory, Modeling and Analysis. Edited by József Tóth. J Colloid Interface Sci. 2003;260(1).
- 66. Ladshaw A, Yiacoumi S, Tsouris C, DePaoli D. Generalized gas-solid adsorption modeling: Single-component equilibria. Fluid Phase Equilib. 2015;388.
- 67. Terzyk AP, Chatłas J, Gauden PA, Rychlicki G, Kowalczyk P. Developing the solution analogue of the Toth adsorption isotherm equation. J Colloid Interface Sci. 2003 Oct;266(2):473–6.
- 68. Ayawei N, Ebelegi AN, Wankasi D. Modelling and Interpretation of Adsorption Isotherms. J Chem. 2017;2017.
- 69. Benzaoui T, Selatnia A, Djabali D. Adsorption of copper (II) ions from aqueous solution using bottom ash of expired drugs incineration. Adsorpt Sci Technol. 2018 Feb;36(1–2):114–29.
- 70. Chowdhury S, Balasubramanian R. Highly efficient, rapid and selective CO<sub>2</sub> capture by thermally treated graphene nanosheets. J CO<sub>2</sub> Util [Internet]. 2016;13:50–60. Available from: http://dx.doi.org/10.1016/j.jcou.2015.12.001
- 71. Petrovic B, Gorbounov M, Masoudi Soltani S. Synthesis of biomass combustion fly ash derived zeolites for CO<sub>2</sub> adsorption: Optimisation of hydrothermal synthetic pathway. Carbon Capture Sci Technol. 2024 Sep 1;12:100245.
- 72. Mozaffari Majd M, Kordzadeh-Kermani V, Ghalandari V, Askari A, Sillanpää M. Adsorption isotherm models: A comprehensive and systematic review (2010–2020). Sci Total Environ. 2022;812(xxxx).
- 73. Son KN, Cmarik GE, Knox JC, Weibel JA, Garimella S V. Measurement and Prediction of the

- Heat of Adsorption and Equilibrium Concentration of CO<sub>2</sub> on Zeolite 13X. J Chem Eng Data. 2018;63(5):1663–74.
- 74. Ho YS, Porter JF, McKay G. Equilibrium isotherm studies for the sorption of divalent metal ions onto peat: Copper, nickel and lead single component systems. Vol. 141, Water, Air, and Soil Pollution. 2002.
- 75. Langmuir I. The adsorption of gases on plane surfaces of glass, mica and platinum. J Am Chem Soc. 1918;40(9).
- 76. Chen R, Liu J, Dai X. Adsorption equilibrium of ammonia and water on porous adsorbents at low pressure: Machine learning-based models. J Clean Prod. 2022 Sep;134351.
- 77. Mathias PM, Kumar R, Moyer JD, Schork JM, Srinivasan SR, Auvil SR, et al. Correlation of multicomponent gas adsorption by the dual-site Langmuir model. Application to nitrogen/oxygen adsorption on 5A-zeolite. Ind Eng Chem Res. 1996;35(7).
- 78. Lagergren SK. About the theory of so-called adsorption of soluble substances. Sven Vetenskapsakad Handingarl. 1898;24.
- 79. Ho YS, McKay G. Pseudo-second order model for sorption processes. Process Biochem. 1999;34(5).
- 80. Low MJD. Kinetics of chemisorption of gases on solids. Chem Rev. 1960;60(3).
- 81. Boyd GE, Adamson AW, Myers LS. The Exchange Adsorption of Ions from Aqueous Solutions by Organic Zeolites. II. Kinetics. J Am Chem Soc. 1947;69(11).
- 82. Weber WJ, Morris JC. Kinetics of Adsorption on Carbon from Solution. J Sanit Eng Div. 1963;89(2).
- 83. Liu J, Wu L, Chen X. Kinetic model investigation on lead(II) adsorption using silica-based hybrid membranes. Desalin Water Treat. 2015;54(8):2307–13.
- 84. Wang J, Guo X. Rethinking of the intraparticle diffusion adsorption kinetics model: Interpretation, solving methods and applications. Chemosphere [Internet]. 2022;309(P2):136732. Available from: https://doi.org/10.1016/j.chemosphere.2022.136732
- 85. Akhtar F, Bergström L. Colloidal processing and thermal treatment of binderless hierarchically porous zeolite 13X monoliths for CO<sub>2</sub> capture. J Am Ceram Soc. 2011;94(1):92–8.
- 86. Thakkar H, Eastman S, Hajari A, Rownaghi AA, Knox JC, Rezaei F. 3D-Printed Zeolite Monoliths for CO<sub>2</sub> Removal from Enclosed Environments. ACS Appl Mater Interfaces.

- 2016;8(41).
- 87. Alcañiz-Monge J, Marco-Lozar JP, Lillo-Ródenas MÁ. CO<sub>2</sub> separation by carbon molecular sieve monoliths prepared from nitrated coal tar pitch. Fuel Process Technol. 2011;92(5):915–9.
- 88. Dhoke C, Zaabout A, Cloete S, Amini S. Review on reactor configurations for adsorption-based CO<sub>2</sub> capture. Ind Eng Chem Res. 2021;60(10):3779–98.
- 89. Grande CA, Ribeiro RPL, Oliveira ELG, Rodrigues AE. Electric swing adsorption as emerging CO<sub>2</sub> capture technique. Energy Procedia. 2009 Feb;1(1):1219–25.
- 90. Luberti M, Oreggioni GD, Ahn H. Design of a rapid vacuum pressure swing adsorption (RVPSA) process for post-combustion CO<sub>2</sub> capture from a biomass-fuelled CHP plant. J Environ Chem Eng [Internet]. 2017;5(4):3973–82. Available from: http://dx.doi.org/10.1016/j.jece.2017.07.029
- 91. Webley PA, Zhang J. Microwave assisted vacuum regeneration for CO<sub>2</sub> capture from wet flue gas. Adsorption. 2014 Jan;20(1):201–10.
- 92. Auta M, Amat Darbis ND, Mohd Din AT, Hameed BH. Fixed-bed column adsorption of carbon dioxide by sodium hydroxide modified activated alumina. Chem Eng J. 2013 Nov;233:80–7.
- 93. Webley PA, Danaci D. CO<sub>2</sub> Capture by Adsorption Processes. In: Carbon Capture and Storage. Royal Society of Chemistry; 2019. p. 106–67.
- 94. Riboldi L, Bolland O. Evaluating Pressure Swing Adsorption as a CO<sub>2</sub> separation technique in coal-fired power plants. Int J Greenh Gas Control. 2015;39(7491):1–16.
- 95. Danaci D, Webley PA, Petit C. Guidelines for Techno-Economic Analysis of Adsorption Processes. Front Chem Eng. 2021;2(January):1–11.
- 96. Dantas TLP, Luna FMT, Silva Jr IJ, Torres AEB, de Azevedo DCS, Rodrigues AE, et al. Modeling of the fixed bed adsorption of carbon dioxide and a carbon dioxide nitrogen mixture on zeolite 13X. Brazilian J Chem Eng. 2011 Sep;28(3):533–44.
- 97. Chao C, Deng Y, Dewil R, Baeyens J, Fan X. Post-combustion carbon capture. Renew Sustain Energy Rev. 2021 Mar 1;138:110490.
- 98. Dhoke C, Zaabout A, Cloete S, Seo H, Park Y, Demoulin L, et al. Demonstration of the Novel Swing Adsorption Reactor Cluster Concept in a Multistage Fluidized Bed with Heat-Transfer Surfaces for Postcombustion CO<sub>2</sub> Capture. Ind Eng Chem Res. 2020 Dec;59(51):22281–91.
- 99. Hofer G, Schöny G, Fuchs J, Pröll T. Investigating wall-to-bed heat transfer in view of a

- continuous temperature swing adsorption process. Fuel Process Technol. 2018 Jan;169:157-69.
- 100. Raganati F, Chirone R, Ammendola P. Calcium-looping for thermochemical energy storage in concentrating solar power applications: Evaluation of the effect of acoustic perturbation on the fluidized bed carbonation. Chem Eng J. 2020 Jul;392:123658.
- 101. Monazam ER, Spenik J, Shadle LJ. Fluid bed adsorption of carbon dioxide on immobilized polyethylenimine (PEI): Kinetic analysis and breakthrough behavior. Chem Eng J. 2013 May;223:795–805.
- 102. Yaghoobi-Khankhajeh S, Alizadeh R, Zarghami R. Adsorption modeling of CO<sub>2</sub> in fluidized bed reactor. Chem Eng Res Des. 2018 Jan;129:111–21.
- 103. Yang W-C, Hoffman J. Exploratory Design Study on Reactor Configurations for Carbon Dioxide Capture from Conventional Power Plants Employing Regenerable Solid Sorbents. Ind Eng Chem Res. 2009 Jan;48(1):341–51.
- 104. Zhang J, Webley PA, Xiao P. Effect of process parameters on power requirements of vacuum swing adsorption technology for CO<sub>2</sub> capture from flue gas. Energy Convers Manag. 2008 Feb;49(2):346–56.
- 105. Gunawardene OHP, Gunathilake CA, Vikrant K, Amaraweera SM. Carbon Dioxide Capture through Physical and Chemical Adsorption Using Porous Carbon Materials: A Review. Vol. 13, Atmosphere. 2022.
- 106. Kim K, Son Y, Lee WB, Lee KS. Moving bed adsorption process with internal heat integration for carbon dioxide capture. Int J Greenh Gas Control. 2013 Sep;17:13–24.
- 107. Mondino G, Grande CA, Blom R, Nord LO. Moving bed temperature swing adsorption for CO<sub>2</sub> capture from a natural gas combined cycle power plant. Int J Greenh Gas Control. 2019 Jun;85:58–70.
- 108. Reiprich B, Weissenberger T, Schwieger W, Inayat A. Layer-like FAU-type zeolites: A comparative view on different preparation routes. Front Chem Sci Eng. 2020;14(2):127–42.
- 109. Liu X, Wang C, Zhou J, Liu C, Liu Z, Shi J, et al. Molecular transport in zeolite catalysts: depicting an integrated picture from macroscopic to microscopic scales. Vol. 51, Chemical Society Reviews. 2022.
- 110. Barrer RM. Zeolites and clay minerals as sorbents and molecular sieves. 1978;
- 111. Sircar S, Hufton JR. Why does the linear driving force model for adsorption kinetics work? Adsorption. 2000;6(2):137–47.

- 112. Ergun S. Fluid flow through packed columns. Chem Eng Prog. 1952;48.
- 113. Casas N, Schell J, Pini R, Mazzotti M. Fixed bed adsorption of CO<sub>2</sub>/H<sub>2</sub> mixtures on activated carbon: experiments and modeling. Adsorption [Internet]. 2012;18(2):143–61. Available from: https://doi.org/10.1007/s10450-012-9389-z
- 114. Sidabutar R, Trisakti B, Irvan, Michael M, Vanness V, Alexander V, et al. Synergistic integration of zeolite engineering and fixed-bed column design for enhanced biogas upgrading: Adsorbent synthesis, CO<sub>2</sub>/CH<sub>4</sub> separation kinetics, and regeneration assessment. Sep Purif Technol [Internet]. 2025;355(PB):129772. Available from: https://doi.org/10.1016/j.seppur.2024.129772
- 115. ASTM C618-22. Standard specification for coal fly ash and raw or calcined natural pozzolan for use in concrete. Annu B ASTM Stand. 2022;
- 116. Samanta NS, Das PP, Mondal P, Changmai M, Purkait MK. Critical review on the synthesis and advancement of industrial and biomass waste-based zeolites and their applications in gas adsorption and biomedical studies. J Indian Chem Soc. 2022;99(11).
- 117. Cundy CS, Cox PA. The hydrothermal synthesis of zeolites: Precursors, intermediates and reaction mechanism. Microporous Mesoporous Mater. 2005;82(1–2):1–78.
- 118. Ansari M, Aroujalian A, Raisi A, Dabir B, Fathizadeh M. Preparation and characterization of nano-NaX zeolite by microwave assisted hydrothermal method. Adv Powder Technol. 2014;25(2).
- 119. Petrovic B, Gorbounov M, Ozmen S, Clough P, Soltani SM. Synthesis of Nanoporous Type A and X Zeolite Mixtures from Biomass Combustion Fly Ash for Post-Combustion Carbon Capture. In: Proceedings of the IEEE Conference on Nanotechnology. 2022.
- 120. Boycheva S, Zgureva D, Lazarova H, Popova M. Comparative Studies of Carbon Capture onto Coal Fly Ash Zeolites Na-X and Na-Ca-X. Chemosphere [Internet]. 2021;271:129505. Available from: https://doi.org/10.1016/j.chemosphere.2020.129505
- 121. Vassilev S V., Vassileva CG. Methods for characterization of composition of fly ashes from coal-fired power stations: A critical overview. Vol. 19, Energy and Fuels. 2005.
- 122. El-Naggar MR, El-Kamash AM, El-Dessouky MI, Ghonaim AK. Two-step method for preparation of NaA-X zeolite blend from fly ash for removal of cesium ions. J Hazard Mater. 2008;154(1–3):963–72.
- 123. Bukhari SS, Behin J, Kazemian H, Rohani S. Conversion of coal fly ash to zeolite utilizing

- microwave and ultrasound energies: A review. Fuel. 2015;140:250-66.
- 124. Ahmaruzzaman M. A review on the utilization of fly ash. Prog Energy Combust Sci. 2010;36(3):327–63.
- 125. Collins F, Rozhkovskaya A, Outram JG, Millar GJ. A critical review of waste resources, synthesis, and applications for Zeolite LTA. Microporous Mesoporous Mater [Internet]. 2020;291(August 2019):109667. Available from: https://doi.org/10.1016/j.micromeso.2019.109667
- 126. Khaleque A, Alam MM, Hoque M, Mondal S, Haider J Bin, Xu B, et al. Zeolite synthesis from low-cost materials and environmental applications: A review. Vol. 2, Environmental Advances. 2020.
- 127. Vassilev VS, Baxter D, Andersen LK, Vassileva CG, Vassilev S V., Baxter D, et al. An overview of the chemical composition of biomass. Fuel. 2010;89(5):913–33.
- 128. Vassilev S V., Baxter D, Andersen LK, Vassileva CG, Vassilev VS, Baxter D, et al. An overview of the chemical composition of biomass. Fuel. 2010;89(5):913–33.
- 129. Molina A, Poole C. A comparative study using two methods to produce zeolites from fly ash. Miner Eng. 2004;17(2):167–73.
- 130. Klunk MA, Das M, Dasgupta S, Impiombato AN, Caetano NR, Wander PR, et al. Comparative study using different external sources of aluminum on the zeolites synthesis from rice husk ash. Mater Res Express. 2019;7(1).
- 131. Cornelius MLU, Price L, Wells SA, Petrik LF, Sartbaeva A. The steric influence of extraframework cations on framework flexibility: An LTA case study. Zeitschrift für Krist - Cryst Mater. 2019;234(7–8):461–8.
- 132. Popova M, Boycheva S, Lazarova H, Zgureva D, Lázár K, Szegedi Á. VOC oxidation and CO<sub>2</sub> adsorption on dual adsorption/catalytic system based on fly ash zeolites. Catal Today [Internet]. 2020;357(June 2019):518–25. Available from: https://doi.org/10.1016/j.cattod.2019.06.070
- 133. Walton KS, Abney MB, LeVan MD. CO<sub>2</sub> adsorption in y and X zeolites modified by alkali metal cation exchange. Microporous Mesoporous Mater. 2006;91(1–3):78–84.
- 134. Querol X, Moreno N, Umaa JC, Alastuey A, Hernández E, López-Soler A, et al. Synthesis of zeolites from coal fly ash: an overview. Int J Coal Geol. 2002;50(1–4):413–23.
- 135. Shigemoto N, Hayashi H, Miyaura K. Selective formation of Na-X zeolite from coal fly ash by fusion with sodium hydroxide prior to hydrothermal reaction. J Mater Sci. 1993;28(17):4781–

- 136. Inada M, Eguchi Y, Enomoto N, Hojo J. Synthesis of zeolite from coal fly ashes with different silica-alumina composition. Fuel. 2005;84(2–3):299–304.
- 137. Mercedes Maroto-Valer M, Lu Z, Zhang Y, Tang Z. Sorbents for CO<sub>2</sub> capture from high carbon fly ashes. Waste Manag. 2008;28(11):2320–8.
- 138. Rayalu S, Meshram SU, Hasan MZ. Highly crystalline faujasitic zeolites from flyash. J Hazard Mater. 2000;77(1–3).
- 139. Shigemoto N, Sugiyama S, Hayashi H, Miyaura K. Characterization of Na-X, Na-A, and coal fly ash zeolites and their amorphous precursors by IR, MAS NMR and XPS. J Mater Sci. 1995;30(22):5777–83.
- 140. Ren X, Qu R, Liu S, Zhao H, Wu W, Song H, et al. Synthesis of zeolites from coal fly ash for the removal of harmful gaseous pollutants: A review. Aerosol Air Qual Res. 2020;20(5):1127–44.
- 141. Ojha K, Pradhan NC, Samanta AN. Zeolite from fly ash: Synthesis and characterization. Bull Mater Sci. 2004;27(6):555–64.
- 142. Volli V, Purkait MK. Selective preparation of zeolite X and A from flyash and its use as catalyst for biodiesel production. J Hazard Mater. 2015;297.
- 143. Lin S, Jiang X, Zhao Y, Yan J. Zeolite greenly synthesized from fly ash and its resource utilization: A review. Sci Total Environ. 2022;851(August).
- 144. Chang HL, Shih WH. A General Method for the Conversion of Fly Ash into Zeolites as Ion Exchangers for Cesium. Ind Eng Chem Res. 1998;37(1):71–8.
- 145. Chan WH, Mazlee MN, Ahmad ZA, Ishak MAM, Shamsul JB. The development of low cost adsorbents from clay and waste materials: a review. J Mater Cycles Waste Manag. 2017;19(1):1–14.
- 146. de Aquino TF, Estevam ST, Viola VO, Marques CRMM, Zancan FL, Vasconcelos LB, et al. CO<sub>2</sub> adsorption capacity of zeolites synthesized from coal fly ashes. Fuel [Internet]. 2020;276(May):118143. Available from: https://doi.org/10.1016/j.fuel.2020.118143
- 147. Zgureva D, Boycheva S. Experimental and model investigations of CO<sub>2</sub> adsorption onto fly ash zeolite surface in dynamic conditions. Sustain Chem Pharm [Internet]. 2020;15(January):100222. Available from: https://doi.org/10.1016/j.scp.2020.100222

- 148. Guo J, Wu H, Wei Y, Miao Y, Qu J, Wang P. Synthesis of a high-iron fly-ash-based Na-X molecular sieve and its application in the adsorption of low concentration of CO<sub>2</sub>. RSC Adv. 2024;14(3):1686–96.
- 149. Morales R, Yan O, Eurico GA, Enrique BT, García V, Bastos M, et al. Assessment of the potential use of zeolites synthesized from power plant fly ash to capture CO<sub>2</sub> under post combustion scenario. Adsorption [Internet]. 2020;(0123456789). Available from: https://doi.org/10.1007/s10450-020-00245-0
- 150. Verrecchia G, Cafiero L, de Caprariis B, Dell'Era A, Pettiti I, Tuffi R, et al. Study of the parameters of zeolites synthesis from coal fly ash in order to optimize their CO<sub>2</sub> adsorption. Fuel [Internet]. 2020;276(January):118041. Available from: https://doi.org/10.1016/j.fuel.2020.118041
- 151. Kongnoo A, Tontisirin S, Worathanakul P, Phalakornkule C. Surface characteristics and CO<sub>2</sub> adsorption capacities of acid-activated zeolite 13X prepared from palm oil mill fly ash. Fuel [Internet]. 2017;193:385–94. Available from: http://dx.doi.org/10.1016/j.fuel.2016.12.087
- 152. Gargiulo N, Shibata K, Peluso A, Aprea P, Valente T, Pezzotti G, et al. Reinventing rice husk ash: derived NaX zeolite as a high-performing CO<sub>2</sub> adsorbent. Int J Environ Sci Technol. 2018;15(7):1543–50.
- 153. Wang Y, Du T, Jia H, Qiu Z, Song Y. Synthesis, characterization and CO<sub>2</sub> adsorption of NaA, NaX and NaZSM-5 from rice husk ash. Solid State Sci [Internet]. 2018;86(September):24–33. Available from: https://doi.org/10.1016/j.solidstatesciences.2018.10.003
- 154. Liang Z, Liu Z, Yu L, Wang W. Fly ash-based zeolites: from waste to value A comprehensive overview of synthesis, properties, and applications. Chem Eng Res Des [Internet]. 2024;212(July):240–60. Available from: https://doi.org/10.1016/j.cherd.2024.10.031
- 155. Park M, Choi CL, Lim WT, Kim MC, Choi J, Heo NH. Molten-salt method for the synthesis of zeolitic materials I. Zeolite formation in alkaline molten-salt system. Microporous Mesoporous Mater. 2000;37(1–2).
- 156. Bukhari SS, Rohani S, Kazemian H. Effect of ultrasound energy on the zeolitization of chemical extracts from fused coal fly ash. Ultrason Sonochem [Internet]. 2016;28:47–53. Available from: http://dx.doi.org/10.1016/j.ultsonch.2015.06.031
- 157. Inada M, Tsujimoto H, Eguchi Y, Enomoto N, Hojo J. Microwave-assisted zeolite synthesis from coal fly ash in hydrothermal process. Fuel. 2005;84(12–13).
- 158. Sivalingam S, Sen S. Optimization of synthesis parameters and characterization of coal fly ash

- derived microporous zeolite X. Appl Surf Sci [Internet]. 2018;455(May):903–10. Available from: https://doi.org/10.1016/j.apsusc.2018.05.222
- 159. Liu L, Singh R, Xiao P, Webley PA, Zhai Y. Zeolite synthesis from waste fly ash and its application in CO<sub>2</sub> capture from flue gas streams. Adsorption. 2011;17(5):795–800.
- 160. Yang L, Qian X, Yuan P, Bai H, Miki T, Men F, et al. Green synthesis of zeolite 4A using fly ash fused with synergism of NaOH and Na<sub>2</sub>CO<sub>3</sub>. J Clean Prod [Internet]. 2019;212:250–60. Available from: https://doi.org/10.1016/j.jclepro.2018.11.259
- 161. Purnomo CW, Salim C, Hinode H. Synthesis of pure Na-X and Na-A zeolite from bagasse fly ash. Microporous Mesoporous Mater. 2012;162:6–13.
- 162. Boycheva S, Zgureva D, Shoumkova A. Recycling of Lignite Coal Fly Ash by its Conversion into Zeolites. Coal Combust Gasif Prod. 2014;6(1):1–8.
- 163. Popova M, Boycheva S, Lazarova H, Zgureva D, Lázár K, Szegedi Á. VOC oxidation and CO<sub>2</sub> adsorption on dual adsorption/catalytic system based on fly ash zeolites. Catal Today [Internet]. 2020;357(November 2018):518–25. Available from: https://doi.org/10.1016/j.cattod.2019.06.070
- 164. Bai S xia, Zhou L mei, Chang Z bing, Zhang C, Chu M. Synthesis of Na-X zeolite from Longkou oil shale ash by alkaline fusion hydrothermal method. Carbon Resour Convers. 2018;1(3):245–50.
- 165. Hong JLX, Maneerung T, Koh SN, Kawi S, Wang CH. Conversion of Coal Fly Ash into Zeolite Materials: Synthesis and Characterizations, Process Design, and Its Cost-Benefit Analysis. Ind Eng Chem Res. 2017;56(40):11565–74.
- 166. Murayama N, Yamamoto H, Shibata J. Mechanism of zeolite synthesis from coal fly ash by alkali hydrothermal reaction. Int J Miner Process. 2002;64(1).
- 167. Hu X, Peng T, Sun H, Zhao E. Synthetic mechanism of hydroxy sodalite. Kuei Suan Jen Hsueh Pao/Journal Chinese Ceram Soc. 2016;44(8).
- 168. Tanaka H, Fujii A, Fujimoto S, Tanaka Y. Microwave-assisted two-step process for the synthesis of a single-phase Na-A zeolite from coal fly ash. Adv Powder Technol. 2008;19(1).
- 169. Gan F, Wang B, Jin Z, Xie L, Dai Z, Zhou T, et al. From typical silicon-rich biomass to porous carbon-zeolite composite: A sustainable approach for efficient adsorption of CO<sub>2</sub>. Sci Total Environ [Internet]. 2021;768:144529. Available from: https://doi.org/10.1016/j.scitotenv.2020.144529

- 170. Hollman GG, Steenbruggen G, Janssen-Jurkovičová M. Two-step process for the synthesis of zeolites from coal fly ash. Fuel. 1999;78(10):1225–30.
- 171. Smallwood HM. Design of Experiments in Industrial Research. Anal Chem. 1947;19(12):950–2.
- 172. Gorbounov M, Taylor J, Petrovic B, Masoudi Soltani S. To DoE or not to DoE? A Technical Review on & Roadmap for Optimisation of Carbonaceous Adsorbents and Adsorption Processes. Vol. 41, South African Journal of Chemical Engineering. 2022.
- 173. Mongomery DC. Montgomery: Design and Analysis of Experiments. John Willy & Sons. 2017.
- 174. Ross PJ. Taguchi Techniques for Quality Engineering: Loss Function, Orthogonal Experiments, Parameter and Tolerance Design. 2nd ed. Vol. 5, Loss Fuction, Orthogonal Experiments, Parameter and Tolerance Design. McGraw-Hill; 1995. 1–73 p.
- 175. Doumit P, Clark MW, Yee LH, Rose A. Response surface statistical optimisation of zeolite-X / silica by hydrothermal synthesis. J Mater Sci [Internet]. 2019;54(24):14677–89. Available from: https://doi.org/10.1007/s10853-019-03913-x
- 176. Box GEP, Wilson KB. On the Experimental Attainment of Optimum Conditions. J R Stat Soc Ser B. 1951;
- 177. Alaoui A, Kacemi KEL, Ass KEL, Kitane S. Application of box-behnken design to determine the optimal conditions of reductive leaching of MnO2 from manganese mine tailings. Trans Indian Inst Met. 2015;68(5).
- 178. Ferreira SLC, Bruns RE, da Silva EGP, dos Santos WNL, Quintella CM, David JM, et al. Statistical designs and response surface techniques for the optimization of chromatographic systems. Vol. 1158, Journal of Chromatography A. 2007.
- 179. Semioshkina N, Voigt G. An overview on Taguchi Method. J Radiat Res [Internet]. 2006;47 Suppl A(2):A95–100. Available from: http://www.ncbi.nlm.nih.gov/pubmed/19879888
- 180. Yusoff N, Ramasamy M, Yusup S. Taguchi's parametric design approach for the selection of optimization variables in a refrigerated gas plant. Chem Eng Res Des [Internet]. 2011;89(6):665–75. Available from: http://www.sciencedirect.com/science/article/pii/S0263876210002881
- 181. Davis R, John P. Application of Taguchi-Based Design of Experiments for Industrial Chemical Processes. Stat Approaches With Emphas Des Exp Appl to Chem Process. 2018;
- 182. Montgomery D. Design and Analysis of Experiments. 8th ed. John Wiley & Sons, Incorporated;

- 183. Roy RK. A Primer on Taguchi Method, Van Noshtrand Reinhold Int. Co Ltd, New York. 1990;
- 184. Ghasemi A, Zahediasl S. Normality tests for statistical analysis: A guide for non-statisticians. Int J Endocrinol Metab. 2012 Apr;10(2):486–9.
- 185. Khuri A, Mukhopadhyay S. Response Surface Experiments and Designs. In: Dean A, Morris M, Stufken J, Bingham D, editors. Handbook of Design and Analysis of Experiments. 1st ed. CRC Press LLC; 2015. p. 198–235.
- 186. Kastanaki E, Rovithi A, Iatrou E. Conversion of lignite fl y ash into synthetic zeolite by hydrothermal, hydrothermal-sonochemical processes. 2023;(June).
- 187. Verrecchia G, Cafiero L, de Caprariis B, Dell'Era A, Pettiti I, Tuffi R, et al. Study of the parameters of zeolites synthesis from coal fly ash in order to optimize their CO<sub>2</sub> adsorption. Fuel [Internet]. 2020;276(March):118041. Available from: https://doi.org/10.1016/j.fuel.2020.118041
- 188. Chansiriwat W, Tanangteerapong D, Wantala K. Synthesis of zeolite from coal fly ash by hydrothermal method without adding alumina and silica sources: Effect of aging temperature and time Synthesis of Zeolite from Coal Fly Ash by Hydrothermal Method Without Adding Alumina and Silica Sources: Effect. 2016;(November):1–10.
- 189. Tirva D, Ramesh R, Kaushal P. An optimization of synthesis technique for Na X zeolite from coal fly ash using Taguchi experimental design. Chem Pap [Internet]. 2023;77(9):5143–53. Available from: https://doi.org/10.1007/s11696-023-02850-z
- 190. Baha AA, Idouhli KTR, Zakir MKO, Abouelfida BDA. Zeolitization of Fumed Silica and Coal Fly Ash Using the Taguchi Method Toward Organic Pollutant Removal. Silicon [Internet]. 2023;15(14):6173–84. Available from: https://doi.org/10.1007/s12633-023-02501-8
- 191. Dere O, Sabriye O. A Novel Synthesis Method of Zeolite X From Coal Fly Ash: Alkaline Fusion Followed by Ultrasonic-Assisted Synthesis Method. Waste and Biomass Valorization [Internet]. 2019;10(1):143–54. Available from: http://dx.doi.org/10.1007/s12649-017-0050-7
- 192. A. MEDINA ., P. GAMERO M., J. M. ALMANZA R. DACHAGVG. STUDY OF THE ZEOLITIZATION PROCESS OF FLY ASH USING AN ORTHOGONAL ARRAY OF TAGUCHI EXPERIMENTAL DESIGN. 2009;3:244–51. Available from: https://www.scielo.cl/scielo.php?script=sci arttext&pid=S0717-97072009000300009
- 193. Haghjoo S, Lengauer CL, Kazemian H, Roushani M. Facile and innovative application of

- surfactant-modified-zeolite from Austrian fly ash for glyphosate removal from water solution. J Environ Manage [Internet]. 2023;346(June):118976. Available from: https://doi.org/10.1016/j.jenvman.2023.118976
- 194. Tabit K, Waqif M, Saâdi L. Application of the Taguchi method to investigate the effects of experimental parameters in hydrothermal synthesis of Na P1 zeolite from coal fly ash. Res Chem Intermed [Internet]. 2019;45(9):4431–47. Available from: https://doi.org/10.1007/s11164-019-03840-1
- 195. Ji L, Yu H, Zhang R, French D, Grigore M, Yu B, et al. Effects of fly ash properties on carbonation efficiency in CO<sub>2</sub> mineralisation. Fuel Process Technol. 2019;188(January):79–88.
- 196. Konopka J. Options for quantitative analysis of light elements by SEM/EDS. Thermo Fisher Scientific Technical Note 52523. Madison, WI; 2013. p. 1–4.
- 197. Mozgawa W, Król M, Dyczek J, Deja J. Investigation of the coal fly ashes using IR spectroscopy. Spectrochim Acta Part A Mol Biomol Spectrosc [Internet]. 2014 Nov 11 [cited 2021 Jun 2];132:889–94. Available from: http://dx.doi.org/10.1016/j.saa.2014.05.052
- 198. Ros A, Lillo-Ródenas MA, Fuente E, Montes-Morán MA, Martín MJ, Linares-Solano A. High surface area materials prepared from sewage sludge-based precursors. Chemosphere. 2006;65(1):132–40.
- 199. Li Z, Yan W, Dai S. Surface functionalization of ordered mesoporous carbons A comparative study. Langmuir. 2005;21(25):11999–2006.
- 200. ASTM International. ASTM D4365-19 Standard Test Method for Determining Micropore Volume and Zeolite Area of a Catalyst. In: Annual Book of ASTM Standards. 2019.
- 201. Rouquerol J, Llewellyn P, Rouquerol F. Is the BET equation applicable to microporous adsorbents? Stud Surf Sci Catal. 2007;160.
- 202. Barrett EP, Joyner LG, Halenda PP. The Determination of Pore Volume and Area Distributions in Porous Substances. I. Computations from Nitrogen Isotherms. J Am Chem Soc. 1951;
- 203. Monson PA. Understanding adsorption/desorption hysteresis for fluids in mesoporous materials using simple molecular models and classical density functional theory. Vol. 160, Microporous and Mesoporous Materials. 2012.
- 204. Landers J, Gor GY, Neimark A V. Density functional theory methods for characterization of porous materials. Colloids Surfaces A Physicochem Eng Asp. 2013;437.
- 205. Zheng Y. Evaluation of a New Method to Estimate the Micropore Volume and External Surface

- Area of Single-walled Carbon Nanotubes. The University of Tennessee; 2008.
- 206. de Boer JH, Lippens BC, Linsen BG, Broekhoff JCP, van den Heuvel A, Osinga TJ. Thet-curve of multimolecular N2-adsorption. J Colloid Interface Sci. 1966;21(4).
- 207. Lippens BC, de Boer JH. Studies on pore systems in catalysts. V. The t method. J Catal. 1965;4(3).
- 208. ASTM D 7582-15. Standard Test Methods for Proximate Analysis of Coal and Coke by Macro. Program. 2012;i:1–9.
- 209. Karimi M, Rodrigues AE, Silva JAC. Designing a simple volumetric apparatus for measuring gas adsorption equilibria and kinetics of sorption. Application and validation for CO<sub>2</sub>, CH<sub>4</sub> and N<sub>2</sub> adsorption in binder-free beads of 4A zeolite. Chem Eng J. 2021 Dec 1;425:130538.
- 210. Mason JA, McDonald TM, Bae TH, Bachman JE, Sumida K, Dutton JJ, et al. Application of a High-Throughput Analyzer in Evaluating Solid Adsorbents for Post-Combustion Carbon Capture via Multicomponent Adsorption of CO<sub>2</sub>, N<sub>2</sub>, and H<sub>2</sub>O. J Am Chem Soc. 2015;137(14).
- 211. Boer DG, Langerak J, Pescarmona PP. Zeolites as Selective Adsorbents for CO<sub>2</sub> Separation. ACS Appl Energy Mater. 2023;6(5):2634–56.
- 212. Li P, Handan Tezel F. Adsorption separation of N<sub>2</sub>, O<sub>2</sub>, CO<sub>2</sub> and CH<sub>4</sub> gases by β-zeolite. Microporous Mesoporous Mater. 2007;98(1–3).
- 213. Dabbawala AA, Ismail I, Vaithilingam B V., Polychronopoulou K, Singaravel G, Morin S, et al. Synthesis of hierarchical porous Zeolite-Y for enhanced CO<sub>2</sub> capture. Vol. 303, Microporous and Mesoporous Materials. 2020.
- 214. Garshasbi V, Jahangiri M, Anbia M. Equilibrium CO<sub>2</sub> adsorption on zeolite 13X prepared from natural clays. Appl Surf Sci [Internet]. 2017;393:225–33. Available from: http://dx.doi.org/10.1016/j.apsusc.2016.09.161
- 215. Yang RT. Adsorbents: Fundamentals and Applications. Adsorbents: Fundamentals and Applications. 2003.
- 216. Nuhnen A, Janiak C. A practical guide to calculate the isosteric heat/enthalpy of adsorption: Via adsorption isotherms in metal-organic frameworks, MOFs. Dalt Trans. 2020;49(30):10295–307.
- 217. David E. Mechanical strength and reliability of the porous materials used as adsorbents/ catalysts and the new development trends. Arch Mater Sci Eng. 2015;73(1):5–17.
- 218. Li Y, Wu D, Lin YS. Mechanical strength and reliability of solid catalysts. China Particuology

- [Internet]. 2004 Apr;2(2):53–62. Available from: https://linkinghub.elsevier.com/retrieve/pii/S1672251507600244
- 219. ASTM International. ASTM Standard D6175 03 Standard Test Method for Radial Crush Strength of Extruded Catalyst and Catalyst. Vol. i, ASTM International. 2003. p. 1–3.
- 220. Kaithwas A, Prasad M, Kulshreshtha A, Verma S. Industrial wastes derived solid adsorbents for CO<sub>2</sub> capture: A mini review. Chem Eng Res Des [Internet]. 2012;90(10):1632–41. Available from: http://dx.doi.org/10.1016/j.cherd.2012.02.011
- 221. Yan J, Zhao C, Wang P, Lu P. Studies on several fly ashes and their modified materials for CO<sub>2</sub> capture [Internet]. Vol. 1, American Society of Mechanical Engineers, Power Division (Publication) POWER. 2017. Available from: https://doi.org/10.1115/POWER-ICOPE2017-3420
- 222. Guo Y, Tan C, Wang P, Sun J, Yan J, Li W, et al. Kinetic study on CO<sub>2</sub> adsorption behaviors of amine-modified co-firing fly ash. J Taiwan Inst Chem Eng [Internet]. 2019;96(xxxx):374–81. Available from: https://doi.org/10.1016/j.jtice.2018.12.003
- 223. Yaumi AL, Hussien IA, Shawabkeh RA. Surface modification of oil fly ash and its application in selective capturing of carbon dioxide. Appl Surf Sci [Internet]. 2013;266:118–25. Available from: http://dx.doi.org/10.1016/j.apsusc.2012.11.109
- 224. Wang P, Guo Y, Zhao C, Yan J, Lu P. Biomass derived wood ash with amine modification for post-combustion CO<sub>2</sub> capture. Appl Energy [Internet]. 2017 Sep;201(2):34–44. Available from: https://search.proquest.com/docview/2297045587
- 225. Zhao C, Guo Y, Yan J, Sun J, Li W, Lu P. Enhanced CO<sub>2</sub> sorption capacity of amine-tethered fly ash residues derived from co-firing of coal and biomass blends. Appl Energy [Internet]. 2019;242(March):453–61. Available from: https://www.sciencedirect.com/science/article/pii/S0306261919305525
- 226. Miklová B, Staf M, Kyselová V. Influence of ash composition on high temperature CO<sub>2</sub> sorption. J Environ Chem Eng. 2019;7(2):9–14.
- 227. Guo Y, Zhao C, Chen X, Li C. CO<sub>2</sub> capture and sorbent regeneration performances of some wood ash materials. Appl Energy [Internet]. 2015;137(X):26–36. Available from: http://dx.doi.org/10.1016/j.apenergy.2014.09.086
- 228. Davidson T. A Simple and Accurate Method for Calculating Viscosity of Gaseous Mixtures. Rep Investig. 1993;741.

- 229. American Society of Mechanical Engineers. ASME Boiler and Pressure Vessel Code Section VIII: Division 1 Rules for Construction of pressure vessels. ASME Boiler and Pressure Vessel Code 2010.
- 230. ASME. BPVC Section VIII-Rules for Construction of Pressure Vessels Division 1. ASME BPVCVIII1-2019. 2019;
- 231. British Standards Institution. BSI Standards Publication Unfired pressure vessels Part 1: General. 2014;(August 2015):64.
- 232. Swagelok. Tubing Data. 2017;224–39.
- 233. Vassilev S V., Baxter D, Andersen LK, Vassileva CG, Vassilev VS, Baxter D, et al. An overview of the composition and application of biomass ash.: Part 2. Potential utilisation, technological and ecological advantages and challenges. Fuel [Internet]. 2013;105:19–39. Available from: http://dx.doi.org/10.1016/j.fuel.2012.10.001
- 234. Someshwar A V. Wood and Combination Wood-Fired Boiler Ash Characterization. J Environ Qual. 1996;
- 235. Senelwa K, Sims REH. Fuel characteristics of short rotation forest biomass. Biomass and Bioenergy. 1999;
- 236. Obernberger I, Thek G. Physical characterisation and chemical composition of densified biomass fuels with regard to their combustion behaviour. Biomass and Bioenergy. 2004;
- 237. Mainganye D, Ojumu TV, Petrik L. Synthesis of zeolites Na-P1 from South African coal fly ash: Effect of impeller design and agitation. Materials (Basel). 2013;
- 238. Boycheva S, Zgureva D, Lazarova H, Popova M. Comparative studies of carbon capture onto coal fly ash zeolites Na-X and Na-Ca-X. Chemosphere [Internet]. 2021;271:129505. Available from: https://doi.org/10.1016/j.chemosphere.2020.129505
- 239. Vassilev S V., Menendez R, Diaz-Somoano M, Martinez-Tarazona MR. Phase-mineral and chemical composition of coal fly ashes as a basis for their multicomponent utilization. 2. Characterization of ceramic cenosphere and salt concentrates. Fuel. 2004 Mar 1;83(4–5):585–603.
- 240. Franus W, Wdowin M, Franus M. Synthesis and characterization of zeolites prepared from industrial fly ash. Environ Monit Assess. 2014;186(9):5721–9.
- 241. Kleinhans U, Wieland C, Frandsen FJ, Spliethoff H. Ash formation and deposition in coal and biomass fired combustion systems: Progress and challenges in the field of ash particle sticking

- and rebound behavior. Vol. 68, Progress in Energy and Combustion Science. 2018.
- 242. Vassilev S V., Baxter D, Vassileva CG. An overview of the behaviour of biomass during combustion: Part II. Ash fusion and ash formation mechanisms of biomass types. Fuel [Internet]. 2014;117(PART A):152–83. Available from: http://dx.doi.org/10.1016/j.fuel.2013.09.024
- 243. Williams A. Understanding slagging and fouling during PF combustion Gordon Couch IEA Coal Research, London, 1994, pp. 109, ISBN 92-9029-240-7, £85. Fuel. 1995;74(10).
- 244. Kleinhans U, Wieland C, Frandsen FJ, Spliethoff H. Ash formation and deposition in coal and biomass fired combustion systems: Progress and challenges in the field of ash particle sticking and rebound behavior. Prog Energy Combust Sci [Internet]. 2018;68:65–168. Available from: https://doi.org/10.1016/j.pecs.2018.02.001
- 245. Hall GEM, Bonham-Carter GF, Buchar A. Evaluation of portable X-ray fluorescence (pXRF) in exploration and mining: Phase 1, control reference materials. Geochemistry Explor Environ Anal. 2014;14(2).
- 246. Vassilev VS, Baxter D, Andersen LK, Vassileva CG, Vassilev S V., Baxter D, et al. An overview of the composition and application of biomass ash. Part 1. Phase-mineral and chemical composition and classification. Fuel [Internet]. 2013;105:40–76. Available from: http://dx.doi.org/10.1016/j.fuel.2012.09.041
- 247. Kulprathipanja S. Zeolites in Industrial Separation and Catalysis. Zeolites in Industrial Separation and Catalysis. 2010.
- 248. Beltrao-Nunes AP, Sennour R, Arus VA, Anoma S, Pires M, Bouazizi N, et al. CO<sub>2</sub> capture by coal ash-derived zeolites- roles of the intrinsic basicity and hydrophilic character. J Alloys Compd. 2019;778:866–77.
- 249. De Rossi A, Simão L, Ribeiro MJ, Novais RM, Labrincha JA, Hotza D, et al. In-situ synthesis of zeolites by geopolymerization of biomass fly ash and metakaolin. Mater Lett. 2019;236:644–8.
- 250. Sivalingam S, Sen S. Optimization of synthesis parameters and characterization of coal fly ash derived microporous zeolite X. Appl Surf Sci [Internet]. 2018;455(February):903–10. Available from: https://doi.org/10.1016/j.apsusc.2018.05.222
- 251. Baxter LL, Miles TR, Miles TR, Jenkins BM, Milne T, Dayton D, et al. The behavior of inorganic material in biomass-fired power boilers: Field and laboratory experiences. Fuel Process Technol. 1998;54(1–3):47–78.

- 252. Fan M, Brown RC. Comparison of the loss-on-ignition and thermogravimetric analysis techniques in measuring unburned carbon in coal fly ash. Energy and Fuels. 2001;15(6).
- 253. Wang W, Zheng Y, Liu X, Wang P. Characterization of typical biomass ashes and study on their potential of CO 2 fixation. Energy and Fuels. 2012;26(9):6047–52.
- 254. Riaza J, Mason PE, Jones JM, Williams A, Gibbins J, Chalmers H. Shape and size transformations of biomass particles during combustion. Fuel [Internet]. 2020;261(October 2019):116334. Available from: https://doi.org/10.1016/j.fuel.2019.116334
- 255. Vassilev S V., Vassileva CG. Extra CO<sub>2</sub> capture and storage by carbonation of biomass ashes. Energy Convers Manag [Internet]. 2020;204(November):112331. Available from: https://doi.org/10.1016/j.enconman.2019.112331
- 256. Panek R, Madej J, Bandura L, Słowik G. Recycling of waste solution after hydrothermal conversion of fly ash on a semi-technical scale for Zeolite synthesis. Materials (Basel). 2021;14(6):1–16.
- 257. Babajide O, Musyoka N, Petrik L, Ameer F. Novel zeolite Na-X synthesized from fly ash as a heterogeneous catalyst in biodiesel production. Catal Today. 2012;190(1).
- 258. Wang G, Shen L, Sheng C. Characterization of biomass ashes from power plants firing agricultural residues. In: Energy and Fuels. 2012.
- 259. Boström D, Skoglund N, Grimm A, Boman C, Öhman M, Broström M, et al. Ash transformation chemistry during combustion of biomass. In: Energy and Fuels. 2012.
- 260. Hills CD, Tripathi N, Carey PJ. Mineralization Technology for Carbon Capture, Utilization, and Storage. Front Energy Res. 2020;8(July):1–14.
- 261. Soong Y, Fauth DL, Howard BH, Jones JR, Harrison DK, Goodman AL, et al. CO<sub>2</sub> sequestration with brine solution and fly ashes. Energy Convers Manag. 2006;47(13–14):1676–85.
- 262. Yadav S, Mehra A. A review on ex situ mineral carbonation. 2021;
- 263. Vamvuka D, Kakaras E. Ash properties and environmental impact of various biomass and coal fuels and their blends. Fuel Process Technol. 2011;
- 264. Dou B, Wang C, Song Y, Chen H, Jiang B, Yang M, et al. Solid sorbents for in-situ CO<sub>2</sub> removal during sorption-enhanced steam reforming process: A review. Renew Sustain Energy Rev [Internet]. 2016;53:536–46. Available from: http://dx.doi.org/10.1016/j.rser.2015.08.068
- 265. Koukouzas N, Hämäläinen J, Papanikolaou D, Tourunen A, Jäntti T. Mineralogical and

- elemental composition of fly ash from pilot scale fluidised bed combustion of lignite, bituminous coal, wood chips and their blends. Fuel. 2007;86(14 SPEC. ISS.):2186–93.
- 266. Córdoba P. Status of Flue Gas Desulphurisation (FGD) systems from coal-fired power plants: Overview of the physic-chemical control processes of wet limestone FGDs. Vol. 144, Fuel. 2015.
- 267. Srinivasachar S, Boni AA. A kinetic model for pyrite transformations in a combustion environment. Fuel. 1989 Jul 1;68(7):829–36.
- 268. Dai S, Zhao L, Peng S, Chou CL, Wang X, Zhang Y, et al. Abundances and distribution of minerals and elements in high-alumina coal fly ash from the Jungar Power Plant, Inner Mongolia, China. Int J Coal Geol. 2010;81(4).
- 269. Vassilev S V., Kitano K, Takeda S, Tsurue T. Influence of mineral and chemical composition of coal ashes on their fusibility. Fuel Process Technol. 1995;45(1).
- 270. Benson SA, Hurley JP, Zygarlicke CJ, Steadman EN, Erickson TA. Predicting Ash Behavior in Utility Boilers. Energy and Fuels. 1993;7(6).
- 271. Zhao M, Han Z, Sheng C, Wu H. Characterization of residual carbon in fly ashes from power plants firing biomass. Energy and Fuels. 2013;27(2).
- 272. Vassilev S V., Vassileva CG, Petrova NL. Thermal behaviour of biomass ashes in air and inert atmosphere with respect to their decarbonation. Fuel [Internet]. 2022;314(December 2021):122766. Available from: https://doi.org/10.1016/j.fuel.2021.122766
- 273. Montes-Hernandez G, Renard F, Chiriac R, Findling N, Ghanbaja J, Toche F. Sequential precipitation of a new goethite-calcite nanocomposite and its possible application in the removal of toxic ions from polluted water. Chem Eng J. 2013;214.
- 274. Ćwik A, Casanova I, Rausis K, Zarębska K. Utilization of high-calcium fly ashes through mineral carbonation: The cases for Greece, Poland and Spain. J CO<sub>2</sub> Util. 2019;32(January):155–62.
- 275. Lee J, Han SJ, Wee JH. Synthesis of dry sorbents for carbon dioxide capture using coal fly ash and its performance. Appl Energy [Internet]. 2014;131:40–7. Available from: http://dx.doi.org/10.1016/j.apenergy.2014.06.009
- 276. Santos RM, François D, Mertens G, Elsen J, Van Gerven T. Ultrasound-intensified mineral carbonation. Appl Therm Eng. 2013;57(1–2):154–63.
- 277. Huijgen WJJ, Witkamp GJ, Comans RNJ. Mineral CO<sub>2</sub> sequestration by steel slag carbonation.

- Environ Sci Technol. 2005;39(24):9676-82.
- 278. Tomeczek J, Palugniok H. Kinetics of mineral matter transformation during coal combustion. Fuel. 2002;81(10).
- 279. Kirnbauer F, Koch M, Koch R, Aichernig C, Hofbauer H. Behavior of inorganic matter in a dual fluidized steam gasification plant. Energy and Fuels. 2013;27(6).
- 280. Hao J, Dou Z he, Zhang T an, Wang K, Wan X yuan, Qi S. A clean and efficient utilization of fly ash with a focus on the strengthening decomposition mechanism of mullite. Fuel. 2023;333.
- 281. Gómez M, Pizarro J, Castillo X, Ghisolfi A, Díaz C, de Lourdes Chávez M, et al. Development of mesoporous materials from biomass ash with future applications as adsorbent materials. Microporous Mesoporous Mater. 2020 Jun 1;299(January):110085.
- 282. Guo Y, Yan K, Cui L, Cheng F. Improved extraction of alumina from coal gangue by surface mechanically grinding modification. Powder Technol. 2016 Nov 1;302:33–41.
- 283. Assad Munawar M, Hussain Khoja A, Hassan M, Liaquat R, Raza Naqvi S, Taqi Mehran M, et al. Biomass ash characterization, fusion analysis and its application in catalytic decomposition of methane. Fuel [Internet]. 2021 Feb 1 [cited 2021 Jun 2];285(May 2020):119107. Available from: https://doi.org/10.1016/j.fuel.2020.119107
- 284. Chindaprasirt P, Rattanasak U. Characterization of porous alkali-activated fly ash composite as a solid absorbent. Int J Greenh Gas Control [Internet]. 2019;85(March):30–5. Available from: https://doi.org/10.1016/j.ijggc.2019.03.011
- 285. Assad Munawar M, Hussain Khoja A, Hassan M, Liaquat R, Raza Naqvi S, Taqi Mehran M, et al. Biomass ash characterization, fusion analysis and its application in catalytic decomposition of methane. Fuel. 2021 Feb 1;285:119107.
- 286. Chen Y, Zou C, Mastalerz M, Hu S, Gasaway C, Tao X. Applications of Micro-Fourier Transform Infrared Spectroscopy (FTIR) in the Geological Sciences-A Review. 2015; Available from: www.mdpi.com/journal/ijms
- 287. Chen YH, Lu DL. CO<sub>2</sub> capture by kaolinite and its adsorption mechanism. Appl Clay Sci [Internet]. 2015;104:221–8. Available from: http://dx.doi.org/10.1016/j.clay.2014.11.036
- 288. Mozgawa W, Król M, Dyczek J, Deja J. Investigation of the coal fly ashes using IR spectroscopy. Spectrochim Acta Part A Mol Biomol Spectrosc. 2014 Nov 11;132:889–94.
- 289. Horiba Scientific A GUIDEBOOK TO PARTICLE SIZE ANALYSIS. Horiba Instruments, Inc. 2012;

- 290. Wang J, Guo X. Adsorption isotherm models: Classification, physical meaning, application and solving method. Chemosphere [Internet]. 2020;258:127279. Available from: https://doi.org/10.1016/j.chemosphere.2020.127279
- 291. Tanaka H, Sakai Y, Hino R. Formation of Na-A and -X zeolites from waste solutions in conversion of coal fly ash to zeolites. Mater Res Bull. 2002;37(11).
- 292. Abd AA, Naji SZ, Hashim AS, Othman MR. Carbon dioxide removal through physical adsorption using carbonaceous and non-carbonaceous adsorbents: A review. J Environ Chem Eng [Internet]. 2020;8(5):104142. Available from: https://doi.org/10.1016/j.jece.2020.104142
- 293. Sakamoto Y, Nagata K, Yogo K, Yamada K. Preparation and CO<sub>2</sub> separation properties of amine-modified mesoporous silica membranes. Microporous Mesoporous Mater. 2007;101(1-2 SPEC. ISS.).
- 294. Mondragon F, Rincon F, Sierra L, Escobar J, Ramirez J, Fernandez J. New perspectives for coal ash utilization: synthesis of zeolitic materials. Fuel. 1990;69(2).
- 295. Querol X, Alastuey A, López-Soler A, Plana F, Andrés JM, Juan R, et al. A fast method for recycling fly ash: Microwave-assisted zeolite synthesis. Environ Sci Technol. 1997;31(9).
- 296. Hui KS, Chao CYH. Effects of step-change of synthesis temperature on synthesis of zeolite 4A from coal fly ash. Microporous Mesoporous Mater. 2006;88(1–3).
- 297. Park J, Kim BC, Park SS, Park HC. Conventional versus ultrasonic synthesis of zeolite 4A from kaolin. J Mater Sci Lett. 2001;20(6).
- 298. Morales-Ospino R, Goltzman Y, Torres AEB, Vilarrasa-García E, Bastos-Neto M, Cavalcante CL, et al. Assessment of the potential use of zeolites synthesized from power plant fly ash to capture CO<sub>2</sub> under post-combustion scenario. Adsorption [Internet]. 2020;26(7):1153–64. Available from: https://doi.org/10.1007/s10450-020-00245-0
- 299. Catalfamo P, Di Pasquale SD, Corigliano F, Mavilia L. Influence of the calcium content on the coal fly ash features in some innovative applications. Resour Conserv Recycl. 1997;20(2).
- 300. Pourazar MB, Mohammadi T, Jafari Nasr MR, Javanbakht M, Bakhtiari O. Preparation of 13X zeolite powder and membrane: Investigation of synthesis parameters impacts using experimental design. Mater Res Express. 2020;7(3).
- 301. Grand J, Awala H, Mintova S. Mechanism of zeolites crystal growth: New findings and open questions. CrystEngComm. 2016;18(5):650–64.
- 302. Price L, Leung KM, Sartbaeva A. Local and average structural changes in zeolite a upon ion

- exchange. Magnetochemistry. 2017;3(4).
- 303. Chandwadkar AJ, Chandwadkar JG, Kulkarni SB. The influence of the size and concentration of alkaline earth ions on the structural and sorption properties of faujasites. J Colloid Interface Sci. 1984;97(2).
- 304. Petrovic BA, Soltani SM. Optimization of post combustion CO<sub>2</sub> capture from a combined-cycle gas turbine power plant via taguchi design of experiment. Processes. 2019;7(6).
- 305. Das SK, Sahoo P. Wear performance optimization of electroless Ni-B coating using Taguchi design of experiments. Tribol Ind. 2010;32(4).
- 306. Gorbounov M, Diaz-Vasseur E, Danaci D, Masoudi Soltani S. Chemical activation of porous carbon extracted from biomass combustion bottom ash for CO<sub>2</sub> adsorption. Carbon Capture Sci Technol. 2024 Mar 1;10:100151.
- 307. Anbia M, Nejati FM, Jahangiri M, Eskandari A, Garshasbi V. Optimization of synthesis procedure for NaX zeolite by taguchi experimental design and its application in CO<sub>2</sub> adsorption. J Sci Islam Repub Iran. 2015;26(3):213–22.
- 308. Aldahri T, Behin J, Kazemian H, Rohani S. Effect of microwave irradiation on crystal growth of zeolitized coal fly ash with different solid/liquid ratios. Adv Powder Technol. 2017;28(11):2865–74.
- 309. Gitari MW, Petrik LF, Musyoka NM. Hydrothermal Conversion of South African Coal Fly Ash into Pure Phase Zeolite Na-P1. In: Zeolites Useful Minerals. 2016.
- 310. Jentys A, Lercher JA. Techniques of zeolite characterization. In: Studies in Surface Science and Catalysis. 2001.
- 311. Sohn JR, DeCanio SJ, Lunsford JH, O'Donnell DJ. Determination of framework aluminium content in dealuminated Y-type zeolites: a comparison based on unit cell size and wavenumber of i.r. bands. Zeolites. 1986;6(3).
- 312. Dempsey E, Kühl GH, Olson DH. Variation of the lattice parameter with aluminum content in synthetic sodium faujasites. Evidence for ordering of the framework ions. J Phys Chem. 1969;73(2):387–90.
- 313. Lührs H, Derr J, Fischer RX. K and Ca exchange behavior of zeolite A. Microporous Mesoporous Mater. 2012;151.
- 314. Soe JT, Kim SS, Lee YR, Ahn JW, Ahn WS. CO<sub>2</sub> capture and Ca<sup>2+</sup> exchange using zeolite a and 13X prepared from power plant fly ash. Bull Korean Chem Soc. 2016;37(4):490–3.

- 315. Boycheva S, Marinov I, Miteva S, Zgureva D. Conversion of coal fly ash into nanozeolite Na-X by applying ultrasound assisted hydrothermal and fusion-hydrothermal alkaline activation. Sustain Chem Pharm. 2020;15(January).
- 316. Belviso C, Cavalcante F, Javier Huertas F, Lettino A, Ragone P, Fiore S. The crystallisation of zeolite (X- and A-type) from fly ash at 25 °c in artificial sea water. Microporous Mesoporous Mater. 2012;162.
- 317. Čejka J, Van Bekkum H, Corma A, Schuth F. Introduction to zeolite science and practice: Preface 1st edition. Vol. 1094, Studies in Surface Science and Catalysis. 2007.
- 318. Zeolite Microporous Solids: Synthesis, Structure, and Reactivity. Zeolite Microporous Solids: Synthesis, Structure, and Reactivity. 1992.
- 319. Feijen EJP, Martens JA, Jacobs PA. Zeolites and their Mechanism of Synthesis. Stud Surf Sci Catal. 1994;84(C).
- 320. Sing K. The use of nitrogen adsorption for the characterisation of porous materials. In: Colloids and Surfaces A: Physicochemical and Engineering Aspects. 2001.
- 321. Boycheva S, Zgureva D, Lazarova K, Babeva T, Popov C, Lazarova H, et al. Progress in the Utilization of Coal Fly Ash by Conversion to Zeolites with Green Energy Applications. Materials (Basel). 2020;13(9):2014.
- 322. Bukhari SS, Behin J, Kazemian H, Rohani S. A comparative study using direct hydrothermal and indirect fusion methods to produce zeolites from coal fly ash utilizing single-mode microwave energy. J Mater Sci. 2014;49(24):8261–71.
- 323. Hartmann M, Thommes M, Schwieger W. Hierarchically-Ordered Zeolites: A Critical Assessment. Adv Mater Interfaces. 2021;8(4).
- 324. Sarker AI, Aroonwilas A, Veawab A. Equilibrium and Kinetic Behaviour of CO<sub>2</sub> Adsorption onto Zeolites, Carbon Molecular Sieve and Activated Carbons. In: Energy Procedia. 2017. p. 2450–9.
- 325. Yu Q, Cai Y, Zhang Q, Li Y, Sun N, Liu W, et al. Silica-alumina zeolite adsorbents for oxygen generation via pressure swing adsorption: Mechanisms and challenge. Chem Eng J. 2024 Feb 1;481:148788.
- 326. Candamano S, Policicchio A, Conte G, Abarca R, Algieri C, Chakraborty S, et al. Preparation of foamed and unfoamed geopolymer/NaX zeolite/activated carbon composites for CO<sub>2</sub> adsorption. J Clean Prod. 2022 Jan 1;330:129843.

- 327. Cui Y, Xing Y, Tian J, Su W, Sun FZ, Liu Y. Insights into the adsorption performance and separation mechanisms for CO<sub>2</sub> and CO on NaX and CaA zeolites by experiments and simulation. Fuel [Internet]. 2023;337(October 2022):127179. Available from: https://doi.org/10.1016/j.fuel.2022.127179
- 328. Bonenfant D, Kharoune M, Niquette P, Mimeault M, Hausler R. Advances in principal factors influencing carbon dioxide adsorption on zeolites. Sci Technol Adv Mater. 2008;9(1).
- 329. Kumar KV, Gadipelli S, Howard CA, Kwapinski W, Brett DJL. Probing adsorbent heterogeneity using Toth isotherms. J Mater Chem A. 2021;9(2):944–62.
- 330. Ebelegi AN, Ayawei N, Wankasi D. Interpretation of Adsorption Thermodynamics and Kinetics. Open J Phys Chem. 2020;10(03):166–82.
- 331. Wang J, Guo X. Adsorption kinetic models: Physical meanings, applications, and solving methods. J Hazard Mater [Internet]. 2020;390(January):122156. Available from: https://doi.org/10.1016/j.jhazmat.2020.122156
- 332. Dabrowski A. Adsorption From theory to practice. Vol. 93, Advances in Colloid and Interface Science. 2001.
- 333. Aharoni C, Tompkins FC. Kinetics of Adsorption and Desorption and the Elovich Equation. Adv Catal. 1970;21(C).
- 334. Loganathan S, Tikmani M, Edubilli S, Mishra A, Ghoshal AK. CO<sub>2</sub> adsorption kinetics on mesoporous silica under wide range of pressure and temperature. Chem Eng J. 2014;256.
- 335. Najafi AM, Soltanali S, Ghassabzadeh H. Enhancing the CO<sub>2</sub>, CH<sub>2</sub>, and N<sub>2</sub> adsorption and kinetic performance on FAU zeolites for CO<sub>2</sub> capture from flue gas by metal incorporation technique. Chem Eng J. 2023;468(March).
- 336. Grajciar L, Čejka J, Zukal A, Otero Areán C, Turnes Palomino G, Nachtigall P. Controlling the adsorption enthalpy of CO<sub>2</sub> in zeolites by framework topology and composition. ChemSusChem. 2012;5(10):2011–22.
- 337. De Oliveira LH, Pereira M V., Meneguin JG, De Barros MASD, Do Nascimento JF, Arroyo PA, et al. Influence of regeneration conditions on cyclic CO<sub>2</sub>adsorption on NaA zeolite at high pressures. Energy and Fuels. 2023;67(April 2022):6641–9.
- 338. D.W. Breck. Zeolite Molecular Sieves: Structure, Chemistry and Use. Anal Chim Acta. 1975;75(2).
- 339. Bertolini TCR, Fungaro DA, Mahmoud AED. The influence of separately and combined

- bentonite and kaolinite as binders for pelletization of NaA zeolite from coal fly ash. Ceramica. 2022;68(387):375–84.
- 340. Whiting GT, Chowdhury AD, Oord R, Paalanen P, Weckhuysen BM. The curious case of zeolite-clay/binder interactions and their consequences for catalyst preparation. Faraday Discuss. 2016;188:369–86.
- 341. Wu D, Tang M. Effects of process factors on extrusion of hierarchically porous ZSM-5 zeolite. Powder Technol [Internet]. 2019;352:79–90. Available from: https://doi.org/10.1016/j.powtec.2019.04.052
- 342. Yu H, Wang L, Li J, Sun X, Han W, Shen J. Synthesis and characterization of zeolitic pellets manufactured from coal fly ash. Proc 3rd Int Conf Meas Technol Mechatronics Autom ICMTMA 2011. 2011;3:621–4.
- 343. Tanaka H, Fujii A. Effect of stirring on the dissolution of coal fly ash and synthesis of pure-form Na-A and -X zeolites by two-step process. Adv Powder Technol [Internet]. 2009;20(5):473–9. Available from: http://dx.doi.org/10.1016/j.apt.2009.05.004
- 344. Ogura M, Kawazu Y, Takahashi H, Okubo T. Aluminosilicate species in the hydrogel phase formed during the aging process for the crystallization of FAU zeolite. Chem Mater. 2003;15(13):2661–7.
- 345. Ginter DM, Went GT, Bell AT, Radke CJ. A physicochemical study of the againg of colloidal silica gels used in zeolite Y synthesis. Zeolites. 1992;12(6).
- 346. Li Q, Mihailova B, Creaser D, Sterte J. Aging effects on the nucleation and crystallization kinetics of colloidal TPA-silicalite-1. Microporous Mesoporous Mater. 2001;43(1):51–9.
- 347. Reinoso D, Adrover M, Pedernera M. Green synthesis of nanocrystalline faujasite zeolite. Ultrason Sonochem [Internet]. 2018;42(October 2017):303–9. Available from: https://doi.org/10.1016/j.ultsonch.2017.11.034
- 348. Kunecki P, Panek R, Wdowin M, Bień T, Franus W. Influence of the fly ash fraction after grinding process on the hydrothermal synthesis efficiency of Na-A, Na-P1, Na-X and sodalite zeolite types. Int J Coal Sci Technol. 2021;8(2):291–311.
- 349. Izidoro JDC, Fungaro DA, Dos Santos FS, Wang S. Characteristics of Brazilian coal fly ashes and their synthesized zeolites. Fuel Process Technol [Internet]. 2012;97:38–44. Available from: http://dx.doi.org/10.1016/j.fuproc.2012.01.009
- 350. Dindi A, Viet Quang D, Abu-Zahra MRM. CO<sub>2</sub> adsorption testing on fly ash derived cancrinite-

- type zeolite and its amine-functionalized derivatives. Environ Prog Sustain Energy. 2019;38(1):77–88.
- 351. Gao D, Duan A, Zhang X, Zhao Z, E H, Qin Y, et al. Synthesis of CoMo catalysts supported on EMT/FAU intergrowth zeolites with different morphologies and their hydro-upgrading performances for FCC gasoline. Chem Eng J. 2015;270.
- 352. Wang B, Dutta PK. Synthesis method for introducing mesoporosity in a faujasitic-like zeolite system from a sodium aluminosilicate gel composition. Microporous Mesoporous Mater [Internet]. 2017;239:195–208. Available from: http://dx.doi.org/10.1016/j.micromeso.2016.10.008
- 353. Liu XD, Wang YP, Cui XM, He Y, Mao J. Influence of synthesis parameters on NaA zeolite crystals. Powder Technol. 2013;243:184–93.
- 354. Zhang X, Wang K, Huang H, Chen S, Liu S. Influences of crystallization time, batch molar ratios Al<sub>2</sub>O<sub>3</sub>/SiO<sub>2</sub> and Na<sub>2</sub>O/SiO<sub>2</sub> on particulate properties of sodalite crystals prepared under room-temperature conditions. Adv Powder Technol [Internet]. 2023;34(2):103957. Available from: https://doi.org/10.1016/j.apt.2023.103957
- 355. Greer H, Wheatley PS, Ashbrook SE, Morris RE, Zhou W. Early stage reversed crystal growth of zeolite A and its phase transformation to sodalite. J Am Chem Soc. 2009;131(49):17986–92.
- 356. Li R, Chawla A, Linares N, Sutjianto JG, Chapman KW, Martínez JG, et al. Diverse Physical States of Amorphous Precursors in Zeolite Sol Gel Syntheses. Ind Eng Chem Res. 2018;57(25):8460–71.
- 357. Yang XY, Chen LH, Li Y, Rooke JC, Sanchez C, Su BL. Hierarchically porous materials: Synthesis strategies and structure design. Chem Soc Rev. 2017;46(2):481–558.
- 358. Zhu H, Liu Z, Wang Y, Kong D, Yuan X, Xie Z. Nanosized CaCO<sub>3</sub> as hard template for creation of intracrystal pores within silicalite-1 crystal. Chem Mater. 2008;20(3).
- 359. Romero MD, Ovejero G, Rodríguez A, Gómez JM. Impregnation of X zeolite with alkaline hydroxide during the synthesis. J Porous Mater. 2004;11(1):31–9.
- 360. Ferrarini SF, Cardoso AM, Paprocki A, Pires M. Integrated synthesis of zeolites using coal fly ash: Element distribution in the products, washing waters and effluent. J Braz Chem Soc. 2016;27(11):2034–45.
- 361. Rayalu SS, Udhoji JS, Munshi KN, Hasan MZ. Highly crystalline zeolite A from flyash of bituminous and lignite coal combustion. J Hazard Mater. 2001;88(1):107–21.

- 362. Lakiss L, Gilson JP, Valtchev V, Mintova S, Vicente A, Vimont A, et al. Zeolites in a good shape: Catalyst forming by extrusion modifies their performances. Microporous Mesoporous Mater. 2020;299(November 2019).
- 363. Musyoka NM, Petrik LF, Hums E, Kuhnt A, Schwieger W. Thermal stability studies of zeolites A and X synthesized from South African coal fly ash. Res Chem Intermed. 2015;41(2):575–82.
- 364. Majchrzak-Kucęba I. A simple thermogravimetric method for the evaluation of the degree of fly ash conversion into zeolite material. J Porous Mater. 2013;20(2):407–15.
- 365. Stoch L, Waclawska I. Phase transformations in amorphous solids. High Temp Mater Process. 1994;13(3):181–202.
- 366. Cruciani G. Zeolites upon heating: Factors governing their thermal stability and structural changes. J Phys Chem Solids. 2006;67(9–10):1973–94.
- 367. Majchrzak-Kucęba I, Nowak W. A thermogravimetric study of the adsorption of CO<sub>2</sub> on zeolites synthesized from fly ash. Thermochim Acta. 2005;437(1–2):67–74.
- 368. Usachev NY, Belanova EP, Krukovsky IM, Kanaev SA, Atal'yan OK, Kazakov A V. Thermal transformations in systems based on zeolites Y, X, and A containing zinc and sodium nitrates. Russ Chem Bull. 2003;52(9):1940–9.
- 369. Salem A, Akbari Sene R. Removal of lead from solution by combination of natural zeolite-kaolin-bentonite as a new low-cost adsorbent. Chem Eng J [Internet]. 2011;174(2–3):619–28. Available from: http://dx.doi.org/10.1016/j.cej.2011.09.075
- 370. Kakali G, Perraki T, Tsivilis S, Badogiannis E. Thermal treatment of kaolin: The effect of mineralogy on the pozzolanic activity. Appl Clay Sci. 2001;20(1–2).
- 371. Mohammadi T, Pak A. Effect of calcination temperature of kaolin as a support for zeolite membranes. Sep Purif Technol. 2003;30(3):241–9.
- 372. Saeidi N, Lotfollahi MN. A procedure to form powder activated carbon into activated carbon monolith. Int J Adv Manuf Technol. 2015;81(5–8):1281–8.
- 373. Antonyuk S, Tomas J, Heinrich S, Mörl L. Breakage behaviour of spherical granulates by compression. Chem Eng Sci. 2005;60(14):4031–44.
- 374. Lefevere J, Protasova L, Mullens S, Meynen V. 3D-printing of hierarchical porous ZSM-5: The importance of the binder system. Mater Des. 2017;134.
- 375. Yu L, Gong J, Zeng C, Zhang L. Synthesis of monodisperse zeolite A/chitosan hybrid

- microspheres and binderless zeolite A microspheres. Ind Eng Chem Res. 2012;51(5):2299–308.
- 376. Özcan A, Kalipçilar H. Preparation of zeolite a tubes from amorphous aluminosilicate extrudates. Ind Eng Chem Res. 2006;45(14):4977–84.
- 377. Najafi AM, Soltanali S, Khorashe F, Ghassabzadeh H. Effect of binder on CO<sub>2</sub>, CH<sub>4</sub>, and N<sub>2</sub> adsorption behavior, structural properties, and diffusion coefficients on extruded zeolite 13X. Chemosphere. 2023;324.
- 378. Asgar Pour Z, Abduljawad MM, Alassmy YA, Cardon L, Van Steenberge PHM, Sebakhy KO. A Comparative Review of Binder-Containing Extrusion and Alternative Shaping Techniques for Structuring of Zeolites into Different Geometrical Bodies. Catalysts. 2023;13(4).
- 379. Böhlmann W, Beta IA, Hunger B, Jobic H. Dehydration of LTA type zeolites studied by 1H, 27Al, 29Si MAS NMR, and DRIFT spectroscopy. In: Studies in Surface Science and Catalysis. 2005.
- 380. Myers P. Handbook of porous solids. Chromatographia [Internet]. 2003 Mar;57(5–6):413–413. Available from: http://link.springer.com/10.1007/BF02492417
- 381. Thomas WJ, Crittenden B. The development of adsorption technology [Internet]. Adsorption Technology & Design. 1998. 1–7 p. Available from: http://books.google.com/books?id=tXOqBBn8m-sC&pgis=1
- 382. Shanmugam S. Granulation techniques and technologies: Recent progresses. BioImpacts. 2015;5(1).
- 383. Mehlhorn D, Valiullin R, Kärger J, Schumann K, Brandt A, Unger B. Transport enhancement in binderless zeolite X- and A-type molecular sieves revealed by PFG NMR diffusometry. Microporous Mesoporous Mater [Internet]. 2014;188:126–32. Available from: http://dx.doi.org/10.1016/j.micromeso.2014.01.011
- 384. Akhtar F, Andersson L, Keshavarzi N, Bergström L. Colloidal processing and CO<sub>2</sub> capture performance of sacrificially templated zeolite monoliths. Appl Energy [Internet]. 2012;97:289–96. Available from: http://dx.doi.org/10.1016/j.apenergy.2011.12.064
- 385. López-Luna J, Ramírez-Montes LE, Martinez-Vargas S, Martínez AI, Mijangos-Ricardez OF, González-Chávez M del CA, et al. Linear and nonlinear kinetic and isotherm adsorption models for arsenic removal by manganese ferrite nanoparticles. SN Appl Sci [Internet]. 2019;1(8):1–19. Available from: https://doi.org/10.1007/s42452-019-0977-3
- 386. Feng L, Shen Y, Wu T, Liu B, Zhang D, Tang Z. Adsorption equilibrium isotherms and

- thermodynamic analysis of CH<sub>4</sub>, CO<sub>2</sub>, CO, N<sub>2</sub> and H<sub>2</sub> on NaY Zeolite. Adsorption. 2020;26(7).
- 387. Garcés-Polo SI, Villarroel-Rocha J, Sapag K, Korili SA, Gil A. A comparative study of CO<sub>2</sub> diffusion from adsorption kinetic measurements on microporous materials at low pressures and temperatures. Chem Eng J. 2016;302:278–86.
- 388. Zhou Y, Li Y, Yuan X, Hou G, Chu M, Kang H, et al. Stacked nano FAU zeolite as hierarchical Murray material for enhancing CO<sub>2</sub> diffusion kinetics. Sep Purif Technol. 2023;325.
- 389. Tao Z, Tian Y, Wu W, Liu Z, Fu W, Kung C-W, et al. Development of zeolite adsorbents for CO2 separation in achieving carbon neutrality. npj Mater Sustain. 2024;2(1):1–16.
- 390. Nguyen TH, Kim S, Yoon M, Bae TH. Hierarchical Zeolites with Amine-Functionalized Mesoporous Domains for Carbon Dioxide Capture. ChemSusChem. 2016;9(5):455–61.
- 391. Tao Z, Tian Y, Hanif A, Chan V, Gu Q, Shang J. Metal cation-exchanged LTA zeolites for CO<sub>2</sub>/N<sub>2</sub> and CO<sub>2</sub>/CH<sub>4</sub> separation: The roles of gas-framework and gas-cation interactions. Carbon Capture Sci Technol [Internet]. 2023;8(May):100126. Available from: https://doi.org/10.1016/j.ccst.2023.100126
- 392. Liu S, Chen Y, Yue B, Wang C, Qin B, Chai Y, et al. Regulating Extra-Framework Cations in Faujasite Zeolites for Capture of Trace Carbon Dioxide. Chem A Eur J. 2022;28(50).
- 393. Barthomeuf D. Framework induced basicity in zeolites. Microporous Mesoporous Mater. 2003;66(1).
- 394. Barthomeuf D. Conjugate acid-base pairs in zeolites. J Phys Chem. 1984;88(1).
- 395. Pauling L. The nature of the chemical bond. IV. The energy of single bonds and the relative electronegativity of atoms. J Am Chem Soc. 1932;54(9).
- 396. The Nature of the Chemical Bond and the Structure of Molecules and Crystals. Nature. 1941;148(3762).
- 397. Mortier WJ. Zeolite electronegativity related to physicochemical properties. J Catal. 1978;55(2).
- 398. Barthomeuf D, Coudurier G, Vedrine JC. Basicity and basic catalytic properties of zeolites. Mater Chem Phys. 1988;18(5–6).
- 399. McCabe WL, Smith JC, Harriott P. Unit operations of chemical engineering. Vol. 30, Choice Reviews Online. Singapore; 1993. p. 30-6200-30–6200.
- 400. Zhao R, Liu L, Zhao L, Deng S, Li S, Zhang Y. A comprehensive performance evaluation of temperature swing adsorption for post-combustion carbon dioxide capture. Renew Sustain

- Energy Rev. 2019;114(July).
- 401. Al Mesfer MK, Danish M, Khan MI, Ali IH, Hasan M, Jery A El. Continuous fixed bed CO<sub>2</sub> adsorption: Breakthrough, column efficiency, mass transfer zone. Processes. 2020;8(10).
- 402. Scholes C, Ho M, Wiley D. Membrane-Cryogenic Post-Combustion Carbon Capture of Flue Gases from NGCC. Technologies. 2016 Apr;4(2):14.
- 403. Holmes HE, Lively RP, Realff MJ. Defining Targets for Adsorbent Material Performance to Enable Viable BECCS Processes. JACS Au. 2021;1(6):795–806.
- 404. Otsuka N. Fireside Corrosion. In: Shreir's Corrosion. Elsevier; 2010. p. 457–81.
- 405. Boonchuay A, Worathanakul P. The Diffusion Behavior of CO2 Adsorption from a CO<sub>2</sub>/N<sub>2</sub> Gas Mixture on Zeolite 5A in a Fixed-Bed Column. Atmosphere (Basel). 2022;13(4):1–15.
- 406. Nouh SA, Lau KK, Shariff AM. Modeling and simulation of fixed bed adsorption column using integrated CFD approach. Vol. 10, Journal of Applied Sciences. 2010. p. 3229–35.
- 407. Medhat A, El-Maghrabi HH, Abdelghany A, Abdel Menem NM, Raynaud P, Moustafa YM, et al. Efficiently activated carbons from corn cob for methylene blue adsorption. Appl Surf Sci Adv. 2021;3.
- 408. Knaebel KSK. A How "To Guide" for Adsorber Design. Adsorpt Res Inc Dublin, Ohio [Internet]. 2007;23. Available from: http://www.adsorption.com/publications/adsorberdes2.pdf
- 409. Al-Janabi N, Vakili R, Kalumpasut P, Gorgojo P, Siperstein FR, Fan X, et al. Velocity variation effect in fixed bed columns: A case study of CO<sub>2</sub> capture using porous solid adsorbents. AIChE J. 2018;64(6):2189–97.
- 410. Shafeeyan MS, Daud WMAW, Shamiri A, Aghamohammadi N. Modeling of Carbon Dioxide Adsorption onto Ammonia-Modified Activated Carbon: Kinetic Analysis and Breakthrough Behavior. Energy and Fuels. 2015;29(10).

## Appendix A - CO<sub>2</sub> Adsorption Isotherms

Table A1: ZOPT-OG Equilibrium CO<sub>2</sub> Adsorption Isotherms at 0, 10, 20, 25, 30, 40 and 50 °C.

Equilibrium Pressure	Amount Adsorbed	Equilibrium Pressure	Amount Adsorbed	Equilibrium Pressure	Amount Adsorbed
kPa	mmol/g	kPa	mmol/g	kPa	mmol/g
	0°C		10°C		20°C
0.019161	0.123867	0.028292	0.118706	0.038563	0.122416
0.04147	0.246449	0.072318	0.243063	0.106881	0.237674
0.076167	0.366338	0.138811	0.363407	0.223745	0.35601
0.129235	0.483033	0.223175	0.477231	0.377334	0.462135
0.192768	0.595903	0.348938	0.593879	0.571381	0.566385
0.281612	0.715007	0.496393	0.698482	0.809307	0.667326
0.394599	0.824777	0.676802	0.802811	1.08886	0.763207
0.545426	0.938161	0.904429	0.904506	1.41365	0.85366
0.71578	1.04098	1.18145	1.00117	1.79483	0.939459
0.949228	1.13898	1.50974	1.08969	2.24083	1.02157
1.26751	1.23508	1.90667	1.17328	2.7461	1.09591
1.66371	1.32259	2.37038	1.24945	3.30322	1.16377
2.12998	1.40347	2.88434	1.31649	3.92239	1.22603
2.66458	1.47382	3.46187	1.37772	4.60343	1.28227
3.28828	1.53869	4.08068	1.43221	5.26598	1.32917
3.97798	1.59572	4.77291	1.48254	5.992	1.37241
4.72449	1.64753	5.50899	1.52831	6.80017	1.41532
5.46369	1.69044	6.18237	1.565	7.64577	1.45305
6.22329	1.72857	6.91807	1.59946	8.51926	1.48782
6.98307	1.76133	7.74359	1.63437	9.4148	1.51954
7.893	1.79579	8.59671	1.66516	10.336	1.54824
8.83511	1.82677	9.4729	1.69399	11.2755	1.57477
9.79451	1.85465	10.3722	1.72007	16.2447	1.6866
10.7776	1.88048	11.2798	1.74366	21.58	1.77145
16.2616	1.98823	16.2594	1.84576	26.3894	1.82906
20.958	2.05367	20.9981	1.91538	31.7431	1.88147
26.3518	2.11179	26.386	1.97647	37.1618	1.92628
31.8002	2.16018	31.8099	2.0265	42.5534	1.96493
37.1737	2.20059	37.1996	2.06816	47.9185	1.99812
42.5851	2.2357	42.5984	2.10472	53.1286	2.02791
47.9448	2.26686	47.9404	2.13596	58.6468	2.05582
53.3355	2.29496	53.1764	2.16443	63.9389	2.08029
58.7044	2.32021	58.8676	2.19163	69.2761	2.1025
63.9649	2.34373	63.98	2.21398	74.8174	2.12443
69.3625	2.3654	69.181	2.2354	79.8718	2.14284
74.6903	2.38543	74.6473	2.25704	85.3633	2.16218
80.0999	2.40421	80.0941	2.27629	90.6963	2.17996
85.1447	2.42175	85.3367	2.2942	95.8807	2.19787
90.6965	2.43913	90.6498	2.31231	101.349	2.21575
96.1206	2.45497	96.0525	2.32986	106.13	2.23061
101.304	2.47005	101.361	2.34713		
106.195	2.48337	106.097	2.36303		

Equilibrium	Amount	Equilibrium	Amount	Equilibrium	Amount	Equilibrium	Amount
Pressure	Adsorbed	Pressure	Adsorbed	Pressure	Adsorbed	Pressure	Adsorbed
kPa	mmol/g	kPa	mmol/g	kPa	mmol/g	kPa	mmol/g
	25°C		30°C		40°C		50°C
0.0406	0.1123	0.061235	0.118944	0.091591	0.103654	0.141945	0.110668
0.115548	0.218856	0.177374	0.226186	0.260521	0.205932	0.395151	0.209208
0.227211	0.319763	0.356269	0.330907	0.497652	0.297819	0.713761	0.294586
0.394432	0.425814	0.590149	0.430136	0.812066	0.389651	1.12456	0.377337
0.60912	0.525558	0.876898	0.521907	1.15026	0.466854	1.53507	0.446423
0.856567	0.619032	1.19862	0.606132	1.57151	0.548624	2.06045	0.517645
1.12332	0.704548	1.60126	0.694879	2.03826	0.623646	2.63738	0.585278
1.43451	0.785695	2.04036	0.775712	2.55012	0.695329	3.24011	0.645963
1.76727	0.85884	2.5255	0.850559	3.09041	0.760644	3.87808	0.705099
2.20068	0.938058	3.04992	0.919486	3.63763	0.81929	4.56485	0.761242
2.6588	1.00998	3.63632	0.98458	4.23328	0.873893	5.28672	0.81279
3.16663	1.07513	4.28457	1.04656	4.88812	0.928009	6.00416	0.859652
3.73507	1.13595	4.92957	1.09758	5.58198	0.977396	6.7798	0.905847
4.31471	1.18865	5.67366	1.14932	6.29672	1.02347	7.58091	0.948046
4.93871	1.2375	6.46267	1.19599	7.04012	1.06612	8.40404	0.988442
5.61281	1.28306	7.22639	1.23463	7.81459	1.10468	9.25481	1.02463
6.32867	1.3242	8.08046	1.27384	8.60292	1.1411	10.1271	1.05972
6.99348	1.35894	8.9669	1.30947	9.42307	1.17409	11.0214	1.0916
7.75643	1.39354	9.87412	1.34291	10.2607	1.20419	16.2348	1.24024
8.54079	1.42553	10.8085	1.37257	11.1136	1.23318	21.6045	1.34909
9.34594	1.45494	16.2513	1.50788	16.247	1.36828	26.2682	1.42147
10.1634	1.48226	21.6294	1.59932	21.6035	1.46682	31.6102	1.4892
11.0041	1.50719	26.31	1.66144	26.364	1.53327	37.0674	1.54653
16.2906	1.63116	31.7151	1.71999	31.7136	1.59388	42.4821	1.59616
20.985	1.70921	37.1418	1.7695	37.125	1.64508	47.8179	1.63925
26.3611	1.77742	42.5624	1.81223	42.5202	1.68878	53.1862	1.67729
31.7959	1.8331	47.8975	1.849	47.9578	1.72725	58.5066	1.71145
37.2494	1.87961	53.1346	1.88131	53.1564	1.76128	63.9518	1.74313
42.6409	1.9186	58.4758	1.91181	58.6564	1.79249	69.2573	1.77216
48.0235	1.95361	63.9333	1.93959	63.8991	1.81915	74.585	1.79936
53.3585	1.9844	69.2231	1.9647	69.2303	1.84422	80.0094	1.82571
58.5785	2.01261	74.6216	1.98814	74.6046	1.86763	85.3797	1.84951
63.9514	2.0393	80.0093	2.01063	80.071	1.88991	90.6908	1.87231
69.3691	2.06249	85.415	2.03127	85.5899	1.91076	95.9644	1.89413
74.7505	2.08405	90.7665	2.05058	90.8512	1.93091	101.263	1.91378
80.1051	2.10438	96.1152	2.06957	95.9758	1.94988	106.211	1.93215
85.4539	2.12343	101.221	2.08741	101.462	1.96883		
90.7417	2.14133	106.05	2.10714	106.041	1.98606		
96.0697	2.16034						
101.258	2.17826						
106.26	2.19758						

Table A2: ZOPT-BULK Equilibrium  $CO_2$  Adsorption Isotherms at 0, 10, 20, 25, 30, 40 and 50 °C.

J.C.			1	1	
Equilibrium	Amount	Equilibrium	Amount	Equilibrium	Amount
Pressure	Adsorbed	Pressure	Adsorbed	Pressure	Adsorbed
kPa	mmol/g	kPa	mmol/g	kPa	mmol/g
	0°C		10°C		20°C
0.01899	0.118063	0.042775	0.127393	0.047053	0.111735
0.041149	0.233609	0.08109	0.251763	0.117613	0.230109
0.075417	0.347588	0.159421	0.369593	0.240394	0.34206
0.135406	0.458154	0.28686	0.47728	0.434806	0.442781
0.256884	0.572198	0.487939	0.577814	0.721855	0.537619
0.436152	0.674637	0.763627	0.668712	1.15652	0.629735
0.691184	0.772236	1.10462	0.746514	1.6902	0.710114
1.04738	0.860695	1.54715	0.821507	2.34748	0.782153
1.52448	0.944712	2.07962	0.889442	3.10701	0.845897
2.10758	1.02008	2.68502	0.94893	3.97217	0.903989
2.77392	1.08569	3.31607	1.00017	4.87375	0.953281
3.4972	1.14273	4.01481	1.04726	5.81616	0.996553
4.33212	1.19518	4.77888	1.0902	6.7916	1.03621
5.19087	1.2401	5.54827	1.12779	7.90761	1.07498
6.04759	1.27831	6.37565	1.16258	9.06025	1.11033
7.04261	1.31594	7.10811	1.1903	10.2641	1.14254
8.0283	1.34928	7.98376	1.21968	11.489	1.17227
9.09342	1.38018	8.86826	1.24729	16.1485	1.26014
10.1878	1.40898	9.77188	1.27247	21.5136	1.3356
11.301	1.43559	10.6905	1.29577	26.8327	1.39538
16.1882	1.52588	16.2504	1.40273	31.6699	1.43965
21.5703	1.60066	20.9926	1.47047	36.9946	1.48253
26.359	1.65134	26.3409	1.53085	42.2963	1.52081
31.6709	1.70013	31.8011	1.58267	47.7976	1.55671
37.0661	1.74257	37.1378	1.62553	53.1461	1.58737
42.3358	1.7796	42.3443	1.66466	58.5999	1.61707
47.8116	1.81416	48.019	1.70297	63.7717	1.64212
53.2621	1.84488	53.2716	1.73495	69.1879	1.66805
58.556	1.87255	58.6563	1.76497	74.5798	1.69401
63.9	1.89847	63.7619	1.79241	79.8093	1.71629
69.3149	1.92254	69.4295	1.81987	85.3108	1.73899
74.4743	1.94555	74.6337	1.84834	90.5943	1.75897
79.8918	1.96737	80.0532	1.87558	96.0016	1.77967
85.3099	1.98847	85.1968	1.89911	101.302	1.7978
90.5085	2.00809	90.4817	1.92146	106.039	1.81593
96.0231	2.02856	95.9277	1.94411	100.007	1.01273
101.206	2.04653	101.171	1.96608		
106.128	2.06257	106.196	1.986		

Equilibrium	Amount	Equilibrium	Amount	Equilibrium	Amount	Equilibrium	Amount
Pressure	Adsorbed	Pressure	Adsorbed	Pressure	Adsorbed	Pressure	Adsorbed
kPa	mmol/g	kPa	mmol/g	kPa	mmol/g	kPa	mmol/g
	25°C		30°C		40°C		50°C
0.05139	0.112981	0.073819	0.109767	0.143836	0.114154	0.158292	0.113237
0.14231	0.227402	0.203739	0.223407	0.357459	0.215569	0.446649	0.207961
0.305818	0.340237	0.427349	0.332472	0.651723	0.313133	0.84008	0.292549
0.537852	0.437952	0.76159	0.431741	1.11287	0.403868	1.38245	0.373973
0.863365	0.527205	1.23825	0.524496	1.68254	0.485164	2.03315	0.444681
1.26554	0.602256	1.86364	0.606984	2.3815	0.555825	2.80468	0.507925
1.80841	0.677781	2.62076	0.679885	3.18596	0.618353	3.65025	0.56272
2.44642	0.74407	3.47538	0.743872	4.09898	0.675364	4.6102	0.614574
3.1448	0.800654	4.44574	0.800413	5.04692	0.724074	5.62307	0.65992
3.948	0.853245	5.53195	0.851947	6.10877	0.769137	6.60655	0.698225
4.76256	0.897434	6.7277	0.899689	7.23297	0.809623	7.74657	0.735806
5.67265	0.940045	8.01623	0.942422	8.40321	0.846845	8.91597	0.770096
6.54372	0.975053	9.34752	0.982017	9.62263	0.880816	10.1286	0.801878
7.52587	1.01027	10.7445	1.01769	10.8592	0.912925	11.3667	0.83186
8.53613	1.04218	16.097	1.11994	16.1454	1.01341	16.1972	0.922239
9.56793	1.07118	21.4795	1.19697	21.5226	1.09112	21.5501	0.998701
10.6215	1.0981	26.801	1.2574	26.7984	1.1515	26.8704	1.05871
11.6958	1.12359	32.2032	1.30725	31.648	1.19645	31.6525	1.10301
16.2248	1.20769	36.9426	1.3453	36.9824	1.23985	37.0111	1.14712
21.5622	1.28283	42.7729	1.38867	42.2643	1.27896	42.8829	1.19241
26.3641	1.3361	47.7525	1.41967	47.7383	1.31453	47.8056	1.22386
31.6766	1.38632	53.0415	1.45069	53.1523	1.34742	53.1083	1.25479
37.0774	1.42939	58.4137	1.48012	58.542	1.37703	58.4299	1.28295
42.3207	1.46862	63.8327	1.50652	63.8948	1.40343	63.8798	1.30958
47.8299	1.50478	69.1562	1.5313	69.2493	1.42931	69.1823	1.3334
53.2739	1.53728	74.4311	1.55635	74.541	1.45643	74.6137	1.35781
58.499	1.56554	79.6844	1.58018	79.9669	1.48029	79.9746	1.38043
63.939	1.59331	85.0922	1.60346	85.1365	1.50231	85.3134	1.40112
69.3505	1.61921	90.3492	1.62381	90.5352	1.52229	90.5017	1.42237
74.5635	1.64336	95.842	1.6436	95.898	1.54315	95.6134	1.43992
80.009	1.66953	101.046	1.66221	101.214	1.56154	101.12	1.4605
85.1444	1.69336	106.04	1.67963	106.163	1.57904	105.944	1.47586
90.491	1.71499						
95.6444	1.73519						
101.15	1.75565						
106.135	1.77352						

## Appendix B - 2 Adsorption Isotherms

Table B1: ZOPT-OG Equilibrium  $N_2$  Adsorption Isotherms at 0, 25 and 50 °C.

Equilibrium	Amount	Equilibrium	Amount	Equilibrium	Amount
Pressure	Adsorbed	Pressure	Adsorbed	Pressure	Adsorbed
kPa	mmol/g	kPa	mmol/g	kPa	mmol/g
	0°C		25°C		50°C
5.24295	0.022361	5.23216	0.009836	5.33571	0.005688
7.97372	0.033315	8.02495	0.015016	8.03678	0.008548
10.6036	0.043603	10.5633	0.01935	10.639	0.010839
13.3212	0.053492	13.3864	0.024327	13.3993	0.013436
15.9684	0.063412	16.0031	0.02889	16.0239	0.016273
18.5659	0.073007	18.6497	0.033351	18.6641	0.018916
21.12	0.082079	21.1952	0.037915	21.2378	0.021509
23.8532	0.09135	23.8477	0.042527	23.908	0.024415
26.4075	0.100009	26.508	0.047106	26.5705	0.026897
29.121	0.10941	29.175	0.051836	29.1864	0.029326
31.7541	0.118111	31.7748	0.056155	31.8293	0.032161
36.8438	0.134158	36.9592	0.06502	37.0701	0.037555
42.133	0.150869	42.2223	0.073856	42.2592	0.042832
47.5166	0.167061	47.5636	0.082722	47.6151	0.048368
52.6411	0.182075	52.7466	0.09099	52.849	0.05346
57.8558	0.197369	57.9005	0.099053	58.057	0.058292
63.0787	0.211935	63.2613	0.107726	63.3702	0.063596
68.3488	0.226394	68.4661	0.115606	68.6738	0.068739
73.8419	0.240889	73.8373	0.123799	73.9452	0.073816
79.1365	0.254571	79.1647	0.131814	79.1392	0.078584
84.3184	0.267682	84.3924	0.139511	84.4785	0.083596
89.5667	0.280754	89.4961	0.146829	89.5133	0.088042
94.9651	0.293452	94.9965	0.154932	95.0302	0.093191
100.067	0.306027	100.217	0.162274	100.063	0.097434
104.97	0.31732	104.752	0.168896	104.832	0.101852

Table B2: ZOPT-BULK Equilibrium N2 Adsorption Isotherms at 0, 25 and 50 °C.

Equilibrium	Amount	Equilibrium	Amount	Equilibrium	Amount
Pressure	Adsorbed	Pressure	Adsorbed	Pressure	Adsorbed
kPa	mmol/g	kPa	mmol/g	kPa	mmol/g
	0°C		25°C		50°C
5.14108	0.012943	5.3693	0.006515	5.19164	0.003852
7.97726	0.019984	8.0453	0.009436	8.04998	0.005955
10.6025	0.026214	10.6654	0.012304	10.6914	0.007491
13.3165	0.032695	13.3905	0.0153	13.3936	0.009104
15.9558	0.038983	16.0157	0.018584	16.0314	0.010739
18.5862	0.045206	18.6542	0.021322	18.6722	0.012364
21.2283	0.051453	21.2604	0.024163	21.2603	0.014042
23.8708	0.057133	23.9089	0.0273	23.9062	0.015454
26.4681	0.062918	26.5347	0.030342	26.492	0.017145
29.073	0.068684	29.0457	0.033236	29.1238	0.018868
31.7264	0.074707	31.7717	0.036535	31.8432	0.020596
36.9162	0.085815	37.004	0.042355	37.0575	0.024384
42.1675	0.096861	41.94	0.047654	42.361	0.028098
47.4853	0.107801	47.548	0.053903	47.5622	0.031525
52.7501	0.118598	52.7594	0.059679	52.8297	0.035246
58.0659	0.129282	58.1341	0.06579	58.0483	0.038839
63.2805	0.139565	63.2409	0.071689	63.4788	0.042699
68.6403	0.149876	68.6189	0.077386	68.6076	0.046226
73.8121	0.159718	73.7984	0.082796	73.7082	0.049905
78.9973	0.169434	79.0968	0.088635	79.0494	0.053316
84.2486	0.178905	84.4086	0.094025	84.3849	0.056945
89.513	0.188351	89.7172	0.099495	89.699	0.060235
94.9797	0.19796	94.9079	0.105024	95.0313	0.063778
100.177	0.207028	100.113	0.110461	100.195	0.067389
104.887	0.215048	105.119	0.115483	105.002	0.070128

## Appendix C - N<sub>2</sub> Adsorption/Desorption Isotherms at 77K

Table C1: ZOPT-OG Equilibrium  $N_2$  Adsorption Isotherms at 0, 25 and 50 °C.

Ads	orption	Desorption		
Relative Pressure	Volume Adsorbed	Relative Pressure	Volume Adsorbed	
p/p0	@STP cm <sup>3</sup> /g	p/p0	@STP cm <sup>3</sup> /g	
0.001229	67.1635	0.992097	186.001	
0.003948	70.898	0.953862	181.432	
0.013386	74.7192	0.901555	162.591	
0.024601	76.7485	0.851539	143.038	
0.032435	77.7371	0.802136	130.182	
0.049911	79.4202	0.701245	118.188	
0.075487	81.2372	0.602789	112.445	
0.096684	82.4543	0.501732	107.471	
0.121896	83.7406	0.400646	96.4496	
0.147279	84.9109	0.300625	91.9451	
0.172419	86.0012	0.199049	88.12	
0.197061	87.0383	0.102471	83.9564	
0.226004	88.2157	0.052406	80.928	
0.24824	89.0772	0.027203	78.5344	
0.271676	89.9744	0.011087	75.6234	
0.297171	90.937	0.005653	73.5175	
0.349537	92.9218			
0.400216	94.8642			
0.448328	96.9529			
0.499095	99.3323			
0.549899	101.907			
0.598947	104.649			
0.648119	107.559			
0.698179	110.826			
0.746761	114.549			
0.79673	119.076			
0.848022	125.808			
0.897022	136.332			
0.948795	157.429			
0.992097	186.001			

Table C2: ZOPT-BULK Equilibrium N2 Adsorption Isotherms at 0, 25 and 50 °C.

Adsorption		Desorption		
Relative Pressure	Volume Adsorbed	Relative Pressure	Volume Adsorbed	
p/p0	@STP cm <sup>3</sup> /g	p/p0	@STP cm <sup>3</sup> /g	
0.001245	27.7786	0.99084	160.607	
0.004071	30.2292	0.95275	153.481	
0.01725	33.7666	0.903379	138.063	
0.02299	34.5951	0.853336	121.905	
0.031984	35.6757	0.801836	105.522	
0.046202	37.0465	0.702154	87.3657	
0.076106	39.2935	0.603136	77.6604	
0.096227	40.572	0.501416	70.4509	
0.121364	42.0322	0.401458	58.4009	
0.146606	43.4192	0.301529	52.5439	
0.171636	44.7479	0.201087	47.3184	
0.196217	46.014	0.102958	41.9696	
0.221109	47.303	0.050979	38.4061	
0.246363	48.5922	0.023887	35.668	
0.271286	49.857	0.00962	33.1385	
0.296252	51.1666	0.005597	31.8081	
0.349239	53.9224			
0.398824	56.6046			
0.44831	59.3457			
0.498884	62.3215			
0.547875	65.4767			
0.597693	68.8163			
0.647893	72.6767			
0.697086	77.0145			
0.746822	81.8629			
0.796657	88.9579			
0.848129	98.8605			
0.896835	112.786			
0.946546	133.124			
0.99084	160.607			